A Multi-Material Approach to Beam Hardening Correction and Calibration in X-Ray Microtomography

Anthony N. Z. Evershed

Thesis submitted in fulfilment of the requirements for the degree of
Doctor of Philosophy in the Faculty of Medicine

Centre for Oral Growth and Development
Institute of Dentistry
Barts and The London School of Medicine and Dentistry
Queen Mary University of London

September 2013

Barts and The London
School of Medicine and Dentistry

Declaration Regarding Plagiarism

I declare that the coursework material attached herewith is entirely my own work and that I have attributed any brief quotations both at the appropriate point in the text and in the bibliography at the end of this piece of work.

I also declare that I have not used extensive quotations or close paraphrasing and that I have neither copied from the work of another person, nor used the ideas of another person, without proper acknowledgement.

Name: Anthony Neil Zbigniew Evershed

Course: PhD

Title of work submitted: A Multi-Material Approach to Beam Hardening Correction and Calibration in X-Ray Microtomography

Examination: A thesis submitted for the degree of Doctor of Philosophy, University of London

Signature:

Date:

A Multi-Material Approach to Beam Hardening Correction and Calibration in X-Ray Microtomography

Anthony N. Z. Evershed

Abstract

X-ray microtomogaphy is a non-clinical, non-destructive, and quantitative technique for determining three-dimensional mineral concentration distributions in variably radiolucent samples with a spatial resolution on the micron scale. For reasons of practicality, particularly for long-term studies, it is often not possible or desirable to utilise a monochromatic X-ray source and so microtomography using a conventional impact-source X-ray generator to produce a polychromatic photon beam is carried out instead. The use of photons of multiple energies causes the production of projection artefacts arising from preferential absorption, which impair the greyscale accuracy of the resulting reconstruction and the material concentration measurements that are derived from the linear attenuation coefficients (LACs).

The purpose of the project described in this thesis is to identify weaknesses in the current method of beam hardening correction and to develop and test a tomographic calibration and projection processing method which may demonstrably improve the quality of current beam hardening correction methods as used with the *MuCAT* microtomography equipment, which provides a world-class impact-source microtomography research and production facility at Barts and The London School of Medicine and Dentistry.

An overview of the physical basis of X-ray computed tomography and X-ray microtomography is given from first principles, and examples of quantitative applications of the techniques, which generally depend on accurate reconstruction of linear attenuation coefficient values, are discussed. The major sources of artefacts in X-ray microtomography are discussed, particularly

those with a direct impact on reconstructed linear attenuation coefficient values. Beam hardening is identified as an error source of particular interest, with secondary research on the effects of any beam hardening correction method on the severity of Compton scatter artefacts, and a critical review is carried out of historical attempts to reduce or mitigate these artefacts, particularly the single-material parameter-optimisation approach in service at the beginning of the research project.

A 'carousel' test piece comprising multiple attenuators of multiple materials along with attenuation optimisation software based on varying multiple system parameters in order to extend the functionality and usability of the existing correction model, and qualitative results have so far been gathered suggesting the use of this system over the pre-existing attenuation wedge and parameter-optimisation method.

A study of the effects of tuning the photon energy to which calibrations are made is carried out, showing improved linear attenuation coefficient recovery at a higher energy than was previously believed to be optimal, and a significant effect arising from X-ray generator target evaporation leading to spatial changes and time-dependence of the target thickness parameter is measured, suggesting that automated calibration as a standard part of the measurement process is required. A stability experiment is carried out using this method in order to examine the possibility of inconsistency resulting from ageing of the filament cathode, which is found not to significantly impact the quality of results.

An immersion tank is developed in order to ensure beam hardening correction validity in the case of dual-material specimens where a radiodensity-matching fluid can be provided and the sample is suitable for immersion. Experimental comparison using a commercial beam hardening calibration device as the specimen reveals significantly improved hydroxyapatite concentration measurement recovery. An in-scatter experiment was carried out on the immersion tank, and it was found that there was a significant scatter contribution when the tank was filled in the case where the sample thickness is much less than the tank thickness. Proposals are presented for further work to improve reconstruction quality through of scatter reduction techniques in impact-source microtomographic systems, and to utilise the immersion tank for in situ chemical erosion

experiments.

The effects of the improvements to the beam hardening process are demonstrated using a biological specimen to demonstrate qualitative changes in reconstruction, particularly in improved dark levels surrounding the specimen. A second experiment is carried out in order to test the reproducibility of results, which is found to be improved by approximately four times over the same dataset corrected using the pre-existing beam-hardening calibration method.

Contents

Declaration **2**

Abstract **3**

Table of Contents **6**

List of Figures **13**

List of Tables **18**

Glossary **19**

Acknowledgements and Dedication **21**

---

1 Introduction and Background **22**

1.1 Physical Background to X-Ray Imaging 23

1.1.1 The Electromagnetic Spectrum 23

1.1.2 X-Ray Production 24

1.1.2.1 Synchrotron Radiation 24

1.1.2.2 Impact-Source X-Ray Production 25

1.1.2.3 Practicalities of X-Ray Production 26

1.1.3 X-Ray Interactions 27

1.1.3.1 Photoelectric Absorption 27

1.1.3.2 Compton Scattering 28

1.1.3.3 Pair Production 29

1.1.3.4 Interaction Dominance 29

1.1.4 X-Ray Detection 30

1.1.4.1 Photographic Film . . . 30
1.1.4.2 Scintillators . . . 30
1.1.4.3 Photomultipliers . . . 31
1.1.4.4 Image Intensifiers . . . 31
1.1.4.5 Charge-Coupled Devices . . . 32
1.1.4.6 Flat-Panel Detectors . . . 34
1.2 Computed Tomography . . . 34
1.2.1 Computed Tomography Generations . . . 34
1.2.1.1 First-Generation Tomography . . . 34
1.2.1.2 Second-, Third- and Fourth-Generation Tomography . . . 34
1.2.1.3 Volumetric Tomography . . . 36
1.2.2 Tomographic Reconstruction . . . 37
1.2.2.1 The Radon Transform . . . 37
1.2.2.2 Filtered Back-Projection . . . 38
1.2.2.3 Mineral Concentration Recovery . . . 38
1.2.3 Phase-Contrast Computed Tomography . . . 40
1.2.3.1 Phase Contrast by Interferometry . . . 40
1.2.3.2 Phase Contrast by Refraction . . . 41
1.2.3.3 Phase Contrast by Direct Imaging . . . 41
1.2.4 Comparison with Other Quantitative Methods . . . 42
1.2.4.1 Mass Spectrometry . . . 42
1.2.4.2 Nuclear Magnetic Resonance Spectroscopy . . . 42
1.2.4.3 X-ray Absorption Spectroscopy . . . 42
1.2.4.4 Dual-Energy X-Ray Absorptiometry . . . 42
1.3 The *MuCAT* Scanners . . . 43

2 X-Ray Microtomography: Applications 46

2.1 Biological X-ray Microtomography . . . 46
2.1.1 Hard-Tissue Studies . . . 47
2.1.2 Soft-Tissue Studies . . . 47
2.2 X-Ray Microtomography in Materials Science and Industry . . . 48
2.3 Microtomography in Historical and Archaeological Contexts . . . 49

2.3.1 Fossil Examination 49
2.3.2 Project *Apocalypto* 50

3 Microtomographic Artefacts **53**
3.1 Ring artefacts 53
3.1.1 Time-Delay Integration 56
3.2 Beam Hardening 59
3.2.1 Causes of Beam Hardening 59
3.2.2 Effects on Reconstruction 61
3.2.3 X-Ray Target Self-Absorption 62
3.2.3.1 Pitting-Induced Beam Hardening Variation 63
3.2.4 X-ray Beam Filtering 65
3.2.4.1 Absorption Edges and Band-Pass Filtering 65
3.3 Scatter Artefacts 66
3.3.1 Scatter Distribution 67
3.3.2 Scatter Effects on Reconstruction 67
3.4 Other Artefacts 69
3.4.1 Motion Artefacts 69
3.4.2 Centre of Rotation Artefacts 70
3.4.3 Field-of-View Artefacts 70
3.5 Chapter Conclusion 71

4 Literature Review: Artefact Mitigation Strategies **72**
4.1 Beam Hardening Calibration and Reduction 72
4.1.1 Water Bags in Computed Tomography 72
4.1.2 Dual-Emission Scanning 73
4.1.3 Segmentation 73
4.1.4 Modelling and the Role of *A Priori* Knowledge 74
4.2 X-Ray Scatter 75
4.2.1 Scatter Detection 75
4.2.2 Scatter Reduction and Correction 76
4.2.3 Scatter Quantification 77

4.3 Chapter Conclusion 78

5 Beam Hardening Correction of *MuCAT* Scans **79**

5.1 Aluminium Step Wedge 79

5.2 Correction Software 82

5.3 Performance and Limitations 83

5.4 Chapter Conclusion 84

6 Materials and Methods **86**

6.1 *MuCAT* Data Processing and Reconstruction 86

6.1.1 M2PREPROC 86

6.1.2 SHIFTFIX 88

6.1.3 ConeRec 88

6.1.4 MTRIM 88

6.1.5 Aluminium Correction 89

6.2 *MuCAT* Data Analysis and Visualisation 90

6.2.1 Tomview 90

6.2.2 Drishti 90

6.3 X-ray Field Measurements 90

6.3.1 Multi-Element Carousel 90

6.3.2 Beam Hardening Correction Software: Infrastructure 94

6.3.2.1 Computer Hardware and Operating System 94

6.3.2.2 Spekcalc 94

6.3.2.3 XCOM 95

6.3.2.4 Interactive Data Language 95

6.3.2.5 AMOEBA Optimisation Function 95

6.3.3 Beam Hardening Correction Software: Implementation 96

6.4 Dual-Species Beam Hardening 97

6.4.1 Immersion Tanks 97

6.4.2 Scanco Medical Phantom 102

6.4.3 Beam Hardening Correction Procedure 103

7 Beam Hardening Correction **104**

7.1 Experimental Implementation 104

7.1.1 Synthesis of Test Piece 104

7.1.2 Scanning and Beam Hardening Correction Measurement 105

7.1.3 Reconstruction Analysis 105

7.2 Results and Discussion 106

7.3 Conclusion 106

8 Calibration Energy Determination **108**

8.1 Simulation Design 108

8.2 Simulation Results and Validation 110

8.3 Conclusion 114

9 Time-Dependent Tungsten Beam Hardening Variation **115**

9.1 Experimental Context 115

9.2 Experimental Implementation 115

9.3 Projection Analysis 116

9.4 Results and Discussion 117

9.5 Conclusion 121

10 Time-Dependent Attenuation Coefficient Variation **122**

10.1 Experimental Context 122

10.2 Experimental Implementation 122

10.3 Reconstruction Analysis 123

10.4 Results 123

10.5 Conclusion 129

11 Multi-Modal Beam Hardening Correction **130**

11.1 Experimental Implementation 130

11.2 Reconstruction Analysis 131

11.3 Results and Discussion 131

11.4 Conclusion 133

12 Demonstration of Utility **135**

12.1 Biological Experiment 135

12.1.1 Experimental Implementation 135

12.1.2 Reconstruction Analysis 136

12.1.3 Results and Discussion 136

12.2 Repeatability and Reliability Experiment 139

12.2.1 Experimental Implementation 139

12.2.2 Reconstruction Analysis 139

12.2.3 Results and Discussion 140

12.3 Chapter Conclusions 140

13 General Discussion, Conclusions and Further Work **141**

13.1 The *Status Quo Ante* 141

13.2 Thesis' Implications for Beam Hardening Correction 143

13.3 Effects in Production Scanning 144

13.4 General Conclusions and Practical Significance 144

13.5 Further Research 145

13.5.1 Long-Term Calibration Stability Experiment 146

13.5.2 Dual-Emission Scanning and Anti-Scatter Grids 146

13.5.3 Real-Time Dissolution Experiment 146

Appendices **164**

A Spekcalc Input Files **164**

B Carousel Correction Script **167**

C Calibration Energy Determination Scripts **195**

C.1 Attenuation Finder 195

C.2 HVL to LAC/MAC Converter 199

D Program Reference **200**

E Abstracts for Conference Presentations and Papers **202**

E.1 List of conference presentations arising from work presented in this thesis 202

E.2 List of papers arising from work presented in this thesis 204

E.3 Samples of poster presentations 206

List of Figures

1.1 Schematic of the 'Soleil' synchrotron facility near Paris, France (EPSIM 3D/JF Santarelli), showing the electron linear accelerator (centre) and undulators (at the start of each beamline.) 25

1.2 Schematic of a Coolidge X-ray tube, showing the cathode heated by potential U_h and the electrons being drawn down potential U_a to the anode, as well as a water cooling system (W_{in} and W_{out}). 26

1.3 Graph showing the contributions to X-ray attenuation from the photoelectric effect, Compton scatter and Thomson scatter in hydroxyapatite for photon energies 0 – 150 keV. 30

1.4 Schematic of the clocking process in charge-coupled devices, showing part of a row of CCD elements. (Adapted from (Schmid, 2005).) 33

1.5 Schematics of CT scanner generations: 1st-generation (a), 2nd-generation (b), 3rd-generation (c) and 4th-generation (d), showing X-ray source (S), beam plan and detector (D). Rotating-specimen and rotating-source geometries are geometrically equivalent. 35

1.6 Schematic of cone-beam tomography geometry, showing X-ray tube, beam plan, sample and detector (Davis, 2011). 36

1.7 Generation of a sinogram of a virtual specimen based on 180 projections, using the Radon Transform plugin for ImageJ (Abramoff et al., 2004; Farrell, 2006). . . 39

1.8 Graph showing the linear attenuation coefficient of air at the International Standard Atmosphere (15 °C and 101.325 kPa.) 40

1.9 Interior of *MuCAT* 2, showing X-ray tube and rotatable target (left, with blue cooling hoses) with aluminium and copper filters, dental specimen (foreground, centre) mounted on rotation stage via a chuck-based stand, itself mounted on an elevation-translation stage, and the X-ray camera (right) in a shielded container to reduce scattered X-ray photon detection. 44

2.1 Cross-section of a tooth imaged by XMT, showing demineralisation in the enamel and dentin 48

2.2 Cutaway rendering of an oak gall, showing gall wasp larvae gestating inside. Rendered by Ajay Limaye using Drishti. 50

2.3 Horizontal section of a large loose-wound scroll imaged by XMT, showing areas of possible ink (brighter spots) and regions of contact between layers of parchment, rendered using Tomview. 51

2.4 Vertical cutaway section of a smaller loose-wound scroll imaged by XMT, showing visibility of iron gall ink on parchment, rendered using Drishti. 52

3.1 Simulated ring artefact, using the Radon Transform plugin for ImageJ (Abramoff et al., 2004; Farrell, 2006). 54

3.2 Time sequence showing TDI readout of captured image (red column of pixes on the left of the array) with camera motion (Ahmed, 2010). 58

3.3 Unfiltered tungsten X-ray emission spectrum at a peak potential of 90 kVand a take-off angle of 22°. The cut-off below 9 keV is an artefact of the *Spekcalc* spectrum generation software. (Poludniowski et al., 2009) 59

3.4 Photoelectric absorption spectra for common filter materials. 60

3.5 Beam hardening of a 90 kV, 22° tungsten emission beam, by copper and aluminium. The median energy is approximately 26.5 keV in the unfiltered spectrum, and 44.0 keV in the filtered spectrum. 61

3.6 Demonstration of dishing artefacts arising from uncorrected beam hardening in a uniform specimen. 62

3.7 Schematic of a cylindrical X-ray target and window, with the takeoff angle of the centre of the cone-beam labelled φ. The inset shows the formation of a pit and its effect on X-ray beam hardness distribution. 64

3.8 Simulated detected spectrum of a 60 kVp, 22° tungsten emission beam. 67

3.9 Compton scatter differential cross-section distribution for the tomographically-relevant energy 40 keV, with 400 keV and 4 MeV distributions to show decrease in backscatter with increasing photon energy. The distributions have been normalised to 1 at $\theta = 0°$. 68

5.1 Aluminium step wedge viewed perpendicular to beam path, showing layers of filter and frame. 81

6.1 Flow diagram showing the interaction of the files and programs used in preprocessing and reconstruction. Red outlining of data elements and processes denotes creation as part of this thesis. 87

6.2 Schematic of the beam hardening 'carousel', showing filter types and illumination of the copper filter by the X-ray beam. 92

6.3 'Carousel' test piece, showing attenuation filters and frame, including early low-attenuation PMMA filter (since replaced with aluminium). 93

6.4 User interface to the calibration program, running under Microsoft Windows 7 with the Aero interface running. The toolbar icons allow the `settings.txt` file in the current working directory to be reloaded, another settings file to be loaded or the current settings to be saved at an arbitrary location. The inactive text-entry fields are activated on a click of the additional filer or liquid immersion checkboxes. 98

6.5 Example visual output of the calibration program. The red and black lines denote measured and calculated attenuation values of the carousel respectively (plotted once for each horizontal line, with the filter number serving as the abscissa axis). The final point is a zero-attenuating virtual filter. The green lines connect measures of error. 99

6.6 Schematic of the large immersion tank in plan (a) and front elevation (b) views, showing the thin perspex windows added in order to most closely approximate a water-only system. The specimen is placed between the two thin PMMA windows. 100

6.7 Schematic of the smaller immersion tank system, including multi-species specimen on mounting post. Clamps not shown for clarity. 101

6.8 Plan and side views of the Scanco Medical phantom, showing HA/PMMA rods and mounting pin. Increasing greyscale level (with white = 0) denotes increasing radiodensity, though this is not depicted to scale. 102

8.1 Graph showing the relation between virtual step wedge element thickness and the natural logarithm of mass attenuation from the calibration of the in-situ carousel projections from the `te_alrod8` scan. 111
8.2 Graph showing reconstructed linear attenuation coefficients for eight scans of an aluminium rod, calibrated to 40 keVusing accelerating voltage optimisation. . . . 112
8.3 Graph showing reconstructed linear attenuation coefficients for eight scans of an aluminium rod, calibrated to 44.5 keVusing accelerating voltage optimisation. . . 113
8.4 Graph showing reconstructed linear attenuation coefficients for eight scans of an aluminium rod, calibrated to 44.5 keVusing copper filter optimisation. 113

9.1 Graph showing the relation between calibration block number and the value of the tungsten filter thickness parameter. 118
9.2 Graph showing the relation between calibration block number and the value of the caesium iodide scintillator thickness parameter. 118
9.3 Graph showing the relation between line number and the value of the tungsten filter thickness parameter. 119
9.4 Graph showing the relation between line number and the value of the caesium iodide filter thickness parameter. 120
9.5 Graph showing the relation between the attenuator number and the ratio of mass attenuation between first and last block, calibrated with the first block's attenuations. 121

10.1 Linear attenuation coefficient measurements of hyperpure aluminium rod scanned at 90 kV, with theoretical LAC of aluminium at 40 keVmonochromatic (National Institute of Standards and Technology, 2010). Error bars (showing standard deviation) added for completeness.). 124
10.2 Graph of percentage reconstructed LAC deviations from the nominal value. . . . 125

10.3 Graph of optimised tungsten filter thicknesses. Errors not shown due to comparatively large systematic error in results arising from line-dependent tungsten beam hardening (as described in Chapter 9.) Red lines denote filament changes. . 126
10.4 Graph of optimised caesium iodide scintillator thicknesses. Errors removed as before; red lines denote filament changes. 126
10.5 Graph of optimised electron gun accelerating voltages. Error is not shown here as the voltages are arrived at for the whole projection rather than on a line-by-line basis, so there is no variation across the height of the detector. Red lines denote filament changes. 127
10.6 Tungsten thickness parameter plotted against X-ray filament life. 127
10.7 Caesium iodide thickness parameter plotted against X-ray filament life. 128
10.8 Accelerating voltage parameter plotted against X-ray filament life. 128

11.1 Renderings of the Scanco Medical phantom, made using `Drishti`. 132

12.1 `TOMVIEW` image of X-Y slice 321 of the zygomatic bone specimen, showing cortical and trabecular bone regions and voids within both. 137
12.2 Comparison of reconstructions (from top to bottom, carousel correction, step wedge correction and no beam hardening correction) of X-Y slice 321, rotated clockwise by 90° to allow viewing of all three images. 138

List of Tables

3.1 *MuCAT* 2 filter thicknesses. 65
3.2 Composition of BG36 didymium glass. 66

5.1 *MuCAT* 2 aluminium step wedge filter thicknesses. 82
5.2 Commonly-used accelerating voltages and monochromatic calibration energies. . 83

6.1 Material profile of the beam hardening carousel. 91

7.1 Hydroxyapatite disc measurements of density as calculated volumetrically and from LAC measurements made by XMT. 106

8.1 Calculated calibration energies for regularly-used accelerating voltages. 110
8.2 Calculated calibration energies for regularly-used accelerating voltages. 112

10.1 Results of repeated scanning of a hyperpure aluminium rod over time, with correction time-dependence eliminated as a confounding factor. 124

11.1 Results of non-immersed scan of the Scanco Medical phantom. 133
11.2 Results of immersed scan of the Scanco Medical phantom. 133

12.1 Mean and standard deviation values of linear attenuation coefficient in *O. aries* cortical bone, demonstrating changes due to beam hardening correction. 136
12.2 Mean and standard deviation values of linear attenuation coefficient in aluminium rod, demonstrating changes due to use of multi-material carousel with multi-variable correction method over aluminium step-wedge beam hardening correction. 140

Glossary

BLSMD

Barts and The London School of Medicine and Dentistry, the medical faculty of QMUL.

CCD

Charge-Coupled Device.

CT

Computed Tomography.

CWD

Current Working Directory.

HA, HAP

Hydroxyapatite.

HVL

Half-Value Layer.

IDL

Interactive Data Language.

LAC

Linear Attenuation Coefficient.

MAC

Mass Attenuation Coefficient.

PMMA

Poly(methyl methacrylate).

QMUL

Queen Mary University of London.

SNR

Signal-to-Noise Ratio.

XMT

X-ray Microtomography.

Z

Atomic Number.

Acknowledgements

My thanks:

to my supervisors, Graham Davis and Pete Tomlins, for keeping me on course.

to the Engineering and Physical Sciences Research Council for their financial support under grant number EP/G007845/1.

to David Mills and Steve Figaro for their advice.

to Kathleen, for keeping me sane.

"*We wish to pursue the truth no matter where it leads. But to find the truth, we need imagination and skepticism both. We will not be afraid to speculate, but we will be careful to distinguish speculation from fact. The cosmos is full beyond measure of elegant truths; of exquisite interrelationships; of the awesome machinery of nature.*"

Carl Sagan – Cosmos: A Personal Voyage

Chapter 1

Introduction and Background

The use of X-rays as a means to provide structural and compositional information about the world has a long and varied history, from the first uses of "Röntgen rays" to examine the placement of the bones of the hand and foot onwards. In the early 1970s the use of computed tomography (CT) was pioneered by Hounsfield and Cormack, and the production of true three-dimensional data-sets became a possibility with the development of cone-beam reconstruction algorithms in the 1980s.

At the same time, the use of tomography at the micro-scale to provide accurate mineral concentration measurements by the analysis of reconstructed linear attenuation coefficients (LACs) was demonstrated in Elliott and Dover (1982), named X-ray Microtomography (XMT). The work presented in this thesis is a result of the combination of the need for determination of linear attenuation coefficients with the compromises required for performing XMT in a laboratory environment. XMT is a method by which computed tomography may be applied to the non-destructive investigation of microscopic structures and high-resolution mineral concentration measurement (Cesareo et al., 1999). For this reason, most of the discussion presented here will be applicable equally to XMT and CT, and therefore in most cases the terms will be used interchangeably.

1.1 Physical Background to X-Ray Imaging

In order to understand the compromises required in order to perform tomography in a laboratory environment it is necessary to briefly explain the physical theory involved.

1.1.1 The Electromagnetic Spectrum

Electromagnetism is one of the four fundamental forces of physics, and is mediated by the photon, a chargeless particle with zero rest mass (Kobychev and Popov, 2005). The wavelength λ and frequency ν of a photon are determined by the photon energy through the formula $E = h\nu = \frac{hc}{\lambda}$, where c is the speed of light in a vacuum and h is the Planck constant (Cassidy et al., 2002, p. 341). The energy spectrum of photons is by convention divided into named (albeit sometimes overlapping) ranges, where the photons' interactions with matter are similar. In order of increasing photon energy, these ranges are named in ISO (2007) as:

- Radio waves (<82.66 μeV)
- Microwaves (82.66 μeV to 1.24 meV)
- Infra-red/IR (1.24 meV to 1.631 eV)
- Visible light (1.631 eV to 3.263 eV)
- Ultraviolet/UV (3.1 eV to 12.4 eV)
- Extreme Ultraviolet (10.33 eV to 124 eV)
- X-rays
  - Soft X-rays (124 eV to 12.4 keV)
  - Hard X-rays (12.4 keV to 1.24 MeV)
- Gamma (γ) rays (>1.24 MeV)

By further convention, in radiation science the term 'X-ray' is reserved for photons produced by the acceleration of electrons, while 'Gamma rays' are photons produced by atomic process such as pair production (L'Annunziata, 2003, p. 58) Thus, notwithstanding the energy ranges above, it may be correct to refer to a 'gamma ray' photon in the keVrange, which is indistinguishable

from an X-ray photon of the same energy if the source is unknown. Photons that are more energetic than an atom's ionization energy (between 3.89 and 24.59 eV) can cause the removal of electrons from their orbitals (as discussed later), and are therefore known collectively as ionizing radiation. While computed tomography (CT) can be carried out using visible light and gamma rays, the scope of my project is limited to X-ray tomography.

1.1.2 X-Ray Production

X-rays are produced by Bremsstrahlung (German: *lit.* 'braking radiation'), which is emitted when a charged particle undergoes deceleration, in order to satisfy conservation of energy. There are two major types of system which are used to produce X-rays for the purposes of CT and XMT, whose properties affect the nature of the X-ray fluxes they produce.

1.1.2.1 Synchrotron Radiation

A synchrotron is essentially a toroidal accelerator of charged particles, mainly comprising an evacuated storage ring. Electrons are ejected from a hot cathode by thermionic emission and given an initial velocity using a potential gradient in a linear accelerator before being injected either into a synchrotron ring of intermediate size to increase the velocity further or directly into the storage ring, as shown in Figure 1.1. By the point of injection the electrons have been accelerated to a significant fraction of the speed of light c, are forced into a closed path around the centre of the torus by constant-frequency electromagnets (Dia, 2010). Insertion devices placed on the storage ring cause the Bremsstrahlung emission of X-rays on the straight line tangential to the circular beam-path, either as a broad-band beam in the case of undulators or as a more intense narrow-band beam in the case of wigglers (Knoll, 2000, p. 19) (Iwanenko and Pomeranchuk, 1944; Elder et al., 1947). This beam emerges from the storage ring onto a beamline. A monochromatic beam can be easily obtained using a double crystal monochromator to select a specific wavelength through Bragg's law for diffraction,

$$n\lambda = 2dsin\theta \tag{1.1}$$

where d is the crystal lattice spacing and θ is the scattering angle for photons of the desired wavelength (Bragg, 1913). X-ray microtomography has been carried out at a large number of

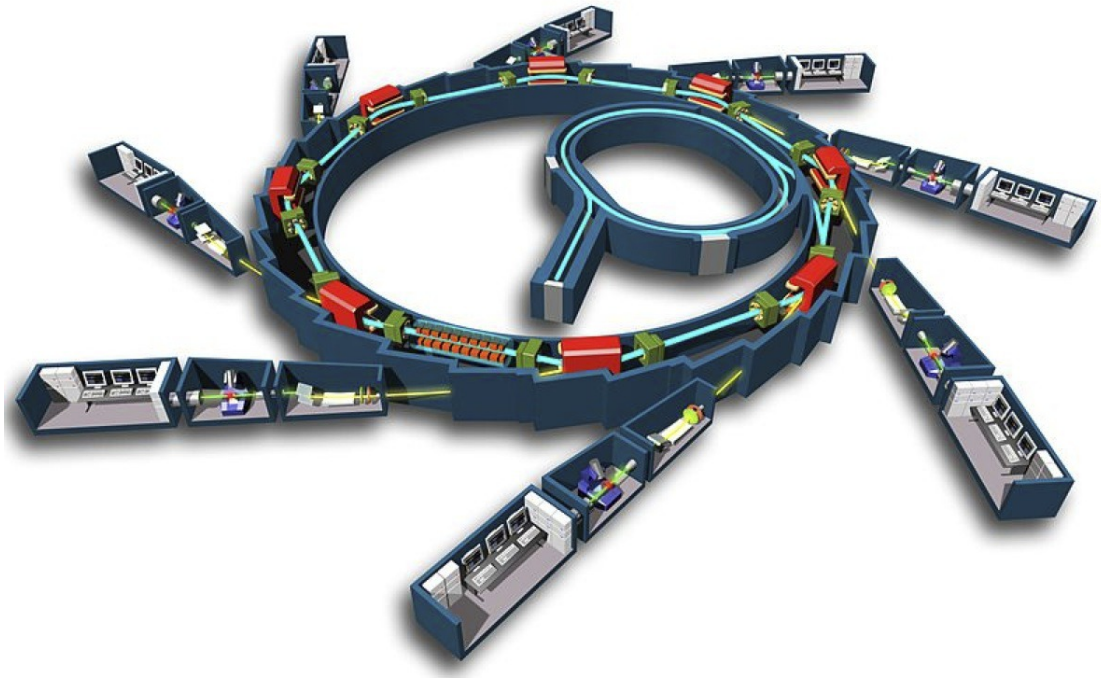

Figure 1.1: Schematic of the 'Soleil' synchrotron facility near Paris, France (EPSIM 3D/JF Santarelli), showing the electron linear accelerator (centre) and undulators (at the start of each beamline.)

synchrotron beamlines (Kinney et al., 1989; Ham et al., 2006; Papadimitropoulos et al., 2008; Drews et al., 2008).

1.1.2.2 Impact-Source X-Ray Production

X-rays can also be produced using a target (tungsten, for example) to achieve rapid deceleration of electrons. Again, electrons are produced by a heated cathode (*C*) as shown in Figure 1.2 and accelerated down a potential gradient spanning anywhere from 12 kV (the lower limit required to produce 'hard' X-ray photons as defined by ISO 21348) to several hundred kilovolts. The electrons impact on a metal target surface on the anode (*A*), causing them to decelerate almost instantaneously to rest, and to emit X-rays via Bremsstrahlung (Knoll, 2000, pp. 17-18). This is then collimated by the X-ray tube's aperture. Waste heat is removed from the anode by water cooling. Since the X-ray flux produced by this method is much smaller than that of a synchrotron and the beam is divergent from the 'pencil beam' produced by a synchrotron, it is not possible to use a crystal monochromator to make the beam monochromatic; a beam so tightly collimated as to be effectively parallel (and therefore suitable for the monochromator) would require the collimator to be placed at a sufficient distance from the source that the beam would have too

low a flux to be of practical use. The beam therefore retains the Bremmstrahlung spectrum with characteristic spikes of intensity caused by electrons transitioning into lower shells (known as K- or L-emission from the names of the receiving shells). (Shultis and Faw, 2008, pp. 468-470) This spread of X-ray energies leads to tomographic artefacts which will be discussed later.

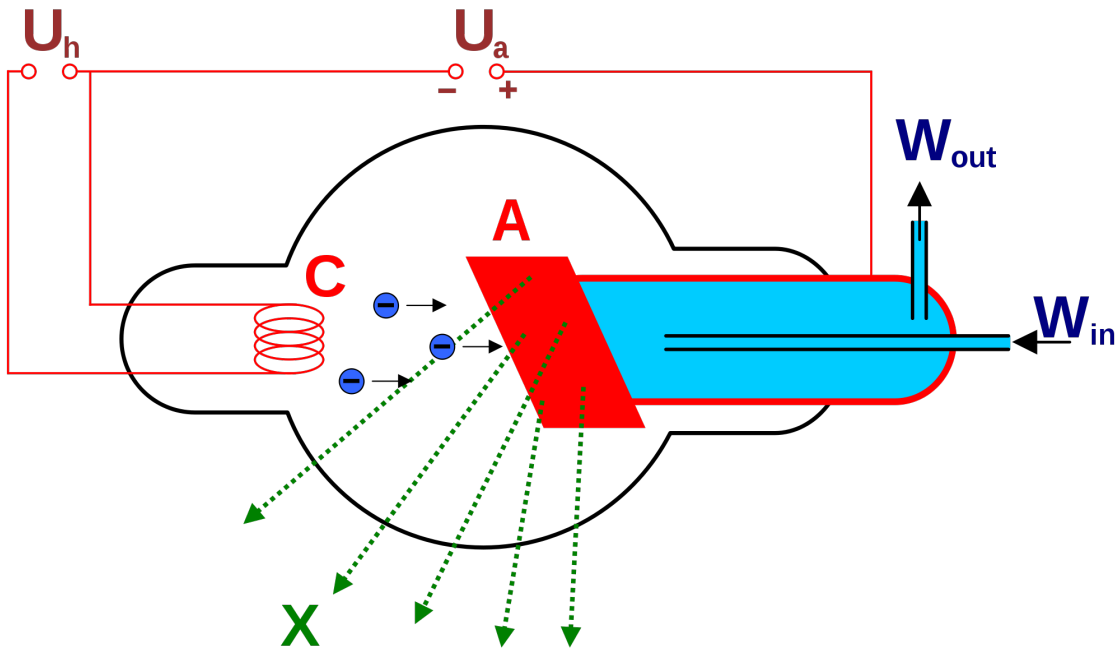

Figure 1.2: Schematic of a Coolidge X-ray tube, showing the cathode heated by potential U_h and the electrons being drawn down potential U_a to the anode, as well as a water cooling system (W_{in} and W_{out}).

1.1.2.3 Practicalities of X-Ray Production

Although a synchrotron can produce an X-ray beam that is both more intense and more spatially well-defined than that of a conventional X-ray tube, permitting the use of a monochromator while preserving sufficient beam power for tomography in a reasonable scan duration (and therefore not subject to beam hardening artefacts as will be discussed in Section 3.2) (Papadimitropoulos et al., 2008; Lee et al., 2008), it should be noted that an X-ray tube is both vastly smaller and less expensive to operate (Drews et al., 2008), and therefore can be used on the bench-top in an academic, industrial or medical setting without the expense of experimental time on an SR beamline (Sasov and van Dyck, 1998). Impact-source systems also have the advantages of large scanning volume and field of view and ease of use (Brunke et al., 2008), and are used in the Institute of Dentistry at Barts and The London School of Medicine and Dentistry (BLSMD) as the basis for the *Mu-CAT* microtomographic systems developed in Davis and Elliott (2004) and Davis et al. (2010),

which are described in detail in Section 1.3.

1.1.3 X-Ray Interactions

There are three dominant photon—matter interaction processes over the X-ray energy range: photoelectric absorption, Compton scattering and pair production, though there are other minor interactions such as Thomson scattering as shown in ((Shultis and Faw, 2008, p. 178)). While Thomson scatter interactions dominate over Compton scattering at low photon energies (below approximately 30 kiloeV in the case of interactions in hydroxyapatite), the interaction coefficient for photoelectric absorption is still one or more orders of magnitude greater, as shown in Figure 1.3.

1.1.3.1 Photoelectric Absorption

Photoelectric absorption occurs when a photon is absorbed by an electron in a material and imparts enough energy to the electron to overcome its binding energy (this amount of energy is also known as the 'work function' of the electron), thereby causing the electron to be freed from its atom and casting an X-ray 'shadow'. Despite this energy requirement, photoelectric absorption dominates the attenuation characteristics of a material at low photon energies, particularly for materials with a high atomic number Z, as the absorbers' photoelectric cross-sections have a Z^4 to Z^5 dependence.

In the simplest case, we can consider the radiation incident on the sample volume to be a beam of photons, all travelling parallel to the x axis. The transmission of X-rays through the volume is, if scattering is neglected, then described by Beer's law:

$$I^o(x) = I^o(0)e^{-\mu_t x} \tag{1.2}$$

where $\mu_t = \lim_{x\to 0} \frac{P(\Delta x)}{\delta x}$. Note that this only holds for non-scattering monochromatic radiation. (Shultis and Faw, 2008, p. 168) Radiocontrast agents such as compounds of iodine or barium may be used where the attenuation due to photoelectric absorption of structures of interest in a specimen are too similar to their surroundings, particularly in living biological tissues where normal physiological processes will cause the agent to spread through the area of interest

before the patient is scanned (Grabherr et al., 2008).

1.1.3.2 Compton Scattering

Compton scattering[1] is an intermediate-energy interaction, again occuring between the incident X-ray photon and an electron, where the photon energy is greater than the energy required to eject the electron from its atom. In this case, the photon is not absorbed but retains the remaining energy, thereby becoming a 'softer' X-ray travelling at some angle θ to its original trajectory (known as the scattering angle) (Knoll, 2000, p. 50). Thus, in the photon's frame of reference, the net momentum component perpendicular to the photon's initial path remains zero, satisfying conservation of momentum. (Shultis and Faw, 2008, pp. 27-28) The interaction's energy exchange is described by the formula:

$$\lambda' - \lambda = \frac{h}{m_0 c}(1 - cos\theta) \tag{1.3}$$

where λ and λ' are the incident and scattered photon wavelengths and m_0 is the electron mass, as derived by (Compton, 1923). It should therefore be noted that the interaction does not remove the X-ray photon from consideration, and that the process is stochastic rather than deterministic in terms of photon scattering angle, the distribution of which is governed by the function derived by (Klein and Nishina, 1994, pp. 113-129), shown in Equation 1.4.

$$\frac{d\sigma}{d\Omega} = Zr_0^2\left(\frac{1}{1+\alpha(1-cos\theta)}\right)^2\left(\frac{1+cos^2\theta}{2}\right)\left(1+\frac{\alpha^2(1-cos\theta)^2}{(1+cos^2\theta)[1+\alpha(1-cos\theta)]}\right) \tag{1.4}$$

where r_0 is the classical electron radius and α is the ratio of the photon energy and the electron rest-mass energy

$$\alpha = \frac{h\nu}{m_0 c^2}.$$

(Knoll, 2000, p. 51).

The Compton scatter cross-section is proportional to Z while photoelectric absorption has a cross-section proportional to Z^{4-5} (Knoll, 2000, pp. 49-51). Low-Z specimens are particularly common in medical CT and biological XMT, owing to the large water component of living tissues.

[1] An excellent work on the history and theory of Compton scattering may be found in (Williams, 1977).

1.1.3.3 Pair Production

A high-energy X-ray photon may decay into a particle-antiparticle pair (of which the least energetic is the electron-positron pair) due to mass-energy equivalence. Since the laws of conservation of mass and conservation of energy are only satisfied in this case when the particle-antiparticle pair have equal and opposite velocities, the photon's initial momentum must be absorbed by an atomic nucleus. Under all normal circumstances, the particle-antiparticle pair will immediately annihilate. The probability of this interaction is related to the atomic number of the nucleus by approximately Z^2 (Hubbell, 2006).

This section is included mostly for completeness, since pair production is a phenomenon which occurs only when the photon has an energy of at least 1.022 MeV or more (twice the rest energy of an electron, permitting the creation of an electron-positron pair) (Shultis and Faw, 2008, p. 181), and can therefore be ignored for the purposes of impact-source tomography (van de Casteele et al., 2002).

1.1.3.4 Interaction Dominance

Since the interactions between X-ray photons and matter are atomic number-dependent, the dominance of attenuation modes will vary from material to material (Abdel-Rahman and Podgorsak, 2010). However, Compton scatter is dominant at higher energies than photoelectric absorption since it requires both enough energy to free an electron from its host atom and remaining energy for the emission of a longer-wavelength photon. Using hydroxyapatite (HAP, chemically $Ca_5(PO_4)\cdot 3\,(OH)$) as an example of a material of interest for medical and biophysical tomography (in Figure 1.3), it can be seen that the interaction cross-sections are equal at approximately 55 keV.

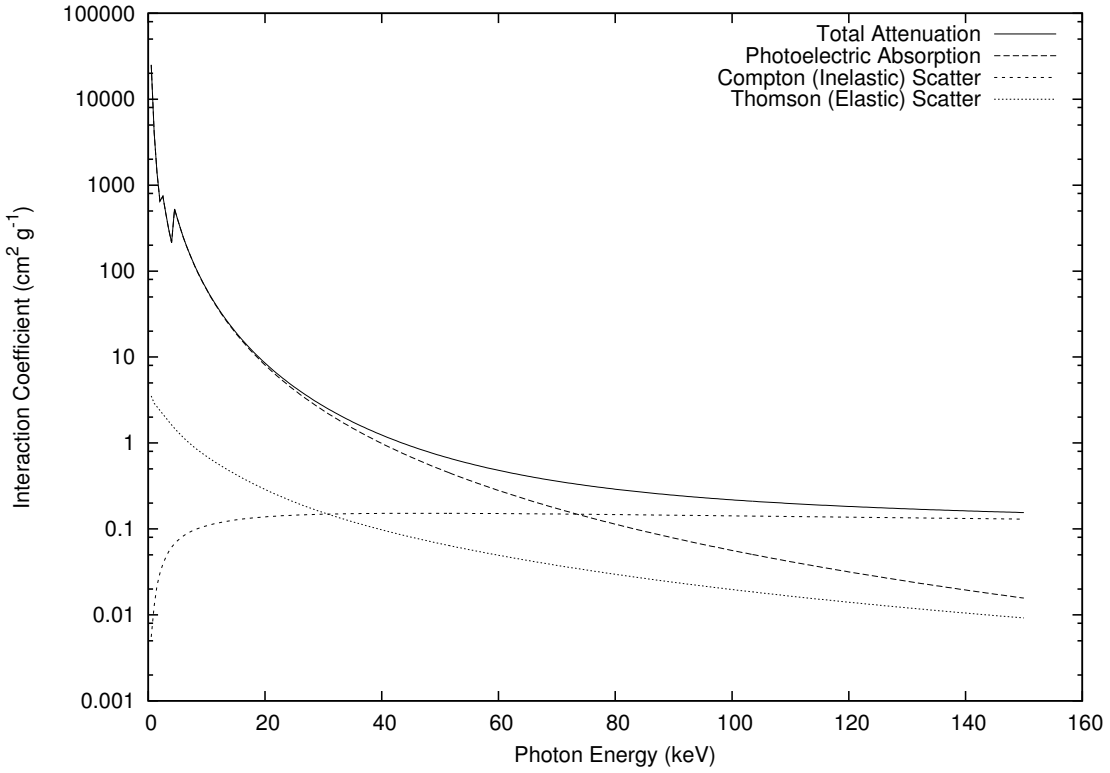

Figure 1.3: Graph showing the contributions to X-ray attenuation from the photoelectric effect, Compton scatter and Thomson scatter in hydroxyapatite for photon energies 0 – 150 keV.

1.1.4 X-Ray Detection

1.1.4.1 Photographic Film

Photographic emulsions composed of gelatin and a silver halide on the surface of a film have been used throughout the history of X-ray imaging for their direct sensitivity to X-ray photons. In tomography, however, the X-ray projections must be combined and processed into a two-dimensional slice or three-dimensional volume. While it would be possible in principle to use film as a projection storage medium for optical scanning and reconstruction — and indeed film was used in X-ray planography, a similar technique which was sometimes referred to as tomography (Pollak, 1953) — it is more convenient to record the projections electronically.

1.1.4.2 Scintillators

In order to capture X-ray photons electronically they must first be converted into a less penetrating form of radiation by the use of a scintillator material, such as sodium iodide or caesium iodide with a suitable dopant. Electrons in the scintillator absorb X-ray photons by the photo-

electric effect, but the scintillator material's threshold energy is sufficiently high to prevent the escape of a photoelectron. Instead, the excited electron returns to its original state via a number of lower-energy transitions, each releasing a longer-wavelength photon. The structure of the scintillator may be amorphous or crystalline, with columnar crystals providing a smaller spread of light than amorphous phosphors.

1.1.4.3 Photomultipliers

Photomultipliers, or photomultiplier tubes, use a negatively charged electrode coated with a photosensitive material to emit an electron in response to photonic stimulus. The electron is accelerated down a series of potential gradients into progressively more positively charged electrodes (called dynodes), which themselves release electrons. The final potential gradient draws the electrons to the anode, producing a current pulse as the device signal.

The photomultiplier tube is a particularly sensitive device which can be used for photon counting, and is therefore particularly suitable for scanning high-attenuation specimens. It is, however, a complex and bulky non-solid state device which relies on the maintenance of a high vacuum for its operation. While in use for synchrotron-based tomography, it is unsuitable for second- or later-generation tomography (as described in Section 1.2.1) in a laboratory environment.

1.1.4.4 Image Intensifiers

An alternative photon-gathering system to the scintillator or photomultiplier tube is the microchannel plate image intensifier, which is an electro-optical device comprising a photocathode coupled to a thin plate made of parallel glass tubes at a small angle to the plate's axis, which is sandwiched between Nichrome electrodes across which a bias voltage is applied. The amplification effect is similar to that of a photomultiplier tube in that large numbers of secondary electrons are released from the incident electron's contacts with the edges of the glass tubes, thereby achieving high gain of the photon signal (Yin, 1979).

The electrons are directed onto a fluorescent screen via an optical fibre bundle or lenses (Baba et al., 2002), and the resulting image (similar in principle to that produced by a cathode ray tube television) is recorded by a CCD or other imaging device. Unlike a photomultiplier tube, it is a

high-spatial-resolution device, and can therefore be used to acquire 2D images efficiently, which led to their initial use in night-vision optics.

1.1.4.5 Charge-Coupled Devices

Charge-coupled devices (CCDs) are the most widely-used solid-state systems for image acquisition despite being an outgrowth of research into solid-state memory. CCDs used in cameras for astronomy (Martinez and Klotz, 1998), in consumer devices and as a data-gathering device elsewhere in the sciences, replacing either film or earlier video tube systems such as Vidicon (Barbe, 1980, pp. 2-3).

A two-dimensional CCD is an array of gate electrodes mounted to a photoactive substrate (generally p-doped silicon) via a silica insulating layer in order to produce a grid of capacitors. A sufficiently energetic photon incident on the silicon will excite an electron from the valence band into the conduction band, creating an electron-hole pair (Janesick, 2001, p. 26). If a voltage is applied to the electrode, the electrons so released will be attracted, forming a depleted region in the silicon. By sequentially applying a voltage to the electrodes in one row, the accumulated charge can be moved across the device in the manner of a bucket chain as shown in Figure 1.4. Once the charge reaches the end of the row, the final 'column' of electrodes can be switched sequentially in order to read the column out vertically to some charge measurement device at the corner of the array (Michon and Burke, 1980, p. 17).

Charge-coupled devices have historically been the standard detection device for impact-source XMT. While they have a high quantum efficiency in themselves, this is dependent upon good coupling between the scintillator and CCD (Jaffray and Siewerdsen, 2000). Nevertheless, their good linearity over a large dynamic range makes them of great use when scan time is not the most important factor in detector choice.

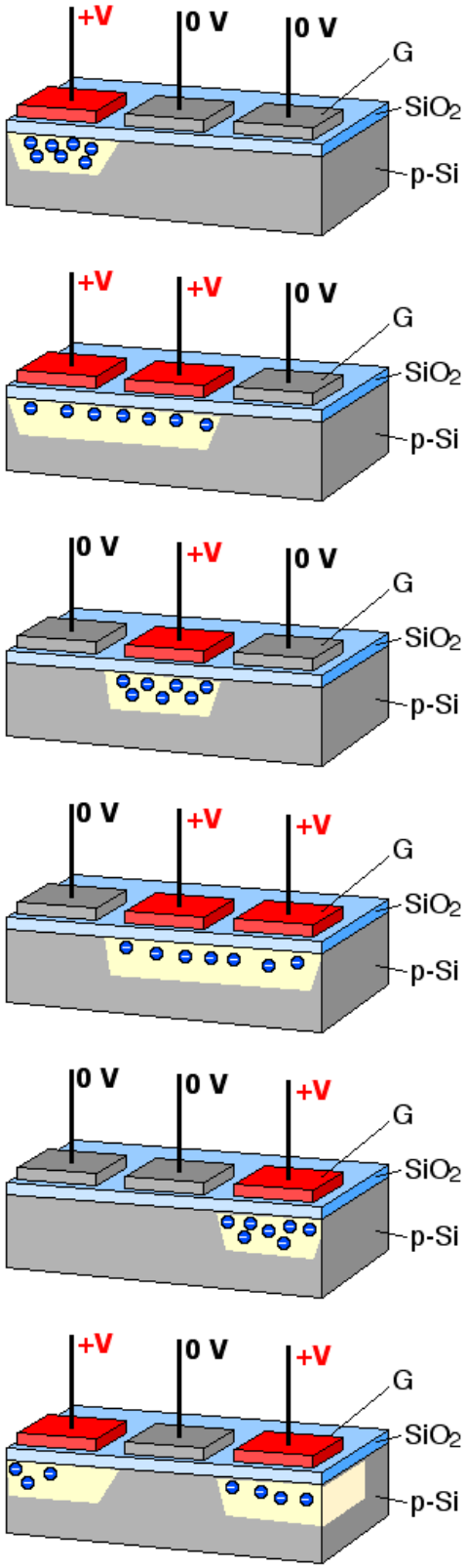

Figure 1.4: Schematic of the clocking process in charge-coupled devices, showing part of a row of CCD elements. (Adapted from (Schmid, 2005).)

1.1.4.6 Flat-Panel Detectors

An alternative to CCDs was developed based on thin-film hydrogenated amorphous silicon arrays, which act as photodiodes, integrated with a thin-film transistor array which is scanned up to several times a second. As with CCDs, the photon's absorption creates an electron-hole pair (Varian Medical Systems, 2004). The scanning process, while sequential over each line of the array, interrogates each pixel separately. Their large size gives rise to geometrical opportunities which allow a much deeper scintillator to be used than with CCDs, increasing their efficiency. Because of the rapid projection time they are particularly suitable for high-throughput environments such as gated tomography.

1.2 Computed Tomography

1.2.1 Computed Tomography Generations

The X-ray beam can be used for CT in several ways, as evolved during the first decade of tomographic development.

1.2.1.1 First-Generation Tomography

The ideal case for ease of reconstruction is a parallel-beam geometry, which uses a tightly-collimated 'pencil' beam and a small detector, which take a projection by scanning across the sample volume. The system is then rotated through a small angle and the process is repeated. This arrangement formed the basis of first-generation CT scanners described in (Hounsfield, 1973), and the process both eliminates variation across the detector and means that all parts of the X-ray beam travel the same distance before reaching the detector. As the beam is tightly collimated, however, the X-ray flux is lower than it would be if all of the source's emission were allowed to pass through the sample. Additionally, the requirement of moving the source-detector apparatus laterally as well as by rotation leads to a very slow data acquisition rate.

1.2.1.2 Second-, Third- and Fourth-Generation Tomography

Second-generation CT replaced the pencil-beam with a fan-beam geometry. This required the use of a linear or curved multi-element detector, sacrificing guaranteed consistency of detection for faster data acquisition, as the X-ray flux is greater in proportion to the fan angle (Maravilla

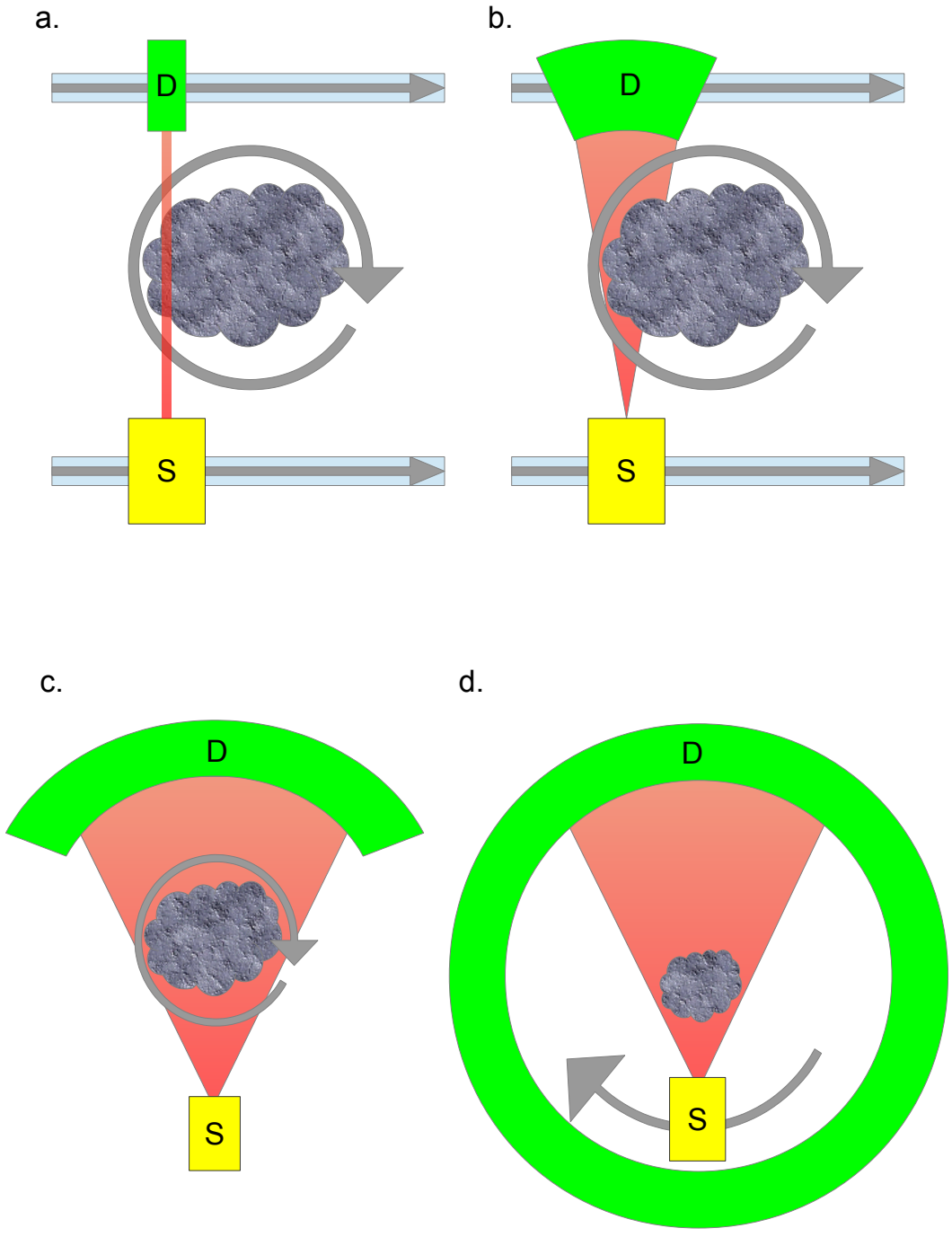

Figure 1.5: Schematics of CT scanner generations: 1st-generation (a), 2nd-generation (b), 3rd-generation (c) and 4th-generation (d), showing X-ray source (S), beam plan and detector (D). Rotating-specimen and rotating-source geometries are geometrically equivalent.

and Pastel, 1978). Third-generation CT expanded the fan angle to illuminate the entirety of the sample, removing the need for translation of the source and detector entirely and reducing scan times even further (Holt, 2007). Fourth-generation CT, the most recent fan-beam arrangement, extended the detectors into a complete circle surrounding the sample, so that only the X-ray source needed to be rotated (Ketcham and Carlson, 2001; Kropas-Hughes and Neel, 2000).

1.2.1.3 Volumetric Tomography

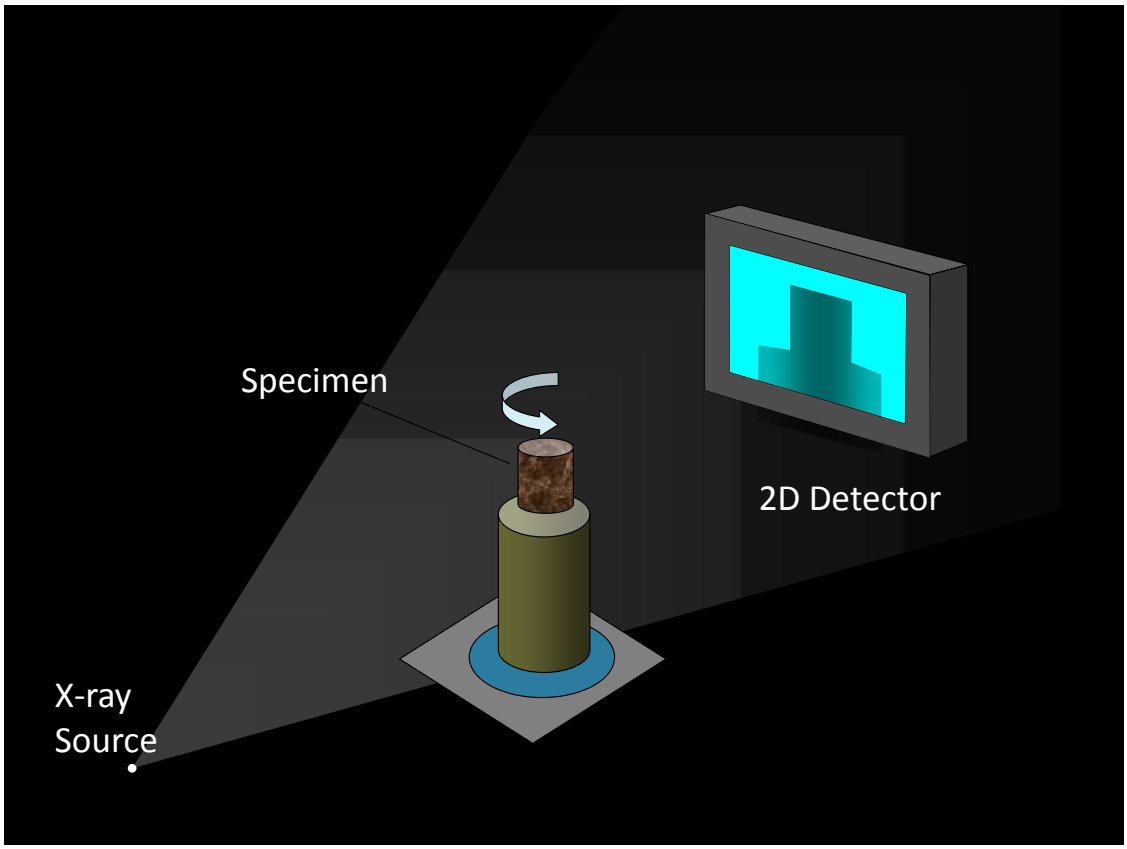

Figure 1.6: Schematic of cone-beam tomography geometry, showing X-ray tube, beam plan, sample and detector (Davis, 2011).

Volumetric CT makes use of a cone-beam (or, in the case of synchrotron-based scanning, a wide parallel-beam) geometry, which allows true three-dimensional reconstruction of a sample rather than the layered slices to which pencil- and fan-beam geometries are restricted. The geometry is otherwise similar to that of third-generation CT, albeit with a two-dimensional detector array rather than a line of detectors (Kropas-Hughes and Neel, 2000). It is more computationally intensive, as the photon path to a flat detector diverges in two dimensions, but there is an exact reconstruction algorithm for cone-beam geometries when the source trajectory passes though all

possible planes that intersect the sample volume (Tuy, 1983; Smith, 1985). Exact reconstruction algorithms have been found for spiral-trajectory scanning (Tam et al., 1998; Wang et al., 2006; Flohr and Ohnesorge, 2006), saddle-trajectory scanning (Lu et al., 2009), and for two-tilting-arc scanning (Zeng et al., 2006), but there is no exact reconstruction method for cone-beam scanning with a planar source locus (Wang et al., 1995). Data collection time is faster using this method than with parallel-beam or fan-beam reconstruction, as a whole volume (the size of which depends on the angle of divergence of the beam and the size of the detector array) may be recorded in the same time as a single slice would take using the previous geometries (Kak and Slaney, 2001, p. 100).

1.2.2 Tomographic Reconstruction

XMT, like conventional CT, relies upon the reconstruction of the distribution of X-ray linear attenuation coefficients in a sample volume from a large number of individual projections (Davis and Elliott, 1997), each of which is a sample or set of samples of the product of the mean linear attenuation coefficient of the material through which the photon passes (including the air surrounding the sample material) and the distance that the photon travels between source and detector.

The geometry of the specimen's rotation sets a lower limit on the number of projections N_{min} required in order to reconstruct from projections of width w pixels:

$$N_{min} = \frac{\pi}{2} w \tag{1.5}$$

The projections are generally taken either over 180° or 360°. In the latter case, the centre of rotation can be determined using the mean of the centres of mass for each projection (Davis, 1994).

1.2.2.1 The Radon Transform

The projection of the sample volume is related to the geometry of the sample by the Fourier Slice Theorem, which shows that the Fourier transform of the projection $P_\theta(t)$ gives the values of the two-dimensional Fourier transform of the linear attenuation coefficient distribution in the sample along a radial line in Fourier space of angle θ (see Figure 12.2a). The projection of the set of

points which lie along a line rotated through θ from the y axis and displaced t from the origin is described by the function

$$P_\theta(t) = \int_{-\infty}^{\infty} f(x,y)\delta(x\cos\theta + y\sin\theta - t)\,dx\,dy. \tag{1.6}$$

This is known as the Radon transform, and the set of Radon transforms which covers the entire range of values of t and θ can be plotted using a sinogram (Kak and Slaney, 2001, pp. 49-50), as shown in Figure 12.2c

1.2.2.2 Filtered Back-Projection

The reconstruction method in use at BLSMD is Filtered Back-projection, in which the rows of the sinogram (each corresponding to a given θ for a vertically-oriented sinogram) are filtered and projected onto the ray-path passing through the centre of rotation at that angle (Van). In impact-source systems, since individual photons will be travelling different distances through the sample volume due to the diverging beam (even neglecting, for the moment, the effect of scattering) the back-projection of the X-rays must now be weighted to compensate (Feldkamp et al., 1984). As with parallel-beam reconstruction, fan beam reconstruction (i.e. a beam that diverges in the y direction with increasing distance x) produces a two-dimensional image of a slice through the sample volume, which must be repeated at different heights z to be built up into a full rendering of the sample (Kak and Slaney, 2001, p.99).

1.2.2.3 Mineral Concentration Recovery

The tomographic reconstruction process should ideally produce an accurate distribution of LAC values. If one wishes to measure mineral concentration, then Equation 1.7 may be used when the mineral of interest and the major background material are known.

$$C = \frac{\mu}{\mu_m - \mu_b}\rho_m \tag{1.7}$$

Here, C is the mineral concentration (expressed in units of density), μ is the measured linear attenuation coefficient, μ_m is the LAC of a pure sample of the mineral and μ_b is the LAC of the background material (generally air, which is almost negligible at CT-relevant photon energies as shown in Figure 1.8.)

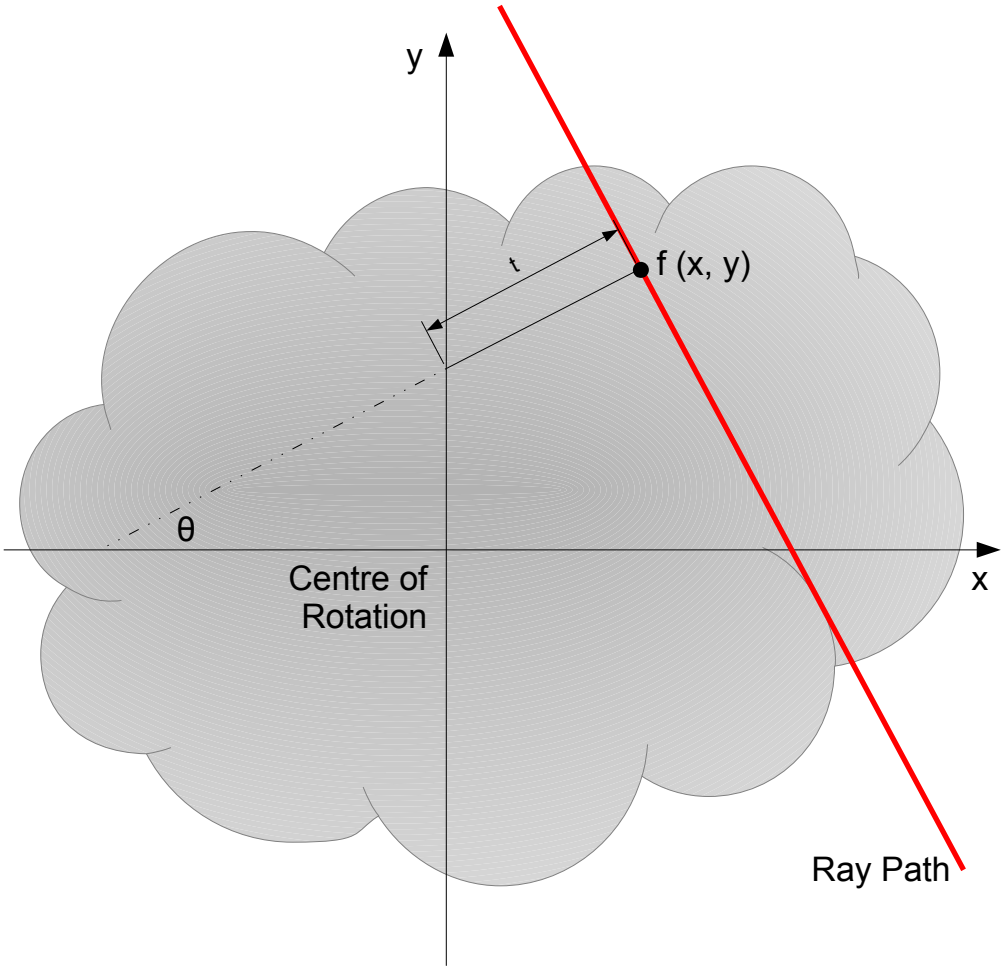

(a) Simplified X-ray interaction with a sample, showing parameters for Radon transform.

(b) Sinogram of the specimen shape in Figure 12.2a. The vertical axis denotes the projection angle θ, while the horizontal axis denotes t.

Figure 1.7: Generation of a sinogram of a virtual specimen based on 180 projections, using the Radon Transform plugin for ImageJ (Abramoff et al., 2004; Farrell, 2006).

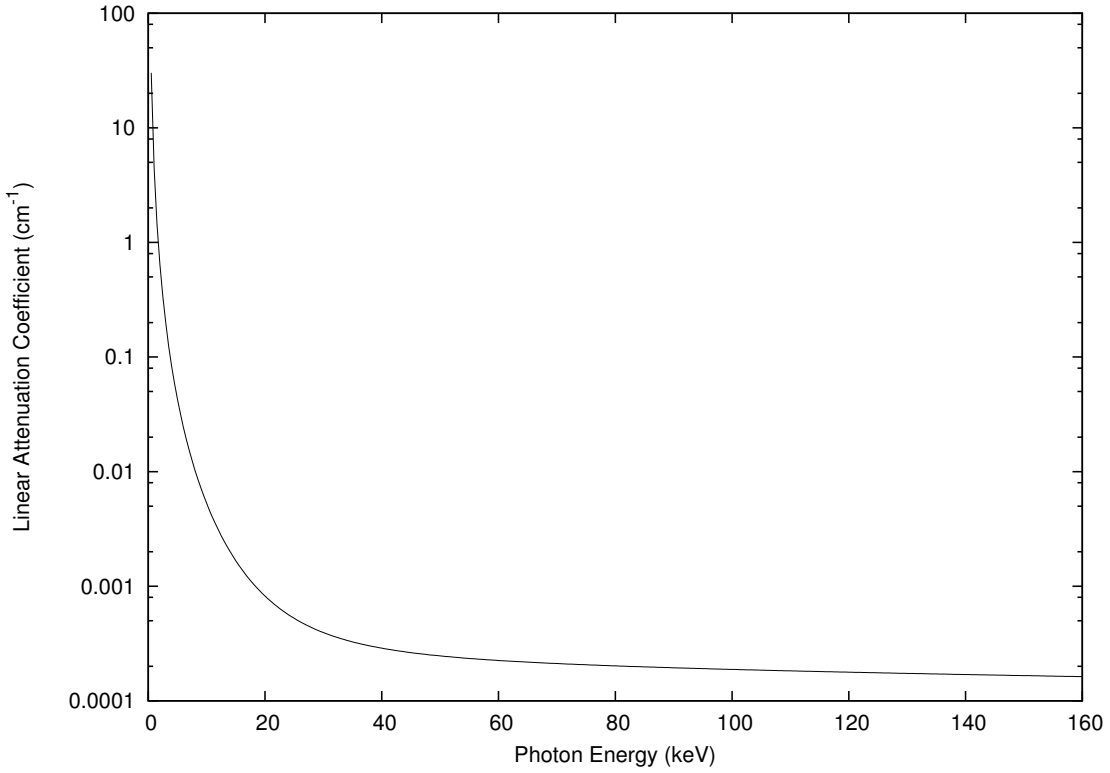

Figure 1.8: Graph showing the linear attenuation coefficient of air at the International Standard Atmosphere (15 °C and 101.325 kPa.)

1.2.3 Phase-Contrast Computed Tomography

If structure and absence of modification is of particular importance in the imaging of a low-radiodensity specimen, then an alternative to the introduction of a radiocontrast agent is required. The phase-shift effect of a specimen on the X-ray wavefront allows the use of phase-contrast imaging in samples which are insufficiently attenuating to permit absorption-contrast imaging, as well as in high-sensitivity applications on more attenuating specimens.

1.2.3.1 Phase Contrast by Interferometry

An X-ray beam is introduced into an X-ray interferometer, which causes the beam to split into an object beam and a reference beam. The object beam is incident on the specimen under study, which causes a phase shift in the beam according to its refractive index distribution. This causes the object beam's X-ray wavefront to bend and develop interference fringes. Concurrently, the reference beam is passed through a phase shifter in order to adjust the relative phase difference between the beams. Finally, the beams are recombined and the resulting interference pattern is detected in the same way as for absorption-contrast imaging (Momose et al., 1996).

Phase-contrast imaging by this method requires the X-ray photons to have a large spatial coherence in order to provide high contrast when the phase-shifted beams are recombined, and was therefore restricted to use with undulator-sourced synchrotron radiation at a high brightness (approximately 10^{15} to 10^{19} $\mathrm{mm}^{-2} \cdot \mathrm{s}^{-1} \cdot \mathrm{mrad}^{-2}$ per 0.1% bandwidth) to allow the scanning of comparatively large specimens, which requires a distant source (Winick, 1998), (Otendal, 2006, pp. 39-40).

1.2.3.2 Phase Contrast by Refraction

Monochromatic radiation incident on a specimen will be refracted through some angle according to Snell's law, dependent on the refractive index distribution in the sample. By placing an 'analyser' crystal after the specimen such that it reflects X-ray photons onto the detector, it is possible to establish a dependence between reflectivity and the difference in angle between photons' angle of incidence on the crystal and the Bragg angle of the analyzer, by setting the crystal at a small angle to the incident beam. Since the angle of refraction for X-rays is on the order of μrad, a significant reflectivity contrast is obtained, thereby indirectly providing phase information via refractive index measurement (Fitzgerald, 2000).

1.2.3.3 Phase Contrast by Direct Imaging

If photoelectric absorption can be regarded as negligible, it can be shown that given moderate spatial coherence of the incident beam, phase information can be recorded directly (also known as in-line holography, out-line phase contrast, and phase-propagation imaging (Otendal, 2006, pp. 42-45). This requires a long exposure time (on the order of minutes per projection) but can be achieved without the use of equipment additional to an X-ray source, specimen mount and detector.

Once detected, the interference patterns form the projections for tomographic reconstruction. Points of large phase change correspond to edges in the specimen, allowing edge detection to be carried out. Impact-source X-ray tubes using a liquid-medal-jet anode, which offer sufficiently high output for phase-contrast imaging by refraction or direct imaging under reasonably short time-scales, have been developed (Tuohimaa et al., 2007), though it remains to be seen whether they can be practically applied to tomography.

1.2.4 Comparison with Other Quantitative Methods

1.2.4.1 Mass Spectrometry

Mass spectrometry permits the elemental composition of a sample to be determined by vaporising the sample and ionising it using an electron beam. The ionised sample is then electrically accelerated through a magnetic field in order to spatially separate elements by their charge/mass ratio. The ions can then be detected individually. This is a destructive process, which gives only compositional information and not structural, as tomography does.

1.2.4.2 Nuclear Magnetic Resonance Spectroscopy

Nuclear magnetic resonance (NMR) spectroscopy is a non-destructive method of partial determination of the composition of a sample by measuring the resonant frequencies detected by aligning the magnetic moment of the atoms in the sample using a strong, constant magnetic field (of several T), then perturbing the magnetic moments using radio frequency waves of an energy appropriate to the atom of interest. This is appropriate for nuclei of non-zero spin (with odd numbers of protons or neutrons), which can absorb the RF energy, but not usable for conductive or ferromagnetic samples and can therefore not be used on an unknown specimen.

1.2.4.3 X-ray Absorption Spectroscopy

X-ray Absorption Spectroscopy (XAS) is a technique used to recover structural and compositional information from the measurement of photoelectric absorption of monochromatic beam, particularly at energies near absorption edges (Glen and Dodd, 1968). Because a monochromatic beam is required, this method suffers from the same affordability and ease-of-use disadvantages as synchrotron-based XMT. In addition, XAS is a local method — that is, it measures only those atoms or groups of atoms that are bound to the target element, while XMT is used for scanning at much larger length scales.

1.2.4.4 Dual-Energy X-Ray Absorptiometry

Dual-Energy X-ray Absorptiometry (abbreviated in the literature as DEXA or DXA) uses two different X-ray spectra, either as two separate beams or as a beam that has been energy-filtered

using a band-stop filter, to provide quantitative and non-destructive information by examining the difference in transmission through a sample in different parts of the energy spectrum, particularly above and below an absorption edge for the material of interest. It is similar in concept to Dual-Photon Absorptiometry (DPA), which uses a radioactive source as a γ-ray emitter (though at X-ray energies - see Section 1.1.1) instead of an X-ray tube, and is used clinically in the measurement of tissue density for the diagnosis of osteoporosis, and other tissue-related disorders (Mazess et al., 1990).

1.3 The *MuCAT* Scanners

The XMT scanning system used to gather data for the experiments described in this thesis was named *MuCAT* 2 (the interior of which is shown in Figure 1.9), and is the one of three similar cone-beam rotating-specimen systems which have been developed for use in the Dental Physical Sciences group at BLSMD. Currently *MuCAT* 1 has reached the end of its service life and is being upgraded, and *MuCAT* 3 (designed for equiangular rather than equispatial projection, and with improvements to allow correction for X-ray field-based ring artefacts) is in pre-service testing.

MuCAT 2 is an in-house development based on an X-Tek[2] (Tring, Hertfordshire, UK) 225 kV microfocus X-ray generator and cabinet. The X-ray source is demountable, with a focal spot size of 5 μm on a tungsten target. The specimen and camera are mounted on mechanical stages supplied by Physique Instrumente (Palmbach, Karlsruhe, Germany). The detection system comprises a 100 μm (approximate) columnar caesium iodide scintillator made by Applied Scintillation Technologies (Harlow, Essex, UK), coupled via a parallel optical-fibre faceplate (Davis and Elliott, 2006b) to a 800-series thermoelectrically-cooled CCD camera made by Spectral Instruments (Tucson, Arizona). The camera incorporates a 16 megapixel Fairchild CCD485 sensor, of size 60 mm square. This sensor has a pixel size of 15 μm, binned initially on the chip and later in software to 60 μm.

Projections on *MuCAT* 2 are taken over a 360°arc, in order to gain centre of rotation information

[2]X-Tek was acquired in 2008 by Metris, and in 2009 by Nikon to become part of Nikon Metrology.

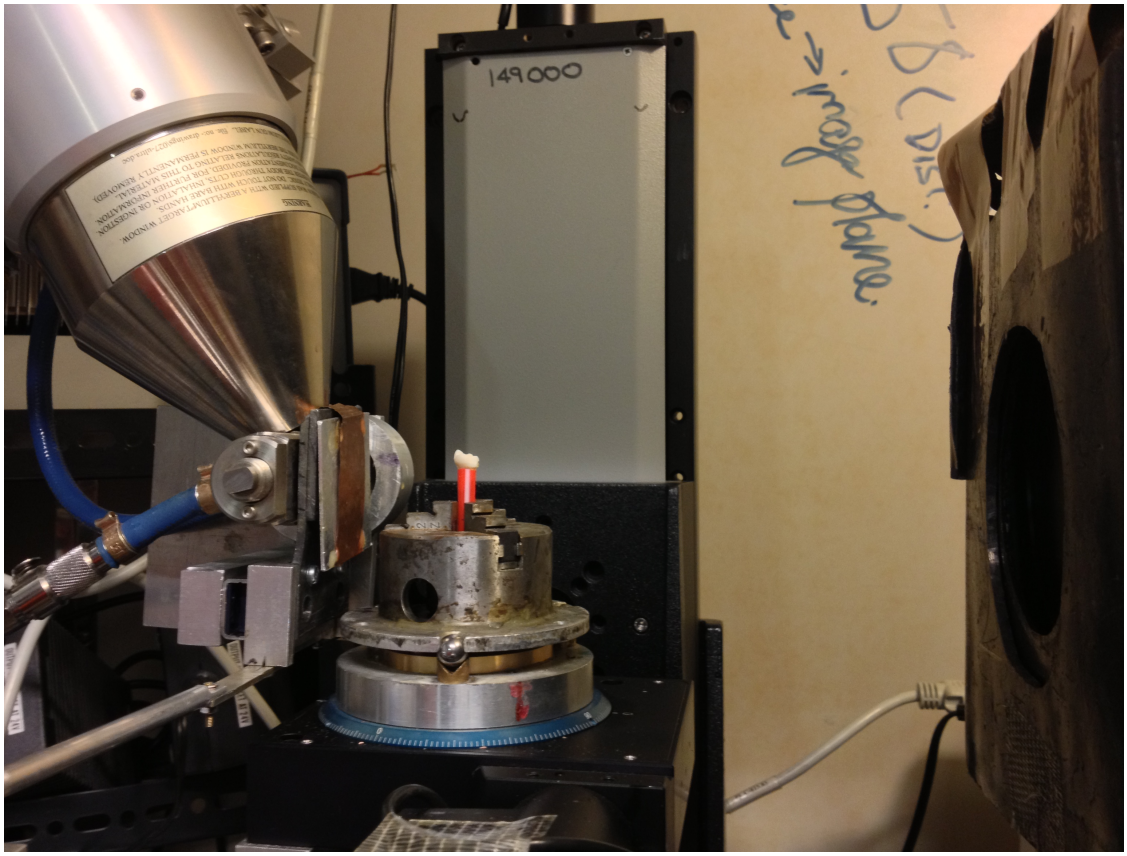

Figure 1.9: Interior of *MuCAT* 2, showing X-ray tube and rotatable target (left, with blue cooling hoses) with aluminium and copper filters, dental specimen (foreground, centre) mounted on rotation stage via a chuck-based stand, itself mounted on an elevation-translation stage, and the X-ray camera (right) in a shielded container to reduce scattered X-ray photon detection.

as described in Section 1.2.2. An odd number of projections are taken when a scan is expected to be used for reconstruction, so that the ray-paths interlace with those taken from the scan's antipodal point, ensuring uniqueness.

As a result of the time-delay integration feature described in Section 3.1.1, the maximum sample size is determined by scan time and the beam width, and is approximately 80 mm in diameter. The vertical (ie. perpendicular to the plane of rotation) bounds may be extended by scanning a long object in multiple blocks and 'stitching' them together after reconstruction.

Projections are read out from the bottom to the top of the detector. As a result of this, tabulated projection data i9n a text file is inverted from the expected order, and when projection data or projection-derived data is displayed as a histogram the origin of the graph corresponds to the lowed used row of the detector.

The *MuCAT* devices are in near-continuous use (when not undergoing maintenance) for the scanning of specimens, most of which are biological samples either for research within the department or from external sources. Further applications of tomography and XMT, particularly where quantitative results are required, are shown in the following chapter. The duty cycle of *MuCAT* 2 requires that scans for purposes of process improvement be used as efficiently as possible.

Chapter 2

X-Ray Microtomography: Applications

While X-ray microtomography was first developed for use in the field of dental materials, a number of applications have been discovered in other specialisations.

2.1 Biological X-ray Microtomography

As an outgrowth of computed tomography, XMT is often used as a tool for uncovering structure in three dimensions at high spatial resolutions. This is particularly effective for hard tissues (bones and teeth), but can also be carried out for soft tissues with a suitable radiocontrast agent.

X-ray computed tomography is a much higher-dose technique than conventional radiography (Golding and Shrimpton, 2002), due to the large number of projections that must be taken in order to produce a reconstruction, given in Equation 1.5. In addition, there is an inverse fourth-order relationship between reconstructed volume element (voxel) size and photon count required in order to produce a reconstruction of given signal to noise ratio (SNR) (Davis, 1999). As a result of this and the resulting extended scan times, XMT is unsuitable for *in vivo* studies apart from a few small animal studies in specialised scanners.

2.1.1 Hard-Tissue Studies

The quantitative study of hard tissue mineralisation is the research question which led to the initial development of microtomography as a technique, since bone and dental mineralisation can be discussed in terms of concentrations of hydroxyapatite (HA), the dominant absorbing compound (Berkovitz et al., 2010). The first XMT scanner built at the London Hospital Medical College (the predecessor of BLSMD) was a first-generation device using a high-purity germanium or silicon detector (Elliott et al., 1994). While the first-generation geometry requires very long scan times compared with later-generation systems, it provides vey accurate reconstructions and was used in (Elliott and Dover, 1984) to map mineral distribution in human femoral bone and in (Gao et al., 1993) to show partial remineralisation of dental enamel to 10 μm spatial resolution. A similar technique was used by (Postnov et al., 2003) using a cone-beam geometry to measure demineralisation in newt bones as a result of prolonged exposure to microgravity.

Microtomography using *MuCAT* 1 was used in (Ahmed, 2011) to survey healthy and osteoporotic human femoral heads both for bone mineral density and structural parameters such as bone volume fraction. Similarly, (Stock et al., 2006) used the ability of XMT to provide complete 3D datasets to use appropriate LAC thresholds to examine the volume fraction of calcite ($CaCO_3$) in sea urchins and suggest structural functions for their central cylinders. Another quantitative structural study was carried out by (Léonard et al., 2007) into pore size distribution in *Cervus Elaphus* antlers, as a non-destructive three-dimensional alternative to histological sectioning.

XMT can also be used in a more visual fashion, for example to determine the effectiveness of a clinical technique by defining a success criterion that can be expressed in terms of LAC values. In (Ahmed, 2010) 'before' and 'after' datasets were taken of teeth with carious cavities (of which an example is shown in Figure 2.1) in order to distinguish between unassisted hand excavation, assisted hand excavation and chemo-mechanical excavation of the carious tissue.

2.1.2 Soft-Tissue Studies

By their nature, soft tissues in the body are primarily composed of low-Z elements. Discriminating between these to carry out quantitative tomography based on fine changes in linear attenuation

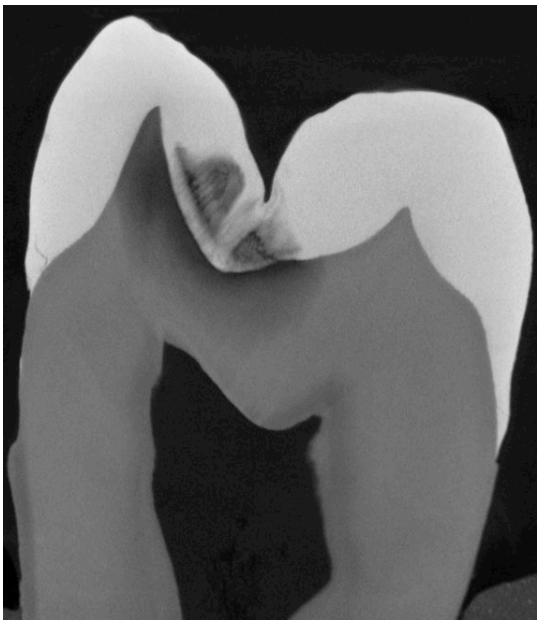

Figure 2.1: Cross-section of a tooth imaged by XMT, showing demineralisation in the enamel and dentin

coefficient is therefore much less practical than for hard tissues. It is possible, however, to use thresholding in order to gain quantitative structural information on a specimen. In medical CT, radiocontrast agents were used to outline the structures and periodic motions in the human heart (Boyd and Lipton, 1983). Similarly, *in vitro* microvasculature studies (Bentley et al., 2002) using appropriate radiocontrast agents have been performed for small animal organs, and in (Cody et al., 2004) an *in vivo* small animal study was carried out to examine pulmonary fibrosis, which requires good spatial and contrast resolution at the lung-air interface.

2.2 X-Ray Microtomography in Materials Science and Industry

The tomographic inspection of non-biological materials and manufactured samples has been a topic of interest for some years (Cesareo et al., 1999), generally to examine microstructural features. In the earth sciences, there have been several fields of study proposed using X-ray CT as a technique (Rivers et al., 1999; Ketcham and Carlson, 2001). In (Cruvinel et al., 1990), soil water content and bulk density were measured by tomographic analysis. While this was carried out in a biomedical scanner at a relatively poor spatial resolution of 1 mm, the use of LAC as a direct proxy for other measurements is a technique of great utility in quantitative microtomography. Microtomography has been used in the characterisation of causes of strain in glacial sediment

samples in Tarplee et al. (2011), and the use of combined XMT/X-ray Fluorescence tomography scanning devices to undertake combined structural and chemical analysis of a specimen was developed by Sasov et al. (2008a).

The study of cements (Bentz et al., 1994), metals (Ludwig et al., 2003) and other industrial materials liable to chemical or mechanical attack is of particular interest, particularly since microtomographic scanning is a non-destructive process and therefore 'before and after' measurements can be carried out on the same specimen without affecting the validity of the result. Since XMT offers a high spatial resolution, it has also attracted interest as a metrological technique (Suppes and Neuser, 2008). One example of this use is in the assessment of radiocontrast-enhanced polymers, as was carried out in (Anderson et al., 2006).

2.3 Microtomography in Historical and Archaeological Contexts

The non-destructive nature of microtomography makes it of great use in the study of historically and archaeologically valuable specimens, which are often rare or irreplaceable. Since XMT permits interior imaging of such samples without requiring sectioning, as shown in Figure 2.2, some museums of natural history have therefore developed in-house microtomography facilities in order to examine their own collections (Natural History Museum, 2012).

2.3.1 Fossil Examination

Fossils are the preserved remains of animals or plants dating from before the Holocene epoch. Since these are found as casts, impressions or mineralised regions in sedimentary rock, comparatively high X-ray beam energies must be used in order to provide sufficient penetration to give an adequate SNR.

The first known application of CT to the fossil record was by (Conroy and Vannier (1984), cited in Haubitz et al. (1988)), in the examination of fossil skulls. Haubtiz et al. used a medical CT scanner in order to examine the double-headed quadrate bone in an *Archaeopteryx* skull, lending weight to the argument that *Archaeopteryx* was a primitive avian. The use of synchrotron

Figure 2.2: Cutaway rendering of an oak gall, showing gall wasp larvae gestating inside. Rendered by Ajay Limaye using Drishti.

radiation microtomography, with much greater beam fluxes available, has also been used to characterise morphology of fossil remnants (Mazurier et al., 2006).

2.3.2 Project *Apocalypto*

The combination of high spatial and contrast resolution gives XMT utility in the recovery of textual information from historical documents. In Western civilisation, the preferred medium for recording information, particularly for legal record keeping, was parchment, of which the major component is collagen. Over time, and particularly with poor storage conditions, this can degrade into gelatine, causing adherence in multi-layer documents such as scrolls and rendering the document unreadable (Popescu et al., 2008).

A major source of ink between the medieval period and the 20^{th} century was iron gall ink, which — as the name implies — contains iron in the form of Fe^{2+}/Fe^{3+} ions (Arčon et al., 2007). Since the parchment has a much lower effective atomic number than iron, the presence of ink can be detected by LAC contrast as shown in Figures 2.3 and 2.4. Preliminary experiments were carried out as part of the *Apocalypto* collaboration between BLSMD and Cardiff University to detect ink in a previously-unreadable 19^{th} century scroll, and unroll the text *in silico* to recover the information (Mills et al., 2012).

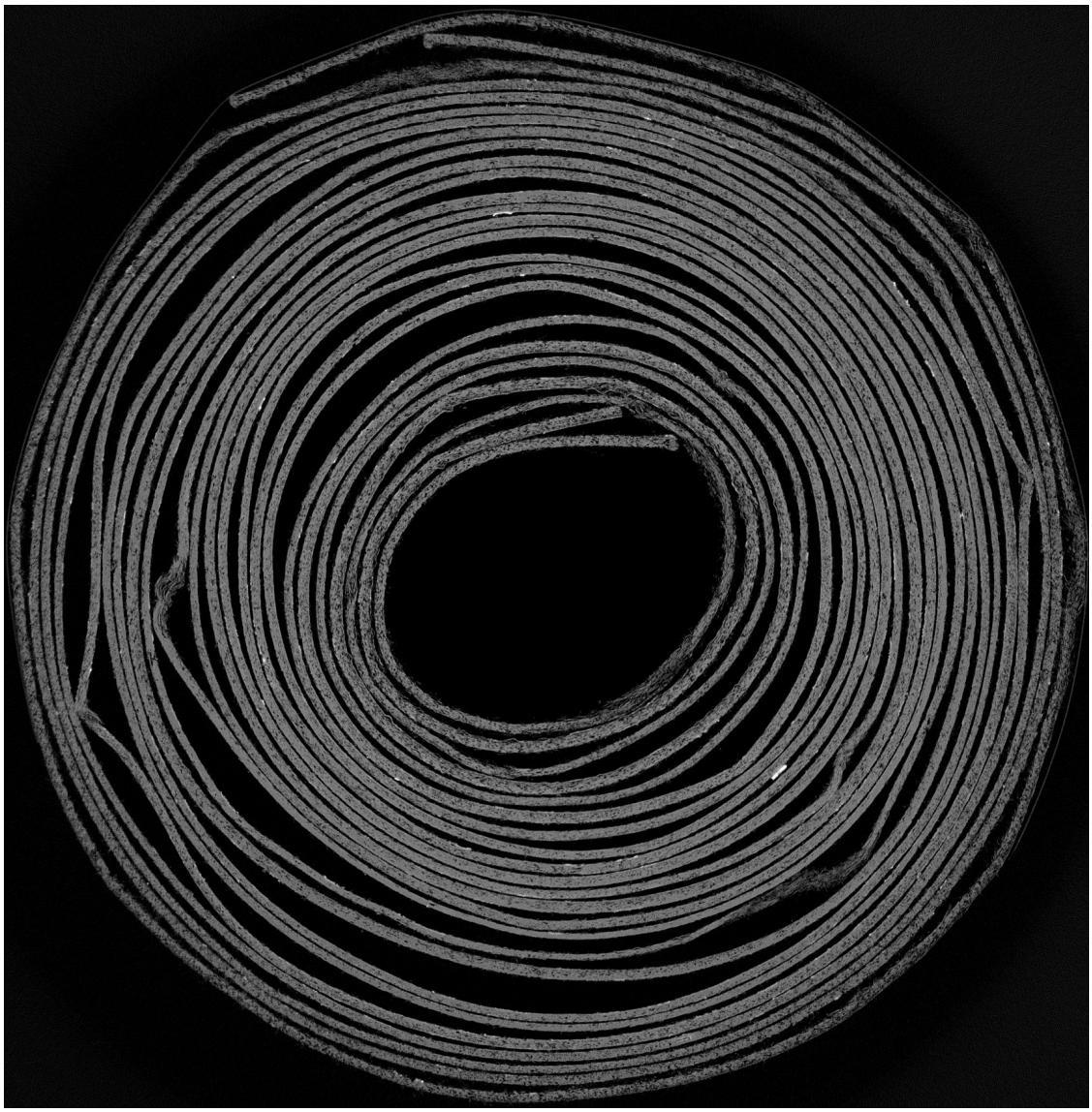

Figure 2.3: Horizontal section of a large loose-wound scroll imaged by XMT, showing areas of possible ink (brighter spots) and regions of contact between layers of parchment, rendered using Tomview.

While this experiment was ultimately about the ability to recover a structure (ie. the text) and therefore the recovery of information of importance to cultural and legal heritage, it requires both good spatial resolution and high contrast resolution due to the thinness of the ink reducing the linear attenuation to a fraction of, for example, that of a dental specimen, and possible leaching of the ink layer out of the paper over time.

Figure 2.4: Vertical cutaway section of a smaller loose-wound scroll imaged by XMT, showing visibility of iron gall ink on parchment, rendered using Drishti.

Chapter 3

Microtomographic Artefacts

When CT or XMT are used to recover gross structural information from a patient or a specimen, generally artefacts are at most a distraction for the operator. If precise LAC measurements are at stake, however, any inaccuracy in the greyscale data produced is a matter of concern. In Section 1.1.3.1 Beer's law was given for non-scattering monochromatic radiation. In reality X-ray sources produce a spectrum of X-ray energies, and scattering is not a negligible effect for highly-attenuating specimens requiring high photon energies, particularly if the median LAC of the specimen is low. Additionally, practically-required compromises in the scanner can lead to inaccurate reconstructions (Tofts and Gore, 1980). The production of artefacts in a virtual phantom was demonstrated in Davis and Elliott (2006a).

3.1 Ring artefacts

Any variation in XMT scanner efficiency, whether from a slight difference in detector element sensitivity on a third-generation scanner or a systematic spatial change in X-ray spectrum, will cause a corresponding variation in the detected attenuation. For a single one- or two-dimensional projection this systematic error will be on the order of 1 %, which may be considered negligible. As the projections are reconstructed, however, the presence of an artificially light or dark pixel at a constant distance from the centre of rotation causes the buildup of a ring or half-ring (depending on the angle through which the specimen is rotated over the course of the scan) on the projection (Kinney et al., 1989), as shown in Figure 3.1b.

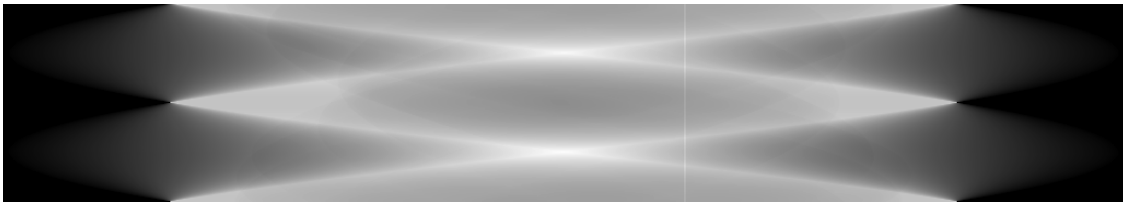

(a) Sinogram of the specimen shape in Figure 12.2a, with a simulated over-performing (150% scale) detector pixel. The vertical axis denotes the projection angle θ, while the horizontal axis denotes t. The effect of the dead pixel can be seen as a pair of dark vertical bands.

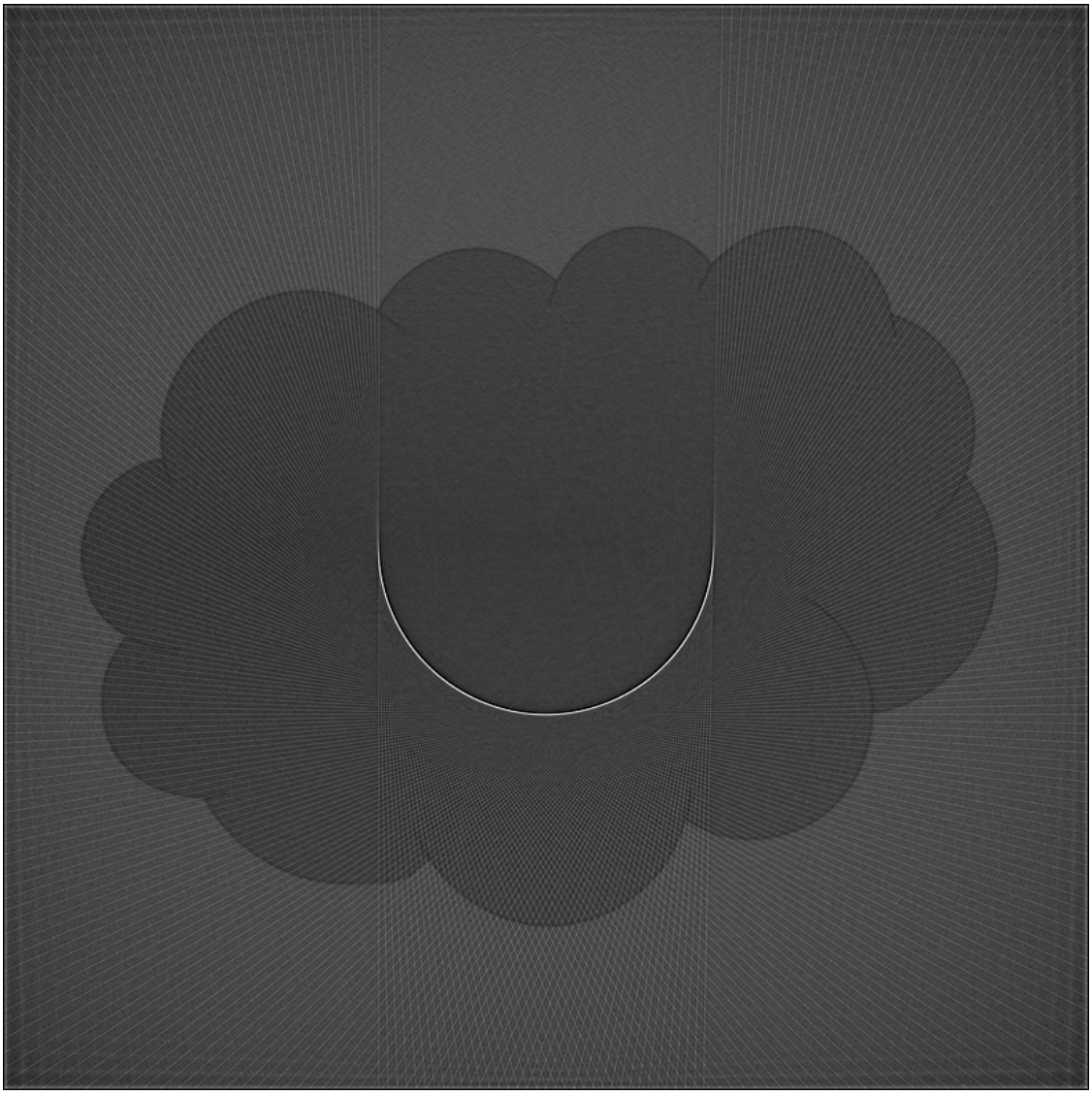

(b) Reconstructed specimen, showing ring artifact. The reconstruction was performed over 180°, causing a half-ring artefact with streaking. An error this large is unlikely, but presented here for clarity.

Figure 3.1: Simulated ring artefact, using the Radon Transform plugin for ImageJ (Abramoff et al., 2004; Farrell, 2006).

Because the abnormal pixel is a constant distance from the centre of rotation, it leaves a centred pair of lines on the sinogram (as seen in Figure 3.1a). It is therefore possible to blur the ring artefact out by taking the discrete Fourier transform of the $N \times M$ sinogram (Equation 3.1) and applying a localised smoothing function such as the one-dimensional Butterworth low-pass filter shown in Equation 3.2 before reconstructing. In this method, developed by (Raven, 1998), $n = 4$, u_0 is the spatial Nyquist frequency of the detector, and v_0 is a threshold frequency.

$$P(u,v) = \frac{1}{NM} \sum_{k=0}^{N-1} \sum_{l=0}^{M-1} p(k,l) e^{-2\pi[u\frac{k}{N} + v\frac{l}{M}]} \tag{3.1}$$

$$H(u,v) = \begin{cases} \frac{1}{1+\left(\frac{u}{u_0}\right)^{2n}} & \text{if } |v| \leq v_0 \\ 1 & \text{otherwise} \end{cases} \tag{3.2}$$

This method reduced but does not entirely remove ring artefacts in the reconstruction, depending on the threshold value set, and comes at the cost of Gibbs phenomena as a result of the Fourier transform, which can lead to further artefacts in the reconstruction. A real-sapce equivalent was developed by (Boin and Haibel, 2006), using a moving average filter to suppress variations (Equation 3.4) on the sinogram itself, taking advantage of the narrow width of ring artefacts.

$$y(t) = \sum_{\theta} p_\theta(t) \tag{3.3}$$

$$y_s(t) = \frac{1}{2N+1}[y(t+N) + y(t+N-1) + \cdots + y(t-N)] \tag{3.4}$$

$$p'_\theta(t) = p_\theta(t)\frac{y_s(t)}{y(t)} \tag{3.5}$$

Again, their method is dependent on the value selected for the averaging window half-size N, which requires a compromise between suppression of ring artefacts (for which a large N is ideal) and the avoidance of blurring over a large number of pixels (small N).

In some circumstances the sinogram may not be available for direct manipulation (for example, when using commercial reconstruction software). (Ketcham, 2006) developed a smoothing algorithm that is applied to a polar transform of the reconstructed slices. This correction method can, however, introduce secondary artefacts to the reconstruction, particularly Moiré patterns near the

centre of rotation and streak artefacts where the correction intersects an unfavourably-oriented material boundary. The author notes that the correction achieved in this way is in most cases inferior to sinogram-based correction.

3.1.1 Time-Delay Integration

At BLSMD the problem of ring artefacts arising from detector element variability has been eliminated entirely by making use of the CCD readout mechanism. As noted in Section 1.1.4.5, the X-ray signal is captured as a charge packet in a semiconducting layer of the detector and stepped across the device. This process is regulated by a clocking signal, the frequency of which can be adjusted to allow 'time delay integration' of charge (TDI) - imaging the same part of an object with multiple detector elements in succession. This capability was used historically (Schroder, 1980) to increase the detectivity of the device, particularly for imaging fast-moving objects.

In the *MuCAT* scanners, the clocking is synchronised to the camera's motion across the plane of rotation, perpendicular to the X-ray beam, such that the charge packets are held stationary (Davis and Elliott, 1997; Davis, 1997). Each element will image the X-ray field through a small portion of the sample as the charge accumulated by previous elements from that same small portion is moved underneath it (i.e., adding a time delay to the integration of charge), as shown in Figure 3.2. Thus, at the edge of the CCD the readout will be the sum of all the elements' responses to that one sample portion, effectively combining the responses of all of the elements across that row of the CCD and removing the spurious variation in detector output. Additionally, the use of a beam collimator attached by an arm to the camera permits the reduction of X-ray dose applied to the specimen to those areas which are directly between the source and the detector area of the camera (Davis et al., 2010).

This method also allows the width of a projection to be unconstrained by the area of the CCD array, but significantly increases the time taken to scan each projection as the camera must be translated across the X-ray beam (Davis and Elliott, 2003). It also does not account for ring artefacts produced by anomalies in the X-ray beam, since these do not translate along with the camera. A lesser degree of correction can be achieved by moving the camera only a few pixels between projections, thereby moving the projections of the locus of points distance t from the

centre of rotation (see 12.2a) onto a different camera pixel with each projection. This prevents the buildup of high or low systematic errors in the detector into a ring artefact, at the cost of reduced effective detector area.

The major limitation of TDI is that it limits the detector options to CCDs with the ability provided to adjust the clocking frequency, and that correction of horizontal distortion is not possible (Davis and Elliott, 2006b). This means that the coupling between the scintillator layer and the CCD must have very low distortion, preventing (at the time of *MuCAT* 2's construction) the use of tapering optical fibre faceplates and economically-viable lens systems with sufficient transmission efficiency. As described in Section 1.3, a parallel faceplate was used in this scanner.

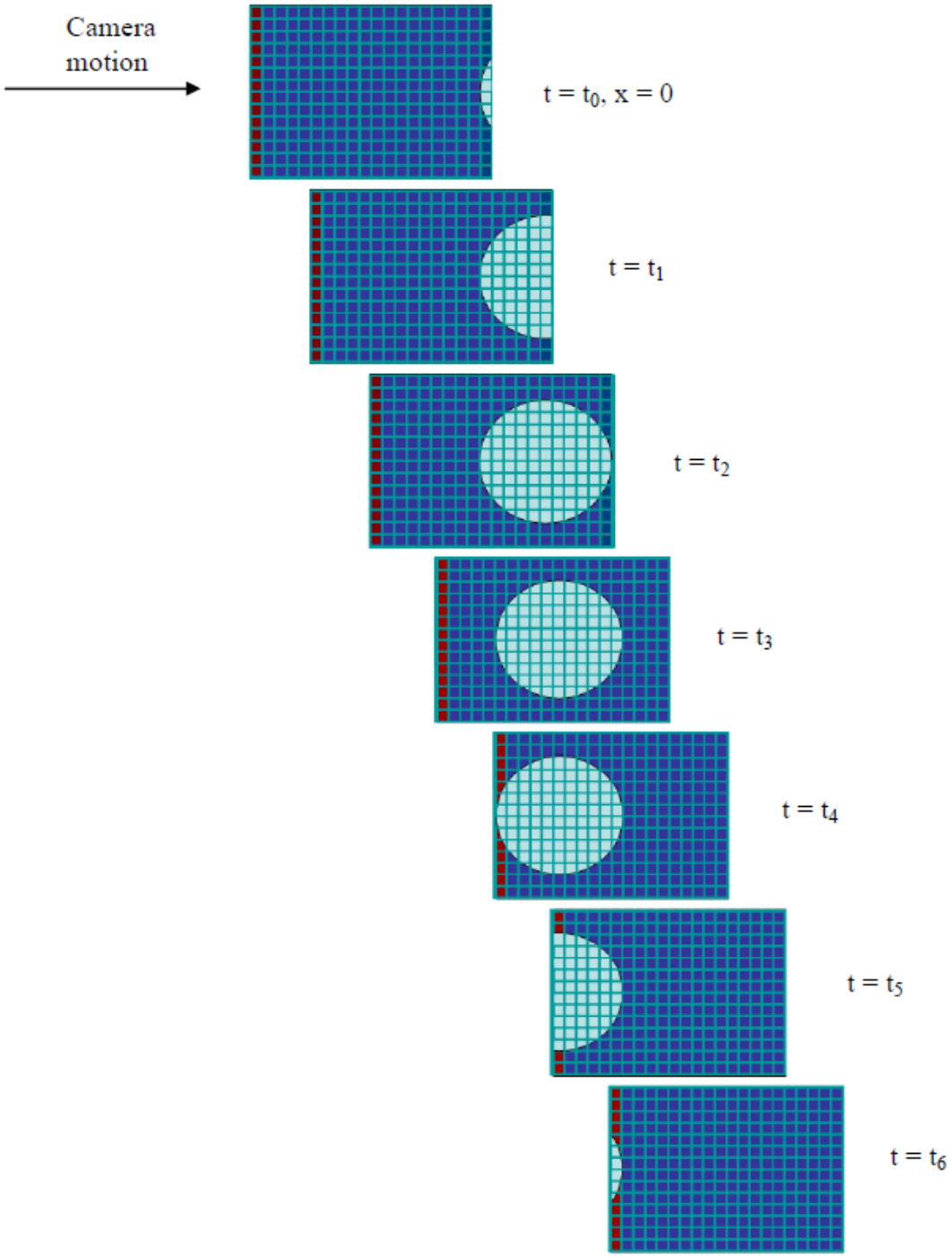

Figure 3.2: Time sequence showing TDI readout of captured image (red column of pixes on the left of the array) with camera motion (Ahmed, 2010).

3.2 Beam Hardening

Impact-source microtomography uses a polychromatic beam, which gives rise to departures from the ideal Beer law case known as 'beam hardening'. This effect has been studied in the context of X-ray CT since almost immediately after Hounsfield's original paper was published in 1973 (Brooks and Chiro, 1976).

3.2.1 Causes of Beam Hardening

The bulk of an X-ray beam from an impact source, as described in Section 1.1.2.2, is a Bremsstrahlung spectrum covering the entire energy range from zero to the electron accelerating potential, as shown in Figure 3.3. Beer's law for attenuation is therefore better written as in Equation 3.6, where E is the incident photon energy.

$$I^o(x) = I^o(0)e^{-\mu_t(E)x} \tag{3.6}$$

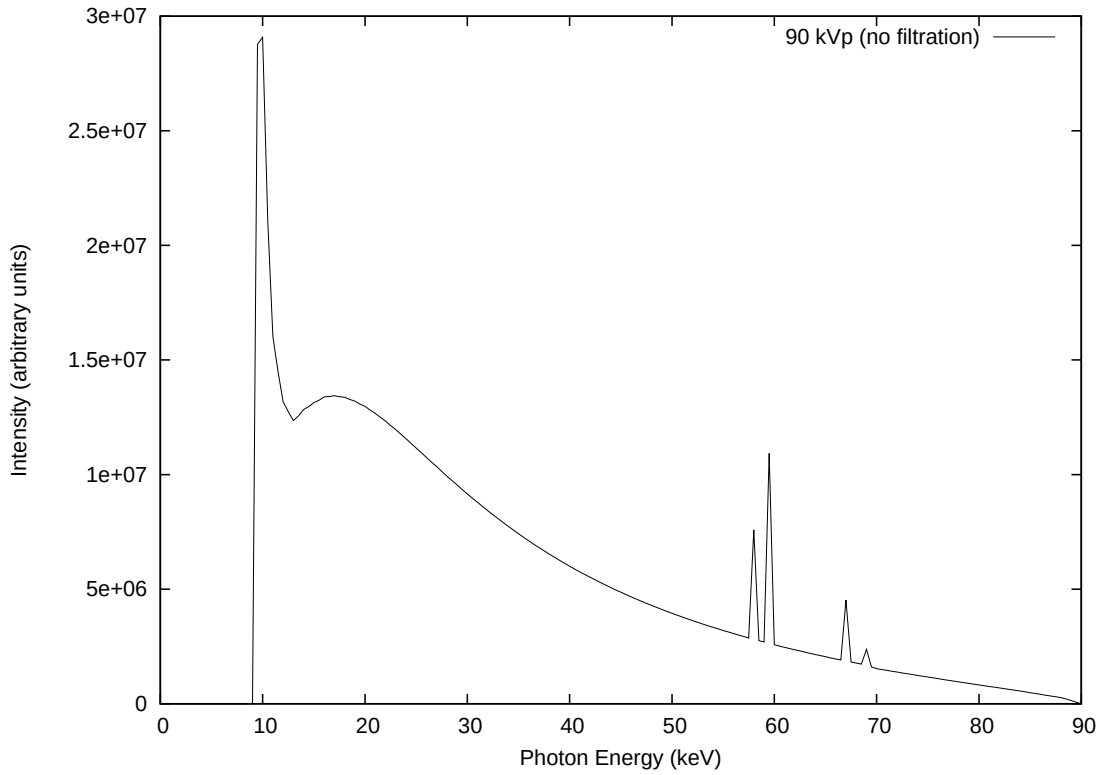

Figure 3.3: Unfiltered tungsten X-ray emission spectrum at a peak potential of 90 kVand a take-off angle of 22°. The cut-off below 9 keV is an artefact of the *Spekcalc* spectrum generation software. (Poludniowski et al., 2009)

In addition to bremsstrahlung, the spectrum produced in the X-ray target exhibits characteristic peaks, with energies dependent on the atomic number of the target. For tungsten, characteristic peaks primarily result from the $K_{\alpha 1}$ and $K_{\beta 1}$ transitions at 59.3 keV and 67.2 keV respectively (National Institute of Standards and Technology, 2005).

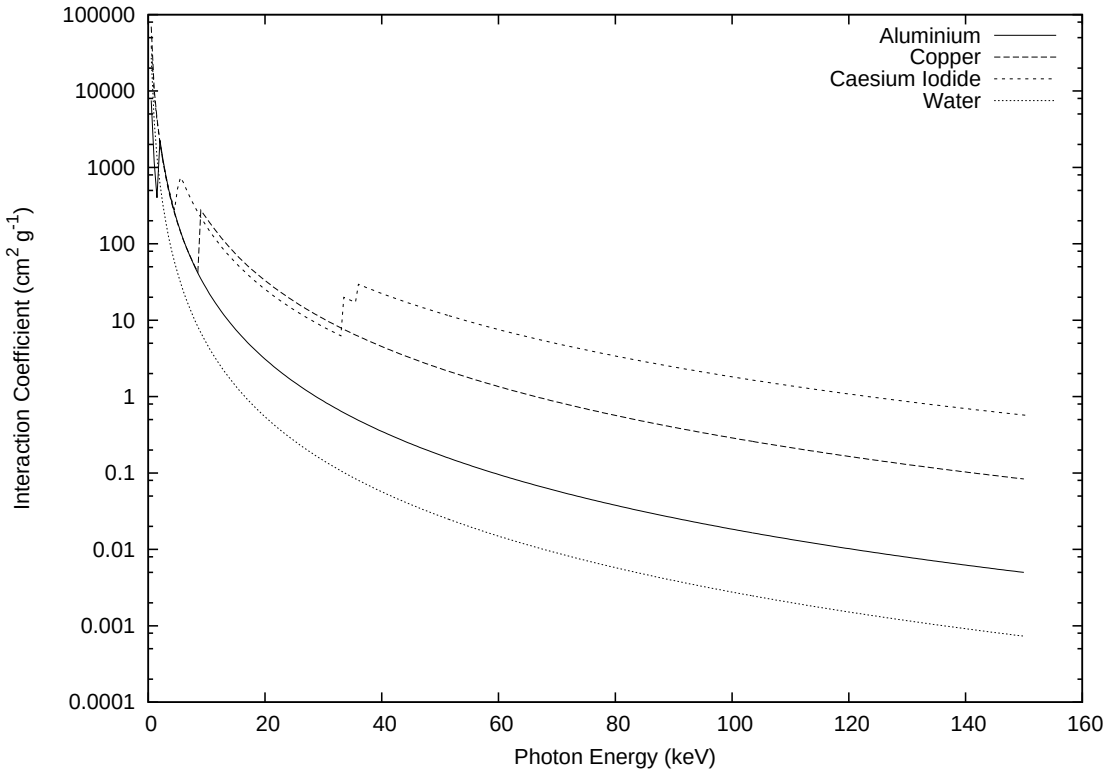

Figure 3.4: Photoelectric absorption spectra for common filter materials.

Since the work function is generally only a few electron volts (depending on the element), which corresponds to ultraviolet light, all X-ray photons are capable of causing photoelectric absorption. However, as was seen for HA in Figure 1.3 and for other materials in Figure 3.4, there is a generally negative relationship between incident photon energy and the cross-section of the photoelectric effect at XMT-relevant energies, and therefore a high-energy photon is generally more likely to be transmitted through a given thickness of a material (neglecting other interaction mechanisms) than a low-energy photon. As a result of this selective culling of low-energy photons, the X-ray field's energy distribution is shifted upwards as the photons travel along the beam path, shown in Figure 3.5 - this effect is called 'beam hardening'. Material further along the beam-path will therefore generally attenuate fewer photons by absorption than if it were simply exposed to a reduced-intensity beam of the original spectral distribution.

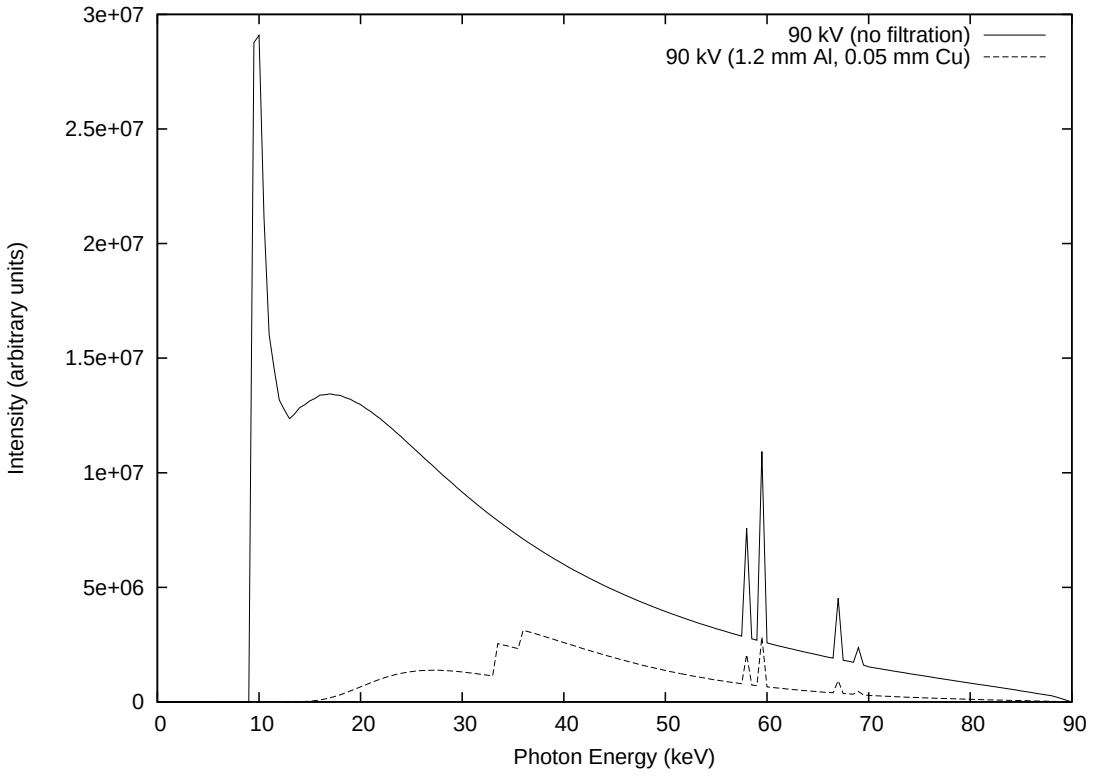

Figure 3.5: Beam hardening of a 90 kV, 22° tungsten emission beam, by copper and aluminium. The median energy is approximately 26.5 keV in the unfiltered spectrum, and 44.0 keV in the filtered spectrum.

3.2.2 Effects on Reconstruction

As the specimen is rotated during the scan, all of the outermost regions are brought closest to the X-ray source in turn, while the centre of rotation is never exposed to the least energetic photons. The effect of this is that a greater number of photons are absorbed in the surface of the specimen. The reconstructed interpretation of this is that the surface is over-absorbing and therefore has a higher LAC than is truly the case. Conversely, the LAC in the centre is depressed leading to dishing artefacts (Davis and Elliott, 2006a), as demonstrated for an approximately uniform HA pellet in Figure 3.6.

While the uniform case is relatively trivial to correct, in situations where high contrast is required, such as studies of mineral concentration in biological materials, it is not possible to correct the reconstructions without some *a priori* knowledge (or assumptions) as continuous variations in LAC are expected. In treatment validation, minor LAC variations are of interest, and therefore

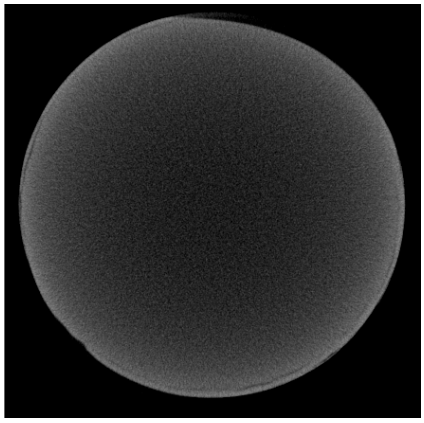

(a) Hydroxyapatite disc, scanned at 90 kVp without beam hardening correction, with contrast enhanced to demonstrate dishing artefact.

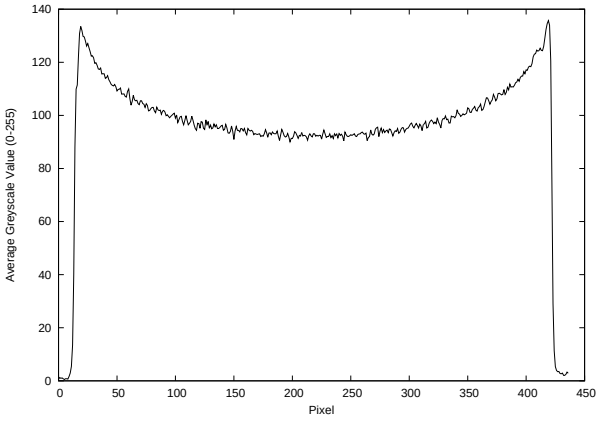

(b) Greyscale profile of 20 pixels surrounding the horizontal centreline of the hydroxyapatite disc.

Figure 3.6: Demonstration of dishing artefacts arising from uncorrected beam hardening in a uniform specimen.

accurate greyscale reconstruction is required.

Other artefacts arising from beam hardening include the generation of streaks in the vicinity of strongly-attenuating inclusions in a specimen, particularly along the most-attenuating axes of the sample or between multiple inclusions as shown in (de Man et al., 1999). These are of particular concern in the validation by XMT of dental caries treatments, as a remineralising therapy would be expected to possess abnormally high mineral concentrations, and the initial area of interest would be in the area of the tooth where the treatment was applied.

3.2.3 X-Ray Target Self-Absorption

When X-rays are produced in the target of the X-ray tube, the electrons penetrate to a depth determined by the target material's stopping power (Thompson, 2009). Since the X-ray photons are produced below the surface of the target, they must traverse some thickness of tungsten dependent on the 'take-off angle' φ between their trajectory and the target's surface, leading to a variation in beam hardening over the vertical axis of the beam.

3.2.3.1 Pitting-Induced Beam Hardening Variation

The release of X-ray photons is very inefficient; most of the electron beam energy is deposited ultimately as waste heat via linear energy transfer to the target. A typical electron beam power on *MuCAT* 2 is 16.2 W, focussed on a 5 μm spot. As the electron beam is applied over time, the tungsten around the focal spot is vaporised, leaving a pit (Cherry and Duxbury, 1998, p. 55). As shown in Figure 3.7, this pitting has an additional effect on the energy distribution of X-ray photons produced in the target. If the take-off angle φ of a given photon is small, and the pit is sufficiently deep, this may increase the level of beam hardening caused by self-absorption in the X-ray target. Additionally, some of the vaporised tungsten may condense on the inner surface of the X-ray window, in effect forming a tungsten filter of variable (but small) thickness.

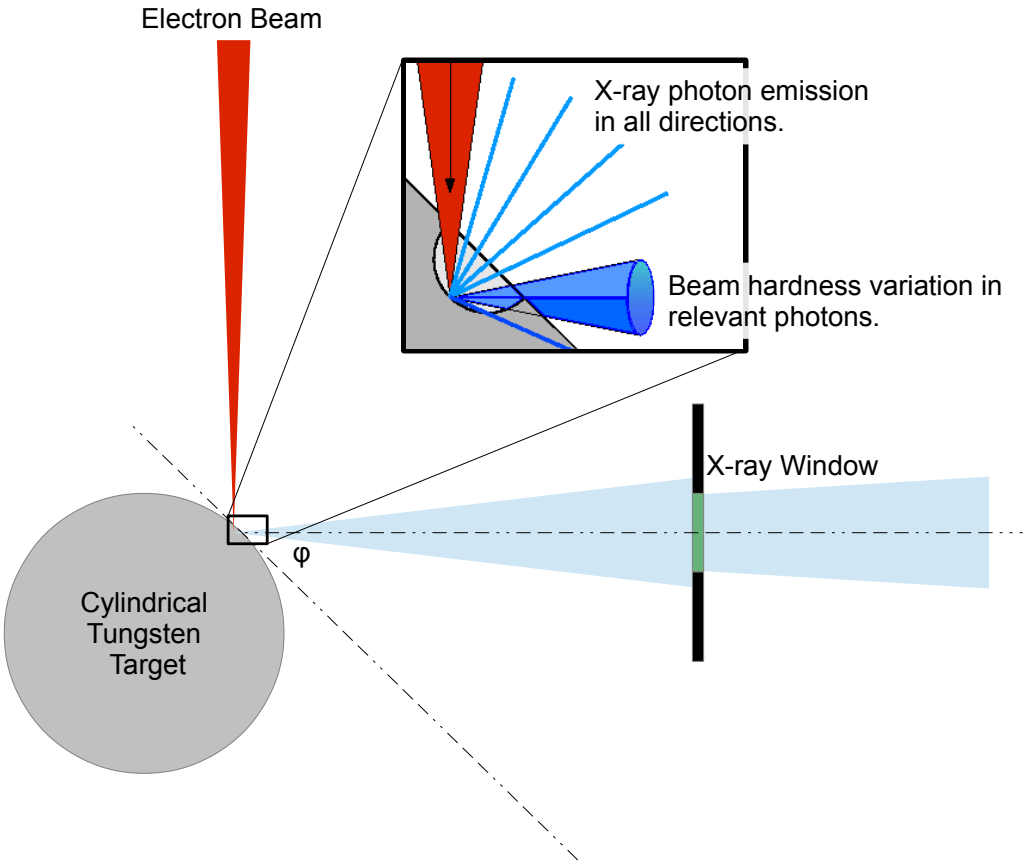

Figure 3.7: Schematic of a cylindrical X-ray target and window, with the takeoff angle of the centre of the cone-beam labelled φ. The inset shows the formation of a pit and its effect on X-ray beam hardness distribution.

3.2.4 X-ray Beam Filtering

As can seen in in Figure 3.5, the beam hardening effect of some elements is very marked - practically all of the photons below an energy of 20 keV are absorbed, while at higher energies a much greater proportion of photons is transmitted. Since metals of very well-characterised composition and high purity (in excess of 99 %) are available, it is therefore possible to pre-harden the beam by placing known thicknesses of an appropriate metal foil between the X-ray source and the specimen (Jennings, 1988). The following filter combinations are used in the *MuCAT* 2 scanner (Table 3.1): Generally filter materials of high atomic number are preferred, due to the

Accelerating Voltage	Aluminium Thickness (cm)	Copper Thickness (cm)
30	0.1	0.0
40, 60	0.05	0.0
90	0.12	0.005
120	0.0	0.0411

Table 3.1: *MuCAT* 2 filter thicknesses.

fourth- to fifth-order dependence of photoelectric absorption cross-section on Z (Knoll, 2000, pp. 49-51) causing such filters to be photoelectric effect-dominant over Compton scattering, which is proportional to Z (Kinahan et al., 2003).

It should also be noted that, since filters remove photons from the X-ray beam, the statistical power of the scan is reduced for a given X-ray tube power and duration of scan, leading either to lower SNR or the requirement of a longer scan time.

3.2.4.1 Absorption Edges and Band-Pass Filtering

As Figure 3.4 shows, there are discontinuities in the likelihood of X-ray absorption for some materials at tomographically-relevant energies. This is caused by the availability of transitions between the electron shells; while electrons in outer shells (though with a high enough work function to prevent Compton scattering) may still be ejected from the atom, electrons in lower shells may be excited to higher energy states, providing a second absorption mechanism and a corresponding jump in LAC. This property can be used in order to 'tune' the physical filters used in order to increase the relative absorption of higher-energy photons, thereby producing a band-gap energy filter.

Didymium oxide ($Nd_2O_6Pm_2$) is a compound used in welding goggles to attenuate sodium emission, and in photography as a band-stop filter around . It has an X-ray attenuation 'step' at approximately 40 keV, making it a material of interest for pre-filtering X-ray beams when used in combination with a caesium iodide scintillator.

Simulations of the detected spectrum for use at an accelerating potential of 60 kV were carried out for BG36 glass (Schott), which has a composition as shown in Table 3.2. The relative photon intensity spectrum is shown in Figure 3.8 for millimetre and half-millimetre filters in addition to the half-millimetre aluminium filter used at that potential (from Table 3.1), with a CsI scintillator thickness of 100 μm and a perfectly efficient detector.

Ingredient	Chemical Formula	Weight Percentage (%)
Boron oxide	B_2O_3	40-50
Didymium oxide	$Nd_2O_6Pm_2$	30-40
Calcium oxide	CaO	10-20
Arsenic trioxide	As_2O_3	0.6

Table 3.2: Composition of BG36 didymium glass.

3.3 Scatter Artefacts

Compton scatter, described in Section 1.1.3.2, is more troublesome to understand than beam hardening, since it encompasses not only the removal of photons from the X-ray field but also the re-addition of lower-energy photons on a different trajectory. As a result, a sufficiently energetic photon may undergo multiple scattering events, each one reducing the photon's energy to some degree. The detected trajectory of the scattered photon can generally not be back-projected onto the X-ray source. A further complication occurs in highly-structured multi-species samples, since scatter is a function of the specimen as well as the system. As a result, modelling of scatter by Monte Carlo simulation was investigated and validated for diagnostic radiology in (Chan and Doi, 1983).

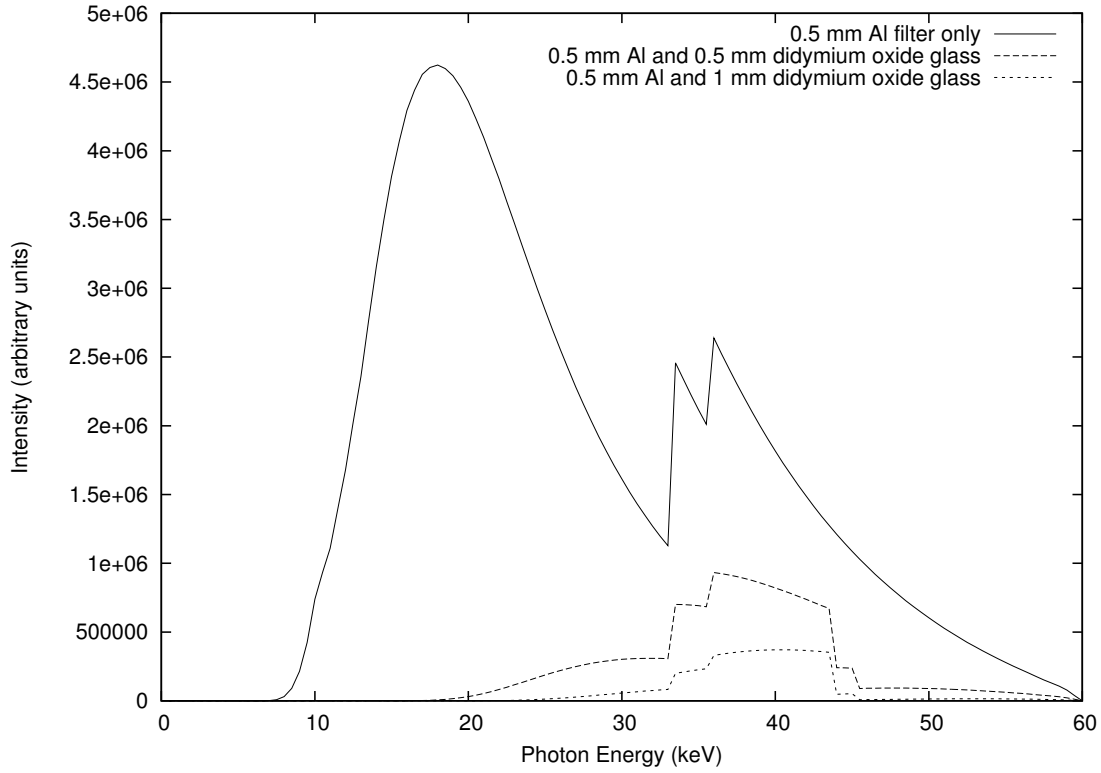

Figure 3.8: Simulated detected spectrum of a 60 kVp, 22° tungsten emission beam.

3.3.1 Scatter Distribution

The Klein-Nishina function described earlier predicts scattering into 4π steradians, with varying probability for a given photon depending on its energy, as shown in Figure 3.9. At tomographically-relevant energies, the distribution is essentially bi-lobal, with the least probable scattering angle (90°) being slightly under half as likely as the most probable (0°).

3.3.2 Scatter Effects on Reconstruction

Scatter may arise both from the specimen under study (sometimes known as 'object scatter') or from parts of the system in the beam-path, such as filters. In both cases, the scattering centre effectively acts as a weak X-ray point source. In a reconstructed CT dataset, object scatter in particular manifests through LAC reduction, cupping (Kanamori et al., 1985), and streak artefacts, as shown by (Joseph and Spital, 1982), similarly to beam hardening artefacts, as well as an increase in image noise (Davis and Elliott, 2006a). Scatter from near the primary beam's source increases the effective focal spot size of the beam, causing blurring effects, though large-angle scatter is likely to miss the detector entirely.

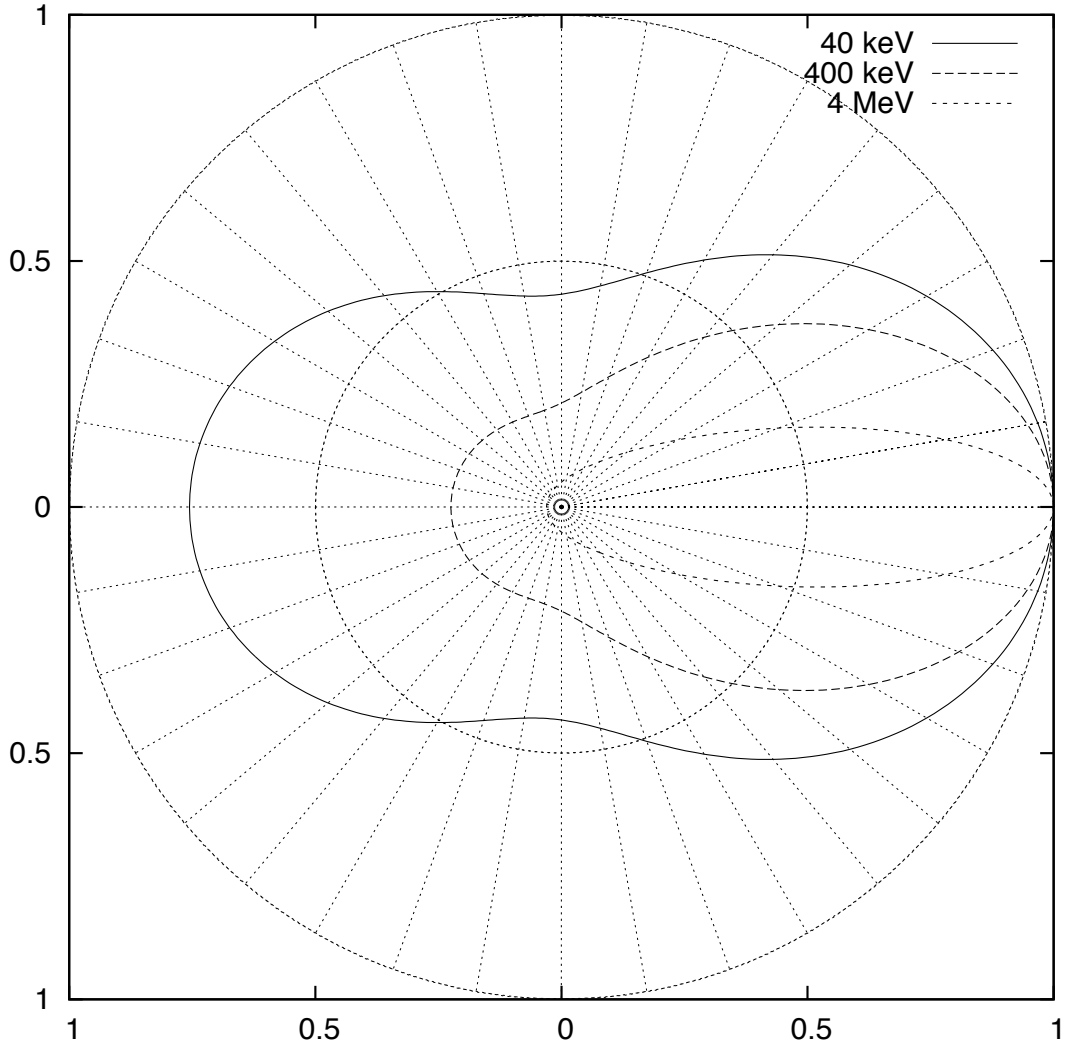

Figure 3.9: Compton scatter differential cross-section distribution for the tomographically-relevant energy 40 keV, with 400 keV and 4 MeV distributions to show decrease in backscatter with increasing photon energy. The distributions have been normalised to 1 at $\theta = 0°$.

Scattering becomes more significant as the specimen size grows since the scattered-to-primary beam intensity ratio increases, and where the mean Z is low, and has therefore historically been a problem of interest in medical CT more than XMT. As the cone angle of XMT systems has increased, however, the volume in which Compton scatter may occur has increased to the point where it is a necessary consideration (Siewerdsen and Jaffray, 2001).

3.4 Other Artefacts

XMT, as the name suggests, is capable of resolving structures at the micron scale if there are significant changes in LAC. Indeed, by making use of electron microscopy techniques to reduce the electron-beam focal spot size of an impact-source system, it is possible to achieve sub-micron spatial resolution (Sasov, 2004; Mayo et al., 2006). With these tight bounds on the sample's geometry, any radial motion of a part of the whole of the specimen or miscalculation of the rotational step size can produce significant inaccuracies in the reconstruction, particularly in non-rigid or dynamic contexts such as *in vivo* experiments. Discussion of these is presented for completeness, as they fall outside the scope of the thesis.

3.4.1 Motion Artefacts

If the source of error is a linear motion (as a result of a jolt or settling of the specimen, for example) streaking (known as a 'tuning fork' artefact) along the beam-path at the time of the motion may be produced, emanating from ray-paths that are tangent to large LAC changes. These streaks may extend across the entire imaged volume, and are particularly indicative of this type of error (Davis and Elliott, 2006a). It is possible to reduce the likelihood of these artefacts occurring by use of gated CT to ensure that all projections are taken at the same point in a repeated motion cycle, such as for cardiac or pulmonary imaging (Boyd and Lipton, 1983; Cody et al., 2004), or by sufficiently fast scanning, or other scan-time methods.

Motion artefacts due to thermal expansion in the sample or other parts of the X-ray system (particularly the X-ray target, into which a large amount of heat is deposited during scanning, and the X-ray detector) are generally reduced by temperature control of the interior of the scanner. This can be assisted by delaying the start of the scan by some time after the X-ray tube is energised, in order to approach thermal equilibrium more closely. Motion-related errors are also correctable during reconstruction by modelling and accounting for the motion of the specimen (Ritchie et al., 1996) or by interative alignment with forward-projected projections for random fast motions (Sasov et al., 2008b).

Motion artefacts due to stage wobble may become particularly apparent when the sample is

mounted a large distance from the rotation stage, as a small shift in the stage's plane of rotation becomes geometrically magnified. This type of artefact may be systematic and therefore correctable if the system is characterised using a known sample, as in Davis et al. (2010).

3.4.2 Centre of Rotation Artefacts

Errors in the determination of centre of sample rotation can arise from imprecisions in calculation or from changes in the sample's positioning over the course of a scan, due to play in the rotation stage or thermal expansion. The error so caused will be generally systematic in nature, and can be corrected for either by applying a fixed correction based on previous experience with the X-ray system or by generating an image metric for optimisation, as demonstrated in (Donath et al., 2006). The result of an error in centre of rotation is a reconstruction with double edges (Davis and Elliott, 2006a) or tuning fork artefacts at attenuation coefficient boundaries. This is similar to the effect of sample motion, except that the artefact may manifest on all sides of the high-attenuation region.

3.4.3 Field-of-View Artefacts

Partial-volume errors occur in filtered back-projection tomography when a highly-attenuating object, stationary with respect to the specimen, partially intrudes on the detector's field of view in some projections of the CT scan. This is particularly likely to occur when a large cone beam angle is used (Hsieh, 2003, p. 183). This situation may be necessary in order to scan a long object in as few blocks as possible, for example in the scanning of rapidly evolving systems such as a breath-hold scan of a patient in medical CT.

The artefacts produced by partial-volume errors generally include a loss of contrast in the reconstruction, and streaking in the vicinity of large LAC changes (Katsumata et al., 2007). These artefacts stem from the mathematical description of the effect having both a linear term and a non-linear term (Hsieh, 2003, p. 184).

In XMT large specimens of which only a small portion is of interest are rare, though tomographic strategies have been developed in order to minimise the structural information lost when there

is a significant portion of the specimen outside the region of interest, as listed and described in Kyrieleis et al. (2011). The specimens usually scanned in the *MuCAT* devices, however, are generally either sufficiently small to be scanned in their entirety or sufficiently well-aligned to the stage's axis of rotation to not cause any significant field-of-view artefacts unless the specimen has been mounted poorly, in which case a re-scan with corrected sample handling is required.

3.5 Chapter Conclusion

While there are several different types of artefact, with a well-prepared experimental design only those pertaining to the evolution of the X-ray field (beam hardening and scatter) are particularly problematic. The two are similar in origin, being a result of an unknown or partially-unknown LAC distribution on the X-ray field, as well as in many of their effects, and so this thesis will concentrate on efforts to mitigate them in tandem.

Chapter 4

Literature Review: Artefact Mitigation Strategies

There is extensive literature on methods used to reduce the occurrence of or to correct for both beam hardening and scattering errors in X-ray computed tomography and microtomography.

4.1 Beam Hardening Calibration and Reduction

In addition to pre-filtering the X-ray beam as discussed in Section 3.2.4, beam hardening has been the subject of correction by both physical and computational methods.

4.1.1 Water Bags in Computed Tomography

Early cortical tomographic imaging in medicine made use of water bags or water-filled skull caps placed around the patient in order to equalise the length of ray paths through the patient and to reduce the dynamic range of the sample volume (Beckmann, 2006), since water has a linear attenuation coefficient similar to that of soft tissues such as muscle, fat and grey/white matter (Hounsfield, 1973). A secondary advantage of this method was found by (Herman, 1979): the use of a water bag to replace air surrounding a two-phase specimen allows the assumption to be made that there are only two types of material between the source and the detector, permitting a polynomial beam hardening correction of order two to be employed.

While the increase in contrast resolution achieved in X-ray detectors since the 1970s makes this

correction statistically unreliable, in the general case a polynomial correction between the attenuation of the measured (polychromatic) beam and an analytically-modelled beam of appropriate intensity has been used successfully since, though using higher-order polynomials.

If the specimen contains several contrasting species, however (such as a tooth containing a metal alloy or amalgam filling, which would have at least three levels of LAC), this approximation becomes inaccurate. Further, the use of a water bag artificially lowers the apparent density of bone and can, in cortical scanning, elevate the greyscale values of soft tissue near the inside edge of the skull, creating a 'pseudo-cortex' artefact as a result of beam hardening in the bone (Brooks and Chiro, 1976).

4.1.2 Dual-Emission Scanning

Dual-energy computed tomography was proposed by Coleman and Sinclair (1985) in order to gain sufficient information to produce a beam hardening correction. This is achieved by either taking two separate scans at different accelerating voltages or by using a line-by-line collimator on the detector to alternate between the primary beam and a hardened beam, thereby deriving spectral information which can be used to calculate a correction (Ritchings and Pullan, 1979).

This method was evaluated as being particularly useful for specimens where the ray-path was unlikely to change significantly between adjacent projections, but that it would be less accurate for scans involving sharp changes in LAC. Additionally, the division of each exposure into interlaced projections decreases the number of primary beam photons available for reconstruction, requiring a doubled scan time for the same SNR.

4.1.3 Segmentation

Hsieh et al. (2000) proposed a different method of correcting for beam hardening in bimodal samples. They segmented out from the initial scan any high-density objects, then forward-projected the high-density areas in a tilted parallel beam configuration, which requires less computational work than forward-projecting for a cone-beam geometry. These projections are reconstructed to form an artefact-only image which can be subtracted from the initial cone-beam reconstruction

to produce a corrected reconstruction. They showed, however, that this only partially suppresses beam hardening artefacts from more complex samples, with minor improvements possible from a two-pass correction using low then high segmentation thresholds. A similar, iterative, approach was taken by Prevrhal (2004) with a bimodal (calcium-hydroxyapatite admixture in a PMMA sample holder), which required *a priori* information regarding the tomographic system and sample.

4.1.4 Modelling and the Role of *A Priori* Knowledge

(Van de Casteele et al., 2002) developed a parametric energy-based model for beam-hardening description, which was developed into a linearisation technique based on a physical model in (van de Casteele, 2004). The energy based model related the photoelectric absorption in a sample of thickness d to the source spectrum $f(E)$ and the detector spectrum $\gamma(E)$, the convolution of which takes on a bimodal form dominated by energies E_1 and E_2, as shown in Equation 4.1

$$-ln\frac{I}{I_0} = \mu(E_2)\cdot d + ln\left[\frac{1+\alpha}{1+\alpha e^{-(\mu(E_1)-\mu(E_2))d}}\right] \tag{4.1}$$

where

$$\alpha = \frac{f(E_1)\gamma(E_1)}{f(E_2)\gamma(E_2)}$$

The model provided a good attenuation correction, shown in Figure 6 of van de Casteele et al. (2002), at the expense of significantly lowered SNR. The test article was a single material (PMMA in air). In van de Casteele (2004) this was extended to correct the reconstruction of a bi-modal sample, with a priori knowledge of the sample's composition (aluminium included in PMMA) assumed. This required the assumption that the aluminium would be included centrally so that only two beam hardening curves would be required (ie. PMMA and aluminium filtered by depth d_1 of PMMA).

Menvielle et al. (2005) published the results of their exploration of a simulation-based approach to beam-hardening correction in 2005. This was based in part on earlier work in the simulation of a fan-beam tomographic system for the analysis of metal streak artefacts (de Man et al., 1999), which were concluded to be caused in part by beam hardening. de Man's simulation produced the incident X-ray spectrum purely as the sum of five monochromatic emissions from a line source

— a drastic simplification of a physical source, which produces a continuum of photon energies. Menvielle's model is based on several assumptions, most of which generalise well across impact-source systems (ie. that the photon beam is thin and polychromatic, that the emission of photons obeys Poisson statistics, and that attenuation is a Bernoulli process) but also requires a perfect detector, an assumption that is not justified, particularly in systems using a multi-element detector. Further, the method used — a nonlinear conjugate algorithm — required a large computational investment: 230 seconds for a 63×63 detector array, on a workstation computer of the day (Menvielle et al., 2005, p. 1867). While the effects of Moore's law and the introduction of graphics processing unit computation for parallel computing would be expected to improve the computation time significantly, the same is true of less computationally-expensive methods.

The simulation approach to spectrum generation was also explored in Taschereau et al. (2006), in that the tomographic system is simulated in its entirety, including the X-ray production, using the GEANT4/GATE Monte Carlo simulation frameworks. This, however depends upon good prior knowledge of the composition and arrangement of the system's components. In particular, while the results that Taschereau et al. generated from their simulation showed "reasonable agreement" to measured spectra, there were significant discrepancies, particularly below 20 keV and near the peak of the photon energy distribution, which they attributed to incomplete simulation of the environment, and uncertainties in composition and positioning.

4.2 X-Ray Scatter

Approaches to X-ray scatter generally have one of two focuses: the removal of scattered photons from the beam or the correction of scattering artefacts after detection.

4.2.1 Scatter Detection

The simplest way to estimate the degree of scatter in a given X-ray projection is by blocking a small angle of the primary beam near the source, then detecting photons in the region of the detector that subtends the blocked angle, which (assuming a well-shielded X-ray system) can only be scattered radiation. As the blocked angle approaches zero, the scattered radiation distribution

in the scatter-only regions approaches that which is caused in an ordinary scan, though the statistical power of measurements of photon distribution becomes less the smaller the number of blocked pixels are available. This technique was used by Siewerdsen et al. (2006) to estimate scatter in the X-ray collimator 'shadow' and interpolate across the detector.

The simulation approach to scatter prediction was first explored in the early 1980s for diagnostic radiology (Chan and Doi, 1983), but was applied to cone-beam CT by Colijn et al. (2004) in the modelling of a Skyscan small-animal XMT device, using a combination of accelerated Monte Carlo simulation and a data fitting procedure based on a deblurring algorithm to more rapidly arrive at a smooth scatter projection based on the traces of 10^5 to 10^6 photons in approximately 2 minutes per projection (Colijn and Beekman, 2004). This method was refined further by Zbijewski and Beekman (2006) — they noted that theirs was, to their knowledge, the first experimental demonstration of scatter correction in combination with all other X-ray beam-related artefacts. A Monte Carlo toolkit (CTmod) for simulating CT projections with scatter taken into account was developed by Malusek et al. (2008) based on the ROOT framework, though it could not be verified with experimental data on scatter-to-primary exposure ratios.

4.2.2 Scatter Reduction and Correction

Anti-scattering grids were investigated for use in digital mammography by Fahrig et al. (1994), using X-rays produced from a 30 kVp source (ie. 30 kV peak potential difference in the X-ray tube) scattered by a lucite breast phantom onto a one-dimensional grid. It was noted that even an ideal grid would require an increase in X-ray exposure of between 1.3 and 2 for mammographic purposes, but significant scatter reduction was shown for third-generation scanner geometries.

Simulation work by Leliveld et al. (1994) showed that collimation was particularly useful in the removal of Compton scatter, while the smaller Thomson scatter component was less susceptible to removal by collimation due to the low scatter angles of coherently-scattered photons. A two-dimensional grid approach was taken by Tang et al. (1998), using the SLIGA X-ray lithography process to produce $5 \times 5 \times 2$ mm nickel grids with 80 μm holes, but these were not tested for their scatter-removal properties. For comparison, the scintillator on the detector of the *MuCAT* 2 scanner measures 60×60 mm.

Bottari et al. (2001) simulated anti-scattering grids of this type using the EGS4 Monte Carlo package as a preliminary study, with only Compton scatter taken into account. They used image contrast reduction and maximum contrast variation in a uniformly-thick virtual breast phantom as their measures of scatter severity. As scatter is highly dependent on the object being imaged, the suitability of a uniform phantom for scatter measurements in the context of mammographic scanning (where the presence and volume of non-uniform parts of the breast is of primary importance) is questionable.

Ohnesorge et al. (1999) published a scatter correction algorithm based on a convolution function which could be used to subtract object scatter from projections in third- and fourth-generation CT, at the cost of reduced signal- to-noise ratio. With a scan of 1024 projections and 1024 (ie. 322) samples per projection, the algorithm required 31 minutes to run on a workstation computer of the day. Malušek et al. (2005) evaluated two optimisation functions for scatter reduction, working under the assumptions of perfect X-ray detection and negligible statistical or electrical noise, as well as axial symmetry of the sample.

In the *MuCAT* devices the use of time-delay integration allows for the scanning of specimens that are wider than the field of view of the X-ray detector. This permits the primary beam's cone angle to be reduced by a collimator coupled to the camera's translation stage, such that only that part of the specimen which is currently within the camera's field of view is illuminated. Since extraneous parts of the sample are not illuminated by the primary beam, object scatter is reduced to a minimum.

4.2.3 Scatter Quantification

Since scattering does not necessarily change the number of photons arriving at the detector, it is not possible to easily compare scattering severities using a single figure of merit. While the uncertainties in the use of tomography as a diagnostic tool for a particular research question can be quantified by calculating the area under a Receiver Operating Characteristics (ROC) curve (Fogarty et al., 2005), or by other methods of comparison with a 'gold standard' technique, the quantification of the severity of artefacts themselves is not generally shown, as the artefact is a

function both of the XMT apparatus (the X-ray beam, sample manipulation and detector characteristics) and of the structure of the sample. This lack of intrinsic quantitative assessment is a major stumbling block in determining the level of validity of general XMT reconstructions.

4.3 Chapter Conclusion

X-ray scatter and beam hardening share some artefact modes, and so beam hardening corrections based on linearisation will go some way to reducing the effects of scatter on the reconstruction. This partial scattering correction effect is also found with beam hardening corrections which use measurements obtained from a test piece which has a similar geometry (and thus similar scattering properties) to the specimen under study.

Chapter 5

Beam Hardening Correction of *MuCAT* Scans

This chapter describes the *status quo ante* at Barts and The London School of Medicine and Dentistry, upon which the project was intended to improve.

At the beginning of the project, the in-service correction was performed using a method developed by Davis et al. (2008), which is a correction derived by optimising self-absorption in the tungsten X-ray target (since the X-ray photons are produced below the surface of the target) and the thickness of the caesium iodide scintillator (into which the photons must be absorbed if they are to be detected.) All other parameters of the X-ray system were believed to be known to sufficient precision for an adequate correction to be made.

5.1 Aluminium Step Wedge

Attenuation measurements were taken of the 10-step aluminium step wedge pictured in Figure 5.1, which is a vertically-oriented (ie. normal to the plane of the rotation stage) sandwich of aluminium sheets, with combined thicknesses as shown in Table 5.1 bolted to a frame beneath. This replaced an earlier horizontally-oriented seven-step wedge developed in Davis and Elliott (2003), which could be measured using a single X-ray projection but suffered from in-scattering artefacts due to the variation in thickness (Ahmed, 2010).

Aluminium was selected for its ease of machining to precise thicknesses and for the ability to

obtain it at high purity. The step wedge is positioned in the beam path close to the source, so that the width of the wedge is only slightly narrower than the field of view of the detector, and a single projection is taken for each step of the wedge by raising the specimen stage between projections (but without rotating the stage), so that each of the projections provides an attenuation measurement for a different thickness of aluminium, with the other steps shielded from the beam to minimise X-ray scatter.

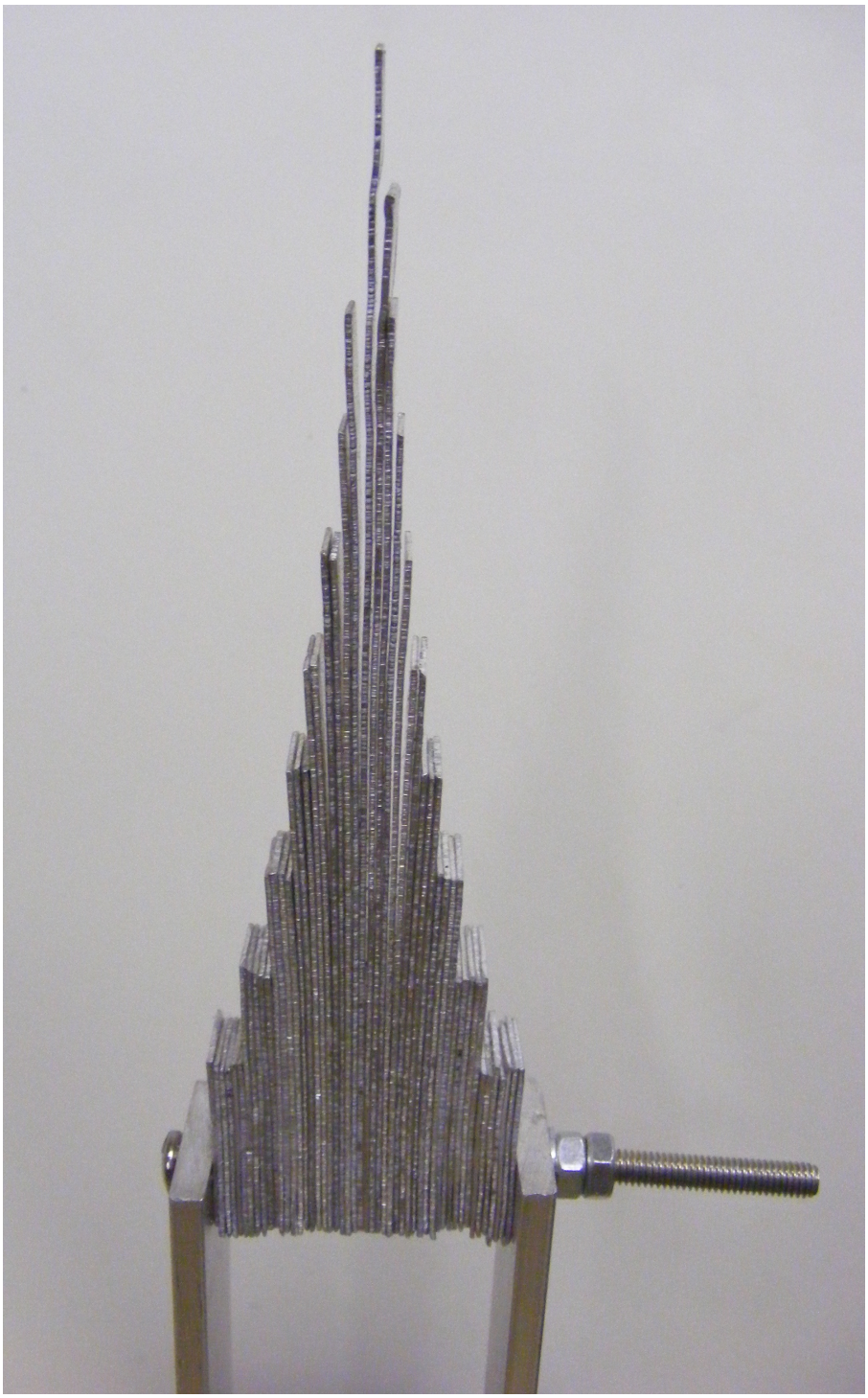

Figure 5.1: Aluminium step wedge viewed perpendicular to beam path, showing layers of filter and frame.

Step Number	Number of Sheets	Aluminium Thickness (cm)
1	50	2.5
2	37	1.85
3	27	1.35
4	19	0.95
5	13	0.65
6	9	0.45
7	6	0.3
8	4	0.2
9	2	0.1
10	1	0.05

Table 5.1: *MuCAT* 2 aluminium step wedge filter thicknesses.

These projections are preprocessed using `M2PREPROC` (as discussed in Section 6.1.1) to apply dark and light field corrections. Unlike a specimen scan, no beam hardening correction is applied. The resulting `CON`-suffixed file is used as an input to the beam hardening correction software.

5.2 Correction Software

The measured attenuations are compared to a model (Equation 5.2) of the detected spectrum of the system $D(E)$, which is the product of the source spectrum $S(E)$ with the simulated spectral responses of the tungsten absorption (subscript w), the X-ray filters (subscripts f_n as detailed for various accelerating voltages in Section 3.2.4), the aluminium step (subscript a) and the caesium iodide scintillator (subscript c). It should be noted that in this model the only quantities that cannot be obtained from *a priori* information are the thicknesses x_w and x_c.

$$D(E) = S(E) \cdot e^{-\mu_w(E)x_w} \cdot \prod_n \left(e^{-\mu_{fn}(E)x_{fn}}\right) \cdot e^{-\mu_a(E)x_a} \cdot \left(1 - e^{-\mu_c(E)x_c}\right) \tag{5.1}$$

Values of $D(E)$ are calculated for each line in each projection, to allow for the expected variation in optimal x_w (Section 3.2.3). Assuming the scintillator light output is proportional to photon energy, then the detected intensity should be

$$I = \int_0^{E_{max}} E \cdot D(E) \ \mathrm{d}E \tag{5.2}$$

By simulating an I_0 projection (ie. with zero thickness of aluminium), the set of attenuation values $ln(I_n/I_0)$ are derived. These are compared to the measured attenuations (taken from the 100

pixels surrounding the centre of attenuation of the projection) in the same projection and line, with the differences squared and summed over all lines l and projections p in order to provide a measure of error in the simulation as shown in Equation 5.3. This error, E is used as the function return value for the `IDL AMOEBA` function described later in Section 6.3.2.5, in order to find an optimal value of x_w and of x_c for each line in the projection.

$$E = \sum_{p=0}^{10} \sum_{l=0}^{799} \left(\left[\frac{I_{p,l}}{I_0} \right]_{measured} - \left[\frac{I_{p,l}}{I_0} \right]_{calculated} \right)^2 \tag{5.3}$$

Once acceptable values have been determined, the attenuations of a 300-step virtual wedge of the specimen material are then simulated for the equivalently-attenuating monochromatic X-ray energy. These 'calibration energies' are selected from a look-up table (Table 5.2), which was originally developed by choosing a virtual aluminium filter of a thickness designed to provide 50% polychromatic X-ray attenuation at the required accelerating voltage, then identifying the approximate monochromatic beam energy at which the same filter again attenuates 50% of the photons.

Accelerating Voltage (kV)	Calibration Energy (keV)	Example Uses
30	15	soft tissue, parchment
40	25	soft tissue
60	35	
90	40	bone, teeth
120	55	metals, filled teeth

Table 5.2: Commonly-used accelerating voltages and monochromatic calibration energies.

The simulated attenuations are used to derive an eighth-order polynomial of attenuation against material thickness, which forms the linearisation correction factor. User feedback is given in the form of an updated graph of the modelled and measured attenuations.

5.3 Performance and Limitations

The rate of successful optimisation of the tungsten and caesium iodide thicknesses was not high, with the optimisation often failing to converge. This was generally fixed on an *ad hoc* basis by adjusting the accelerating voltage used by the optimisation code, since it was noted that there was some variation in the voltage displayed by the X-ray tube's power supply unit.

The performance of this beam hardening correction method is limited by the range of measurable attenuations. While it would be possible to increase the attenuation by making thicker steps, a combined-foil wedge of the type used here would be subject to the mechanical limitations of the material used. Additionally, the magnification effect of the cone beam would mean that the width of the foil would need to be significantly greater at greater distances from the X-ray source in order to intercept the same number of photons and have as much statistical meaning, and the beam path lengths used in the software would have to be adjusted to take account of the extra distance traversed off the beam centre. While this difficulty can be neglected with a step wedge of only a few centimetres' maximum thickness, it would become much more difficult to construct.

It was also recognised that the system was only perfectly applicable to single-species specimens, though the choice of material was irrelevant. This results from the choice of a single-material virtual step wedge after the optimisation process has been completed. Since the proportion of species in a multi-material specimen is in general unknown, it is not possible to construct a mixed-material virtual wedge.

5.4 Chapter Conclusion

It was decided to focus the project on improving the beam harding calibration system to both make it suitable for a production environment (wherein not every user would be expected to require a licensed version of IDL) and to improve the error in the optimisation function by moving to a multi-species calibration device with scope for the systematically-controlled variation of accelerating voltage. The physical component of the calibration system (that is, the test piece) should be made as simple as possible to scan, so that if necessary it can be scanned with every specimen.

The variability of calibration is also a topic of interest — in Wassif, 2008 it was noted that using the beam hardening correction method described in this chapter a re-scanned specimen would be subject to linear attenuation coefficient measurement variations of up to 10%, which is poor for a quantitative method. Quantifying the change in validity of a beam hardening correction polynomial over time is essential to determining how frequently calibration measurements should be carried out.

In addition to this, it was decided to carry out an investigation of an immersion environment in order to scan dual-species samples with improved beam hardening correction validity.

Chapter 6

Materials and Methods

This chapter concerns the materials and investigative methods developed during the project this thesis describes.

6.1 *MuCAT* Data Processing and Reconstruction

A normal reconstruction from a *MuCAT*-produced dataset comprises several stages, as shown in Figure 6.1. At the beginning of the scan, dark and light field projections are taken in order to identify systematic errors due to CCD dark current, amplifier offsets and the beam intensity profile. Once the scan is complete, the resulting dataset is saved as a set of 32-bit floating point values in a file of the form *filename*.MCD, with the dark and light measurements saved as the first two projections. The MCD file also contains a header with scan metadata.

6.1.1 M2PREPROC

The individual X-ray projections are pre-processed using the M2PREPROC program, which firstly applies the dark and light field corrections, then multiplies each pixel's greyscale value by the output of a polynomial function of up to tenth order whose coefficients are determined by a separate script, as will be described later in the chapter. Optionally, the dark and light corrections can be applied without any beam hardening correction; this is generally used when a test specimen is being scanned in order to later assess the severity of the beam hardening effect. The

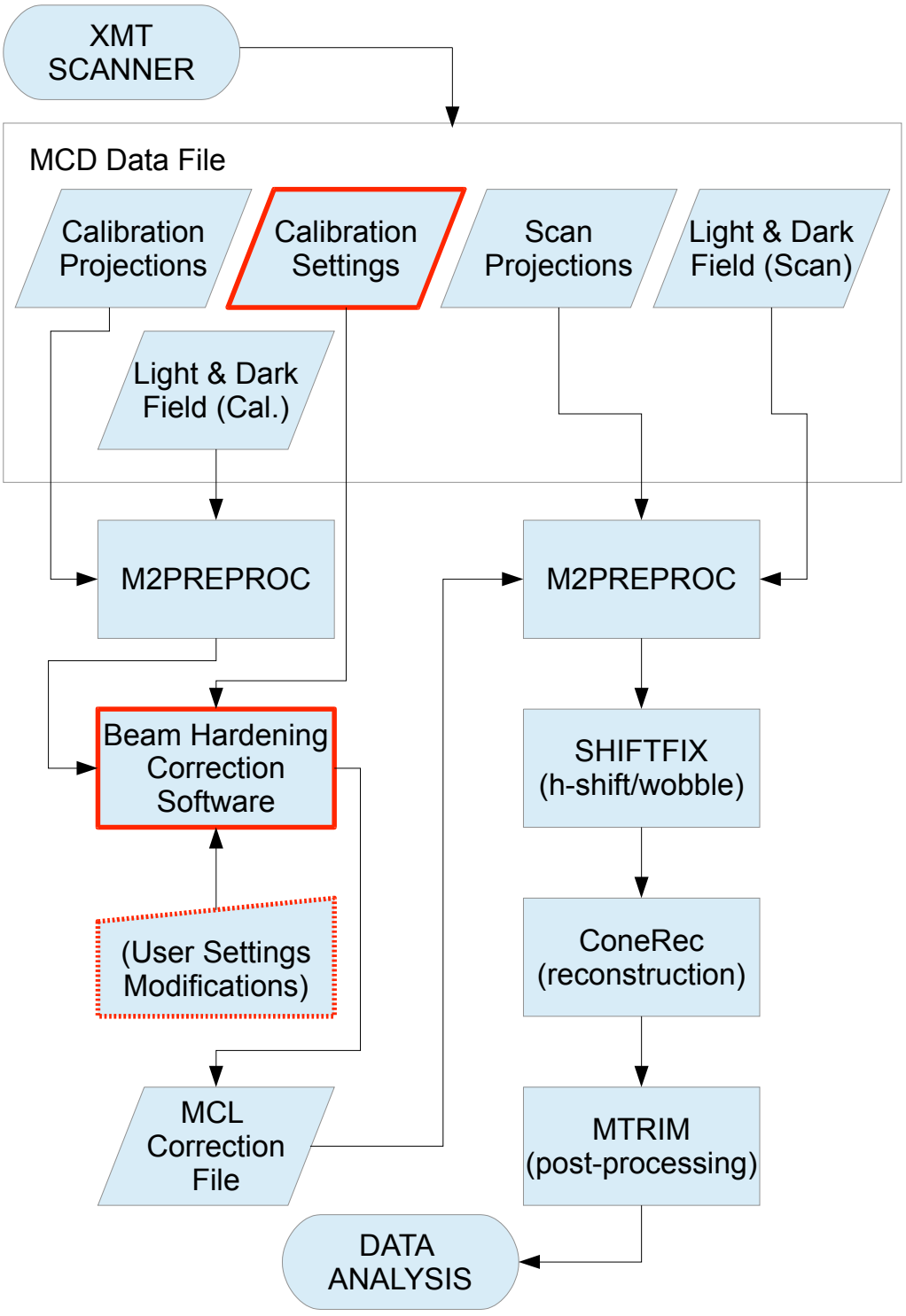

Figure 6.1: Flow diagram showing the interaction of the files and programs used in preprocessing and reconstruction. Red outlining of data elements and processes denotes creation as part of this thesis.

resulting cone-beam projections are saved as *filename*.CON, which may be viewed individually. M2PREPROC also extracts the scan metadata from the MCD file's header and saves it to human-readable form as *filename*.CRA

6.1.2 SHIFTFIX

The IDL script SHIFTFIX1B.PRO implements a correction for the systematic errors in horizontal shift and wobble in the sample rotation stage, based on the procedure described in Davis et al. (2010). These measurements are saved as the library files SHIFT.BIN and WOBBLE2.BIN, which are called by the script. The output is an iteratively-revised *filename*.CON.

6.1.3 ConeRec

ConeRec is the in-house cone-beam reconstruction program used for *MuCAT* reconstructions. It implements the Feldkamp cone-beam reconstruction algorithm, with options to adjust the default angle of the reconstruction, outputting the binary *filename*.BIN reconstruction file and the metadata file *filename*.SIZ, which contains voxel dimensional information.

6.1.4 MTRIM

The program MTRIM.EXE (run from the IDL frontend script MTRIM.PRO) is used to crop the reconstruction for viewing, and to set the relationship between the reconstructed LACs and the displayed 8-bit greyscale values, using the helper program MTOMPROJ.EXE to generate X-Y and X-Z projections as well as a grey-level LAC histogram file. The projections are displayed on a 10×10 voxel-spaced grid to aid in selection of appropriate cropping values, while the grey levels is plotted as a histogram to allow selection of an appropriate scale factor and greyscale offset. These cropping and greyscale variables are passed as arguments to the executable, which outputs the visualisable file *filename*.TOM.

6.1.5 Aluminium Correction

For specimens where the accurate reconstruction of LAC values is particularly important, a high-purity (99.999%) aluminium wire of approximate diameter 1.0 mm was historically affixed vertically to the side of the specimen, so that the wire rotates with it over the course of the scan. This provides a 'ground truth' measurement of LAC, to which the rest of the reconstruction can be scaled. Generally the percentage variation from published attenuation coefficient values is less than 5%.

Once reconstructed, *filename*`.TOM` is read by the IDL script `AL.PRO`, which allows the user to select (either by the voxel's numerical co-ordinates or by mouse click) starting and ending co-ordinates of a straight section of the wire, and to define a radius that fits well within the wire such that a cylinder of that radius with ends at the starting and ending points samples only voxels composed of aluminium. Average and standard deviation measurements are taken of the LAC values, allowing a scaling value to be calculated for the wire at the appropriate accelerating voltage. This value is then applied to all voxels in the reconstruction, and the `BIN` file is operated on by `MTRIM.PRO` again in order to allow cropping of the wire.

The aluminium wire will produce minor beam hardening effects which cannot be fully compensated for when scanning non-aluminium samples, but the small thickness of the wire compared to typical specimens mean that it is generally by far not the dominant absorber, and therefore these effects can be neglected. With larger samples it is also possible to affix the wire as far as possible from the region of greatest interest, thus minimising any beam hardening effect on that area.

Since the development of the step-wedge beam hardening correction, a correction to aluminium is no longer entirely valid for specimens where aluminium is not the dominant absorber. It was, however, occasionally used when scanning the same sample multiple times for comparison purposes, in order to reduce the random error in the reconstructed grey levels at the expense of introducing a source of systematic error.

6.2 *MuCAT* Data Analysis and Visualisation

Once reconstructed, the tomographic data can be analysed either in IDL or using purpose-built visualisation tools. The ones most commonly used for *MuCAT* reconstructions are Tomview and Drishti.

6.2.1 Tomview

`Tomview` is an in-house tomographic slice viewing and analysis tool developed by Dr Graham Davis to read QMUL's `TOM` files. It can be used to view cross-sections of the tomographic dataset in the three Cartesian planes, and to select individual voxels for LAC readout.

6.2.2 Drishti

The `Drishti` volume exploration and presentation tool is a multi-purpose 3D dataset viewer built by Ajay Limaye of the Australian National University (Limaye, 2006) and under regular development (Limaye, 2012).

`Drishti` is a modular program, of which the Import and Renderer modules are of particular use in the visualisation of QMUL `TOM` datasets. The Import module converts the dataset into Drishti's `PVL.NC` file format, while the Renderer module allows the application of one or more transfer functions to a point in the two-dimensional space defined by the LAC value μ and the differential $\frac{d\mu}{dx}$, where dx is the local rate of change of any of the Cartesian spatial co-ordinates.

6.3 X-ray Field Measurements

Standardised X-ray attenuation measurements were developed in order to derive beam hardening corrections, both for process improvement and for in-service correction.

6.3.1 Multi-Element Carousel

A replacement attenuation test piece was constructed, comprising filters of high-purity copper, titanium and aluminium foil with widths shown in Table 6.1 (initially a thicker PMMA sheet

was used as the 9^{th} absorber, but this was found to be insufficiently less absorbing then the 0.5 mm aluminium foil, and was replaced with a thinner aluminium filter as shown). The odd number of filter elements permits the individual illumination of a filter by allowing the beam through the gab between the two sheets nearest the opposite side of the carousel, as shown in Figure 6.2. The filters are mounted at the top and bottom to the edges of two circular aluminium plates, as shown in Figure 6.3, the lower of which has bearings attached in order to interface with the V-blocks on the rotation stage. This arrangement provides a greater range of attenuations than a single-species piece without the geometrical limitations described in Section 5.3, since the copper and titanium filters have significantly higher LACs at relevant energies than aluminium.

Projection	Material	Average Thickness (mm)
1	copper	2.093
2	titanium	4.42
3	titanium	2.21
4	titanium	1.105
5	aluminium	3.976
6	aluminium	1.988
7	aluminium	0.994
8	aluminium	0.497
9	aluminium	0.2

Table 6.1: Material profile of the beam hardening carousel.

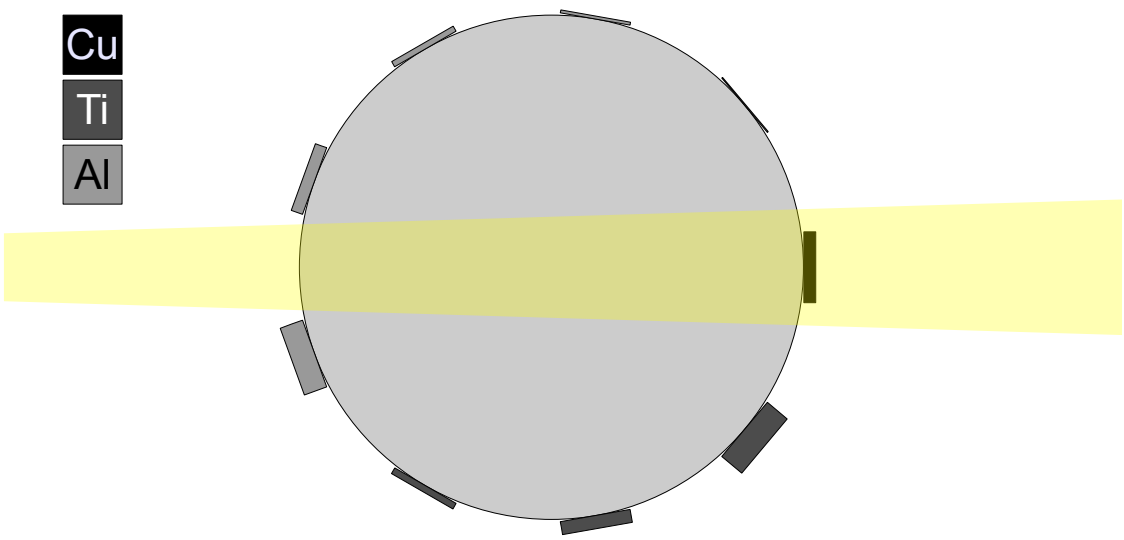

Figure 6.2: Schematic of the beam hardening ‘carousel’, showing filter types and illumination of the copper filter by the X-ray beam.

Figure 6.3: 'Carousel' test piece, showing attenuation filters and frame, including early low-attenuation PMMA filter (since replaced with aluminium).

6.3.2 Beam Hardening Correction Software: Infrastructure

6.3.2.1 Computer Hardware and Operating System

The computational experiments contained in these thesis were carried out on a workstation computer supplied by 3XS Systems (Bolton, United Kingdom), with an Intel Core i7-920 processor operating at 2.67 GHz and 12 MB of random-access memory. Graphics operations used an NVIDIA Quadro FX 5800 card with 4 GB of dedicated memory. The operating system installed was Microsoft Windows 7.

6.3.2.2 Spekcalc

`Spekcalc` was developed to simulate tungsten impact-source X-ray spectra for medical physics applications without recourse to computationally expensive Monte Carol modelling (Poludniowski et al., 2009), based on a given accelerating voltage and takeoff angle, with optional filtration by air, beryllium, aluminium, copper, tin, tungsten, tantalum or water. The program provides binned intensities in terms of number of photons $\mathrm{keV}^{-1} \cdot \mathrm{cm}^{-2} \cdot \mathrm{mAs}^{-1}$, allowing the total photon flux to be calculated for a known tube current.

Originally only usable for accelerating voltages greater than 40 kVand less than 300 kV, newer versions of the program have extended this range below 1 kV. `Spekcalc` has a number of advantages over the `IPEM78` spectrum generation software used for the calibration generator in Section 5.2, in that it permits the use of take-off angles above 22°, is generally marginally closer in its predictions to the 'gold standard' of Monte Carlo simulation (in the case of Poludniowski et al., BEAMnrc was used for comparison), and is available freely.

`Spekcalc` can be run interactively via a graphical user interface, producing half-value layer, energy and absorbed dose information, a graphed intensity spectrum, and two-column text data. The program has also been supplied as a command-line function with inputs from a text file (an example of which is shown in Appendix A), called as `spekcalc -i` *`inputfile`* `-o` *`outputfile`*. The file *`outputfile`* contains the same data as the textual output of the interactive version of the program.

The output of `Spekcalc` is valid only between the the peak energy and 1/10 of this value; pho-

ton energies below this are taken as zero. This is reasonable for the purposes of this thesis, as the *MuCAT* 2 scanner does not operate at accelerating voltages high enough for low-percentile-energy photon transmission through any significant filter. While the scriptable nature of Spekcalc would have made it possible to generate spectra on the fly, it was decided for reasons of computational speed to pre-generate spectra at intervals of 0.5 kV and 1°for use in the correction software.

6.3.2.3 XCOM

The XCOM photon cross-sections database (National Institute of Standards and Technology, 2010) provides cross-section or mass attenuation coefficient data for elements, compounds and mixtures at specified photon energies. It is available both online from the NIST website (as specified in the reference above) or as downloadable FORTRAN source code. A program compiled from the latter was used in order to generate total attenuation (ie. by photoelectric absorption, Compton and Thomson scattering, and pair production) spectra. The `XCOM` program is interactive and runs from the command line, so it would have been possible to automate attenuation spectrum generation by use of a Windows batch file or a shell script using `expect`, but this was felt to be unnecessary for the small number of spectra that were needed.

6.3.2.4 Interactive Data Language

Interactive Data Language, or IDL, is a cross-platform scientific programming language and development environment offered by Exelis Visual Information Systems (Boulder, Colorado, USA) - previously ITT Visual Information Systems (Exelis, 2012). The language contains a large number of specialised procedures for the manipulation and analysis of large datasets, and for displaying results either numerically, in the form of a graph or via an image viewing window. In addition to interactive use, IDL programs making use of a graphical user interface to replace the development environment's console may be compiled for running in the IDL Virtual Machine, which is available free of charge, permitting the use of programs without purchasing an additional IDL license.

6.3.2.5 AMOEBA Optimisation Function

The `AMOEBA` function in IDL implements the Nelder-Mead downhill simplex algorithm, as described in Nelder and Mead (1965). This projects an initial N-dimensional simplex onto the

space of possible variable combinations (where N is the number of variables). The vertex with the highest (ie. least optimal) value is replaced by a new point, which is selected so as to expand or contract the 'volume' bounded by the simplex, or to reflect the vertex in the $N-1$-dimensional 'plane' occupied by the other vertices. The simplex eventually contracts about a point that gives a minimum function return value, and terminates successfully if the fractional decrease in the return value over that of the previous iteration is sufficiently small. This point may be a local minimum if the spatial topography is insufficiently smooth or if the initial simplex is too small.

`AMOEBA` requires an initial simplex to be specified or a characteristic length scale for each dimension, as well as the target function, which must return a floating-point result when called with the values of interest for optimisation. `AMOEBA` also optionally allows adjustments to the number of function calls that may be made before the algorithm will fail.

6.3.3 Beam Hardening Correction Software: Implementation

The correction software developed for use with the multi-element carousel was based on the same theory as the protocol described in Section 5.2, though with significant improvements to both the code structure, the usability and the program logic.

Serious problems were found with maintainability of the original code due it its heavy use of `COMMON` blocks, IDL's implementation of global variables. Since IDL has a global namespace, use of global variables allows alteration of their data from any part of the program without the variable having explicitly passed to that function or procedure, an ability that is detrimental to error analysis and program maintenance (Wulf and Shaw, 1973). As a result it was decided to rebuild the program entirely. An alternative to global variables was found in IDL's data structure type, which permits the passing of large numbers of related variables simply while ensuring that any given function only has access to the data it needs. This required editing the built-in `AMOEBA` function (and thus bringing it into the explicit codebase) in order to allow passing of additional arguments to the function being optimised (see Appendix B for the codebase.)

The optimisation function was extended to include the accelerating voltage, based on the reporting of successful *ad hoc* tweaking by users. Large variations, in excess of ±10%, were permitted

(though optimisation of the carousel filter thicknesses would be expected to make this redundant), and since the voltage does not alter over the spatial dimensions of a projection it was decided to use a double-loop structure so that voltage could be optimised on a per-scan basis while caesium iodide and tungsten thickness optimisation would be performed once per projection line. Since voltage optimisation requires that spectra be available for arbitrary accelerating voltage fractions, adjacent spectra are interpolated using a weighted average in order to produce a spectrum for the desired floating-point voltage. Production of the X-ray spectrum library was migrated from `IPEM78` data to `Spekcalc` output, for accelerating voltages of 1–150 kV and take-off angles of 1–89°.

In order to allow use via the `IDL` virtual machine (which does not allow users to input data via the console), a graphical user interface was developed in order to allow settings to be inputted, as shown in Figure 6.4. This pre-populates from a settings file, `settings.txt`, in the current working directory (CWD, ie. the directory containing the calibration program's `SAV` file.) When the settings are confirmed and the 'start' button is clicked, the current settings overwrite the CWD's `settings.txt`. Line-by-line attenuations are also displayed in graphical form, with the optimisation function return values plotted in green (scaled 100 times for visibility, and offset by +1 in order to preserve the plot's lower boundary at zero) as shown in Figure 6.5. This allows any obvious discrepancies resulting from contaminants on the filters to be quickly identified.

6.4 Dual-Species Beam Hardening

The use of an immersion environment to simplify the LAC distribution being scanned requires that a container be designed such that the specimen is free to rotate and that the composition of the fluid in which it is immersed should be kept approximately spatially-independent within the container.

6.4.1 Immersion Tanks

The immersion tank comprises an open-bottomed PMMA box with a valve in the top, connected by tubing to a peristaltic pump with a maximum flow rate of 528 $\mu l\ s^{-1}$and to a reservoir, as

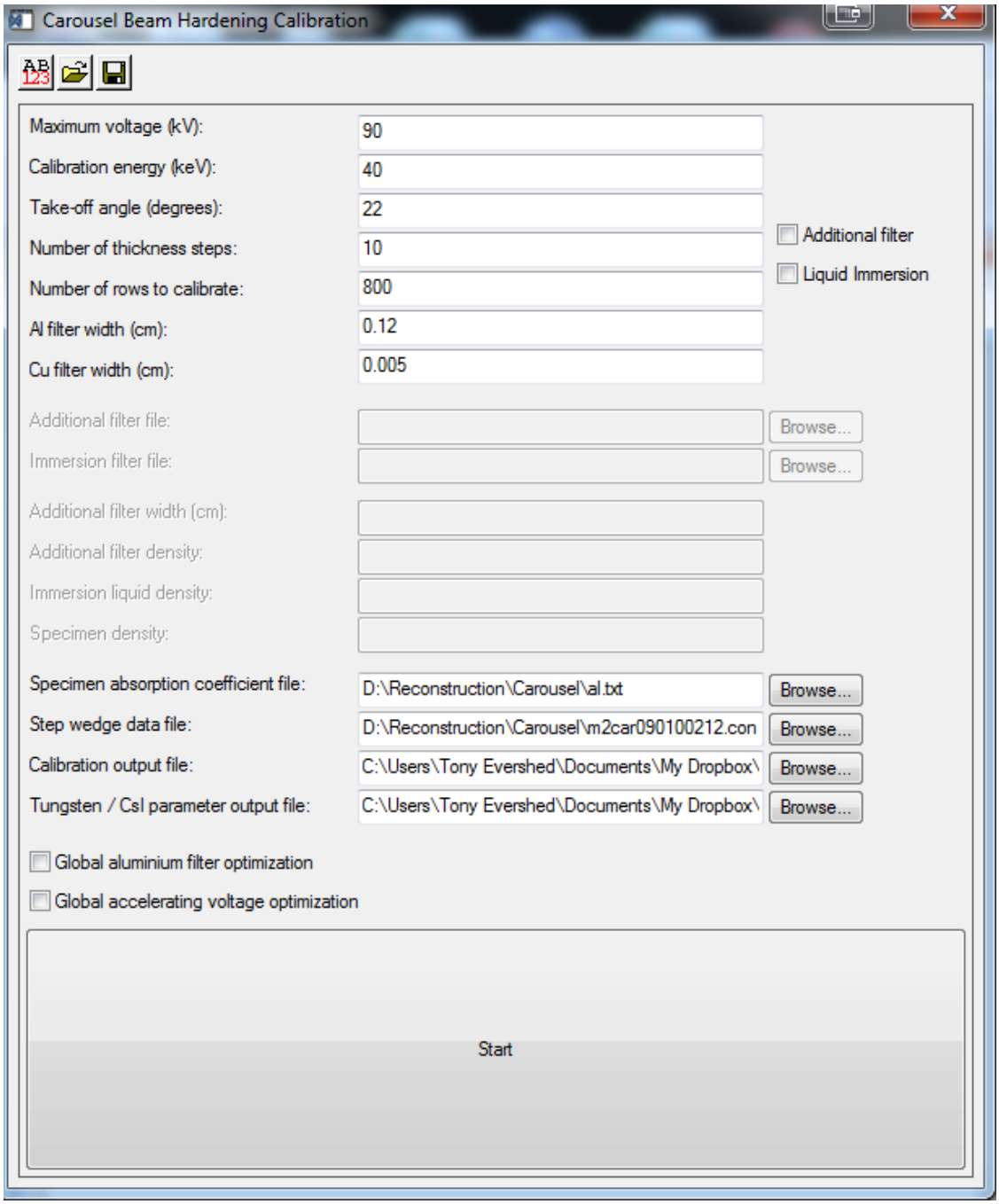

Figure 6.4: User interface to the calibration program, running under Microsoft Windows 7 with the Aero interface running. The toolbar icons allow the `settings.txt` file in the current working directory to be reloaded, another settings file to be loaded or the current settings to be saved at an arbitrary location. The inactive text-entry fields are activated on a click of the additional filer or liquid immersion checkboxes.

shown in Figure 6.7. The fluid is then returned to a walled basin below the tank, allowing the system to act similarly to a simple barometer. Fluid is therefore drawn up into the tank by the pump, while the sample is placed on a stand fixed to the base of the basin — this circulation process also allows mineral concentration variations in the fluid to be dispersed, which is par-

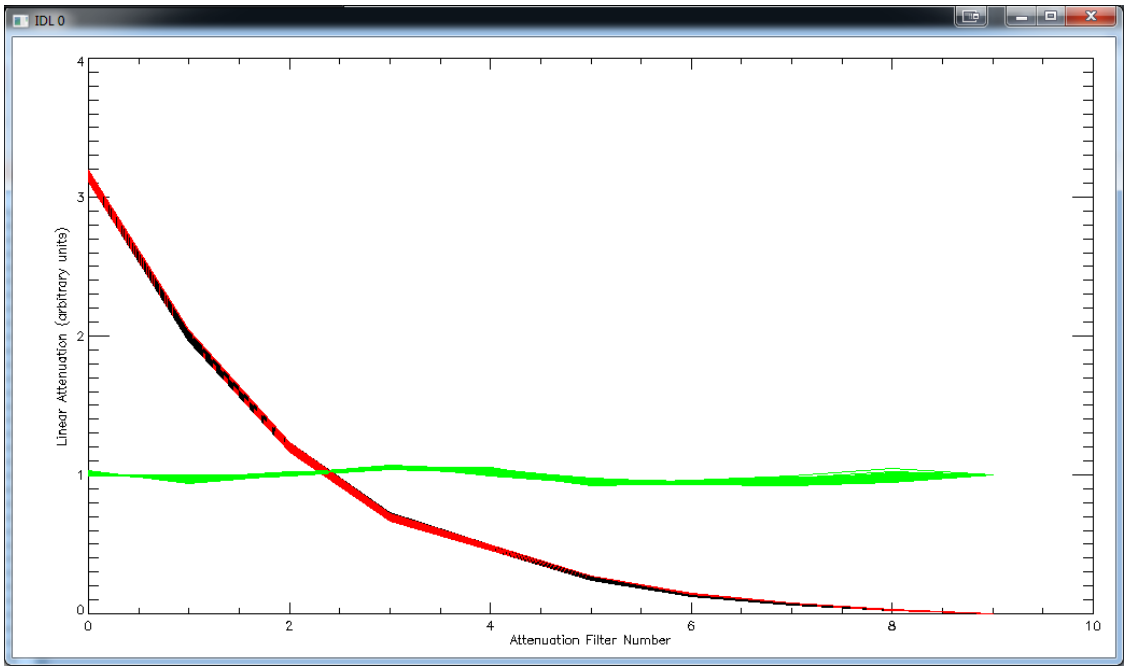

Figure 6.5: Example visual output of the calibration program. The red and black lines denote measured and calculated attenuation values of the carousel respectively (plotted once for each horizontal line, with the filter number serving as the abscissa axis). The final point is a zero-attenuating virtual filter. The green lines connect measures of error.

ticularly necessary if a dynamic study of a fluid-soluble specimen (for example, the demineralisation of dental enamel in acid - a quantitative version of the classic 'tooth in cola' experiment) is being carried out. An escape tube is attached to the outside of the tank and lowered into the basin, providing means of drawing off water to prevent overflowing, since the basin is an open possibly-conducting system inside the X-ray cabinet. The basin rotates on the XMT system's rotation stage, while the tank is clamped perpendicularly to the centre of the X-ray beam. Immersion tanks of different widths can be used, depending on the radial size of the specimen, allowing minimisation of the amount of fluid in the system.

A larger tank was also constructed for use with wider specimens, or specimens which cannot be held from below, as shown in Figure 6.6. In this case, the specimen is fixed to the lower end of a vertical rod clamped in an annular chuck, which is mounted on the rotation stage. The tank is fixed in place in the beam path, and has a capacity of 1.9 l of fluid. The tank is open at the top, removing the need for an external reservoir, as circulation can be achieved using the peristaltic pump only. The availability of a range of tank thicknesses permits the minimisation of excess Compton scattering, by allowing the smallest possible clearance to be used while still permitting

the sample to rotate freely without introducing motion artefacts.

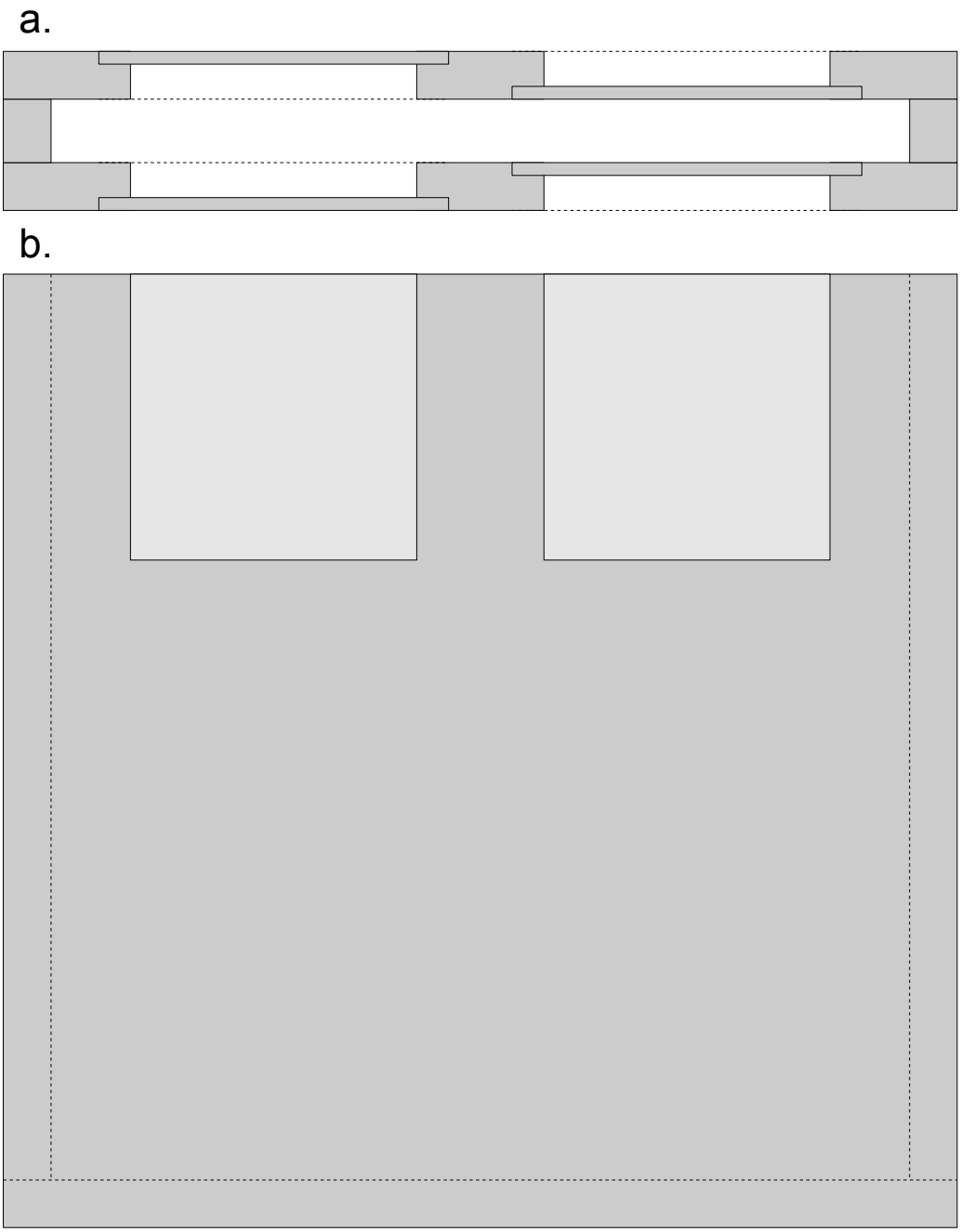

Figure 6.6: Schematic of the large immersion tank in plan (a) and front elevation (b) views, showing the thin perspex windows added in order to most closely approximate a water-only system. The specimen is placed between the two thin PMMA windows.

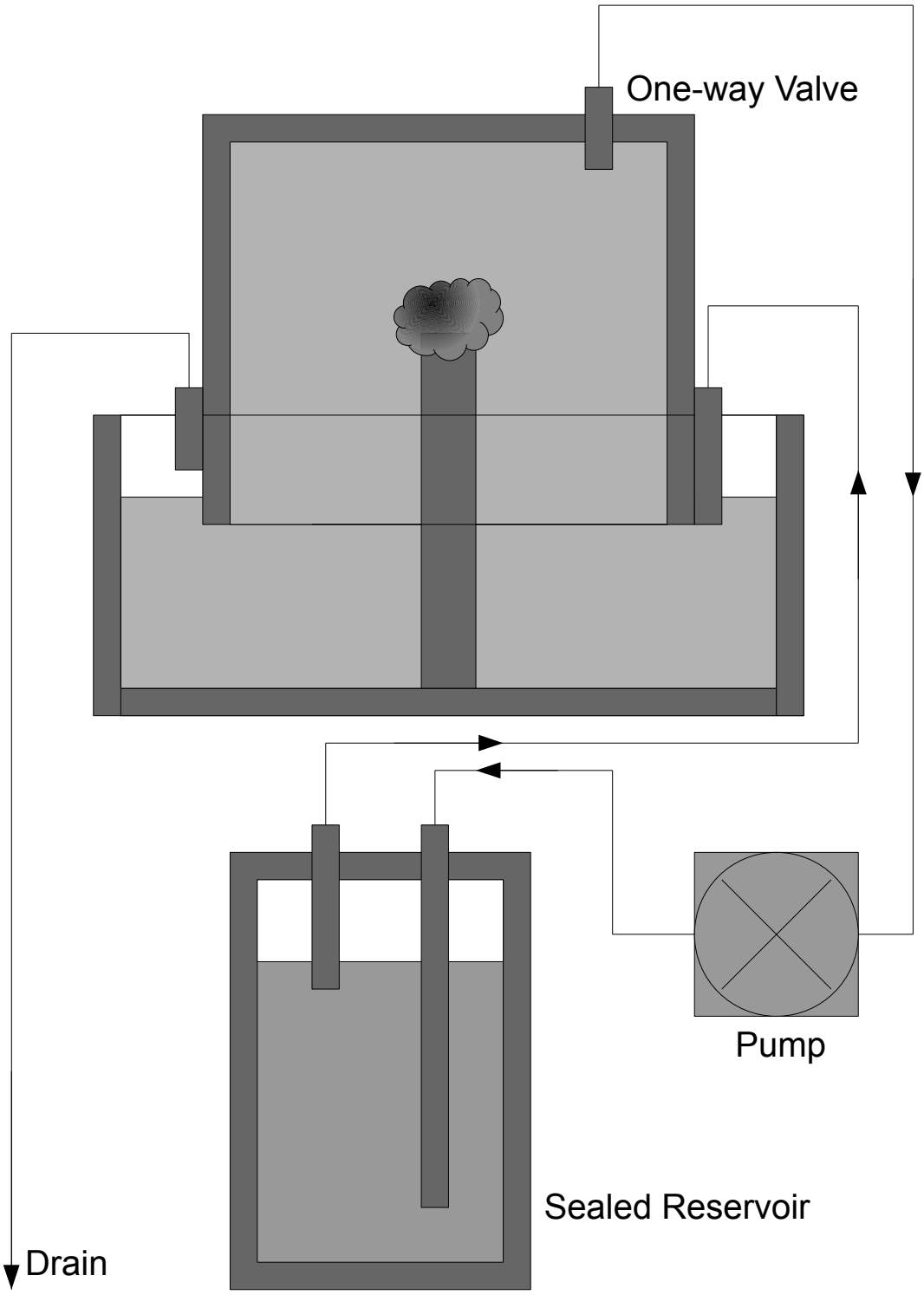

Figure 6.7: Schematic of the smaller immersion tank system, including multi-species specimen on mounting post. Clamps not shown for clarity.

6.4.2 Scanco Medical Phantom

The Scanco phantom (Scanco Medical AG, Brüttisellen, Switzerland) is a cylindrical test piece comprising five composite rods of varying concentrations (approximately 0, 100, 200, 400 and 800 mg cm^{-3}) of hydroxyapatite in a poly-methyl methacrylate (PMMA, $(C_5O_2H_8)_n$) matrix, surrounded by pure PMMA, and on top of a metal mounting pin as shown in Figure 6.8. It is used to calibrate the Scanco AG μCT 40 desktop XMT system, thereby providing the system with distinct advantages in terms of accurate LAC reconstruction over many other commercial devices, which often have no analytically-based beam hardening correction facility at all, but a linearisation correction based on a known uniform sample. This phantom provides a good example of a specimen for which there can be no ideal beam hardening correction for hydroxyapatite using the methods described in Sections 5.2 and 6.3.3, as there is a significant amount of PMMA, which is less attenuating than HA. Since PMMA has a molecular mass of 54, shared between 15 atoms, the effective atomic mass is 3.6, similar to that of water (3.3) — as attenuation mechanisms are Z-dependent, water may be used as an approximate radiodensity-matching fluid.

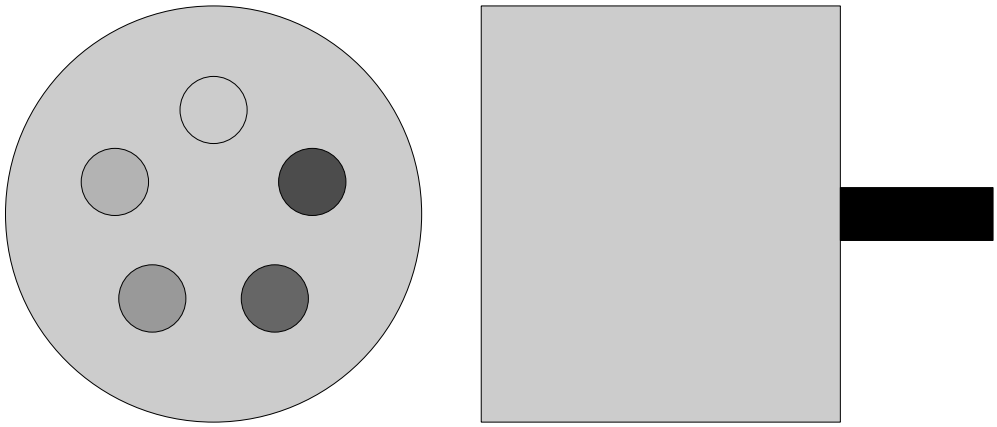

Figure 6.8: Plan and side views of the Scanco Medical phantom, showing HA/PMMA rods and mounting pin. Increasing greyscale level (with white = 0) denotes increasing radiodensity, though this is not depicted to scale.

6.4.3 Beam Hardening Correction Procedure

The beam hardening correction procedure described in Section 6.3.3 was amended to allow beam hardening correction in an immersed environment (since in the software the LAC value of air is approximated as zero.) If the 'immersion' and 'extra filter' checkboxes are set in the settings screen, then the specimen LAC value passed to the virtual step-wedge attenuation function after tungsten and caesium iodide optimisation is reduced by the immersion fluid LAC (thus producing an offset in the reconstruction where the fluid's LAC is displayed as zero.)

Chapter 7

Beam Hardening Correction

7.1 Experimental Implementation

Each of the major experiments in this thesis contains some techniques that cannot be usefully described in a unified materials and methods chapter. The test of beam hardening correction quality requires the scanning of a specimen of well-defined composition and variable mineral concentration in order to approximate a natural sample — the worst case for single-species specimens.

7.1.1 Synthesis of Test Piece

The beam hardening correction was tested by scanning three indistinguishable hydroxyapatite discs, each of diameter 12 mm and approximate thickness 2.5 mm. These discs were made from HA powder synthesised by aqueous precipitation as described in Akao et al. (1981). 1.0 ± 0.2 g of the powder was then pressed uniaxially into discs using a pressure of 88 MPa in a 12 mm stainless steel die, then sintered for 2 h at a temperature of 1250 °C in a Carbolite RF 1600 furnace (Carbolite Ltd, Hope Valley, UK.)

These discs act as good analogues to biological hard tissue materials since hydroxyapatite is the greatest single radio-absorbing component of teeth and bone (Berkovitz et al., 2010, p. 135), and because the compression and sintering process produces a disc with real variations in hydroxyapatite concentration.

7.1.2 Scanning and Beam Hardening Correction Measurement

The three discs were weighed separately, and a scan was carried out for each disc at 90 kV and 180 μA, with a voxel size of 30 μm. Each scan was composed of 651 projections and took 260 min, with the disc mounted horizontally on the rotation stage.

At the end of each scan, a nine-projection carousel attenuation dataset was recorded using the carousel described in Section 6.3.1 and a beam hardening correction for hydroxyapatite was produced using the method described in Section 6.3.3. The three discs were preprocessed using their respective correction polynomials — for comparison purposes, one of the discs was also corrected using a virtual aluminium step wedge of the type described in Chapter 5 — and reconstructed using `CONEREC`.

7.1.3 Reconstruction Analysis

After reconstruction, a threshold value of $0.5\,\mu_{peak}$ was selected in order to discriminate between hydroxyapatite-containing voxels and air. These were assumed to be the only two species in the specimen. The volumes of the discs were defined by counting the non-air voxels (that is, with a measured LAC greater than the threshold value), and the density of each disc was derived using the weight measurements taken before scanning. These values were taken to be the 'ground truth' density of the discs.

A cylindrical sampling volume of size 10 mm diameter ×1.5 mm was defined coaxially with the discs, and centred halfway between the pressed surfaces in order to avoid edge effects and allow for any slight tilt in the disc's placement. The mean LAC in this volume was determined using `AL.PRO`, and divided by the value of the mass attenuation coefficient for hydroxyapatite (0.9877 $\mathrm{cm}^{-2}\ \mathrm{g}^{-1}$) given by National Institute of Standards and Technology (2010), in order to provide a measure of hydroxyapatite density solely dependent on quantitative microtomographic measurements.

7.2 Results and Discussion

The calculated densities of the HA discs, both from the volumetric method (ρ_{vol}) and the attenuation measurement method (ρ_{μ}) using the carousel test piece and beam hardening correction program, are shown in Table 7.1.

Disc	Mass (g)	Volume (cm^3)	ρ_{vol} (g cm^{-3})	LAC (cm^{-1})	ρ_{μ} (g cm^{-3})
1	0.949 ± 0.001	0.302 ± 0.015	3.15 ± 0.02	3.13	3.17
2	0.921 ± 0.001	0.293 ± 0.015	3.14 ± 0.02	3.12	3.16
3	0.962 ± 0.001	0.306 ± 0.015	3.14 ± 0.02	3.12	3.16

Table 7.1: Hydroxyapatite disc measurements of density as calculated volumetrically and from LAC measurements made by XMT.

The magnitude of error in an LAC measurement of this type is not possible to quantify directly, being the result of a reconstruction of an object with real variations in density. However, ρ_{vol} and ρ_{μ} agree to within 1%, and the 0.7% discrepancy between the two appears to be systematic in nature, since it occurs across all three specimens. Since approximately 4.37×10^6 voxels in the sample measurement volume, the standard error in the average LAC would be insignificant in comparison to systematic errors.

Reconstruction of Disc 2 using the older step wedge beam hardening correction resulted in an LAC of 2.64 cm^{-1}, resulting in a 15% under-estimation of density. Additionally, there was a 13% 'dishing' variation in LAC when measured as a line profile (the same method as shown for an uncorrected disc in Section 3.2.2), indicating that the beam hardening correction by this method is insufficient to preclude noticeable artefacts.

7.3 Conclusion

The improvement in agreement between measured and calculated densities (and therefore also between mineral concentrations, the sample being composed of a single species) when beam hardening correction was carried out using the test piece and software described in Chapter 6 over that described in Chapter 5 is significant, though it remains only valid for single-species specimens.

Typical error values produced by the final, 'acceptable', iteration of the optimisation function using the step wedge were calculated as the (unitless) summed squares of attenuation difference as shown in Equation 5.3, which was approximately equal to 2 ± 1, when the optimisation converged at all.

With the initial configuration of the carousel filters (the least-attenuating filter being a 2 mm thickness of PMMA) there was a large under-estimation of attenuation on this projection, causing the typical error to rise to about 5. After replacement with the aluminium filter shown in Table 6.1, typical error values in the carousel-based reconstructions were in the range 0.05—0.2. The design of the carousel allows for quick and easy replacement of the filters, either in case of damage, to permit cleaning, or to improve the quality of the calibration.

Chapter 8

Calibration Energy Determination

In order to perform a beam hardening correction of the type described in Chapter 6 and demonstrated in Chapter 7, the monochromatic X-ray photon energy is required with attenuation properties as near as possible to the polychromatic beam actually being used.

As shown in Table 5.2, the standard conversions for *MuCAT* scanners have been in use for a significant amount of time, without much question as to whether they are optimal. While they were believed to have been selected so that the half-value layer (that is, the thickness of material that attenuated the energy of the beam by one-half) for aluminium attenuation with a monochromatic beam approximately corresponded to that produced with the polychromatic beam, there is no record of the methodology used or indeed the accuracy of the conversions.

This chapter details a simulation study to attempt to verify or falsify the assumption of half-value layer equivalence. If the assumption is verified, it would be possible to use other simulated attenuation materials in order to fine-tune the calibration energies for dental materials (hydroxyapatite), implants (titanium, steel) and so on.

8.1 Simulation Design

Initial experimentation utilised a trial and improvement approach, shown in Appendix C. This approach proved unsatisfactory, taking a large number of iterations to converge, and it was de-

cided to instead recover attenuations from existing software.

The following lines of code were added to the calibration software described in 6 in order to recover mass attenuations (that is, $\frac{I}{\rho I_0}$) made using the virtual step-wedge, along with the step thicknesses which resulted in that attenuation. The software is run with the attenuation material set to aluminium, though this could be changed if another absorbing material was desired. The code was inserted at the end of the `attenuation` function, after the mass attenuations have been calculated.

```
if isspecimen eq 1 then begin
  openw, attenuationfile, 'attenuations.txt', /get_lun
  for i=0, N-1 do begin
      printf, x(i), output(i)
  free_lun, attenuationfile
endif
```

In this code fragment, `N` is the number of steps in the virtual wedge, so the i^{th} step has thickness `x(i)`, and `output(i)` is the mass attenuation for that step. This is then saved to the file `attenuation.txt` in the current working directory, which is a tab-separated two-column array. The file is re-created each time the code is run, and only when the `attenuation` function is called for use with the virtual step wedge (and not for the carousel test piece.)

The half-value layer $x_{1/2}$ of aluminium can be found in the file when $x(i) = -\ln(0.5)$, from which the MAC may be derived using the relation given in Equation 8.1. The equivalent monochromatic photon energy can then be found using the existing aluminium data file produced by the XCOM photon cross-section database, which gives interaction coefficient figures (that is, MACs) at 0.5 keVintervals, which can be interpolated to approximate the calibration energy.

$$\frac{\mu}{\rho} = -\frac{\ln(0.5)}{x_{1/2}} \tag{8.1}$$

8.2 Simulation Results and Validation

The thickness-attenuation graph produced by the above method on the calibration projection file `te_alrod8_CAL.con` is shown at Figure 8.1. These calibration projections were taken at an accelerating voltage of 90 kV for use with an aluminium specimen. The half-value layer determined using a 90 kV calibration was 1.524 mm, which corresponds to a monochromatic photon energy of approximately 44.5 ± 0.25 keV. (Similar calculations were made for 40, 60 and 120 kV, for which recent calibration projections were available, with results as shown in Table 8.2, rounded to the nearest keV.)

Accel. Voltage (kV)	Nominal Energy (keV)	Calibration File Used	Calculated Energy (keV)
40	15	`ab_icelandic_r1b_CAL.con`	20.426
60	35	`NM_06_02_13_CAL.con`	26.871
90	40	`te_alrod8_CAL.con`	44.574
120	55	`FE_tooth7a_CAL.con`	57.685

Table 8.1: Calculated calibration energies for regularly-used accelerating voltages.

While the calculated value for 90 kV is different from the expected value of 40 keV, it is not known to what extent this value, used by convention, was rounded when initially defined. It was therefore decided to test the comparative validity of the calibration energy derived here by using it in the reconstruction of a known sample. The approximation 44.5 keV was selected in order to allow the use of a specific spectrum data file (which are stored at 0.5 keV intervals) rather than interpolating between two files.

A hyper-pure (99.999%) aluminium rod of diameter 10 mm was sourced from Goodfellow Cambridge Ltd. (Cambridge, United Kingdom) and cut to a length of 50 mm, then scanned using *MuCAT* 2 at an accelerating voltage of 90 kV and a beam current of 180 µAover 701 projections for a voxel size of 20 µm. The resulting projections were corrected for beam hardening using both 40 and 44.5 keV as the calibration energy and reconstructed. Five scans were used, shown in Figures 8.2, 8.3 and 8.4, with the 40 kiloeV and 44.5 keVcalibrations used to correct the scans in parallel. While filament changes are not believed to affect the X-ray spectrum, the scans were taken using the same cathode.

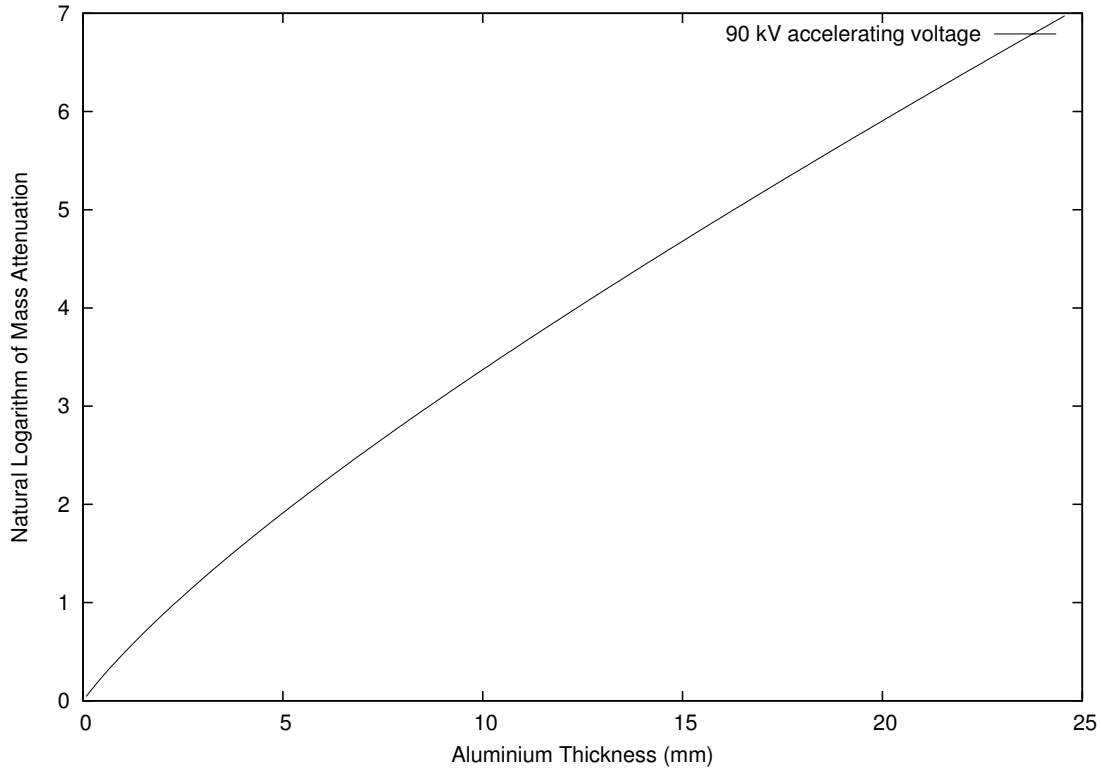

Figure 8.1: Graph showing the relation between virtual step wedge element thickness and the natural logarithm of mass attenuation from the calibration of the in-situ carousel projections from the `te_alrod8` scan.

The calibration and reconstruction process was performed twice at 44.5 keV, once with tungsten and caesium iodide thicknesses and accelerating voltage as the optimising parameters (as was the case for the 40 keVcontrol), and the second time with copper filter thickness replacing voltage. This was done in order to determine the optimum parameter set for this type of specimen, and was based on prior user feedback suggesting that copper-optimised calibrations converged more closely than voltage-optimised calibrations.

Linear attenuation coefficient values were read by averaging over a 4000 μm radius cylinder, co-axial with the aluminium rod and spanning rows 0 to 497 of the reconstruction.

Scan	LAC at 40 keV Voltage Optimisation (cm^{-1})	LAC at 44.5 keV Voltage Optimisation (cm^{-1})	LAC at 44.5 keV Copper Optimisation (cm^{-1})
1	1.58 ± 0.07	1.26 ± 0.06	1.26 ± 0.06
2	1.55 ± 0.1	1.25 ± 0.09	1.25 ± 0.09
3	1.55 ± 0.1	1.24 ± 0.08	1.24 ± 0.08
4	1.56 ± 0.1	1.25 ± 0.08	1.25 ± 0.08
5	1.55 ± 0.1	1.24 ± 0.09	1.24 ± 0.09

Table 8.2: Calculated calibration energies for regularly-used accelerating voltages.

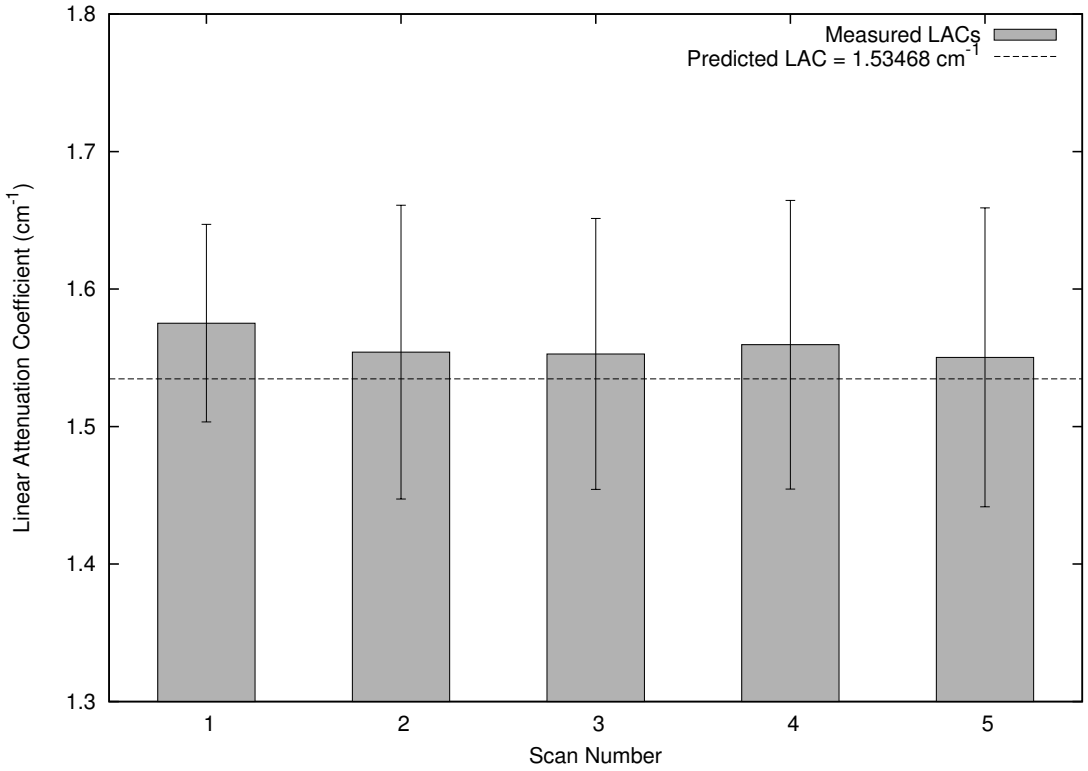

Figure 8.2: Graph showing reconstructed linear attenuation coefficients for eight scans of an aluminium rod, calibrated to 40 keVusing accelerating voltage optimisation.

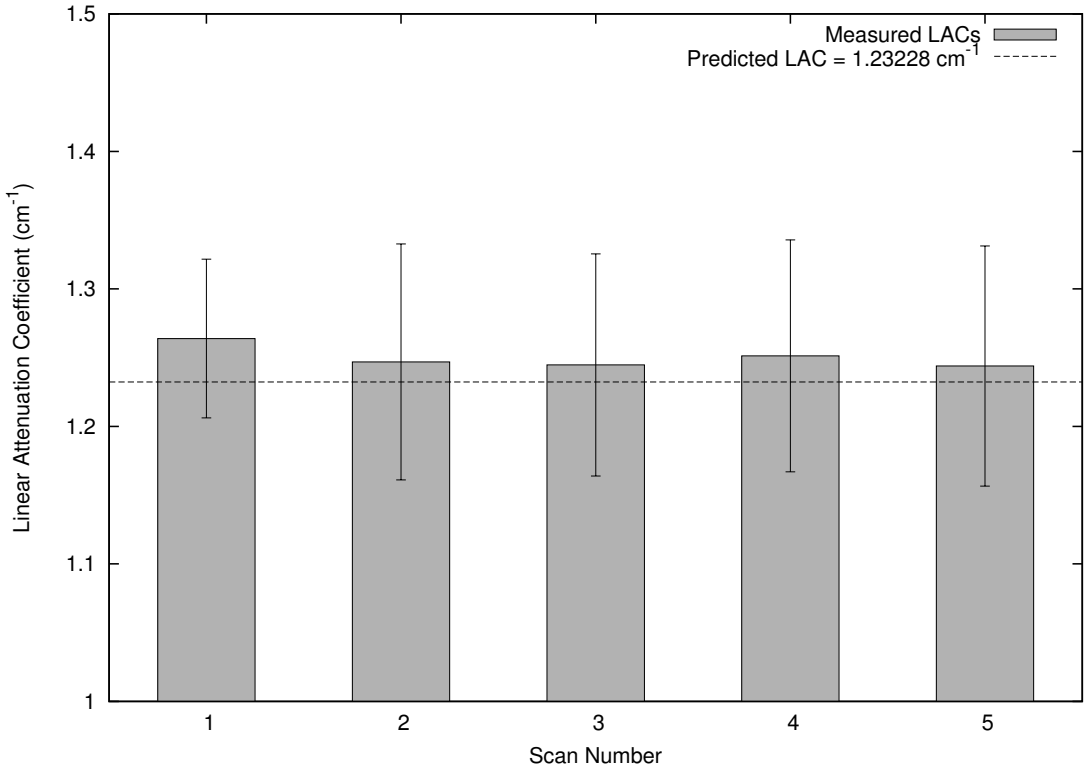

Figure 8.3: Graph showing reconstructed linear attenuation coefficients for eight scans of an aluminium rod, calibrated to 44.5 keVusing accelerating voltage optimisation.

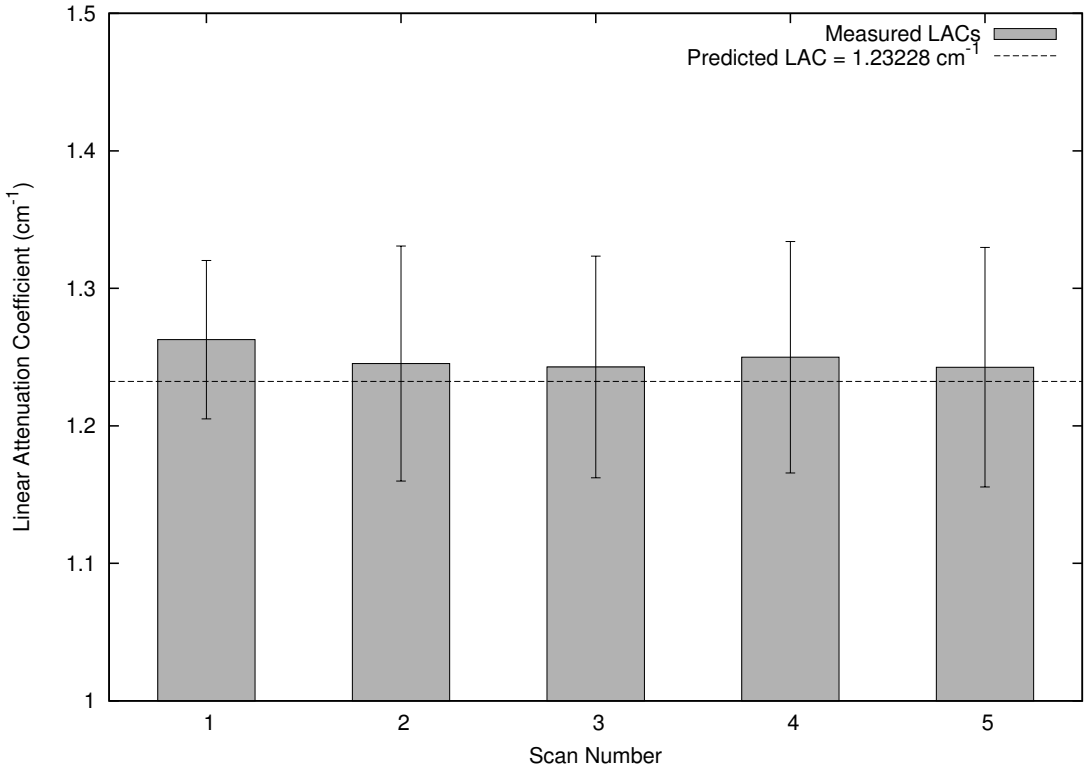

Figure 8.4: Graph showing reconstructed linear attenuation coefficients for eight scans of an aluminium rod, calibrated to 44.5 keVusing copper filter optimisation.

The LAC value of aluminium at 44.5 keV is 1.23228 cm^{-1} (National Institute of Standards and Technology, 2010). The scanned rods calibrated using the voltage and copper optimisations had had average LACs of 1.2501 cm^{-1} and 1.2487 cm^{-1} respectively. Since the standard deviation of the individual measurements was consistently in excess of 0.05 cm^{-1}, these are consistent with the theoretical value. Notably, however, the deviation was consistently smaller with the copper-optimised calibrations. Additionally, all of the values were above the theoretical value, suggesting that systematic error may be the major source of deviation in the results.

The scans corrected using a calibration energy of 40 keV exhibited a mean LAC of 1.5584 cm^{-1}, with the theoretical LAC value being 1.53468 cm^{-1}. Again, the consistency of the results with theory is shown, and a source of systematic error is suggested (see Figure 8.2.)

8.3 Conclusion

Since in both cases the linear attenuation coefficient values were consistent with expectations, it is not suggested that existing reconstructions be re-corrected with this calibration energy value. However, since the variation in LACs between scans was found to be smaller at 44.5 keV, use of this value in the correction of future specimens (particularly in cases where the specimen is expected to be imaged multiple times with independent beam hardening corrections) appears to have merit. Additionally, the copper-optimised calibration appeared to be marginally superior in this case, though both results were consistent with theory.

This experiment suggests that validation of the calibration energies for other kilovoltage beams may be required, particularly for lower-voltage scans since the relative discrepancy between the current and the calculated energies is greater.

Chapter 9

Time-Dependent Tungsten Beam Hardening Variation

9.1 Experimental Context

Since the MuCAT scanners utilise a demountable X-ray source, which can be re-indexed quickly and without difficulty by rotating the cylindrical tungsten electron-beam target through a small angle in order to present an unused surface to the beam, they are generally operated at a higher beam power than for sealed-source units, which must be taken out of service once the target reaches the end of its service life. MuCAT 2, for example, is operated at an electron beam power of 1.62 kW. Previously, re-indexing had been carried out on an *ad hoc* basis, so it was felt that measurement of the change in quality of projections taken over the lifetime of a target spot would be of use in incorporating re-indexing into the scanner's maintenance schedule. For the same reason, the effective lifetime of validity of a given beam hardening correction was desired.

9.2 Experimental Implementation

The MuCAT 2 X-ray scanner was re-indexed, and one thousand calibration 'blocks', each comprising nine sequential cone-beam projections of the carousel beam hardening test piece, were then scanned in succession, thereby producing a time series of attenuation measurements for each carousel filter element. The beam current was increased to 200 μA from the 180 μA used in normal scanning in order to maximise the effects of the electron beam on the X-ray target while still allowing a large number of blocks to be recorded.

It was expected that, as scanning continued, a pit would develop in the surface of the anode near the focal spot (of length scale 5 μm) due to thermal losses (which exceed 90% (Zunick, 1965), so a power loss of at least 1.46 kW within the focal spot) in the anode. The major effect of this pit would be to require the X-ray beam produced in the anode by bremsstrahlung and characteristic emission to traverse a thickness of the anode material that is dependent on the geometry of the pit and the take-off angle of the individual X-ray photons.

An additional effect of this pitting is that X-ray photons with a lower take-off angle would traverse a greater thickness of anode material and therefore be more strongly 'pre-filtered' by photoelectric absorption. It would therefore be expected that the median photon energy at the lower edge of the detector would be greater than that at the upper edge, and that the difference between these two would increase with block number as the depth of pitting increased. This would not be expected to have an effect on the quality of beam-hardening corrected reconstructions, since the calibration software selects thicknesses of tungsten filtration on a line-by-line basis.

Vaporised tungsten from the pitting would be deposited on the internal surface of the X-ray tube, including the X-ray window, forming a beam-hardening filter, though since the window is only a small part of the interior surface this would be expected to be a negligible effect over the timescale of the experiment.

9.3 Projection Analysis

The projection blocks were used in order to derive beam hardening corrections using the optimisation method described in Section 6.3.3, with the initial beam spectrum generalised so that each line of the projection has a unique spectrum based on interpolating the beam intensity values in the histogram file between the single-degree increments in take-off angle allowed for by the `Spekcalc` software. Thus, while the centre line of the projection is still based on a take-off angle of 22°, the take-off angles at the upper and lower edges of the projection vary by ±5.73° for a projection of 800 rows at the detector's pitch of 60 μm, given the source-detector distance 239.03 mm reported by *MuCAT* 2.

Since this calibration method, as well as producing the beam hardening correction coefficients, also produces a file containing the optimised parameters, the values of tungsten and caesium iodide thickness were recovered. It was expected that over the course of the experiment the tungsten value would increase due to ingress of the focal spot into the bulk of the target. This would lead to inaccuracies in beam hardening calibration, which can be detected directly by calibrating the carousel's attenuators with the correction polynomial resulting from the first calibration block. If pitting is a significant source of error over the duration of the experiment, the corrected attenuations of the attenuators should diverge from the self-calibrated first block as block number increases.

9.4 Results and Discussion

The optimised tungsten and caesium iodide parameters are shown in Figures 9.1 and 9.2 for the first calibration block and for blocks 100, 200, 300 and so on. While both show a general increase in the thickness parameter under investigation, in the case of the caesium iodide parameter this is small compared with the absolute value of the parameter.

Note that the values shown for the first calibration block are significant outliers from the other blocks pictured. It is believed that this is a result of thermal equilibrium in the system not being reached during early scans. Since block 100 is not similarly unusual, it is believed that thermal equilibrium had been reached by this point (approximately 100 minutes after scanning commenced.)

It should be noted that the value of the tungsten parameter is negative, implying an overestimated filter thickness parameter elsewhere in the calibration, which would lead to a consistent offset in the thicknesses that are being optimised. Since this negative offset is on the order of microns, however, it can be neglected.

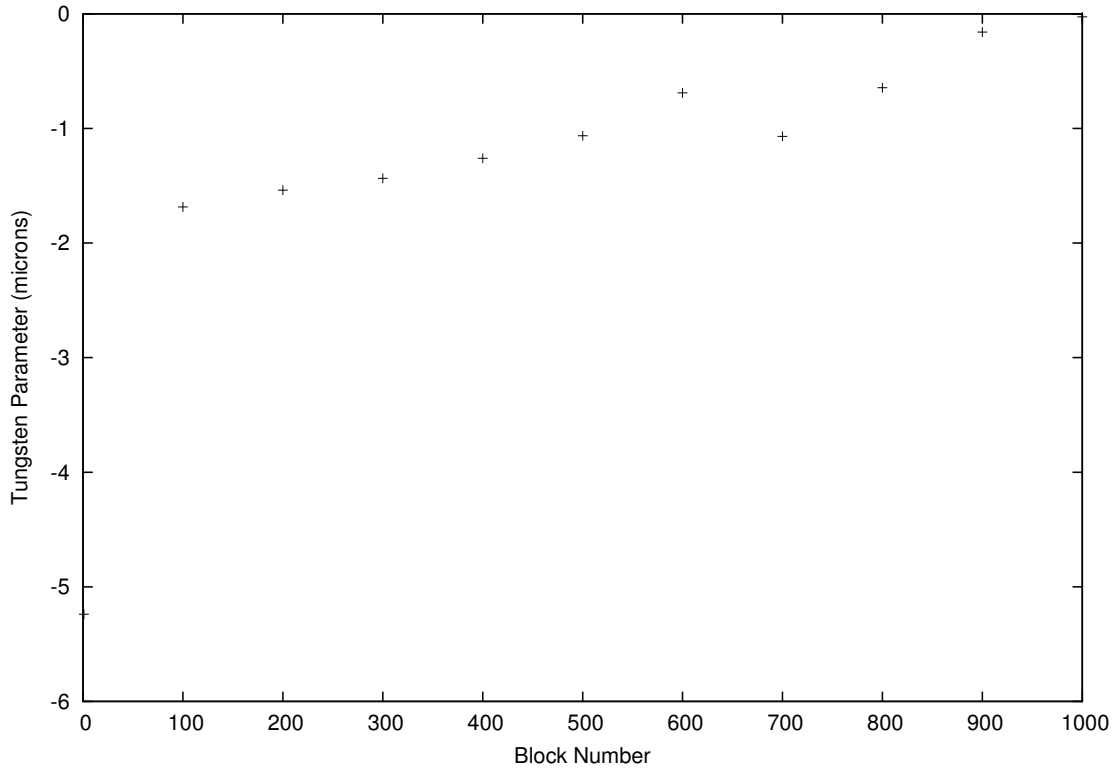

Figure 9.1: Graph showing the relation between calibration block number and the value of the tungsten filter thickness parameter.

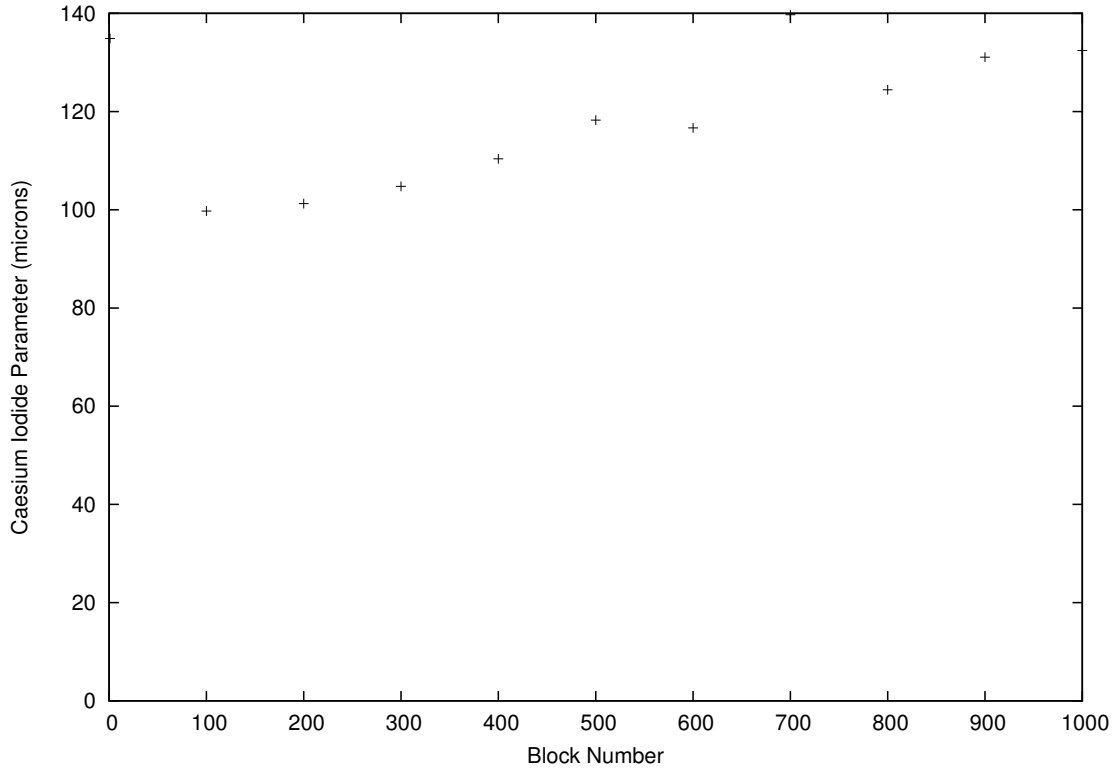

Figure 9.2: Graph showing the relation between calibration block number and the value of the caesium iodide scintillator thickness parameter.

The relation between horizontal line number and tungsten parameter is shown for selected blocks in Figure 9.3, where line 0 represents the bottommost row of the detector. As in the previous figures, the greatest discrepancies between calibration parameters occur within the first hundred blocks as the system warms to thermal equilibrium. The other feature of note in this result is the discontinuity at line 400, which is a result of the dual readout registers attached to the detector, which have slightly differing response functions.

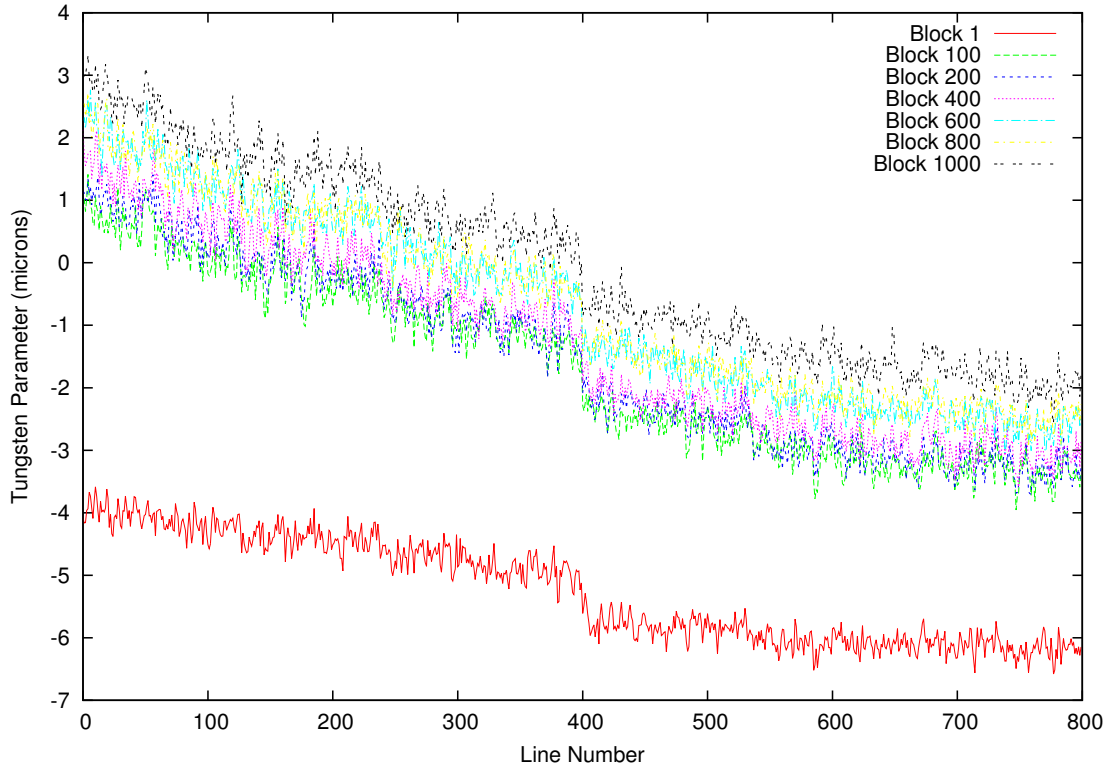

Figure 9.3: Graph showing the relation between line number and the value of the tungsten filter thickness parameter.

A second-order least-squares fit (using Python's `NumPy` library developed by Dubois et al. (1996)) was applied to the initial and final blocks after the discontinuity had been removed, yielding Equations 9.1 and 9.2 respectively, where w_n is the tungsten thickness in µm and l is the line number.

$$w_1 = 1.847 \times 10^{-6}\, l^2 - 3.931 \times 10^{-3}\, l - 3.819 \tag{9.1}$$

$$w_{1000} = 4.092 \times 10^{-6}\, l^2 - 8.106 \times 10^{-3}\, l + 2.794 \tag{9.2}$$

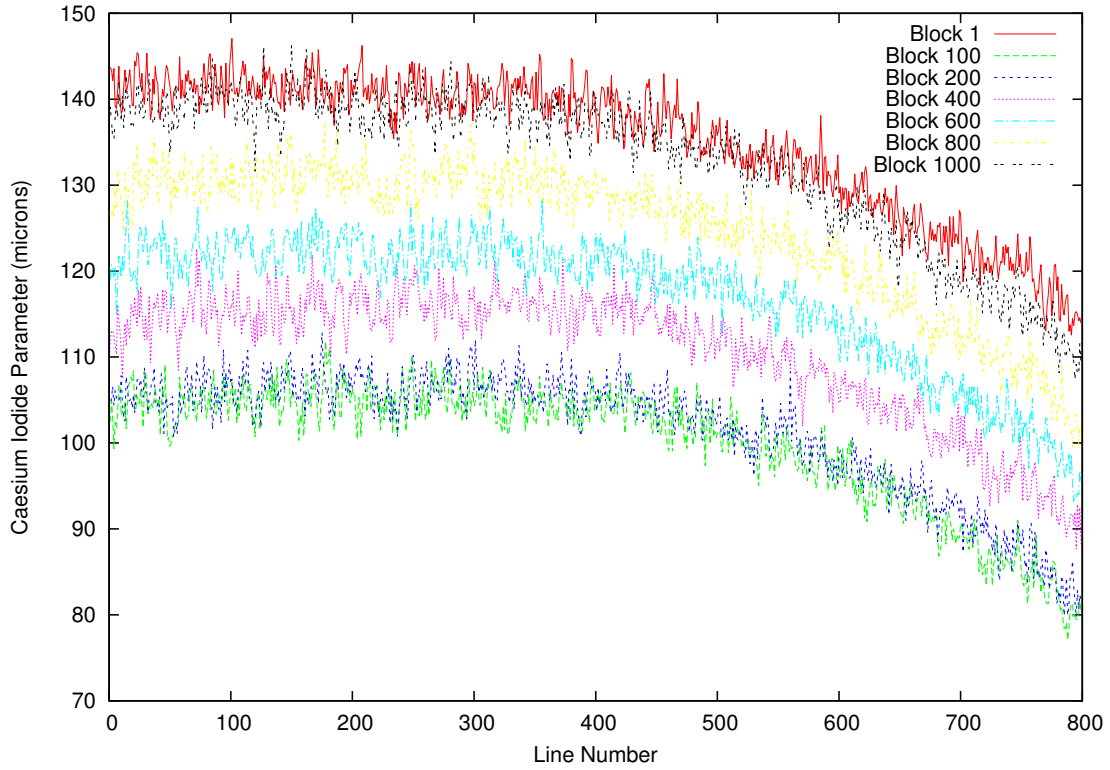

Figure 9.4: Graph showing the relation between line number and the value of the caesium iodide filter thickness parameter.

The caesium iodide parameter was also found to increase with block number (as shown in Figure 9.4), with the exception of the first block, presumably for the same reason as the appearance of the outliers mentioned earlier. Note that the parameter, while approximately constant over lines 1—300, decreases in value toward the upper edge of the detector, signifying an unexpectedly high attenuation of photons. Since the value of the caesium iodide parameter is believed to also act as a proxy for other attenuation sources, this may be a result of longer photon path lengths in this area and thus greater than expected beam hardening if the detector is vertically offset even slightly from the beam centre.

Finally, it was noted that the ratio of deviation between the mass attenuations of the first and last blocks, shown in Figure 9.5, generally increased with attenuator number (that is, with decreasing absolute attenuation), though this change is minor compared to the values of the ratios themselves — the difference between the ratios of attenuators 1 and 9 is 10.4% the value of the ratio seen in attenuator 1.

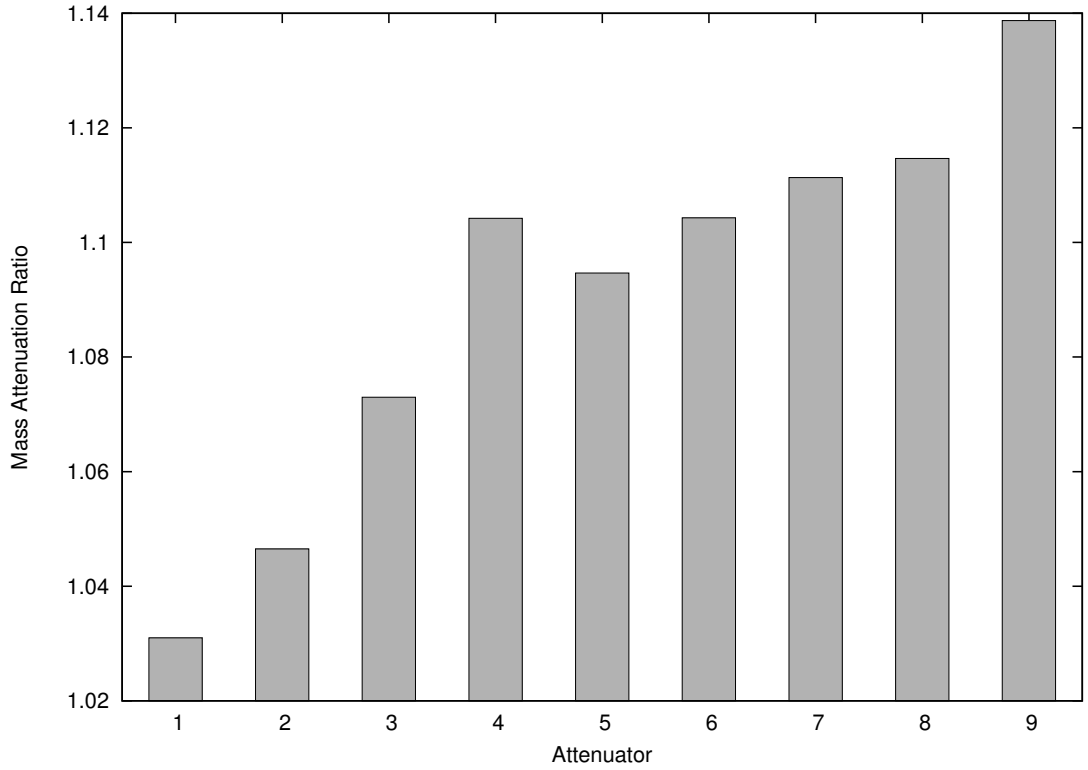

Figure 9.5: Graph showing the relation between the attenuator number and the ratio of mass attenuation between first and last block, calibrated with the first block's attenuations.

9.5 Conclusion

Both the correction parameters and the mass attenuations detected when using an older calibration vary significantly over the course of the experiment, making the acceptable lifetime of a given calibration fairly short. Since the *ad hoc* basis under which calibrations had been performed previously often led to long periods between updated corrections, the applicability of the most recent calibration to a later scan is similarly variable, and it was therefore decided to operate the scanner with calibration measurements taken at the end of every scan where practical.

The beam hardening carousel was attached to the underside of the rotation stage, allowing the stage to be raised at the conclusion of a scan in order to bring the attenuators into the X-ray beam and rotated using a vertical axle in order to expose each attenuator in turn. The projections, when taken, are then appended to the specimen's projection file along with metadata describing the calibration parameters (see Appendix B). These data can afterwards be separated into a `settings.txt` file readable by the calibration program and a conventional *MuCAT* data file with a name of the form `scanname_CAL.mcd` for processing .

Chapter 10

Time-Dependent Attenuation Coefficient Variation

10.1 Experimental Context

Once the stability of a given beam hardening correction and pitting of the X-ray target are removed as factors, the remaining untested question in X-ray beam stability is whether the ageing of the heated cathode alters the X-ray beam spectrum. As noted in Chapter 9, the demountable nature of the X-ray source encourages operation at a higher beam power than for sealed-source units, improving signal to noise ratio at the expense of filament lifetime.

10.2 Experimental Implementation

Given the demands on the *MuCAT* scanner, the LAC measurements used in Chapter 8 were exmined for their time since the previous filament replacement, and supplemented with further measurements as shown below.

A hyper-pure (99.999%) aluminium rod of diameter 10 mm was sourced from Goodfellow Cambridge Ltd. (Cambridge, United Kingdom) and cut to a length of 50 mm. The rod was scanned vertically eleven times (according to availability of the scanner) over a period of several weeks, during which time the scanner was in normal use for other experiments, using *MuCAT* 2 at an accelerating voltage of 90 kV and a beam current of 180 μA, with 701 projections taken for each scan, giving a reconstructed voxel size of 20 μm. Active beam usage during the time between

scans was assumed to be approximately proportional to real time, given the demands upon the *MuCAT* suite. Beam hardening correction attenuations were measured using the carousel test article as described in Chapter 6 immediately after the end of each scan as suggested in Chapter 9, and used to correct the scanned projections of the rod prior to wobble correction using `SHIFTFIX1B.PRO` and reconstruction using `CONEREC`.

10.3 Reconstruction Analysis

The reconstructions were cropped using `MTRIM` and the mean LAC value of the rod was measured using `AL.PRO`. The sampling volume for this measurement was a cylinder of radius 2.500 mm and length 698 rows. Since the rod extended past both the top and bottom of the reconstruction area, maximum use of the reconstructed volume was possible in order to minimise the effect of random error in the result by sampling a large number (3.426×10^7) of voxels.

Additionally, the beam hardening calibration optimisation parameters of tungsten thickness, caesium iodide thickness and accelerating voltage were plotted in order to examine whether the values to which the correction software converges are physically plausible.

10.4 Results

The reconstructed LAC measurements are shown in Table 10.1, and generally agreed well with the predicted value despite being taken at different points in the X-ray source's lifetime, as seen in Figure 10.1. It was noted, however, that the sixth scan did not agree as well (though the error bars shown are only one standard deviation.) Since aluminium, unlike more biologically-relevant materials such as hydroxyapatite, is generally very uniform in its density, and since the quoted purity of the specimen was very high, it seems unlikely that this represents a real variation in the sample.

A first-order least-squares fit (using Python's `SciPy` library developed by Jones et al. (2001-2013)) was applied to the deviations (shown in Figure 10.2) in order to test for time dependence (with a significance threshold of $p < 0.05$ for the two-tailed p-value). No significant correlation

Scan Number	Time Since Filament Change (days)	Linear Attenuation Coefficient ± Standard Error (cm^{-1})	Deviation from Nominal (%)
1	7	1.2627 ± 0.0576	2.467
2	10	1.2453 ± 0.0855	1.055
3	11	1.2428 ± 0.0806	0.852
4	13	1.2499 ± 0.0842	1.428
5	14	1.2426 ± 0.0871	0.836
Filament change			
6	2	1.2546 ± 0.0750	1.810
7	23	1.2552 ± 0.0934	1.858
Filament change			
8	17	1.2427 ± 0.0805	0.844
9	21	1.2746 ± 0.0831	3.433
10	24	1.2354 ± 0.0867	0.252
Filament change			
11	3	1.2458 ± 0.0819	1.096

Table 10.1: Results of repeated scanning of a hyperpure aluminium rod over time, with correction time-dependence eliminated as a confounding factor.

was found ($p = 0.834$).

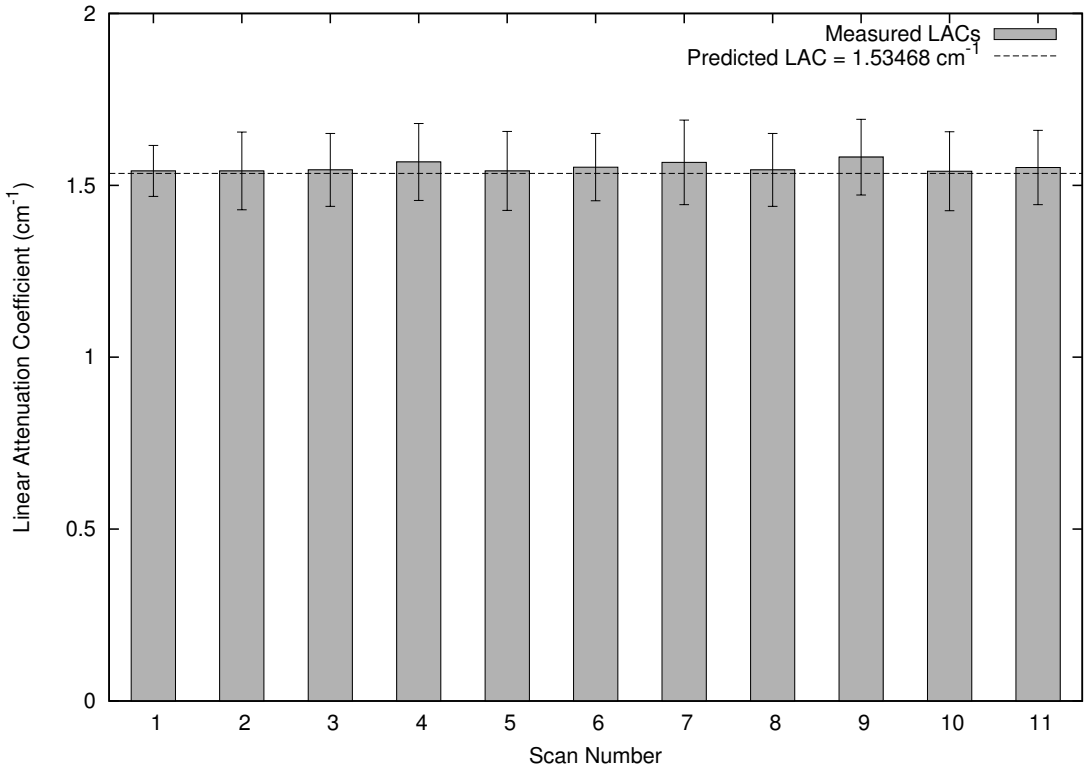

Figure 10.1: Linear attenuation coefficient measurements of hyperpure aluminium rod scanned at 90 kV, with theoretical LAC of aluminium at 40 keVmonochromatic (National Institute of Standards and Technology, 2010). Error bars (showing standard deviation) added for completeness.).

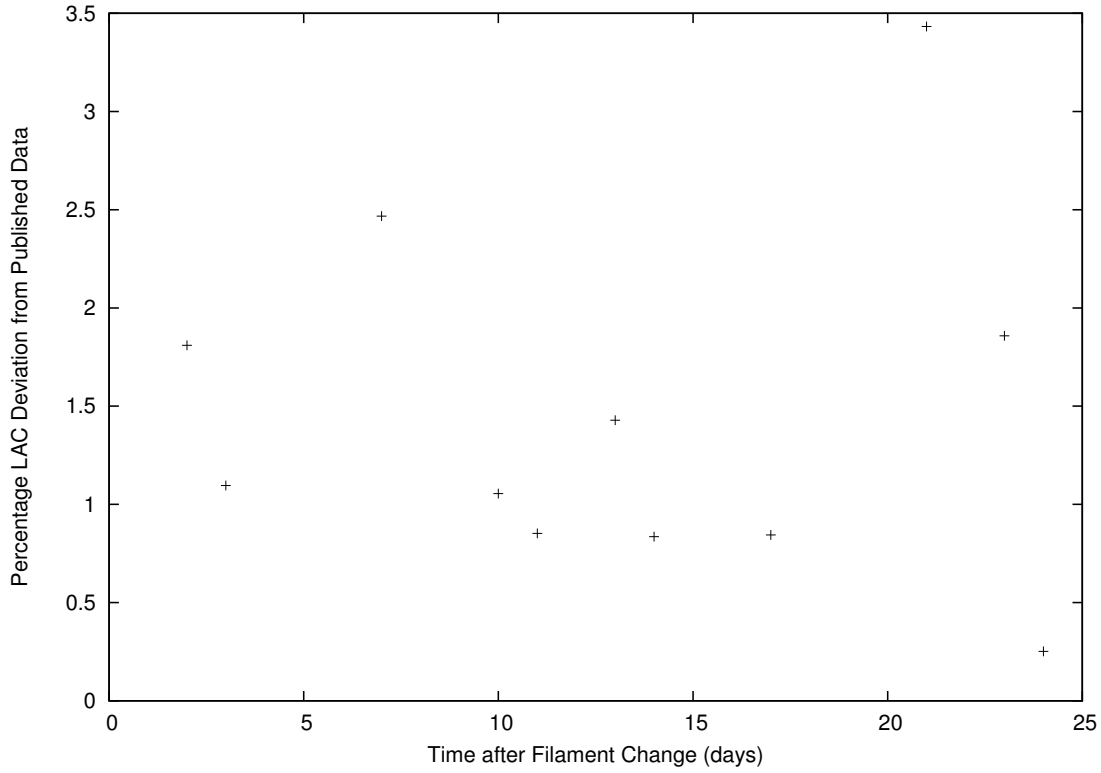

Figure 10.2: Graph of percentage reconstructed LAC deviations from the nominal value.

The average values to which the calibration parameters converged is shown with the inter-scan filament changes in Figures 10.3, 10.4 and 10.5, and plotted as a function of time in Figures 10.6, 10.7 and 10.8. While the parameter values for the two materials are plausible, they are not consistent between scans. Additionally, the accelerating voltage parameter is consistently higher than that selected, with a maximum variation of ±10.28% of the expected value of 90 kV, though some variation in the voltage reading is seen when operating the scanner.

The tungsten and caesium iodide parameters appear have no statistically significant relationship with time (p=0.45 and p=0.61 respectively, using the twin-tailed test.) Accelerating voltage showed an increase of 1.05 $Vd^{-1}$with a day-zero voltage of 97.707 kV, which is 8.56% over the expected value.

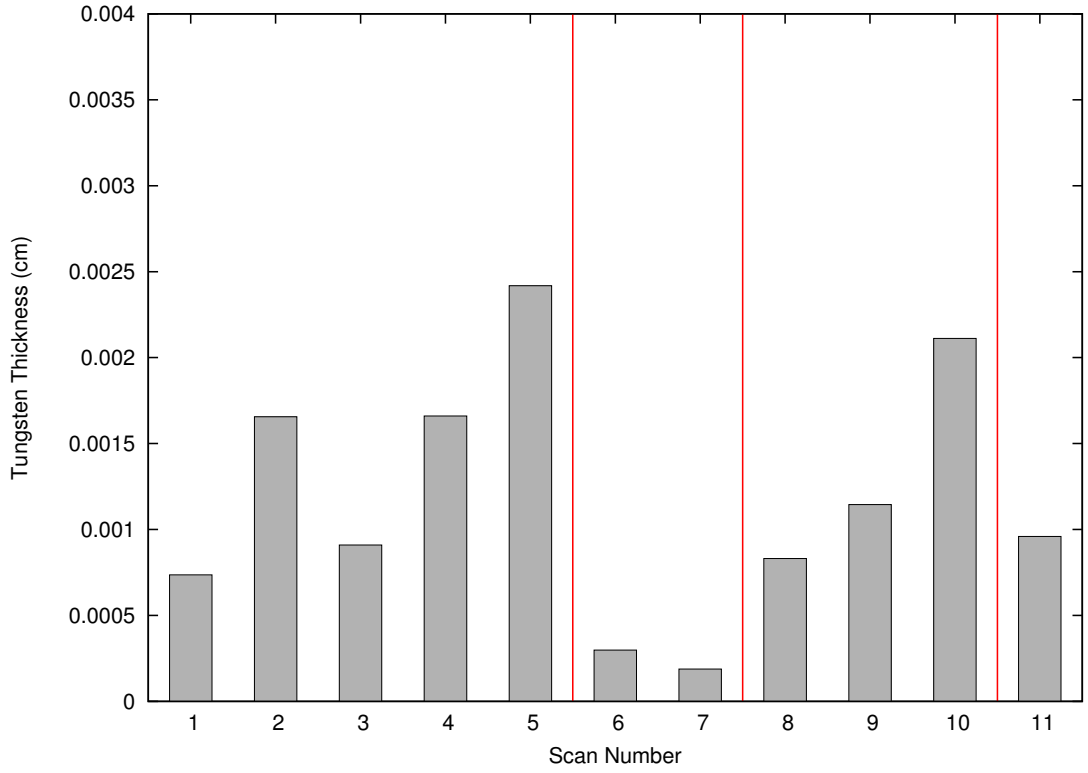

Figure 10.3: Graph of optimised tungsten filter thicknesses. Errors not shown due to comparatively large systematic error in results arising from line-dependent tungsten beam hardening (as described in Chapter 9.) Red lines denote filament changes.

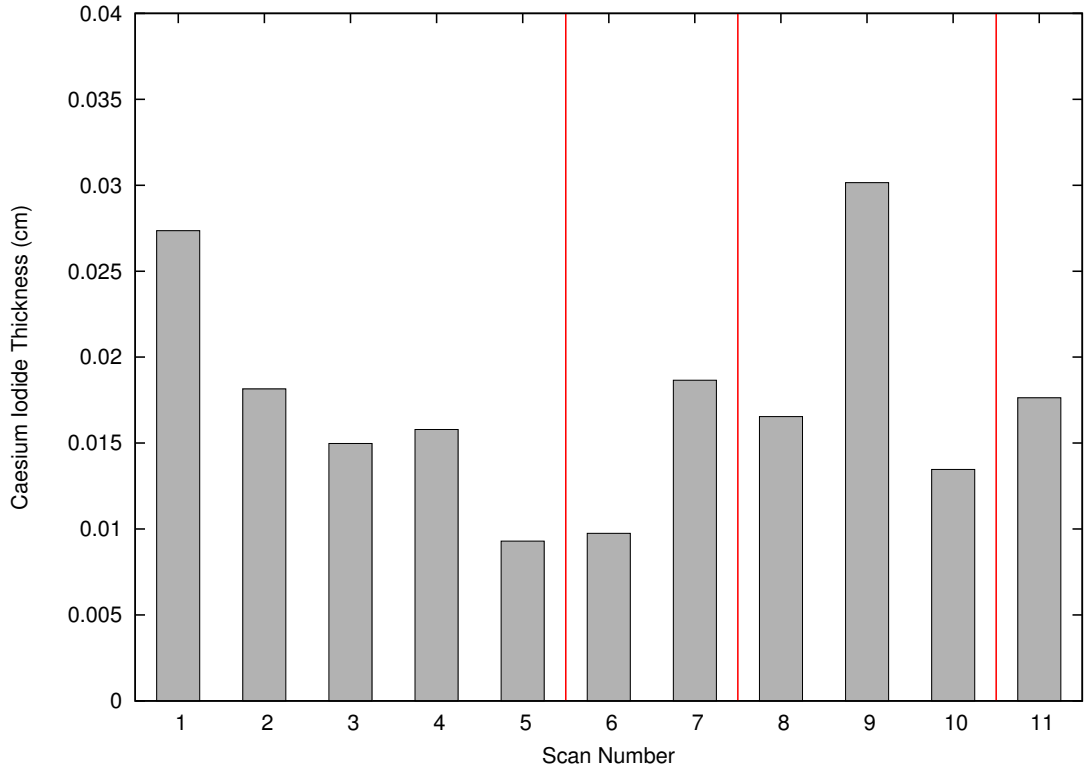

Figure 10.4: Graph of optimised caesium iodide scintillator thicknesses. Errors removed as before; red lines denote filament changes.

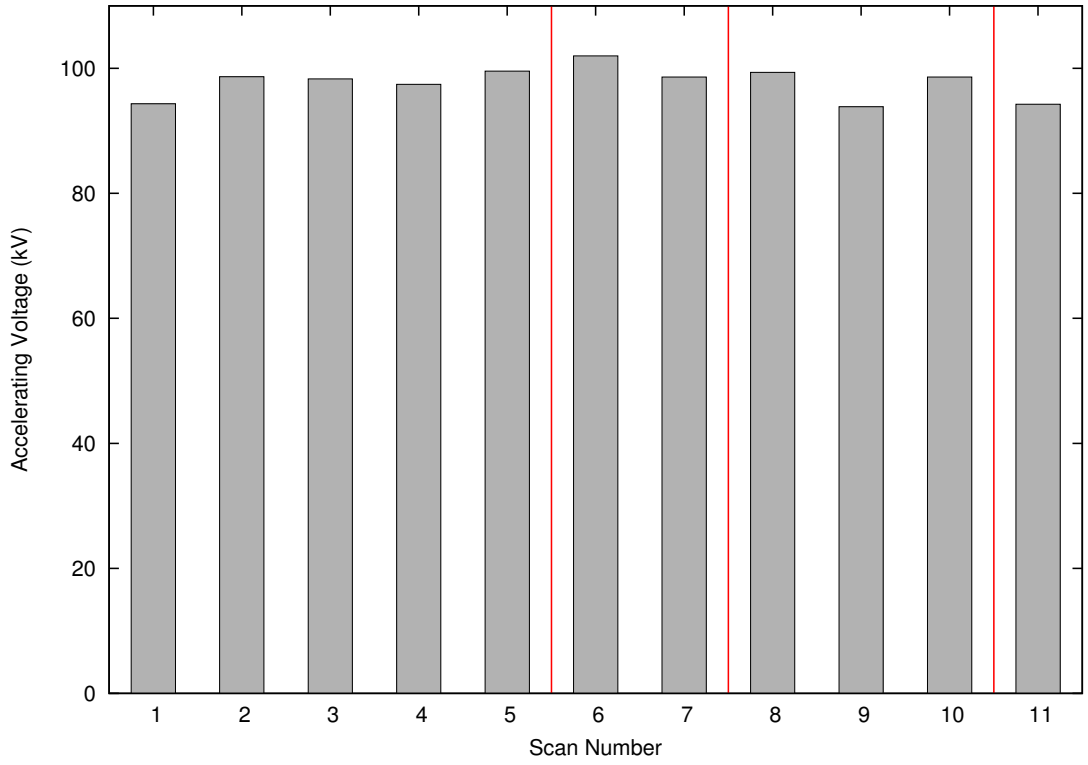

Figure 10.5: Graph of optimised electron gun accelerating voltages. Error is not shown here as the voltages are arrived at for the whole projection rather than on a line-by-line basis, so there is no variation across the height of the detector. Red lines denote filament changes.

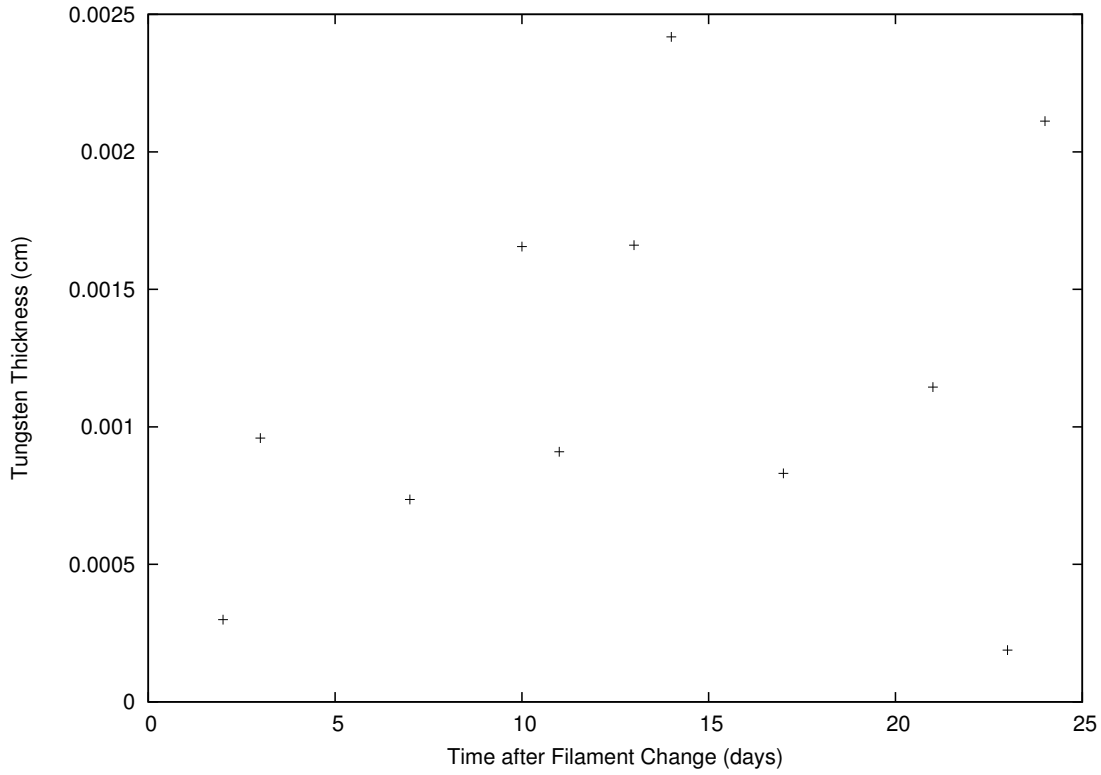

Figure 10.6: Tungsten thickness parameter plotted against X-ray filament life.

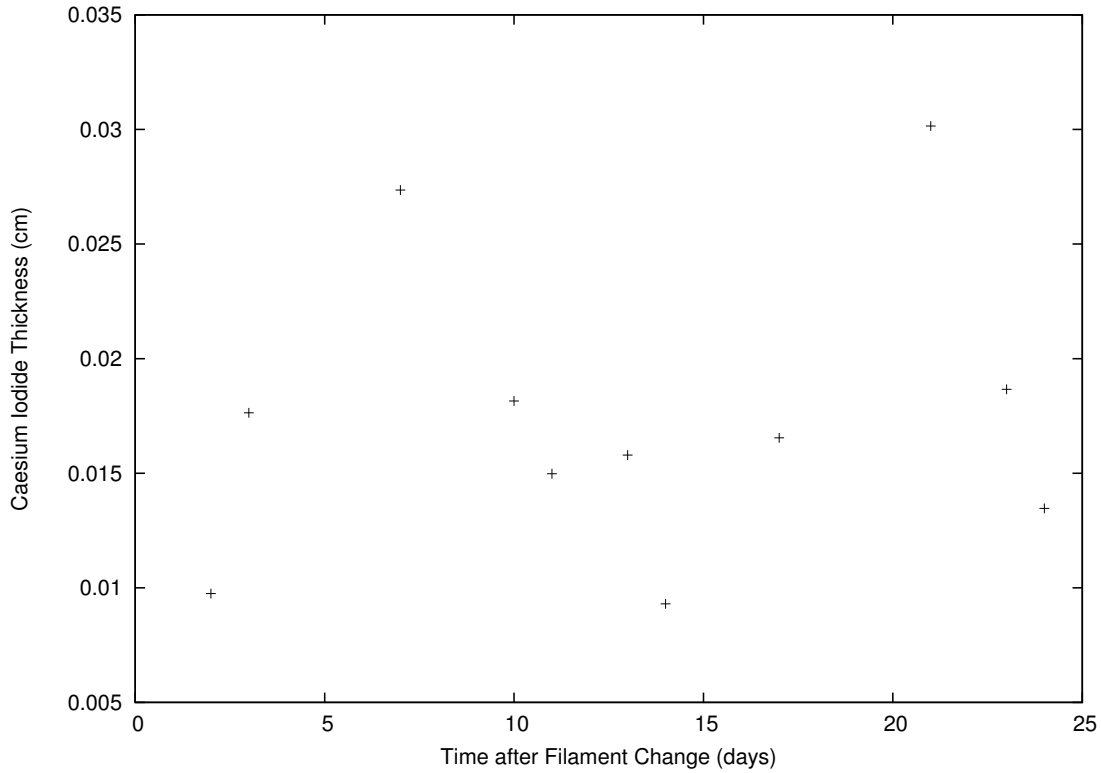

Figure 10.7: Caesium iodide thickness parameter plotted against X-ray filament life.

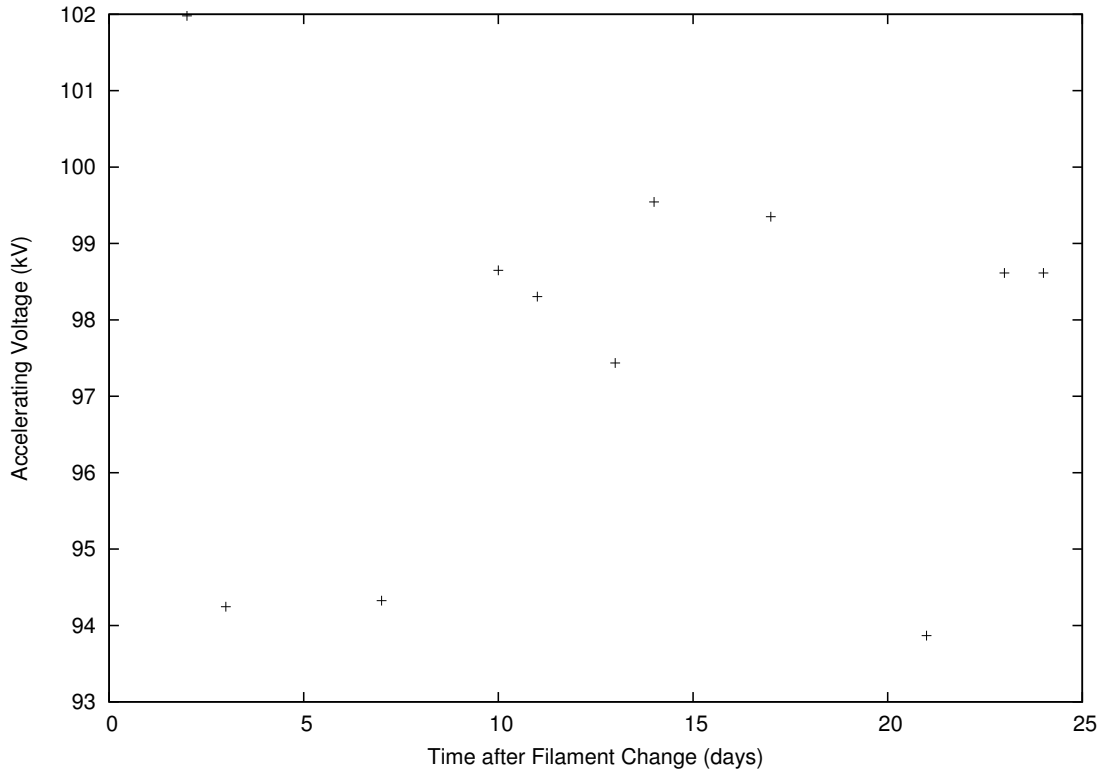

Figure 10.8: Accelerating voltage parameter plotted against X-ray filament life.

10.5 Conclusion

There was no detectable drift in LAC measurements over the two-month course of the experiment. As a result, no suggestions are made for changes to the filament replacement schedule, which is currently carried out as filaments fail. The spread in results (shown in Figure 10.2) appears, however, to be greater as the time since replacement grows — it is suggested that a similar experiment be carried out with a higher scan repetition rate if scanner availability allows.

The parameters to which the calibration software converges, however, are shown not to necessarily be physically meaningful, and caution should be exercised when using these values since they may be partly confounded by other interactions not accounted for here.

The voltage results appear to be approximately consistent with an 8.56% systematic error in either the voltage display or the calibration process since the rate of increase is far smaller than the absolute voltage values, so a spectrometric study of the X-ray beam in order to determine the peak photon energy and confirm or refute this result is suggested. This does not, however, appear to have a significant detrimental impact on the reconstruction quality.

Chapter 11

Multi-Modal Beam Hardening Correction

Since beam hardening calibrations using the methods described in this thesis are accurate only for single-species specimens, it was deemed necessary to consider the effect of immersion on the reconstruction of specimens with a component that has a similar LAC to the working fluid.

11.1 Experimental Implementation

The Scanco Medical AG phantom described in Section 6.4.2 was scanned in the *MuCAT* 2 XMT scanner at an accelerating voltage of 90 kV and a beam current of 180 μA. 3601 projections were taken, each of 1500×600 pixels, giving a reconstructed voxel size of 30 μm.

Scans were taken both in air and immersed in distilled water, using the large tank described in Section 6.4.1 in the latter case with the phantom inverted (ie. with the mounting pin uppermost). The in-air scan was taken with an aluminium wire present in the sample volume, in order to correct LAC scaling. This was considered acceptable as the wire is significantly less attenuating than the much larger phantom.

Beam hardening corrections were generated for hydroxyapatite to a monochromatic photon energy of 40 keV, with the correction for the immersed specimen having a 43 mmwater filter applied and the virtual step-wedge attenuations reduced by the LAC of water, in order to reduce the corrected specimen to HA only in a water background. The corrected projections were then

reconstructed using `CONEREC`.

11.2 Reconstruction Analysis

The specimen reconstructions were sampled over cylindrical volumes, coaxial with the four rods with non-zero HA concentration, between rows 170 and 486 for the non-immersed scan and 175—486 for the immersed scan. This ensures that only the interior of the rod is sampled to avoid contamination of the sample data from the PMMA holder. The sampling radius was 1000 μm, comprising 1080623 voxels per rod for the 'dry' scan and 1063608 voxels per rod for the 'wet' scan.

The mean LAC in this volume was determined using `AL.PRO`, and hydroxyapatite concentrations were derived from the LAC values using the mineral concentration equation introduced in Section 1.2.2.3, with the background LAC value μ_b set to zero (in reality, 2.95×10^{-4} cm^{-1}) for the in-air scan and 0.268 cm^{-1} (for a photon energy of 40 keVat standard temperature and pressure) for the water scan.

11.3 Results and Discussion

The in-air and immersed reconstructions are shown in Figures 11.1a and 11.1b respectively. As Table 11.1 shows, scanning this phantom in air results in a significant deviation in measured concentrations, increasing as the level of HA is reduced.

The measured attenuations and calculated hydroxyapatite concentrations shown in Table 11.2 from the immersed scan, however, are consistent with the values communicated by Scanco Medical AG (Koller, 2011), though it should be noted that even here the least-concentrated rod exhibits a markedly increased deviation from the nominal result, possibly due to the inherent granularity of the HA/PMMA composite.

Note that in both images, only four of the phantom's composite rods are visible; as the fifth rod contains no hydroxyapatite, it is indistinguishable from the PMMA making up the remainder of the phantom. Further, the variation in linear attenuation coefficient within each rod (particularly visible in Figure 11.1b) demonstrates a limitation of the use of composite materials as beam

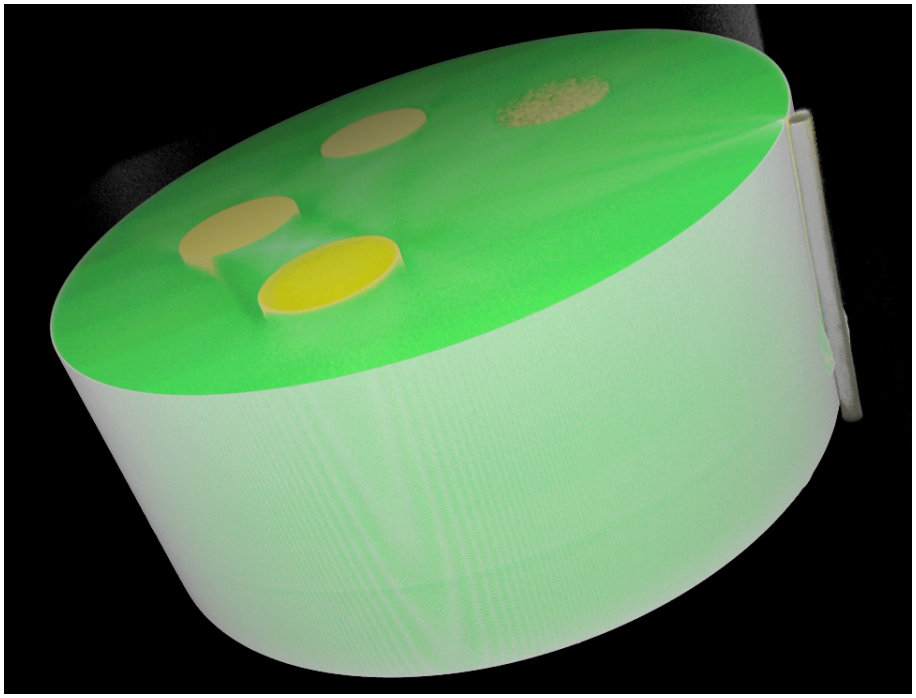

(a) Scanned in air at 90 kVp. The image has been segmented using `Drishti` transfer functions in order to show hydroxyapatite (yellow), PMMA (green) and the aluminium wire (grey).

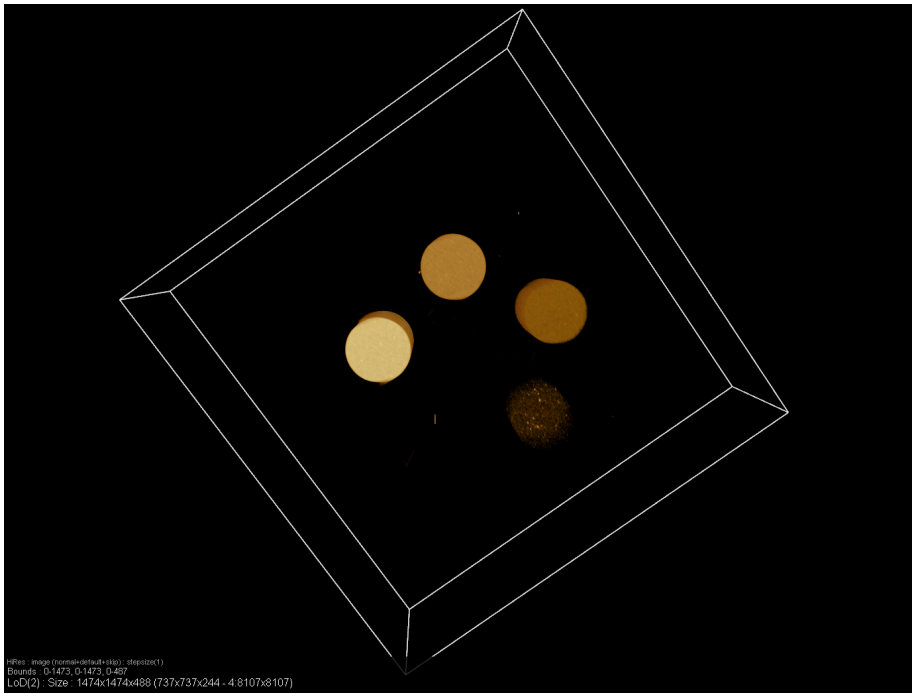

(b) Scanned in water at 90 kVp. No segmentation has been performed, as the PMMA has approximately the same X-ray attenuation as the background fluid.

Figure 11.1: Renderings of the Scanco Medical phantom, made using `Drishti`.

Nominal Concentration ($g\ cm^{-3}$)	Measured LAC (cm^{-1})	Measured Concentration ($g\ cm^{-3}$)	Deviation from Nominal (%)
0.7989	0.77 ± 0.0304	0.78 ± 0.0308	−2.62
0.3984	0.52 ± 0.0366	0.53 ± 0.0371	32.2
0.1990	0.39 ± 0.0367	0.39 ± 0.0372	96.7
0.0992	0.31 ± 0.0305	0.32 ± 0.0309	221

Table 11.1: Results of non-immersed scan of the Scanco Medical phantom.

Nominal Concentration ($g\ cm^{-3}$)	Measured LAC (cm^{-1})	Measured Concentration ($g\ cm^{-3}$)	Deviation from Nominal (%)
0.7989	0.74 ± 0.0436	0.82 ± 0.0483	2.64
0.3984	0.37 ± 0.0489	0.41 ± 0.0542	2.91
0.1990	0.18 ± 0.0464	0.20 ± 0.0524	0.503
0.0992	0.09 ± 0.0374	0.09 ± 0.0414	−9.27

Table 11.2: Results of immersed scan of the Scanco Medical phantom.

hardening calibration standards — the statistical 'clumping' of hydroxyapatite grains requires that the LAC measurements be averaged over a large number of projection pixels in order to produce an attenuation value. The PMMA regions of the phantom are not distinguishable from the fluid ($\Delta\mu = 0.002 \pm 0.00718$), demonstrating that the system does reduce to a uni-modal specimen when the LAC of the fluid is normalised to zero.

The relative difference between the nominal concentrations, which are taken as the 'ground truth', and the concentrations measured by LAC reconstruction are generally low, but increase with the lowest-concentration rod. This may be a result of the variation in hydroxyapatite concentration within the rod, though the large number of voxels samples would tend to suppress this as a source of error.

11.4 Conclusion

This experiment demonstrates that there are specimens whose mineral concentrations cannot be adequately derived using a beam hardening correction tailored to a single material, but which can be reconstructed accurately if placed in an LAC-matching medium for the unwanted lower-radiodensity portion of the specimen.

The combination of a multi-modal beam hardening correction piece comprising uniform metallic attenuation filters with multi-variable optimisation is an effective method of producing high-quality beam hardening corrections for single-material specimens. By use of an immersion tank, two-species specimens with an unwanted low-atomic number component can be reduced to a single-species system, allowing accurate measures of mineral concentration to be derived. The immersion tank system also has applications in the in-situ study of evolving systems, such as demineralisation or remineralisation of biological hard tissue.

Chapter 12

Demonstration of Utility

It was noted that the experiments conducted in the preceding chapters each demonstrate only one of the components that make beam hardening correction a multi-faceted problem in X-ray micro-tomography. It was therefore decided to conduct two comparison trials, one biological and one industrial, which display the combined implications of the modifications made to the corrections as a result of this work.

The test specimens selected for intracomparison were a section of zygomatic bone from the sheep *Ovis aries* (selected for its high level of compact cortical bone, which minimises underestimations of average radiodensity due to internal voids), and the aluminium (99.999% purity) rods described in Chapters 8 and 10, in order to test for repeatability and reliability of measurement in a specimen of known properties. These qualities are untestable in biologically-originated specimens since, due to the natural variation in hydroxyapatite concentration in teeth, it is not possible to establish ground truth.

12.1 Biological Experiment

12.1.1 Experimental Implementation

The bone specimen had previously been scanned at 90 kV and 180 μA, over 1901 projections to produce a theoretical spatial resolution of 25 μm. The `MCD` file produced included a set of in-service 'carousel' calibration projections resulting the improvements made after the experi-

mental results shown in Chapter 9. These calibration projections were taken at the beginning of the scanning process.

A reconstruction was made using the method described in Chapter 6, using a beam hardening correction based on the in-service calibration with a calibration energy of 44.5 keV based on the outcome of the experiments in Chapter 8.

The most recent hydroxyapatite-targeted correction made using the aluminium step wedge and software described in Section 5 was used in order to correct beam hardening errors in the same dataset, producing a parallel reconstruction. A third reconstruction was performed with no beam hardening correction performed at all.

12.1.2 Reconstruction Analysis

As before, after reconstruction the script `AL.PRO` was used to extract LAC values from the specimen. The sampling volume was selected to include cortical bone only; the cortical and trabecular phases are easily distinguishable from each other, though there are some voids throughout the specimen, as can be seen in Figure 12.1. The sampling volume comprised a cylinder oriented normal to the plane of rotation, of radius 500 μm and length 7500 μm, covering 378357 voxels.

12.1.3 Results and Discussion

The resulting mean linear attenuation coefficients are shown in Table 12.1, along with the standard deviation of the values. Note that since some natural variation is expected, the mean values are quoted verbatim, without truncation.

Correction Method	Mean Linear Attenuation (cm^{-1})	Standard Deviation (cm^{-1})
Carousel	0.949	0.132
Step Wedge	1.084	0.153
None	0.683	0.083

Table 12.1: Mean and standard deviation values of linear attenuation coefficient in *O. aries* cortical bone, demonstrating changes due to beam hardening correction.

A visual comparison of the reconstructions is shown in Figure 12.2. The corrected images are

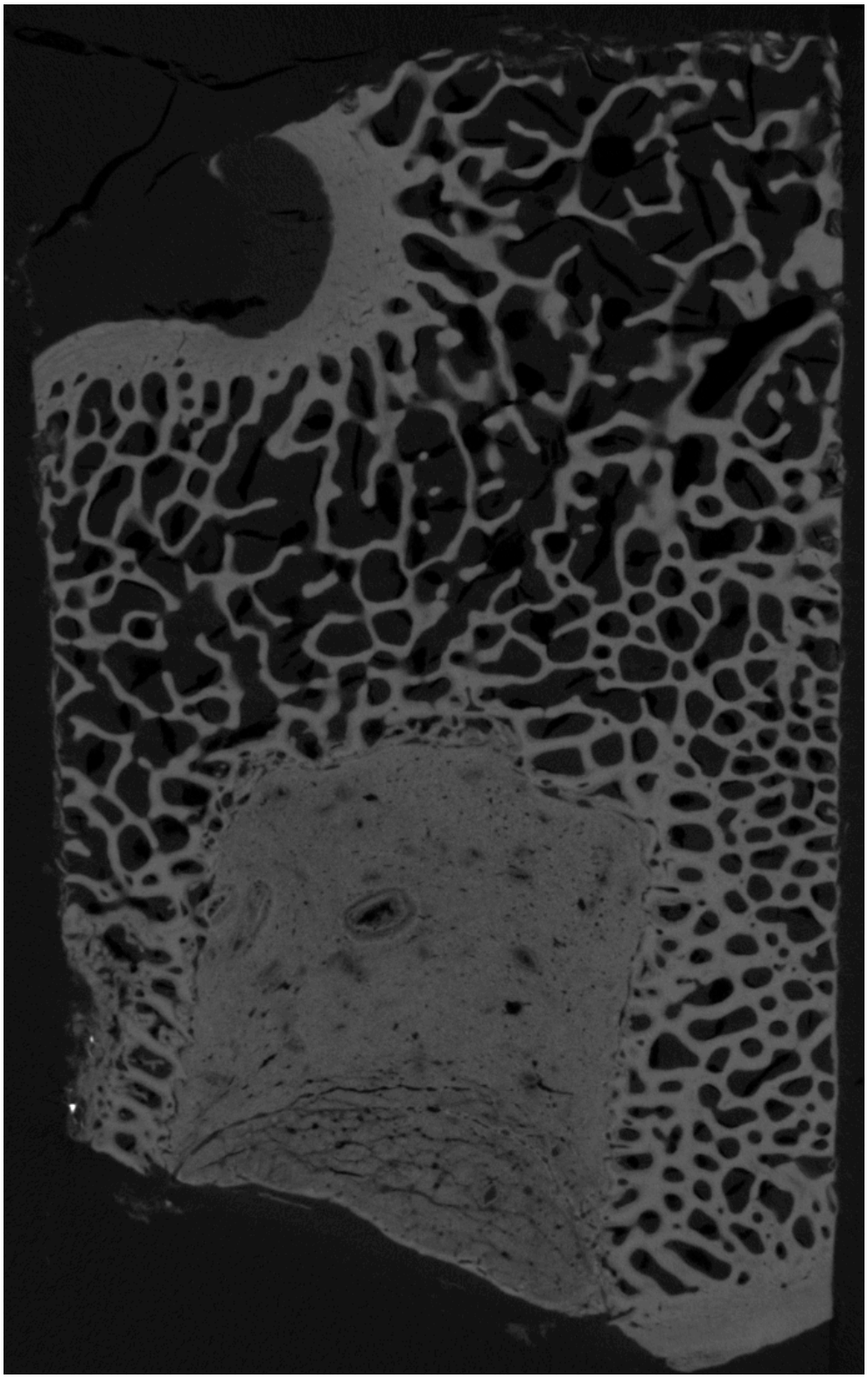

Figure 12.1: `TOMVIEW` image of X-Y slice 321 of the zygomatic bone specimen, showing cortical and trabecular bone regions and voids within both.

noticeably more similar to each other in terms of visible contrast detail than to the uncorrected slice, but the topmost image (reconstructed using the 'carousel' method) shows greater contrast

near the edges of the specimen and lower dark levels outside the sample.

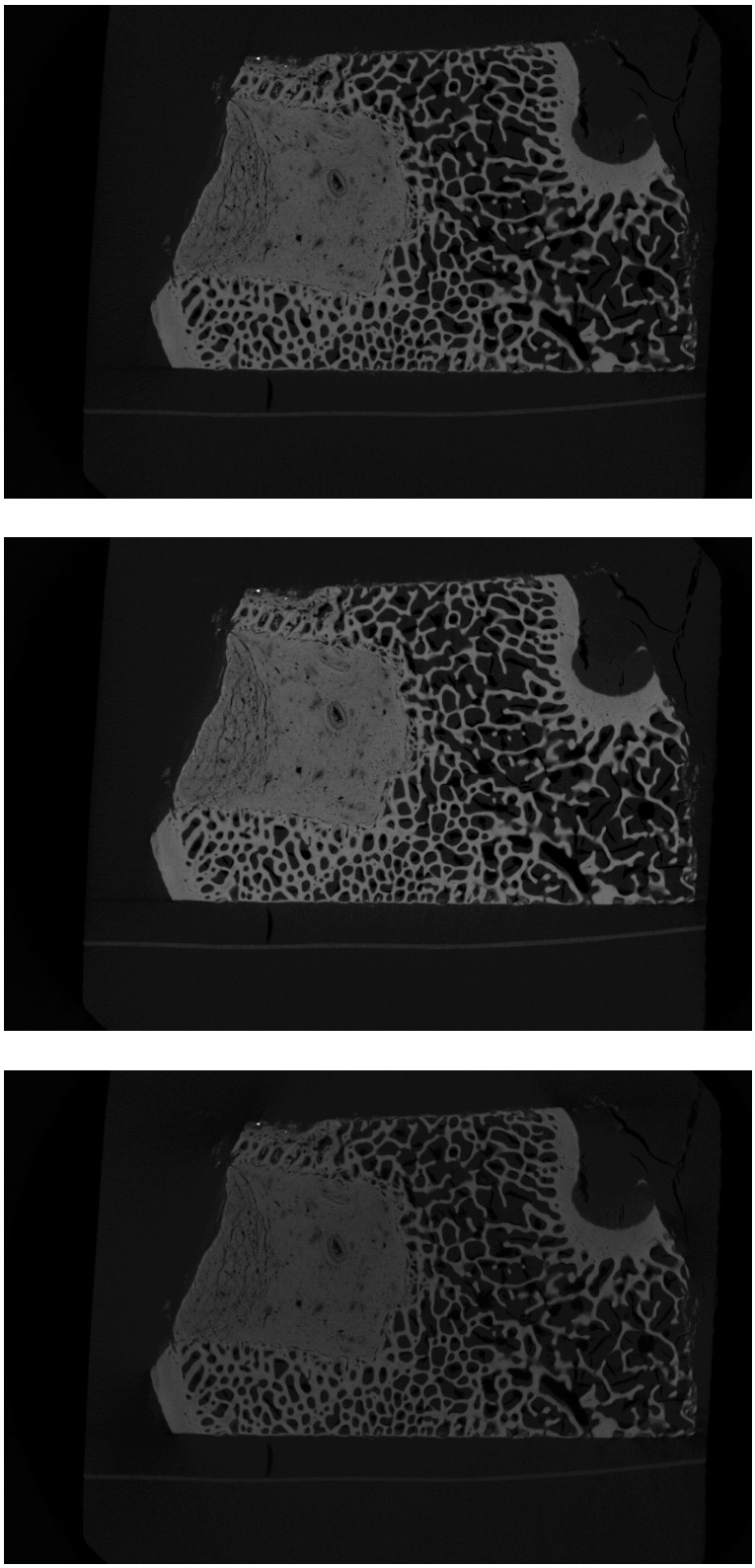

Figure 12.2: Comparison of reconstructions (from top to bottom, carousel correction, step wedge correction and no beam hardening correction) of X-Y slice 321, rotated clockwise by 90° to allow viewing of all three images.

These differences confirm the increased utility of the current method over the step wedge correction, and of both over an absence of correction.

12.2 Repeatability and Reliability Experiment

As mentioned earlier, the difficulty with objectively deriving implications for research protocols from the preceding experiment is that it uses biological tissues as a specimen, that being the major use case for XMT at Barts and The London School of Medicine and Dentistry. As a result, there is significant real variation in the results which can to a certain extent mask some of the effects of inadequate error correction.

12.2.1 Experimental Implementation

Uncorrected X-ray projections of a hyper-pure (99.999%) aluminium rod of diameter 10 mm and length 50 mm, scanned for the experiment detailed in Chapter 10, were corrected for beam hardening using the most recent aluminium-targeted correction values `m2c90_0.13`, which was created on 31 March 2010 using the process described in Chapter 5 prior to wobble correction using `SHIFTFIX1B.PRO` and reconstruction using `CONEREC`. While this correction is significantly older than the scan, it replicates the *ad hoc* nature of beam hardening correction as practised before the 'carousel' was brought into routine use.

The reconstruction based on this correction forms the control measurement against which the corrections used in Chapter 10 were to be compared.

12.2.2 Reconstruction Analysis

Linear attenuation coefficient values were taken by the same method as in Chapter 10: the reconstructions were cropped using `MTRIM` and the mean LAC value of the rod was measured using `AL.PRO`. The sampling volume for this measurement was a cylinder of radius 2.500 mm and length 698 rows, approximately co-axial with the rod. Since the rod extended past both the top and bottom of the reconstruction area, maximum use of the reconstructed volume was possible in order to minimise the effect of random error in the result by sampling a large number

(3.426×10^7) of voxels.

12.2.3 Results and Discussion

The mean linear attenuation coefficient values and their standard deviation is shown in Table 12.2. The relative error is twice the quotient of the standard deviation and the mean LAC. Note the large relative deviation when the older correction method is used; this appears to be indicative if under-correction, given the sampling geometry (being co-axial, the voxels sampled are predominantly near the centre of the rod, which has under-recorded attenuation in the uncorrected case.)

	Mean LAC (cm^{-1})	Relative Deviation (%)	Standard Deviation (cm^{-1})	Relative Error $2 \times S.D.$ (%)
Step Wedge	1.37	−13.5	0.05	7.30
Carousel	1.250	+1.4	0.011	1.77

Table 12.2: Mean and standard deviation values of linear attenuation coefficient in aluminium rod, demonstrating changes due to use of multi-material carousel with multi-variable correction method over aluminium step-wedge beam hardening correction.

The significant reduction in relative error in this case demonstrates the advantages of the system in terms of repeatability: the predominant sources of error remaining are believed to be a result of changes in vertical placement of the aluminium rod between scans and in location of the centre points when defining the sampling volume.

12.3 Chapter Conclusions

This chapter is less experimental in nature than the foregoing, focusing instead on demonstrating the cumulative benefits to repeatability of large attenuation spreads in a beam hardening calibration specimen, proper choice of calibration energy and recency of calibration. Additionally, the scan of the biological specimen demonstrates qualitative changes between reconstructions utilising the step wedge and carousel-based correction methods.

Chapter 13

General Discussion, Conclusions and Further Work

In order to understand the utility of these experiments and changes made to the correction process in impact-source X-ray tomography, it is necessary to revisit the situation faced by users of the *MuCAT* systems before they were implemented and discuss the frequency of calibration, its calibration energy dependence, its accuracy of reconstruction and the limitations of its validity.

13.1 The *Status Quo Ante*

The *MuCAT* devices are TDI-enabled third generation micro-CT scanners, which collect a sequence of X-ray projections of a specimen, with the twin aims of high contrast (precision of measurement of linear attenuation coefficient) and high accuracy through a series of correction methods. The projections, once collected, are corrected for beam hardening as well as dark and light fields, then corrected for shift and wobble in the rotation stage and reconstructed. The reconstructions are cropped to a volume of interest and grey-level scaling applied. Finally, an aluminium wire of high purity is used as an LAC reference in order to scale the grey-level/LAC ratio to a known level.

Beam hardening correction measurements were taken on an *ad hoc* basis, or when a specimen with LAC features of particular interest was to be scanned. Generally, however, these measurements would be taken less frequently than once a week.

The calibrations were based on the equivalency for practical purposes of polychromatic X-ray

spectra to specific photon energies when considering a monochromatic beam, shown in Table 5.2. This was of particular importance since the selection method for these energies was previously undocumented.

When calibration measurements were taken, a single dataset would be used to make correction polynomials for all sample materials as needed. The correction algorithm would not infrequently fail to converge, and the agreement between the measured attenuations and simulated attenuations, while significantly better than previous models, left much to be desired, with a typical total error (sum of the squared differences in attenuation over all attenuators) of between 1.5 and 2.

As shown in Chapter 7, the quality of reconstructions made using an aluminium step wedge to provide beam hardening corrections can be very poor (see Section 7.2, where an underestimate of 15% and dishing artefact of 13% the expected value are produced), though significantly better than the preceding seven-step horizontal wedge, even when an idealised simulated wedge is used, eliminating the effects of impurities or contamination from the measurements.

The calibration method is limited in its applicability to single-species specimens. As the presence of a lower-radiodensity secondary species increases in the sample, the calibration method will under-correct the beam hardening error in the primary species (which is generally the species of interest in unmodified natural materials) with increasing severity. Conversely, an over-correction will occur in mineralised specimens with a more-attenuating secondary species, such as a tooth which has been re-seated using an implanted screw. While a minor mis-correction may, under certain circumstances, be acceptable, it results in unacceptable artefacts when the mineralised species is embedded in a large quantity of a mounting medium such as PMMA.

This correction method does allow separation of calibration material from specimen material - that is, an aluminium calibration standard can be used in the calibration of aluminium, hydroxyapatite, organic or any other material which is the dominant absorber in the specimen. With the increasing use of the *MuCAT* scanners in applications where ever-higher contrast reconstruction is a necessity, however, (see Chapter 2) this was realised to no longer be a tenable situation.

13.2 Thesis' Implications for Beam Hardening Correction

In Chapter 7 it was shown that, for a naturalistic sample, linear attenuation coefficient reconstruction accuracy could be improved to 0.7% using the same reconstruction process apart from the beam hardening correction as that which gave the underestimate in the previous section. If this is taken to be a figure of merit, the beam hardening correction process using the carousel and the associated IDL software may be said to be at least 18 times more effective than the previous generation. This is probably an underestimate of the improvement, since the error in the improved reconstruction appears to be mostly systematic.

Chapter 8 addressed one of the assumptions underlying the calibration software: that the photon energy used in the calibrate an X-ray beam of a given accelerating voltage is the most appropriate available. The experiments showed that a smaller variation in results is obtained when using the newly-derived energy of 44.5 keV for a 90 kV scan than when the same scans were corrected with the conventional value, and that derived energies for other accelerating voltages vary further from the conventional values. These energies, particularly for low-voltage beams where the effect of a given energy change is relatively greater, should be examined similarly.

The investigation of the effects of long-term wear of the X-ray target, in Chapter 9, showed both variation in beam hardening effects across the vertical dimension of the projections and a deterioration in quality of correction as beam-time between the calibration measurements and the scan to be corrected increases. The attachment of the beam hardening carousel to the rotation stage to permit automatic calibration measurement after individual scans allows the scans to be calibrated using the best possible parameters. For particularly sensitive or long scans, it is recommended that calibration measurements also be taken immediately before the scan commences, and a weighted average of the correction polynomials be used to correct the projections separately.

In Chapter 10, the automation of the calibration procedure made as a result of the experiments in Chapter 9 in order to study the effect of X-ray tube filament ageing on the quality of reconstructions of a known specimen without bias from changes in the quality of the beam hardening correction.

Chapter 11 addressed the limitations arising from beam hardening when scanning dual-species specimens by the introduction of an immersion tank to mask the lower-attenuating species in a medium of known thickness, thereby reducing the problem to a single-species sample. While this is only suitable for certain samples (iethose with low permeability or where fluid permeation of the sample is necessary for the answering of a research question), it nevertheless extends accurate mineral concentration measurement by XMT to a much wider range of specimens than was previously possible.

Finally, Chapter 12 provided two comparisons of 'dry' specimen reconstructions, between the pre-existing beam-hardening correction method described in Chapter 5 and a method combining the 'carousel' calibration device described in Chapter 6, the corrected calibration energy (Chapter 8) and the integration of the calibration scan as an automatically-completed part of the normal scanning process (a result of the experiment carried out in Chapter 9). These experiments, performed on biological and metallic specimens, demonstrated both qualitative and quantitative improvements in the reconstruction. Arising from the changes to methodology arising from this thesis.

13.3 Effects in Production Scanning

Since its introduction into service and extension into use by default with XMT scans, the 'carousel' test piece has been used for scans with *MuCAT* 2 at the five primary accelerating voltages listed in Section 5.2. As noted in Davis et al. (2013), this technique has permitted the resolution of ion transport in extracted teeth filled with a glass-ionomer cement, as well as the three-dimensional tracing of dead tracts in dentin, which occur when a dentinal tubule is exposed or irritated (Fish, 1928).

13.4 General Conclusions and Practical Significance

The research that forms this thesis, while based on the previous methodology discussed in Sections 5.2 and 13.1 and published in Davis et al. (2008), generalises the material-independent

nature of the calibration system in order to permit a greater range of attenuation measurements to be made using a device which did not become impractically thick at the most-attenuating point. Additionally, the modelling algorithm has been improved in order to take account of uncertainties in the X-ray generator voltage, which unlike the tungsten and caesium iodide thickness parameters vary solely with projection number rather than spatially, which permits a greatly improved (typically forty-fold reduction in summed-squared residuals) agreement between simulated and measured attenuation values when calculating correction coefficient values.

The benefits here are two-fold: firstly, the wider range of attenuations allows confirmation of correction validity for highly-attenuating specimens, and secondly even in cases where a calibration may not be vastly improved over the best-case scans, the ease of use of the carousel device has permitted the device to be fully integrated into the scanning process, so a recent calibration is always available for correcting the projection data. The importance of this, given the inconsistencies in optimised parameter values revealed in Chapter 9, is that it allows greater consistency of LAC measurements, as shown in Chapter 12 with a four-fold improvement in measurement repeatability when scanning a non-biological specimen.

As shown above, the experiments detailed in this thesis have contributed significantly to improving the greyscale accuracy of tomographic reconstructions on the *MuCAT* scanning devices, which are directly applicable to other third-generation impact-source tomographic systems.

In addition to the dental applications experiments described in the previous section, the multi-species beam hardening 'carousel' calibration technique developed for this thesis and described in Section 6.3.1 and tested in Chapter 7 has been used in microtomographic scans by other members of the Dental Physical Sciences research group at BLSMD.

13.5 Further Research

As well as minor variations to the experiments described in this thesis (such as extending the validation of calibration energies across the operational range of the *MuCAT* scanners), the following experiments are suggested in order to further improve the accuracy of high-contrast

impact-source X-ray microtomography.

13.5.1 Long-Term Calibration Stability Experiment

Chapter 9 describes a short-term repeatability experiment for the carousel calibration, carried out over approximately 48 h. Since the beam hardening calibration method was in continuous development throughout this study, it was not possible to extend the scope of the experiment beyond short-term effects from changes to the target.

It would be of interest to extend this experiment over a long period (on the order of several weeks, possibly interspersed between other experiments so as not to monopolise the *MuCAT* scanner) in order to isolate other contributions to calibration error than target pitting, which was the focus of this experiment. This would require that all other operation of the X-ray generator be recorded (including when the X-ray aperture is closed) in order to locate the experimental runs with respect to the scanner's maintenance schedule.

13.5.2 Dual-Emission Scanning and Anti-Scatter Grids

The application of dual-emission scanning techniques to microtomography (specifically the single-beam method using alternating lines of filtering material developed by Ritchings and Pullan (1979) and described in Section 4.1.2) would be a useful way of gaining further information about specimens which do not require particularly high spatial resolution. Similarly, anti-scatter grids are of interest if they can be manufactured to be compatible with TDI-based scanning systems.

13.5.3 Real-Time Dissolution Experiment

The immersion tank developed and tested in Chapter 11 may be used with artificial saliva (with or without the addition of typical food-borne oral contaminants such as citric or phosphoric acid) to examine quantitatively and non-destructively the stability and dissolution processes of natural and artificial dental materials in different simulated oral environments in real time, by scanning the sample while it is immersed and demineralisation is underway.

A similar experiment can be carried out on extracted teeth to which a bioactive glass-based product (for example, a dentifrice) has been applied, in order to determine the effectiveness, if any, of remineralisation processes and suggest means for improving their composition and application.

Both these experiments depend on comparatively long-term continuous and exclusive access to the scanner (on the order of several days) and are therefore difficult to schedule given the scanner's present duty cycle. With the commissioning of *MuCAT* 3 and the repurposing of the *MuCAT* 1 platform to take advantage of more recent developments in technology and processing (including the beam hardening corrections covered in this thesis) it is hoped that experiments such as this will become practical.

Bibliography

Vancouver hospital & health sciences centre medical imaging research group - filtered backprojection algorithm. http://www.physics.ubc.ca/~mirg/home/tutorial/fbp_recon.html. Accessed 17 March 2011.

ISO 21348:2007(E) Space environment (natural and artificial) - process for determining solar irradiances, 2007.

Diamond light source - how do synchrotrons work? http://www.diamond.ac.uk/Home/About/Synchrotrons/Machine.html, August 2010. Accessed 4 January 2011.

W. Abdel-Rahman and E.B. Podgorsak. Energy transfer and energy absorption in photon interactions with matter revisited: A step-by-step illustrated approach. *Radiation Physics and Chemistry*, 79(5):552–566, 2010. ISSN 0969-806X.

M D Abramoff, P J Magalhaes, and S J Ram. Image processing with ImageJ. *Biophotonics International*, 11(7):36–42, 2004.

Farhat Ahmed. *Multiscale Quantitative Imaging of Human Femoral Heads Using X-ray Microtomography*. PhD thesis, University of London, 2011.

M. Ahmed. *X-ray Microtomography Study of Carious Dentine and a Comparison of its Removal by Three Techniques*. PhD thesis, University of London, 2010.

M. Akao, H. Aoki, and K. Kato. Mechanical properties of sintered hydroxyapatite for prosthetic applications. *Journal of Materials Science*, 16(3):809–812, 1981. ISSN 0022-2461.

P. Anderson, Y. Ahmed, M. P. Patel, G. R. Davis, and M. Braden. X-ray microtomographic studies of novel radio-opaque polymeric materials for dental applications. *Materials Science and Technology*, 22(9):1094–1097, 2006.

Iztok Arčon, Jana Kolar, Alojz Kodre, Darko Hanžel, and Matija Strlič. XANES analysis of Fe valence in iron gall inks. *X-Ray Spectrometry*, 36(3):199–205, 2007. ISSN 1097-4539.

Rika Baba, Yasutaka Konno, Ken Ueda, and Shigeyuki Ikeda. Comparison of flat-panel detector and image-intensifier detector for cone-beam CT. *Computerized Medical Imaging and Graphics*, 26:153–158, 2002.

D. F. Barbe. Introduction. In D. F. Barbe, editor, *Charge-Coupled Devices*, volume 38 of *Topics in Applied Physics*, chapter 1. Springer-Verlag, 1980.

E C Beckmann. CT scanning the early days. *British Journal of Radiology*, 79(937):5–8, 2006. doi: 10.1259/bjr/29444122. URL http://bjr.birjournals.org/cgi/content/abstract/79/937/5.

Michael D. Bentley, Maria C. Ortiz, Erik L. Ritman, and J. Carlos Romero. The use of microcomputed tomography to study microvasculature in small rodents. *American Journal of Physiology - Regulatory, Integrative and Comparative Physiology*, 282(5):R1267–R1279, 2002.

D.P. Bentz, Nicos. S. Martys, P. Stutzman, M. S. Levensona, E.J. Garboczi, J. Dunsmuir, and L. M. Schwartz. X-ray microtomography of an ASTM C109 mortar exposed to sulfate attack. In *1994 MRS Fall Meeting*, volume 370 of *MRS Proceedings*, pages 77–82, 1994.

B. K. B. Berkovitz, B. J. Moxham, R. W. A. Linden, and A. J. Sloan. *Master Dentistry Volume Three: Oral Biology*. Churchill Livingstone, October 2010. URL http://www.elsevier.com/wps/find/bookdescription.agents/724805/description#description.

Mirko Boin and Astrid Haibel. Compensation of ring artefacts in synchrotron tomographic images. *Optics Express*, 14(25):12071–12075, 2006. URL http://www.opticsexpress.org/abstract.cfm?URI=oe-14-25-12071.

S. Bottari, M.A. Ciocci, M. Fortunato, P. Maestro, N. Malakhov, P.S. Marrocchesi, M. Meucci, V. Millucci, R. Paoletti, A. Scribano, and N. Turini. Study of a new scatter rejection technique in digital radiography. *Nuclear Instruments and Methods in Physics Research Section A*, 461(1-3):410 – 412, 2001. ISSN 0168-9002. doi: DOI:10.1016/S0168-9002(00)01260-2. URL http://www.sciencedirect.com/science/article/B6TJM-430WX8M-40/2/60fcecdc09f95686ffad6197b8a9998c. 8th Pisa Meeting on Advanced Detectors.

Douglas P. Boyd and Martin J. Lipton. Cardiac computed tomography. *Proceedings of the IEEE*, 71(3):298–307, March 1983.

W. L. Bragg. The structure of some crystals as indicated by their diffraction of x-rays. *Proceedings of the Royal Society of London, Series A: Mathematical, Physical and Engineering Sciences*, 89(610):248–277, 1913. ISSN 09501207.

R A Brooks and G Di Chiro. Beam hardening in X-ray reconstructive tomography. *Physics in Medicine and Biology*, 21(3):390–398, 1976. URL `http://stacks.iop.org/0031-9155/21/390`.

Oliver Brunke, Kathleen Brockdorf, Susanne Drews, Bert Müller, Tilman Donath, Julia Herzen, and Felix Beckmann. Comparison between x-ray tube based and synchrotron radiation based μCT. In Stuart R Stock, editor, *Developments in X-Ray Tomography VI*, volume 7078 of *Proc. SPIE*, page 70780U, 2008.

David Cassidy, Gerald Holton, and James Rutherford. *Understanding Physics*. Springer, 1 edition, 2002.

Roberto Cesareo, Antonio Brunetti, Ricardo Tadeu Lopes, Gianfranco Galli, Donepudi V Rao, Alfredo Castellano, Govanni E Gigante, Sergio Mascarenhas, René Robert, Voitoldo Swinka Filho, Marco Gilardoni, Hamiltoin Pereira da Silva, and Piero Quarta Colosso. X and γ ray tomography for non destructive material testing. In Ulrich Bonse, editor, *Developments in X-Ray Tomography II*, volume 3772 of *Proc. SPIE*, pages 292–303, 1999.

H P Chan and K Doi. The validity of Monte Carlo simulation in studies of scattered radiation in diagnostic radiology. *Physics in Medicine and Biology*, 28(2):109, 1983. URL `http://stacks.iop.org/0031-9155/28/i=2/a=001`.

Pam Cherry and Angela Duxbury, editors. *Practical Radiotherapy: Physics and Equipment*. John Wiley & Sons, 1st edition, 1998.

Dianna D Cody, Dawn Cavanaugh, Roger E Price, Belinda Rivera, Gregory Gladish, and Elizabeth Travis. Lung imaging of laboratory rodents in-vivo. In Ulrich Bonse, editor, *Developments in X-Ray Tomography IV*, volume 5535 of *Proc. SPIE*, pages 43–51, 2004.

A. J. Coleman and M. Sinclair. A beam-hardening correction using dual-energy computed tomography. *Physics in Medicine and Biology*, 30(11):1251–1256, 1985.

A P Colijn, W Zbijewski, A Sasov, and F J Beekman. Experimental validation of a rapid Monte Carlo based micro-CT simulator. *Physics in Medicine and Biology*, 49(18):4321, 2004. URL http://stacks.iop.org/0031-9155/49/i=18/a=009.

A.P. Colijn and F.J. Beekman. Accelerated simulation of cone beam x-ray scatter projections. *IEEE Transactions on Medical Imaging*, 23(5):584 –590, May 2004. ISSN 0278-0062. doi: 10.1109/TMI.2004.825600.

Arthur H Compton. A quantum theory of the scattering of x-rays by light elements. *Physical Review*, 21(5):483–502, May 1923.

Glenn C. Conroy and Michael W. Vannier. Noninvasive three-dimensional computer imaging of matrix-filled fossil skulls by high-resolution computed tomography. *Science*, 226(4673): 456–458, 1984.

P.E. Cruvinel, R. Cesareo, S. Crestana, and S. Mascarenhas. X- and γ-rays computerized minitomograph scanner for soil science. *Instrumentation and Measurement, IEEE Transactions on*, 39(5):745–750, oct 1990. ISSN 0018-9456.

G. R. Davis and J. C. Elliott. X-ray microtomography scanner using time-delay integration for elimination of ring artefacts in the reconstructed image. *Nuclear Instruments and Methods in Physics Research Section A*, 394(1-2):157–162, 1997. ISSN 0168-9002.

G. R. Davis and J. C. Elliott. High definition x-ray microtomography using a conventional impact x-ray source. *Journal de Physique IV*, 104:131–134, 2003.

G R Davis and J C Elliott. Artefacts in x-ray microtomography of materials. *Materials Science and Technology*, 22(9):1011–1018, 2006a.

Graham Davis, Nitin Jain, and James Elliott. A modelling approach to beam hardening correction. In Stuart R Stock, editor, *Developments in X-Ray Tomography VI,*, volume 7078 of *Proceedings of SPIE*, page 70781E. SPIE, 2008.

Graham Davis, Anthony Evershed, James Elliott, and David Mills. Quantitative X-ray microtomography with a conventional source. In Stuart R. Stock, editor, *Developments in X-Ray Tomography VII*, volume 7804 of *Proc. SPIE*, page 78040I, 2010.

Graham R Davis. Image quality in x-ray microtomography. In Ulrich Bonse, editor, *Developments in X-Ray Tomography*, volume 3149, pages 213–221, October 1997. URL http://spie.org/x648.html?product_id=279359.

Graham R Davis. Image quality and accuracy in x-ray microtomography. In Ulrich Bonse, editor, *Developments in X-Ray Tomography II*, volume 3772 of *Proc. SPIE*, pages 147–155, 1999.

Graham R. Davis. Cone-beam tomography. Personal Communication, March 2011.

Graham R Davis and James C Elliott. Aspects of x-ray microtomography equipment design. In Ulrich Bonse, editor, *Developments in X-Ray Tomography IV*, volume 5535 of *Proc. SPIE*, pages 182–190, 2004.

Graham R. Davis and James C. Elliott. Scintillator to CCD coupling in X-ray microtomography. In Ulrich Bonse, editor, *Developments in X-Ray Tomography V*, volume 6318 of *Proc. SPIE*, page 631817, 2006b.

Graham R. Davis, Anthony N.Z. Evershed, and David Mills. Quantitative high contrast x-ray microtomography for dental research. *Jounal of Dentistry*, 2013. doi: 10.1016/j.jdent.2013.01.010. (Article in Press).

Graham Roy Davis. The effect of linear interpolation of the filtered projections on image noise in x-ray computed tomography. *Journal of X-Ray Science and Technology*, 4(3):191 – 199, 1994. ISSN 0895-3996.

B de Man, J Noyts, P Dupont, G MArchal, and P Suetens. Metal streak artifacts in x-ray computed tomography: A simulation study. *IEEE Transactions on Nuclear Science*, 46(3):691–696, 1999. Part 2 216UA Times Cited:32 Cited References Count:21.

Tilman Donath, Felix Beckmann, and Andreas Schreyer. Image metrics for the automated alignment of microtomography data. In Ulrich Bonse, editor, *Developments in X-Ray Tomography V*, volume 6318 of *Proc. SPIE*, page 631818, 2006.

Susanne Drews, Felix Beckmann, Julia Herzen, Oliver Brunke, Phil Salmon, Sebastian Friess, Andres Laib, Bruno Koller, Thomas Hemberger, Magdalena Müller-Gerbl, and Bert Müller. Comparative micro computed tomography study of a vertebral body. In Stuart R Stock, editor, *Developments in X-Ray Tomography VI*, volume 7078 of *Proc. SPIE*, page 70780C, 2008.

Paul F. Dubois, Konrad Hinsen, and James Hugunin. Numerical python. *Computers in Physics*, 10(3):262–267, June 1996. ISSN 0894-1866. URL http://dl.acm.org/citation.cfm?id=229737.229761.

F. R. Elder, A. M. Gurewitsch, R. V. Langmuir, and H. C. Pollock. Radiation from electrons in a synchrotron. *Physical Review*, 71(11):829–830, 1947. URL http://prola.aps.org/abstract/PR/v71/i11/p829_5.

J C Elliott and S D Dover. X-ray microtomography. *Journal of Microscopy*, 126:211–213, 1982.

J C Elliott and S D Dover. Three-dimensional distribution of mineral in bone at a resolution of 15 μmdetermined by x-ray microtomography. *Metabolic Bone Disease and Related Research*, 5(5):219–221, 1984.

James C. Elliott, Paul Anderson, Graham Roy Davis, Ferranti See Leng Wong, and S. David Dover. Computed tomography part ii: The practical use of a single source and detector. *JOM Journal of the Minerals, Metals and Materials Society*, 46:11–19, 1994. ISSN 1047-4838. URL http://dx.doi.org/10.1007/BF03220641. 10.1007/BF03220641.

Synchrotron Soleil EPSIM 3D/JF Santarelli. via Wikipedia: http://en.wikipedia.org/wiki/File:Sch%C3%A9ma_de_principe_du_synchrotron.jpg. Accessed 4 October 2012. Copyright © EPSIM 3D/JF Santarelli, Synchrotron Soleil; used with permission.

Exelis. IDL | Scientific Data Visualization Software from Exelis. http://www.exelisvis.com/ProductsServices/IDL.aspx, 2012. Accessed 7 December 2012.

Rebecca Fahrig, James G. Mainprize, Normand Robert, Arthur Rogers, and Martin J. Yaffe. Performance of glass fiber antiscatter devices at mammographic energies. *Medical Physics*, 21(8):1277–1282, 1994. doi: 10.1118/1.597236. URL http://link.aip.org/link/?MPH/21/1277/1.

Damian Farrell. Radon transform. http://rsbweb.nih.gov/ij/plugins/radon-transform.html, February 2006. Accessed 12 October 2012.

L. A. Feldkamp, L. C. Davis, and J. W. Kress. Practical cone-beam algorithm. *Journal of the Optical Society of America A*, 1(6):612–619, 1984.

Eric Wilfred Fish. Dead tracts in dentine. *Proceedings of the Royal Society of Medicine*, 22(2): 227–236, 1928.

Richard Fitzgerald. Phase-sensitive x-ray imaging. *Physics Today*, 53(7):23–26, 2000.

T Flohr and B Ohnesorge. Developments in CT. *Imaging*, 18(2):45–61, 2006.

James Fogarty, Ryan S. Baker, and Scott E. Hudson. Case studies in the use of ROC curve analysis for sensor-based estimates in human computer interaction. In *Proceedings of Graphics Interface 2005*, GI '05, pages 129–136, School of Computer Science, University of Waterloo, Waterloo, Ontario, Canada, 2005. Canadian Human-Computer Communications Society. ISBN 1-56881-265-5. URL http://portal.acm.org/citation.cfm?id=1089508.1089530.

Xue J Gao, James C Elliott, Paul Anderson, and Graham R Davis. Scanning microradiographic and microtomographic studies of remineralisation of subsurface enamel lesions. *Journal of the Chemical Society, Faraday Transactions*, 89(15):2907–2912, 1993.

G L Glen and Charles G Dodd. Use of molecular orbital theory to interpret x-ray k-absorption spectral data. *Journal of Applied Physics*, 39(12):5372–5377, 1968.

S J Golding and P C Shrimpton. Radiation dose in CT: are we meeting the challenge? *British Journal of Radiology*, 75(889):1–4, 2002.

Silke Grabherr, Marco Domonoetto, Lisa Yu, Valentin Djonov, Bert Müller, and Sebastian Friess. Angofil: a novel radio-contrast agent for post-mortem micro-tomography. In Stuart R Stock, editor, *Developments in X-Ray Tomography VI*, volume 7078 of *Proc. SPIE*, page 70781O, 2008.

Kyungmin Ham, Heath A Barnett, Tolulope Ogunbakin, Dominique G Homberger, Hermann H Bragulla, Kenneth L Matthews II, Clinton S Willson, and Leslie G Butler. Imaging tissue structures: assessment of absorption and phase-contrast x-ray tomography imaging at 2-nd and 3-rd generation synchotrons. In Ulrich Bonse, editor, *Developments in X-Ray Tomography V*, volume 6318 of *Proc. SPIE*, page 631822, 2006.

B. Haubitz, M. Prokop, W. Döhring, J. H. Ostrom, and P. Wellnhofer. Computed tomography of Archaeopteryx. *Paleobiology*, 14(2):206–213, 1988.

G T Herman. Correction for beam hardening in computed tomography. *Physics in Medicine and Biology*, 24:81–106, 1979.

K.M. Holt. Geometric calibration of third-generation computed tomography scanners from scans of unknown objects using complementary rays. In *IEEE International Conference on Image Processing*, volume 4, pages 129–132. IEEE, October 2007.

G. N. Hounsfield. Computerized transverse axial scanning (tomography): Part 1. description of system. *British Journal of Radiology*, 46(552):1016–1022, 1973.

Jiang Hsieh. *Computed Tomography: Principles, Design, Artifacts, and Recent Advances*, volume 114 of *Spie Press Monograph*. SPIE Press, 2003. ISBN 9780819444257.

Jiang Hsieh, Robert C. Molthen, Christopher A. Dawson, and Roger H. Johnson. An iterative approach to the beam hardening correction in cone beam CT. *Medical Physics*, 27(1):23–29, 2000. doi: 10.1118/1.598853. URL `http://link.aip.org/link/?MPH/27/23/1`.

J.H. Hubbell. Electron–positron pair production by photons: A historical overview. *Radiation Physics and Chemistry*, 75(6):614 – 623, 2006. ISSN 0969-806X.

D. Iwanenko and I. Pomeranchuk. On the maximal energy attainable in a betatron. *Physical Review*, 65(11-12):343, June 1944.

D. A. Jaffray and J. H. Siewerdsen. Cone-beam computed tomography with a flat-panel imager: Initial performance characterization. *Medical Physics*, 27(6):1311–1323, 2000.

James R Janesick. *Scientific Charge-Coupled Devices*. SPIE Press, 2001.

Robert J Jennings. A method for comparing beam-hardening filter materials for diagnostic radiology. *Medical Physics*, 15(4):588–599, 1988.

Eric Jones, Travis Oliphant, Pearu Peterson, and others. SciPy: Open source scientific tools for Python. `http://www.scipy.org/`, 2001-2013.

Peter M. Joseph and Robin D. Spital. The effects of scatter in x-ray computed tomography. *Medical Physics*, 9(4):464–472, August 1982.

Avinash C. Kak and Malcolm Slaney. *Principles of computerized tomographic imaging*. Classics in applied mathematics 33. Society for Industrial and Applied Mathematics, Philadelphia PA, USA, 2001.

H Kanamori, N Nakamori, K Inoue, and E Takenaka. Effects of scattered x-rays on CT images. *Physics in Medicine and Biology*, 30(3):239–249, 1985. URL `http://stacks.iop.org/0031-9155/30/i=3/a=004`.

Akitoshi Katsumata, Akiko Hirukawa, Shinji Okumura, Munetaka Naitoh, Masami Fujishita, Eiichiro Ariji, and Robert P Langlais. Effects of image artifacts on gray-value density in limited-volume cone-beam computerized tomography. *Oral Surgery, Oral Medicine, Oral Pathology, Oral Radiology and Endodontology*, 104(6):829–836, 2007.

Richard A Ketcham. New algorithms for ring artifact removal. In Ulrich Bonse, editor, *Developments in X-Ray Tomography V*, volume 6318 of *Proc. SPIE*, page 63180O, 2006.

Richard A. Ketcham and William D. Carlson. Acquisition, optimization and interpretation of x-ray computed tomographic imagery: Applications to the geosciences. *Computers & Geosciences*, 27(4):381–400, May 2001.

Paul E. Kinahan, Bruce H. Hasegawa, and Thomas Beyer. X-ray-based attenuation correction for positron emission tomography/computed tomography scanners. *Seminars in Nuclear Medicine*, 33(3):166–179, July 2003.

J. H. Kinney, Q. C. Johnson, M. C. Nichols, U. Bonse, R. A. Saroyan, R. Nusshardt, and R. Pahl. X-ray microtomography on beamline x at SSRL. *Review of Scientific Instruments*, 60(7): 2471–2474, 1989.

O Klein and Y Nishina. On the scattering of radiation by free electrons according to Dirac's new relativistic quantum dynamics. In Gösta Ekspong, editor, *The Oskar Klein Memorial Lectures, Volume 2*. World Scientific, 1994.

Glenn F Knoll. *Radiation detection and measurement*. Wiley, Hoboken NJ, USA, 3rd edition, 2000.

V. Kobychev and S. Popov. Constraints on the photon charge from observations of extragalactic sources. *Astronomy Letters*, 31:147–151, 2005. ISSN 1063-7737.

Bruno Koller. Personal Comunication, 15 February 2011. Chief Executive Officer, Scanco Medical AG.

Claudia V. Kropas-Hughes and S. Trent Neel. Back to basics: Basics of computed tomography. http://www.asnt.org/publications/Materialseval/basics/may00basics/may00basics.htm, 2000. URL http://www.asnt.org/publications/Materialseval/basics/may00basics/may00basics.htm. Accessed 5 January 2011.

A. Kyrieleis, V. Titarenko, M. Ibison, T. Connolley, and P.J. Withers. Region-of-interest tomography using filtered backprojection: assessing the practical limits. *Journal of Microscopy*, 241 (1):69–82, 2011. ISSN 1365-2818.

Michael F. L'Annunziata, editor. *Handbook of radioactivity analysis*. Academic Press, San Diego CA, USA, 2 edition, 2003.

P D Lee, R C Atwood, P Rockett, M A Konerding, J R Jones, and C A Mitchell. A comparison of three different micro-tomography systems for accurate determination of microvascular parameters. In Stuart R Stock, editor, *Developments in X-Ray Tomography VI*, volume 7078 of *Proc. SPIE*, page 70780E, 2008.

C.J. Leliveld, J.G. Maas, C.W.E. van Eijk, and V.R. Bom. On the significance of scattered radiation in industrial x-ray computerized tomographic imaging. *IEEE Transactions on Nuclear Science*, 41(1):290 –294, February 1994. ISSN 0018-9499.

A. Limaye. Drishti - volume exploration and presentation tool. *IEEE Visual., Baltimore, USA*, 2006.

Ajay Limaye. Drishti-2 - volume exploration and presentation tool. http://code.google.com/p/drishti-2/, October 2012. Accessed 11 December 2012.

Yang Lu, Jun Zhao, and Ge Wang. Exact image reconstruction with triple-source saddle-curve cone-beam scanning. *Physics in Medicine and Biology*, 54:2971–2991, 2009.

W. Ludwig, J-Y. Buffière, S. Savelli, and P. Cloetens. Study of the interaction of a short fatigue crack with grain boundaries in a cast al alloy using x-ray microtomography. *Acta Materialia*, 51(3):585 – 598, 2003. ISSN 1359-6454.

A Léonard, L P Guiot, J-P Pirard, M Crine, M Balligand, and S Blacher. Non-destructive characterization of deer (cervus elaphus) antlers by x-ray microtomography coupled with image analysis. *Journal of Microscopy*, 225(3):258–263, March 2007.

Alexandr Malusek, Michael Sandborg, and Gudrun Alm Carlsson. CTmod–a toolkit for Monte Carlo simulation of projections including scatter in computed tomography. *Computer Methods and Programs in Biomedicine*, 90(2):167 – 178, 2008. ISSN 0169-2607.

Alexandr Malušek, Maria Magnusson Seger, Michael Sandborg, and Gudrun Alm Carlsson. Effect of scatter on reconstructed image quality in cone beam computed tomography: evaluation of a scatter-reduction optimisation function. *Radiation Protection Dosimetry*, 114(1-3):337–340, 2005.

Kenneth R. Maravilla and Mary S. Pastel. Technical aspects of CT scanning. *Computerized Tomography*, 2(3):137–144, 1978.

Patrick Martinez and Alain Klotz. *A Practical Guide to CCD Astronomy*. Cambridge University Press, 1998.

S Mayo, P Miller, S W Wilkins, D Gao, and T Gureyev. Laboratory-based x-ray microtomography with submicron resolution. In Ulrich Bonse, editor, *Developments in X-Ray Tomography V*, volume 6318 of *Proc. SPIE*, page 63181E, 2006.

R B Mazess, H S Barden, J P Bisek, and J Hanson. Dual-energy x-ray absorptiometry for total-body and regional bone-mineral and soft-tissue composition. *The American Journal of Clinical Nutrition*, 51(6):1106–12, 1990.

A. Mazurier, V. Volpato, and R. Macchiarelli. Improved noninvasive microstructural analysis of fossil tissues by means of SR-microtomography. *Applied Physics A*, 83(2):229 – 233, 2006.

N. Menvielle, Y. Goussard, D. Orban, and G. Soulez. Reduction of beam-hardening artifacts in x-ray CT. In *Proceedings of the 2005 IEEE Engineering in Medicine and Biology 27th Annual Conference*, pages 1865 –1868, 2005.

G. J. Michon and H. K. Burke. CID image sensing. In D. F. Barbe, editor, *Charge-Coupled Devices*, volume 38 of *Topics in Applied Physics*, chapter 2. Springer-Verlag, 1980.

David Mills, Oksana Samko, Paul Rosin, Kate Thomas, Tim Wess, and Graham R. Davis. Apocalypto: revealing the unreadable. Number 8506, page 85060A, 2012.

Atsushi Momose, Tohoru Takeda, Yuji Itai, and Keiichi Hirano. Phase-contrast X-ray computed tomography for observing biological soft tissues. *Nature Medicine*, 2(4):473–475, 1996.

National Institute of Standards and Technology. X-ray transition energies database. http://www.nist.gov/physlab/data/xraytrans/index.cfm, September 2005. Accessed 14 May 2010.

National Institute of Standards and Technology. XCOM: Photon Cross Sections Database. http://www.nist.gov/pml/data/xcom/index.cfm, November 2010. Accessed 12 December 2012.

Natural History Museum. Micro-CT | natural history museum. http://www.nhm.ac.uk/research-curation/science-facilities/analytical-imaging/imaging/computed-tomography/micro-ct/index.html, 2012. Accessed 24 October 2012.

J. A. Nelder and R. Mead. A simplex method for function minimization. *The Computer Journal*, 7 (4):308–313, 1965. doi: 10.1093/comjnl/7.4.308. URL http://comjnl.oxfordjournals.org/content/7/4/308.abstract.

B. Ohnesorge, T. Flohr, and K. Klingenbeck-Regn. Efficient object scatter correction algorithm for third and fourth generation ct scanners. *European Radiology*, 9:563–569, 1999. ISSN 0938-7994. 10.1007/s003300050710.

Mikael Otendal. *A Compact High-Brightness Liquid-Metal-Jet X-Ray Source*. PhD thesis, Royal Institute of Technology, 2006.

Adam Papadimitropoulos, Sebastian Friess, Felix Beckmann, Phil Salmon, Stefania Riboldi, Dietmar Hutmacher, Ivan Martin, and Bert Müller. Comparative study of desktop- and synchrotron radiation-based micro computed tomography analyzing cell-seeded scaffolds in tissue engineering of bone. In Stuart R Stock, editor, *Developments in X-Ray Tomography VI*, volume 7078 of *Proc. SPIE*, page 70780T, 2008.

B Pollak. Experiences with planography. *Chest*, 24(6):663–669, 1953.

G Poludniowski, G Landry, F DeBlois, P M Evans, and F Verhaegen. SpekCalc: a program to calculate photon spectra from tungsten anode x-ray tubes. *Physics in Medicine and Biology*, 54:N433–N438, 2009.

C. Popescu, P. Budrugeac, F.-J. Wortmann, L. Miu, D.E. Demco, and M. Baias. Assessment of collagen-based materials which are supports of cultural and historical objects. *Polymer Degradation and Stability*, 93(5):976–982, 2008. ISSN 0141-3910.

A A Postnov, A V Vinogradov, D van Dyck, S V Saveliev, and N M de Clerck. Quantitative analysis of bone mineral content by x-ray microtomography. *Physiological Measurement*, 24 (1):165–178, 2003.

Sven Prevrhal. Beam hardening correction and quantitative micro-CT. In Ulrich Bonse, editor, *Developments in X-Ray Tomography IV*, volume 5535 of *Proc. SPIE*, pages 152–161, 2004.

Carsten Raven. Numerical removal of ring artifacts in microtomography. *Review of Scientific Instruments*, 69(8):2978–2980, 1998. doi: 10.1063/1.1149043. URL `http://link.aip.org/link/?RSI/69/2978/1`.

Cameron J. Ritchie, Carl R. Crawford, J. David Godwin, Kevin F. King, and Yongmin Kim. Correction of computed tomography motion artifacts using pixel-specific back-projection. *IEEE Transactions on Medical Imaging*, 15(3):333–341, 1996.

R T Ritchings and B R Pullan. A technique for simultaneous dual energy scanning. *Journal of Computer Assisted Tomography*, 3(6):842–846, 1979.

Mark L Rivers, Stephen R Sutton, and Peter Eng. Geoscience applications of x-ray computed tomography. In Ulrich Bonse, editor, *Developments in X-Ray Tomography II*, volume 3772 of *Proc. SPIE*, pages 78–86, 1999.

A Sasov and D van Dyck. Desktop x-ray microscopy and microtomography. *Journal of Microscopy*, 191(2):151–158, 1998.

Alexander Sasov. X-ray nanotomography. In Ulrich Bonse, editor, *Developments in X-Ray Tomography IV*, volume 5535 of *Proc. SPIE*, pages 201–211, 2004.

Alexander Sasov, Xuan Liu, and David Rushmer. A compact microCT / microXRF scanner for non-destructive 3D chemical analysis. In Stuart R Stock, editor, *Developments in X-Ray Tomography VI*, volume 7078 of *Proc. SPIE*, page 70780R, 2008a.

Alexander Sasov, Xuan Liu, and Phil L Salmon. Compensation of mechanical inaccuracies in micro-CT and nano-CT. In Stuart R Stock, editor, *Developments in X-Ray Tomography VI*, volume 7078 of *Proc. SPIE*, page 70781C, 2008b.

Michael Schmid. Animation: Charge transfer in a three-phase ccd. `http://upload.`

wikimedia.org/wikipedia/commons/6/66/CCD_charge_transfer_animation.gif, 2005. Released under Creative Commons Attribution 2.5 Generic license.

D. K. Schroder. Extrinsic silicon focal plane arrays. In D. F. Barbe, editor, *Charge-Coupled Devices*, volume 38 of *Topics in Applied Physics*, chapter 4. Springer-Verlag, 1980.

J Kenneth Shultis and Richard E Faw. *Fundamentals of nuclear science and engineering*. CRC Press, Boca Raton FL, USA, 2nd edition, 2008.

J H Siewerdsen, M J Daly, B Bakhtiar, D J Moseley, S Richard, H Keller, and D A Jaffray. A simple, direct method for x-ray scatter estimation and correction in digital radiography and cone-beam ct. *Medical Physics*, 33(1):187–197, 2006.

Jeffrey H. Siewerdsen and David A. Jaffray. Cone-beam computed tomography with a flat-panel imager: Magnitude and effects of x-ray scatter. *Medical Physics*, 28(2):220–231, 2001.

Bruce D. Smith. Image reconstruction from cone-beam projections: Necessary and sufficient conditions and reconstruction methods. *IEEE Transactions on Medical Imaging*, 4(1):14–25, March 1985.

S R Stock, T A Ebert, K Ignatiev, and F de Carlo. Structures, structural hierarchy and function in sea urchin spines. In Ulrich Bonse, editor, *Developments in X-Ray Tomography V*, volume 6318 of *Proc. SPIE*, page 63180A, 2006.

Alexander Suppes and Eberhard Neuser. Metrology with μCT: precision challenge. In Stuart R Stock, editor, *Developments in X-Ray Tomography*, volume 7078 of *Proc. SPIE*, page 70781G, 2008.

K C Tam, S Samarasekera, and F Sauer. Exact cone beam CT with a spiral scan. *Physics in Medicine and Biology*, 43(4):1015, 1998.

C.-M. Tang, E. Stier, K. Fischer, and H. Guckel. Anti-scattering x-ray grid. *Microsystem Technologies*, 4:187–192, 1998. ISSN 0946-7076. 10.1007/s005420050128.

Mark F.V. Tarplee, Jaap J.M. van der Meer, and Graham R. Davis. The 3d microscopic 'signature' of strain within glacial sediments revealed using x-ray computed microtomography. *Quaternary Science Reviews*, 30(23–24):3501–3532, 2011. ISSN 0277-3791.

R Taschereau, P L Chow adn J S Cho, and A F Chatziioannou. A microCT x-ray head model for spectra generation with Monte Carlo simulations. *Nuclear Instruments and Methods in Physics Research Section A*, 569:373–377, 2006.

A. C. Thompson, editor. *X-ray Data Booklet*. Lawrence Berkeley National Laboratory, University of California, 3rd edition, 2009.

P S Tofts and J C Gore. Some sources of artefact in computed tomography. *Physics in Medicine and Biology*, 25(1):117, 1980.

T Tuohimaa, M Otendal, and H M Hertz. Phase-contrast x-ray imaging with a liquid-metal-jet-anode microfocus source. *Applied Physics Letters*, 91:074104, 2007.

Heang K. Tuy. An inversion formula for cone-beam reconstruction. *SIAM Journal on Applied Mathematics*, 43(3):546–552, 1983.

E van de Casteele, D van Dyck, J Sijbers, and E Raman. An energy-based beam hardening model in tomography. *Physics in Medicine and Biology*, 47(23):4181–4190, 2002.

Elke van de Casteele. *Model-based approach for beam hardening correction and resolution measurements in microtomography*. PhD thesis, Universiteit Antwerpen, 2004.

Varian Medical Systems. Flat panel x-ray imaging. `http://www.varian.com/media/xray/products/pdf/Flat%20Panel%20Xray%20Imaging%2011-11-04.pdf`, 2004. Accessed 16 October 2012.

G. Wang, T. H. Lin, and P. C. Cheng. Error analysis on a generalized feldkamp's cone-beam computed tomography algorithm. *Scanning*, 17(6):361–370, 1995. ISSN 1932-8745.

Ge Wang, Yangbo Ye, and Hengyong Yu. Approximate and exact cone-beam reconstruction with standard and non-standard spiral scanning. In Ulrich Bonse, editor, *Developments in X-Ray Tomography V*, volume 6318 of *Proc. SPIE*, page 63180F, 2006.

Brian Williams, editor. *Compton Scattering*. McGraw-Hill, 1977.

Herman Winick. Synchrotron Radiation Sources – Present Capabilities and Future Directions. *Journal of Synchrotron Radiation*, 5(3):168–175, May 1998.

W Wulf and Mary Shaw. Global variable considered harmful. *ACM SIGPLAN notices*, 8(2): 28–34, 1973.

Lo I Yin. US Patent No. 4142101, Low intensity X-ray and Gamma-ray imaging device, 1979.

Wojciech Zbijewski and Freek J Beekman. Efficient Monte Carlo based scatter artifact reduction in cone-beam micro-CT. *IEEE Transactions on Medical Imaging*, 25(7):817–827, July 2006.

Kai Zeng, Hengyong Yu, Laurie L Fajardo, and Ge Wang. Geometrical study on two tilting arcs based exact cone-beam CT for breast imaging. In Ulrich Bonse, editor, *Developments in X-Ray Tomography V*, volume 6318 of *Proc. SPIE*, page 63181M, 2006.

Michael J. Zunick. US Patent No 3165658, Directly cooled x-ray tube anode, 1965.

Appendix A

Spekcalc Input Files

The following is an example of a valid input file for the spectrum generation program `Spekcalc`, described in Section 6.3.2.2.

```
[frame=single]
 **** INPUTS ****
 kVp [kV] hvMIN [keV] Dhv [keV]
  90.  9.  0.1
 Angle [deg.]
  22.
 t_AIR t_BE t_AL t_CU t_SN t_W [mm]
  1000.  0.  0.5  0.  0.  0.
 Nf P
  0.680000007  0.330000013
```

The file comprises an explanatory header line, then alternating lines of explanatory text and numerical inputs. All integers must end with a full stop, though a float such as 5.0 is also acceptable. White-space characters are treated as separators, so the amount of space between entries is unimportant.

This example instructs `Spekcalc` to calculate binned energy intensities for an accelerating voltage of 90 kV with a minimum photon energy of 9 keV, binned at 0.1 keV intervals and with a take-off angle of 22°. The intensities are to be measured through filters corresponding to 1000 mm air and 0.5 mm aluminium.

The following Python function constructs a valid input file of the type shown above for a given accelerating voltage and take-off angle, with no filtration, and sanitises `Spekcalc`'s output return a two-dimensional list with the bin energy in the first column and the intensity in the second column. This can be processed further or saved to a file.

```
def spekcalc(voltage, angle):
  import os, math

  # Construct input file for Spekcalc.
  minvoltage = int(math.ceil(float(voltage)/float(10)))
  filestring = "****␣INPUTS␣****\nkVp␣[kV]␣\
hvMIN␣[keV]␣Dhv␣[keV]\n"
  filestring += `voltage` + ".␣" + `minvoltage` + ".␣0.5\n"
  filestring += "Angle␣[deg.]\n"
  if isinstance(angle, float):
    filestring = filestring + `angle` + "\n"
  else:
    filestring = filestring + `angle` + ".\n"
  filestring += "t_AIR␣t_BE␣t_AL␣t_CU␣t_SN␣t_W␣[mm]\n"
  filestring += "0.␣␣0.␣␣0.␣␣0.␣␣0.␣␣0.\n"
  filestring += + "Nf␣P\n"
  filestring += "0.68␣0.33"

  infile = 'tempinput.spekcalc'
  outfile = 'tempoutput.spekcalc'
```

```
# Save input file.
input = open(infile,'w')
input.write(filestring + "\n")
input.close()

# Run Spekcalc.
os.system('./spekcalc -i ' + infile + ' -o ' + outfile)

# Get output.
output = open(outfile,'r')
data = output.readlines()
output.close()

# Sanitise output with low energies zeroed.
data = data[14:]
spectrum = [[],[]]
for i in range(2, 2*minvoltage):
  spectrum[0].append(`i/2.0`)
  spectrum[1].append('0.0')
for i in data:
  templine = i.split()
  spectrum[0].append(templine[0])
  spectrum[1].append(templine[1])
return spectrum
```

Appendix B

Carousel Correction Script

The carousel correction script is written in IDL, and contains the following functions and procedures.

`amoebatry`

Function implementing a single iteration of the Nelder-Mead algorithm and transforming the simplex accordingly. Returns the test function's return value. Adapted from IDL's built-in function to pass a data structure to the test function.

`amoebafunction`

The Nelder-Mead algorithm function, which constructs initial simplexes and determines whether convergence has occurred. Returns the optimised parameters for the test function, or a non-convergence error with the most recently-used parameters. Adapted from IDL's built-in function to pass a data structure to `amoebatry`.

`userinterface_event`

Procedure defining actions to be taken immediately on click of the user interface's 'get settings', 'save settings file', 'open settings file' or 'browse for input file' buttons, or the 'immersion' or 'additional filters' checkboxes. This also writes a settings file when a calibration is begun by clicking the 'start' button.

`userinterface`

Function setting the layout of and populating the settings screen.

`attenuation`

Procedure applying filter, scintillator, detector and carousel or virtual dominant-material step-wedge responses to the X-ray spectrum and calculating the attenuation. Combined from two functions in previous *MuCAT* calibration programs to eliminate redundant code.

`readfile`

Procedure to sanitise `XCOM` output files and read them into an array.

`funct`

The optimisation test function for the line-by-line optimisation of tungsten and caesium iodide thicknesses. Calls `attenuation` and returns the sum of squared differences between the measured and simulated carousel filters.

`optvoltage`

The optimisation test function for the global-level optimisation (of acceleration voltage, and aluminium and titanium carousel filter thicknesses.) Calls the line-by-line optimisation, and returns the summed errors from all inner-optimisation calls, as well as providing graphical user feedback.

`calibration`

Function comprising a single beam hardening calibration. This function handles the data structuring and file reading as far as possible for the optimisations to improve execution speed, then calls the global optimisation with a partial projection set. After the global parameters are optimised, the global optimisation is called again with nearly-fixed the full projection set in order to optimise the line-by-line parameters. The function returns a binary value signalling whether further calibrations are required.

```
function amoebatry, p, y, psum, func, completeblock, ihi, fac
; Extrapolates by a factor fac through the face of the simplex, across
; from the high point, tries it and replaces the high point if the new
; point is better.

  compile_opt hidden
  fac1 = (1.0 - fac) / n_elements(psum)
  fac2 = fac1  - fac
  ptry = psum * fac1 - p[*,ihi] * fac2
  ytry = call_function(func, ptry, completeblock)  ;Eval fcn at trial point
  if ytry lt y[ihi] then begin    ;If its better than highest, replace highest
    y[ihi] = ytry
    psum = psum + ptry - p[*,ihi]
    p[0,ihi] = ptry
    endif
  return, ytry
end


function amoebafunction, ftol, FUNCTION_NAME=func, FUNCTION_DATA=completeblock, FUNCTION_VALUE=y, $
  NCALLS = ncalls, NMAX = nmax, P0 = p0, SCALE=scale, SIMPLEX=p
if keyword_set(scale) then begin  ;If set, then p0 is initial starting pnt
   ndim = n_elements(p0)
   p = p0 # replicate(1.0, ndim+1)
   for i=0, ndim-1 do p[i,i+1] = p0[i] + scale[i < (n_elements(scale)-1)]
endif

s = size(p)
if s[0] ne 2 then message, 'Either (SCALE,P0) or SIMPLEX must be initialized'
ndim = s[1]     ;Dimensionality of simplex
mpts = ndim+1     ;# of points in simplex
if n_elements(func) eq 0 then func = 'FUNC'
if n_elements(nmax) eq 0 then nmax = 5000L

y = replicate(call_function(func, p[*,0],completeblock), mpts)  ;Init Y to proper type
for i=1, ndim do y[i] = call_function(func, p[*,i],completeblock) ;Fill in rest of the vals
ncalls = 0L
psum = total(p,2)

while 1 eq 1 do begin   ;Each iteration
  s = sort(y)
  ilo = s[0]    ;Lowest point
```

```
  ihi = s[ndim]   ;Highest point
  inhi = s[ndim-1]  ;Next highest point
  d = abs(y[ihi]) + abs(y[ilo]) ;Denominator = interval
  if d ne 0.0 then rtol = 2.0 * abs(y[ihi]-y[ilo])/d $
  else rtol = ftol / 2.         ;Terminate if interval is 0

  if rtol lt ftol or ncalls eq nmax then begin ;Done?
      t = y[0] & y[0] = y[ilo] & y[ilo] = t ;Sort so fcn min is 0th elem
      t = p[*,ilo] & p[*,ilo] = p[*,0] & p[*,0] = t
      return, t                 ;params for fcn min
  endif

  ncalls = ncalls + 2
  ytry = amoebatry(p, y, psum, func, completeblock, ihi, -1.0)
  if ytry le y[ilo] then ytry = amoebatry(p,y,psum, func, completeblock, ihi, 2.0) $
  else if ytry ge y[inhi] then begin
    ysave = y[ihi]
    ytry = amoebatry(p,y,psum,func,completeblock, ihi, 0.5)
    if ytry ge ysave then begin
  for i=0, ndim do if i ne ilo then begin
    psum = 0.5 * (p[*,i] + p[*,ilo])
    p[*,i] = psum
    y[i] = call_function(func, psum, completeblock)
    endif
  ncalls = ncalls + ndim
  psum = total(p,2)
  endif   ;ytry ge ysave
    endif else ncalls = ncalls  - 1
  endwhile
  if n_elements(t) gt 0 then begin
     nonconverge = [-1.0, t, y]
  endif else begin
     nonconverge = -1.0
  endelse
  return, nonconverge    ;Here, the function failed to converge.
end


pro userinterface_event, event

; Get state
widget_control, event.top, get_uvalue=infoptr
```

```
info = *infoptr

; Identify widget causing event
widget_control, event.id, get_uvalue=eventvalue

case eventvalue of
  'settingsbutton': begin
    ; Open file to read state from
    openr, openfile, 'settings.txt', /get_lun
  ; Read data out
    for i=0,18 do begin
      temp=''
      readf, openfile, temp, format='(a)'
      if i eq 0 then widget_control, info.maxtext, set_value = temp
      if i eq 1 then widget_control, info.caltext, set_value = temp
      if i eq 2 then widget_control, info.takeofftext, set_value = temp
      if i eq 3 then widget_control, info.stepstext, set_value = temp
      if i eq 4 then widget_control, info.alwidthtext, set_value = temp
      if i eq 5 then widget_control, info.cuwidthtext, set_value = temp
      if i eq 6 then begin
        widget_control, info.extrabutton, set_button = temp
        if temp eq '1' then begin
          widget_control, info.extrafilelabel, sensitive=1
          widget_control, info.extrafiletext, sensitive=1
          widget_control, info.extrafilebrowse, sensitive=1
          widget_control, info.extrathicknesslabel, sensitive=1
          widget_control, info.extrathicknesstext, sensitive=1
          widget_control, info.extradensitylabel, sensitive=1
          widget_control, info.extradensitytext, sensitive=1
        endif else begin
          widget_control, info.extrafilelabel, sensitive=0
          widget_control, info.extrafiletext, sensitive=0
          widget_control, info.extrafilebrowse, sensitive=0
          widget_control, info.extrathicknesslabel, sensitive=0
          widget_control, info.extrathicknesstext, sensitive=0
          widget_control, info.extradensitylabel, sensitive=0
          widget_control, info.extradensitytext, sensitive=0
        endelse
      endif
      if i eq 7 then begin
        widget_control, info.immersionbutton, set_button = temp
        if temp eq '1' then begin
```

```
          widget_control, info.immersionfilelabel, sensitive=1
          widget_control, info.immersionfiletext, sensitive=1
          widget_control, info.immersionfilebrowse, sensitive=1
          widget_control, info.specimendensitylabel, sensitive=1
          widget_control, info.specimendensitytext, sensitive=1
          widget_control, info.immersiondensitylabel, sensitive=1
          widget_control, info.immersiondensitytext, sensitive=1
        endif else begin
          widget_control, info.immersionfilelabel, sensitive=0
          widget_control, info.immersionfiletext, sensitive=0
          widget_control, info.immersionfilebrowse, sensitive=0
          widget_control, info.specimendensitylabel, sensitive=0
          widget_control, info.specimendensitytext, sensitive=0
          widget_control, info.immersiondensitylabel, sensitive=0
          widget_control, info.immersiondensitytext, sensitive=0
        endelse
      endif
      if i eq 8 then widget_control, info.extrafiletext, set_value = string(temp)
      if i eq 9 then widget_control, info.immersionfiletext, set_value = string(temp)
      if i eq 10 then widget_control, info.extrathicknesstext, set_value = string(temp)
      if i eq 11 then widget_control, info.extradensitytext, set_value = string(temp)
      if i eq 12 then widget_control, info.immersiondensitytext, set_value = string(temp)
      if i eq 13 then widget_control, info.specimendensitytext, set_value = string(temp)
      if i eq 14 then widget_control, info.specimenfiletext, set_value = string(temp)
      if i eq 15 then widget_control, info.wedgefiletext, set_value = string(temp)
      if i eq 16 then widget_control, info.calibrationfiletext, set_value = string(temp)
      if i eq 17 then widget_control, info.parameterfiletext, set_value = string(temp)
      if i eq 18 then widget_control, info.calibrationlinestext, set_value = temp
    endfor
    free_lun, openfile
  end
  'savebutton': begin

; Open file to save state into
    savepath = pickfile(/write)
    openw, savefile, savepath, /get_lun

; Take snapshot of GUI state
    widget_control, info.maxtext, get_value = maxv
    widget_control, info.caltext, get_value = calv
    widget_control, info.takeofftext, get_value = takeoff
    widget_control, info.stepstext, get_value = thicknesssteps
```

```
    widget_control, info.alwidthtext, get_value = althickness
    widget_control, info.cuwidthtext, get_value = cuthickness
    extras = widget_info(info.extrabutton, /button_set)
    immersions = widget_info(info.immersionbutton, /button_set)
    widget_control, info.extrafiletext, get_value = extrapath
    widget_control, info.immersionfiletext, get_value = immersionpath
    widget_control, info.extrathicknesstext, get_value = extrathickness
    widget_control, info.extradensitytext, get_value = extradensity
    widget_control, info.immersiondensitytext, get_value = immersiondensity
    widget_control, info.specimendensitytext, get_value = specimendensity
    widget_control, info.specimenfiletext, get_value = specimenpath
    widget_control, info.wedgefiletext, get_value = wedgefilepath
    widget_control, info.calibrationfiletext, get_value = calibrationpath
    widget_control, info.parameterfiletext, get_value = parameterpath
    widget_control, info.calibrationlinestext, get_value = callines
; Write state to file
    printf, savefile, maxv
    printf, savefile, calv
    printf, savefile, takeoff
    printf, savefile, thicknesssteps
    printf, savefile, althickness
    printf, savefile, cuthickness
    printf, savefile, extras, format='(i1)'
    printf, savefile, immersions, format='(i1)'
    printf, savefile, extrapath
    printf, savefile, immersionpath
    printf, savefile, extrathickness
    printf, savefile, extradensity
    printf, savefile, immersiondensity
    printf, savefile, specimendensity
    printf, savefile, specimenpath
    printf, savefile, wedgefilepath
    printf, savefile, calibrationpath
    printf, savefile, parameterpath
    printf, savefile, callines
; Write context to file
    printf, savefile, '############### Below are context indicators for the items above.'
    printf, savefile, 'Maximum voltage (kV)'
    printf, savefile, 'Calibration voltage (kV)'
    printf, savefile, 'Take-off angle (degrees)'
    printf, savefile, 'Number of thickness steps'
    printf, savefile, 'Al filter width (cm)'
```

```
  printf, savefile, 'Cu filter width (cm)'
  printf, savefile, 'Additional filter (integer - Y/N)*'
  printf, savefile, 'Liquid immersion (integer - Y/N)**'
  printf, savefile, 'Additional filter file'
  printf, savefile, 'Immersion filter file'
  printf, savefile, 'Additional filter width (cm)'
  printf, savefile, 'Additional filter density'
  printf, savefile, 'Immersion liquid density'
  printf, savefile, 'Specimen density'
  printf, savefile, 'Specimen absorption coefficient file'
  printf, savefile, 'Step wedge data file'
  printf, savefile, 'Calibration output file'
  printf, savefile, 'Tungsten / CsI parameter output file'
  printf, savefile, 'Number of lines used for calibration (default: 800)'
  printf, savefile, '############### Empty rows denote empty fields. If * or ** are 0 then rows may well be empty.'
  free_lun, savefile
end

'openbutton': begin
; Open file to read state from
  openpath = pickfile(/read)
  openr, openfile, openpath, /get_lun
; Read data out
  for i=0,17 do begin
    temp=''
    readf, openfile, temp, format='(a)'
    if i eq 0 then widget_control, info.maxtext, set_value = temp
    if i eq 1 then widget_control, info.caltext, set_value = temp
    if i eq 2 then widget_control, info.takeofftext, set_value = temp
    if i eq 3 then widget_control, info.stepstext, set_value = temp
    if i eq 4 then widget_control, info.alwidthtext, set_value = temp
    if i eq 5 then widget_control, info.cuwidthtext, set_value = temp
    if i eq 6 then begin
      widget_control, info.extrabutton, set_button = temp
      if temp eq '1' then begin
        widget_control, info.extrafilelabel, sensitive=1
        widget_control, info.extrafiletext, sensitive=1
        widget_control, info.extrafilebrowse, sensitive=1
        widget_control, info.extrathicknesslabel, sensitive=1
        widget_control, info.extrathicknesstext, sensitive=1
        widget_control, info.extradensitylabel, sensitive=1
        widget_control, info.extradensitytext, sensitive=1
```

```
    endif else begin
      widget_control, info.extrafilelabel, sensitive=0
      widget_control, info.extrafiletext, sensitive=0
      widget_control, info.extrafilebrowse, sensitive=0
      widget_control, info.extrathicknesslabel, sensitive=0
      widget_control, info.extrathicknesstext, sensitive=0
      widget_control, info.extradensitylabel, sensitive=0
      widget_control, info.extradensitytext, sensitive=0
    endelse
  endif
  if i eq 7 then begin
    widget_control, info.immersionbutton, set_button = temp
    if temp eq '1' then begin
      widget_control, info.immersionfilelabel, sensitive=1
      widget_control, info.immersionfiletext, sensitive=1
      widget_control, info.immersionfilebrowse, sensitive=1
      widget_control, info.specimendensitylabel, sensitive=1
      widget_control, info.specimendensitytext, sensitive=1
      widget_control, info.immersiondensitylabel, sensitive=1
      widget_control, info.immersiondensitytext, sensitive=1
    endif else begin
      widget_control, info.immersionfilelabel, sensitive=0
      widget_control, info.immersionfiletext, sensitive=0
      widget_control, info.immersionfilebrowse, sensitive=0
      widget_control, info.specimendensitylabel, sensitive=0
      widget_control, info.specimendensitytext, sensitive=0
      widget_control, info.immersiondensitylabel, sensitive=0
      widget_control, info.immersiondensitytext, sensitive=0
    endelse
  endif
  if i eq 8 then widget_control, info.extrafiletext, set_value = string(temp)
  if i eq 9 then widget_control, info.immersionfiletext, set_value = string(temp)
  if i eq 10 then widget_control, info.extrathicknesstext, set_value = string(temp)
  if i eq 11 then widget_control, info.extradensitytext, set_value = string(temp)
  if i eq 12 then widget_control, info.immersiondensitytext, set_value = string(temp)
  if i eq 13 then widget_control, info.specimendensitytext, set_value = string(temp)
  if i eq 14 then widget_control, info.specimenfiletext, set_value = string(temp)
  if i eq 15 then widget_control, info.wedgefiletext, set_value = string(temp)
  if i eq 16 then widget_control, info.calibrationfiletext, set_value = string(temp)
  if i eq 17 then widget_control, info.parameterfiletext, set_value = string(temp)
  if i eq 17 then widget_control, info.calibrationlinestext, set_value = temp
endfor
```

```
  free_lun, openfile
end

'additional': begin
  checkboxstatus = widget_info(info.extrabutton, /button_set)
  if checkboxstatus eq 1 then begin
    widget_control, info.extrafilelabel, sensitive=1
    widget_control, info.extrafiletext, sensitive=1
    widget_control, info.extrafilebrowse, sensitive=1
    widget_control, info.extrathicknesslabel, sensitive=1
    widget_control, info.extrathicknesstext, sensitive=1
    widget_control, info.extradensitylabel, sensitive=1
    widget_control, info.extradensitytext, sensitive=1
  endif else begin
    widget_control, info.extrafilelabel, sensitive=0
    widget_control, info.extrafiletext, sensitive=0
    widget_control, info.extrafilebrowse, sensitive=0
    widget_control, info.extrathicknesslabel, sensitive=0
    widget_control, info.extrathicknesstext, sensitive=0
    widget_control, info.extradensitylabel, sensitive=0
    widget_control, info.extradensitytext, sensitive=0
  endelse
end

'immersion': begin
  checkboxstatus = widget_info(info.immersionbutton, /button_set)
  if checkboxstatus eq 1 then begin
    widget_control, info.immersionfilelabel, sensitive=1
    widget_control, info.immersionfiletext, sensitive=1
    widget_control, info.immersionfilebrowse, sensitive=1
    widget_control, info.specimendensitylabel, sensitive=1
    widget_control, info.specimendensitytext, sensitive=1
    widget_control, info.immersiondensitylabel, sensitive=1
    widget_control, info.immersiondensitytext, sensitive=1
  endif else begin
    widget_control, info.immersionfilelabel, sensitive=0
    widget_control, info.immersionfiletext, sensitive=0
    widget_control, info.immersionfilebrowse, sensitive=0
    widget_control, info.specimendensitylabel, sensitive=0
    widget_control, info.specimendensitytext, sensitive=0
    widget_control, info.immersiondensitylabel, sensitive=0
    widget_control, info.immersiondensitytext, sensitive=0
```

```
    endelse
  end

  'additionalbrowse': begin
    newpath = pickfile(/read)
    widget_control, info.extrafiletext, set_value = newpath
  end

  'immersionbrowse': begin
    newpath = pickfile(/read)
    widget_control, info.immersionfiletext, set_value = newpath
  end

  'specimenbrowse': begin
    newpath = pickfile(/read)
    widget_control, info.specimenfiletext, set_value = newpath
  end

  'stepwedgebrowse': begin
    newpath = pickfile(/read)
    widget_control, info.wedgefiletext, set_value = newpath
  end

  'calibrationbrowse': begin
    newpath = pickfile(/write)
    widget_control, info.calibrationfiletext, set_value = newpath
  end

  'parameterbrowse': begin
    newpath = pickfile(/write)
    widget_control, info.parameterfiletext, set_value = newpath
  end

  'startbutton': begin
    ; Open file to save state into
    openw, savefile, 'settings.txt', /get_lun

; Take snapshot of GUI state
    widget_control, info.maxtext, get_value = maxv
    widget_control, info.caltext, get_value = calv
    widget_control, info.takeofftext, get_value = takeoff
    widget_control, info.stepstext, get_value = thicknesssteps
```

```
    widget_control, info.alwidthtext, get_value = althickness
    widget_control, info.cuwidthtext, get_value = cuthickness
    extras = widget_info(info.extrabutton, /button_set)
    immersions = widget_info(info.immersionbutton, /button_set)
    widget_control, info.extrafiletext, get_value = extrapath
    widget_control, info.immersionfiletext, get_value = immersionpath
    widget_control, info.extrathicknesstext, get_value = extrathickness
    widget_control, info.extradensitytext, get_value = extradensity
    widget_control, info.immersiondensitytext, get_value = immersiondensity
    widget_control, info.specimendensitytext, get_value = specimendensity
    widget_control, info.specimenfiletext, get_value = specimenpath
    widget_control, info.wedgefiletext, get_value = wedgefilepath
    widget_control, info.calibrationfiletext, get_value = calibrationpath
    widget_control, info.parameterfiletext, get_value = parameterpath
    widget_control, info.calibrationlinestext, get_value = callines
; Write state to file
    printf, savefile, maxv
    printf, savefile, calv
    printf, savefile, takeoff
    printf, savefile, thicknesssteps
    printf, savefile, althickness
    printf, savefile, cuthickness
    printf, savefile, extras, format='(i1)'
    printf, savefile, immersions, format='(i1)'
    printf, savefile, extrapath
    printf, savefile, immersionpath
    printf, savefile, extrathickness
    printf, savefile, extradensity
    printf, savefile, immersiondensity
    printf, savefile, specimendensity
    printf, savefile, specimenpath
    printf, savefile, wedgefilepath
    printf, savefile, calibrationpath
    printf, savefile, parameterpath
    printf, savefile, callines
; Write context to file
    printf, savefile, '######################### Below are context indicators for the items above.'
    printf, savefile, 'Maximum voltage (kV)'
    printf, savefile, 'Calibration voltage (kV)'
    printf, savefile, 'Take-off angle (degrees)'
    printf, savefile, 'Number of thickness steps'
    printf, savefile, 'Al filter width (cm)'
```

```
    printf, savefile, 'Cu filter width (cm)'
    printf, savefile, 'Additional filter (integer - Y/N)*'
    printf, savefile, 'Liquid immersion (integer - Y/N)**'
    printf, savefile, 'Additional filter file'
    printf, savefile, 'Immersion filter file'
    printf, savefile, 'Additional filter width (cm)'
    printf, savefile, 'Additional filter density'
    printf, savefile, 'Immersion liquid density'
    printf, savefile, 'Specimen density'
    printf, savefile, 'Specimen absorption coefficient file'
    printf, savefile, 'Step wedge data file'
    printf, savefile, 'Calibration output file'
    printf, savefile, 'Tungsten / CsI parameter output file'
    printf, savefile, 'Number of lines used for calibration (default: 800)'
    printf, savefile, '######################### Empty rows denote empty fields. If * or ** are 0 then rows may well be empty.'
    free_lun, savefile
    widget_control, event.top, /destroy
  end
endcase
end


function userinterface
openr, openfile, 'settings.txt', /get_lun
  ; Read data out
    for i=0,18 do begin
      temp=''
      readf, openfile, temp, format='(a)'
      if i eq 0 then tempmaxtext = temp
      if i eq 1 then tempcaltext = temp
      if i eq 2 then temptakeofftext = temp
      if i eq 3 then tempstepstext = temp
      if i eq 4 then tempalwidthtext = temp
      if i eq 5 then tempcuwidthtext = temp
      if i eq 6 then tempextrabutton = temp
      if i eq 7 then tempimmersionbutton = temp
      if i eq 8 then tempextrafiletext = string(temp)
      if i eq 9 then tempimmersionfiletext = string(temp)
      if i eq 10 then tempextrathicknesstext = string(temp)
      if i eq 11 then tempextradensitytext = string(temp)
      if i eq 12 then tempimmersiondensitytext = string(temp)
      if i eq 13 then tempspecimendensitytext = string(temp)
```

```
      if i eq 14 then tempspecimenfiletext = string(temp)
      if i eq 15 then tempwedgefiletext = string(temp)
      if i eq 16 then tempcalibrationfiletext = string(temp)
      if i eq 17 then tempparameterfiletext = string(temp)
      if i eq 18 then tempcalibrationlinestext = temp
    endfor
    free_lun, openfile

; Set up constasettingsblock.nts
browsesize = 60
pathsize = 20
labelxsize = 200
labelysize = 23
maxsteps = 10
minsteps = 1

; Define window (column-aligned, non-resizeable) and menu
guibase = widget_base(column=1, title='Carousel Beam Hardening Calibration', tlb_frame_attr=1)
  menubase = widget_base(guibase, row=1, /toolbar)
    subdir = 'resource/bitmaps'
    mapfile = filepath('ascii.bmp', subdir=subdir)
    settingsbutton = widget_button(menubase, value=mapfile, /bitmap, uvalue='settingsbutton')
    mapfile = filepath('open.bmp', subdir=subdir)
    openbutton = widget_button(menubase, value=mapfile, /bitmap, uvalue='openbutton')
    mapfile = filepath('save.bmp', subdir=subdir)
    savebutton = widget_button(menubase, value=mapfile, /bitmap, uvalue='savebutton')

; Define window contents
  progbase = widget_base(guibase, column=1, /base_align_center)
; Define control elements
    controlbase = widget_base(progbase, row=6, /frame, /base_align_center)
      xraybase = widget_base(controlbase, column=2, /base_align_left)
        maxlabel = widget_label(xraybase, value='Maximum voltage (kV): ', xsize = labelxsize, ysize = labelysize)
        callabel = widget_label(xraybase, value='Calibration voltage (kV): ', xsize = labelxsize, ysize = labelysize)
        takeofflabel = widget_label(xraybase, value='Take-off angle (degrees): ', xsize = labelxsize, ysize = labelysize)
        stepslabel = widget_label(xraybase, value='Number of thickness steps: ', xsize = labelxsize, ysize = labelysize)
        lineslabel = widget_label(xraybase, value='Number of rows to calibrate: ', xsize = labelxsize, ysize = labelysize)
        alwidthlabel = widget_label(xraybase, value='Al filter width (cm): ', xsize = labelxsize, ysize = labelysize)
        cuwidthlabel = widget_label(xraybase, value='Cu filter width (cm): ', xsize = labelxsize, ysize = labelysize)
        maxtext = widget_text(xraybase, /editable, value=tempmaxtext, xsize=2*pathsize)
        caltext = widget_text(xraybase, /editable, value=tempcaltext, xsize=2*pathsize)
        takeofftext = widget_text(xraybase, /editable, value=temptakeofftext, xsize=2*pathsize)
```

```
  stepstext = widget_text(xraybase, /editable, value=tempstepstext, xsize=2*pathsize)
  calibrationlinestext = widget_text(xraybase, /editable, value=tempcalibrationlinestext, xsize=2*pathsize)
  alwidthtext = widget_text(xraybase, /editable, value=tempalwidthtext, xsize=2*pathsize)
  cuwidthtext = widget_text(xraybase, /editable, value=tempcuwidthtext, xsize=2*pathsize)

extrabuttonbase = widget_base(controlbase, /grid_layout, /nonexclusive)
  extrabutton = widget_button(extrabuttonbase, value='Additional filter', uvalue='additional')
  immersionbutton = widget_button(extrabuttonbase, value='Liquid Immersion', uvalue='immersion')
  widget_control, extrabutton, set_button = uint(tempextrabutton)
  widget_control, immersionbutton, set_button = uint(tempimmersionbutton)

extrafilesbase = widget_base(controlbase, column=3, /base_align_left)
  extrafilelabel = widget_label(extrafilesbase, value='Additional filter file: ', sensitive=uint(tempextrabutton), $
    xsize = labelxsize, ysize = labelysize)
  immersionfilelabel = widget_label(extrafilesbase, value='Immersion filter file: ', sensitive=uint(tempimmersionbutton), $
    xsize = labelxsize, ysize = labelysize)
  extrafiletext = widget_text(extrafilesbase, /editable, xsize=2*pathsize, sensitive=uint(tempextrabutton), $
    value = tempextrafiletext)
  immersionfiletext = widget_text(extrafilesbase, /editable, xsize=2*pathsize, sensitive=uint(tempimmersionbutton), $
    value = tempimmersionfiletext)
  extrafilebrowse = widget_button(extrafilesbase, value='Browse...', xsize=browsesize, uvalue='additionalbrowse', $
    sensitive=uint(tempextrabutton))
  immersionfilebrowse = widget_button(extrafilesbase, value='Browse...', xsize=browsesize, uvalue='immersionbrowse', $
    sensitive=uint(tempimmersionbutton))

extrainfobase = widget_base(controlbase, column=2, /base_align_left)
  extrathicknesslabel = widget_label(extrainfobase, value='Additional filter width (cm): ', sensitive=uint(tempextrabutton), $
    xsize = labelxsize, ysize = labelysize)
  extradensitylabel = widget_label(extrainfobase, value='Additional filter density: ', sensitive=uint(tempextrabutton), $
    xsize = labelxsize, ysize = labelysize)
  immersiondensitylabel = widget_label(extrainfobase, value='Immersion liquid density: ', $
    sensitive=uint(tempimmersionbutton), xsize = labelxsize, ysize = labelysize)
  specimendensitylabel = widget_label(extrainfobase, value='Specimen density: ', sensitive=uint(tempimmersionbutton), $
    xsize = labelxsize, ysize = labelysize)
  extrathicknesstext = widget_text(extrainfobase, /editable, sensitive=uint(tempextrabutton), value = tempextrathicknesstext, $
    xsize=2*pathsize)
  extradensitytext = widget_text(extrainfobase, /editable, sensitive=uint(tempextrabutton), value = tempextradensitytext, $
    xsize=2*pathsize)
  immersiondensitytext = widget_text(extrainfobase, /editable, sensitive=uint(tempimmersionbutton), $
    value = tempimmersiondensitytext, xsize=2*pathsize)
  specimendensitytext = widget_text(extrainfobase, /editable, sensitive=uint(tempimmersionbutton), $
    value = tempspecimendensitytext, xsize=2*pathsize)
```

```
      datafilesbase = widget_base(controlbase, column=3, /base_align_left)
        specimenfilelabel = widget_label(datafilesbase, value='Specimen absorption coefficient file: ', $
          xsize = labelxsize, ysize = labelysize)
        wedgefilelabel = widget_label(datafilesbase, value='Step wedge data file: ', xsize = labelxsize, ysize = labelysize)
        calibrationfilelabel = widget_label(datafilesbase, value='Calibration output file: ', $
          xsize = labelxsize, ysize = labelysize)
        parameterfilelabel = widget_label(datafilesbase, value='Tungsten / CsI parameter output file: ', $
          xsize = labelxsize, ysize = labelysize)
        specimenfiletext = widget_text(datafilesbase, /editable, value = tempspecimenfiletext, xsize=2*pathsize)
        wedgefiletext = widget_text(datafilesbase, /editable, value = tempwedgefiletext, xsize=2*pathsize)
        calibrationfiletext = widget_text(datafilesbase, /editable, value = tempcalibrationfiletext, xsize=2*pathsize)
        parameterfiletext = widget_text(datafilesbase, /editable, value = tempparameterfiletext, xsize=2*pathsize)
        specimenfilebrowse = widget_button(datafilesbase, value='Browse...', xsize=browsesize, uvalue='specimenbrowse')
        wedgefilebrowse = widget_button(datafilesbase, value='Browse...', xsize=browsesize, uvalue='stepwedgebrowse')
        calibrationfilebrowse = widget_button(datafilesbase, value='Browse...', xsize=browsesize, uvalue='calibrationbrowse')
        parameterfilebrowse = widget_button(datafilesbase, value='Browse...', xsize=browsesize, uvalue='parameterbrowse')

      gobutton = widget_button(controlbase, value='Start', uvalue='startbutton', xsize=580, ysize=150)
; Define output elemesettingsblock.nts
;   outputsbase = widget_base(progbase, column=1)
;     outputdraw = widget_draw(outputsbase, xsize=1000, ysize=750)
;     outputtext = widget_text(outputsbase, value='Enter parameters and press Start.', /scroll, ysize=10)

; Realize widgets
widget_control, guibase, /realize

; Create and store state information
info = {maxtext:maxtext, caltext:caltext, takeofftext:takeofftext, $
        stepstext:stepstext, alwidthtext:alwidthtext, cuwidthtext:cuwidthtext, $
        extrabutton:extrabutton, immersionbutton:immersionbutton, $
        extrafilelabel:extrafilelabel, immersionfilelabel:immersionfilelabel, $
        extrafiletext:extrafiletext, immersionfiletext:immersionfiletext, $
        extrafilebrowse:extrafilebrowse, $
        immersionfilebrowse:immersionfilebrowse, $
        extrathicknesslabel:extrathicknesslabel, $
        extradensitylabel:extradensitylabel, $
        immersiondensitylabel:immersiondensitylabel, $
        specimendensitylabel:specimendensitylabel, $
        extrathicknesstext:extrathicknesstext, extradensitytext:extradensitytext, $
        immersiondensitytext:immersiondensitytext, $
        specimendensitytext:specimendensitytext, $
```

```
        specimenfiletext:specimenfiletext, wedgefiletext:wedgefiletext, $
        calibrationfiletext:calibrationfiletext, $
        parameterfiletext:parameterfiletext, $
        specimenfilebrowse:specimenfilebrowse, $
        wedgefilebrowse:wedgefilebrowse, $
        calibrationfilebrowse:calibrationfilebrowse, $
        parameterfilebrowse:parameterfilebrowse, gobutton:gobutton, calibrationlinestext:calibrationlinestext}
infoptr = ptr_new(info)
widget_control, guibase, set_uvalue=infoptr

xmanager, 'userinterface', guibase

end


Pro attenuation, X, a, completeblock, isspecimen, output
  V1=floor(completeblock.spectrumblock.MaxVoltage)
  D1=completeblock.spectrumblock.MaxVoltage - V1
  DesiredSpectrum = completeblock.spectrumblock.SourceSpectrum(V1,*) * (1 - D1) + $
     completeblock.spectrumblock.SourceSpectrum(V1 + 1,*) * D1
zeros = where(desiredspectrum eq 0)
  completeblock.filterblock.LinAbCoeffW(zeros)=0
  thicknessw = a(0)
  thicknesscsi = a(1)

  N=size(x,/N_Elements)
  TotalOutput = fltarr(N)

; Filter
  FilteredSpectrum =    DesiredSpectrum * $
                        exp(-completeblock.filterblock.LinAbCoeffAl # completeblock.thicknessblock.ThicknessAl - $
                        completeblock.filterblock.LinAbCoeffCu # completeblock.thicknessblock.ThicknessCu - $
                        completeblock.filterblock.LinAbCoeffW # thicknessw)
  if isspecimen eq 1 then begin
    FilteredSpectrum =  FilteredSpectrum * $
                        exp(-completeblock.filterblock.LinAbCoeffExFilter * completeblock.thicknessblock.ThicknessExFilter)
  endif

; Scintillator
  CsISpectrum =         FilteredSpectrum * (1 - exp(-completeblock.filterblock.LinAbCoeffCsI #exp(thicknesscsi)))

; (Calibration) Specimen
```

```
  for i=0, N-1 do begin
    if isspecimen eq 1 then begin
      ModSpectrum =     CsISpectrum*exp(-completeblock.filterblock.LinAbCoeffSpecimen*x(i))
    endif else begin
      case completeblock.variableblock.material(i) of
     "perspex": ModSpectrum = CsISpectrum*exp(-completeblock.filterblock.LinAbCoeffPerspex*x(i))
     "al":           ModSpectrum = CsISpectrum*exp(-completeblock.filterblock.LinAbCoeffAl*x(i))
     "ti":      ModSpectrum = CsISpectrum*exp(-completeblock.filterblock.LinAbCoeffTi*x(i))
     "cu":      ModSpectrum = CsISpectrum*exp(-completeblock.filterblock.LinAbCoeffCu*x(i))
     else:      ModSpectrum = CsISpectrum*exp(-x(i))
      endcase
    endelse

; Detector
    DetectSpectrum =  ModSpectrum * completeblock.spectrumblock.Energy
    TotalOutput(i)=total(DetectSpectrum, /nan)
  endfor

  output = alog(TotalOutput(N-1)/TotalOutput)

  if isspecimen eq 1 then begin
     openw, attenuationfile, 'attenuations.txt', /get_lun
     for i=0, N-1 do printf, x(i), output(i)
     free_lun, attenuationfile
  endif
end


pro ReadFile,FileName,Abcoeff,spectrumblock,MuCal
  NameSubstance = " "
  Line1 = " "
  n=0
  stoploop = 0
  MaxEnergy=150
  AbCoeff = fltarr(2*MaxEnergy+1)
  MuCal = 0.0
  openr, thisfile, FileName, /get_lun
  readf, thisfile, NameSubstance
  while ~ eof(thisfile) do begin
    for i=1,12 do begin
      readf, thisfile, Line1
    endfor
```

```
    for i=1,44 do begin
      readf, thisfile, A1, A2, A3, A4, A5, A6, A7, A8
      AbCoeff(n)= AbCoeff(n) + A7
      A1=A1*1000
      if A1 GE MaxEnergy then begin
        stoploop = 1
        break
      endif
      if A1 EQ spectrumblock.CalVoltage then begin
        MuCal = MuCal + A7
      endif
      n=n+1
    endfor
    if (stoploop EQ 1) then break

    for i=1,2 do begin
        readf, thisfile, Line1
    endfor
  endwhile
  free_lun, thisfile
end


function funct,P,completeblock
  attenuation,completeblock.variableblock.X1,P,completeblock,0,f
  e = f - completeblock.variableblock.Y1
  e *= (e)
  return, total(e)
end

function optvoltage,testcopper,optimizationblock
    Output=fltarr(10)
    thickness=[0.2093,0.44200,0.22100,0.110500,0.3976,0.1988,0.0994,0.0497,0.02]
 ;   thickness=[0.2093,0.44000,0.22000,0.110000,0.3976,0.1988,0.0994,0.0497,0.02]
  ;   thickness=[0.2105,0.4469,0.2235,0.1117,0.40632,0.20316,0.10158,0.05079,0.023]
    material=["cu","ti","ti","ti","al","al","al","al","al","NOTHING"]
    ZDEPTH=optimizationblock.settingsblock.callines
    XWIDTH=600
    abso = fltarr(9,ZDEPTH)
    line = fltarr(XWIDTH)
    filename = "file"
```

```
MaxEnergy=150
TotalError = 0.0
optimizationblock.settingsblock.thicknesscu = testcopper
;optimizationblock.settingsblock.MaxVoltage = testvoltage
;optimizationblock.spectrumblock.MaxVoltage = testvoltage

; Set up 300-step virtual wedge (plus air)
TotalNumber=300
StepThickness=12/(TotalNumber*optimizationblock.filterblock.MuSpecimen)
XX=fltarr(TotalNumber+1)
for j = 0,TotalNumber do begin
    XX(j) = StepThickness*(TotalNumber-j)
endfor

; Initialise output files
openw, calfile, optimizationblock.settingsblock.calibrationfilename, /get_lun
ParaFile = " "
openw, parafile, optimizationblock.settingsblock.parameterfilename, /get_lun

; Find measured attenuations.
for z=0,ZDEPTH-1 do begin
    for step=0,8 do begin
        line=optimizationblock.raw[*,z,step]
        allelements = 0
        sumxy = 0
        for elementnumber=0,XWIDTH-1 do begin
            elementvalue = line(elementnumber)
            allelements = allelements + elementvalue
            sumxy=sumxy + elementnumber * elementvalue
        endfor
        weightedcentre=sumxy/allelements
        windowleft = fix(weightedcentre-99.5)
        windowright = windowleft + 199
        avg=0.0
        for x=windowleft,windowright do avg=avg+line(x)
        avg=avg/200.0
        abso(step,z)=avg
    endfor

    ; Fill in un-needed attenuations with zeroes.
    for ts=0,8-optimizationblock.settingsblock.nts do begin
        abso(ts,z)=0
```

```
            thickness(ts)=0
        endfor
        ; Add zero-attenuation 'air step'
        X1=[thickness,0.0]
        Y1=[abso(*,z),0.0]
        ;a = [0.0,-2]

        ; Initialise variables for inner amoeba.
;        thicknessblock =  {ThicknessAl:optimizationblock.settingsblock.ThicknessAl, ThicknessCu:testcopper, $
;                          ThicknessExFilter:optimizationblock.settingsblock.ThicknessExFilter}
        thicknessblock =  {ThicknessAl:optimizationblock.settingsblock.ThicknessAl, ThicknessCu:testcopper, $
                          ThicknessExFilter:optimizationblock.settingsblock.ThicknessExFilter}
        variableblock =   {X1:X1, Y1:Y1, material:material}
        tungstenattempts = fltarr(100000)
        csiattempts = fltarr(100000)
        attemptnumber = 0
        amoebablock = {tungstenattempts:tungstenattempts, csiattempts:csiattempts, attemptnumber:attemptnumber}
        completeblock = {spectrumblock:optimizationblock.spectrumblock, filterblock:optimizationblock.filterblock,
thicknessblock:thicknessblock, $
                         variableblock:variableblock, amoebablock:amoebablock}

        ; Run and catch exceptions from inner amoeba.
        Result = amoebafunction(0.00001,Function_Name='Funct',Function_Data=completeblock,P0=[0.0d,alog(0.01)],nmax=5000, $
          scale=[0.001,0.2],Function_Value=error)
        if Result(0) EQ -1.0 then begin
            failure = dialog_message("The computation failed to converge. Run again using different parameters")
            error = Result(3)
            printf, parafile, Result(1), Result(2), testcopper
        endif else begin
            printf, parafile, Result(0), exp(Result(1)), testcopper
        endelse
        TotalError += error(0)

        ; Make virtual-wedge attenuations with real thicknesses/materials and optimized inner-amoeba values.
        attenuation,x1,Result,completeblock,0,Output

        ; Plot line attenuations (real=red, simulated=white).
        if z eq 0 then begin
            plot,Output(9-optimizationblock.settingsblock.nts:9), background=16777215, color=0, $
                xtitle="Attenuation Filter Number", ytitle="Linear Attenuation (arbitrary units)"
        endif else begin
            oplot,Output(9-optimizationblock.settingsblock.nts:9), color=0 ; simulated attenuations
```

```
        endelse
        oplot,y1(9-optimizationblock.settingsblock.nts:9),color=255 ; measured attenuations
        oplot,(Output(9-optimizationblock.settingsblock.nts:9) - y1(9-optimizationblock.settingsblock.nts:9))*10+1,color = 65280
        ; residuals+1
        void = WIDGET_EVENT(/NOWAIT)

        ; Make virtual-wedge attns with 300-step wedge, target material and optimized inner-amoeba vals, and create polynom.
        attenuation,XX,Result,completeblock,1,Output
        XX1=Output(0:TotalNumber-1)
        YY1=XX(0:TotalNumber-1)*optimizationblock.filterblock.MuSpecimen/XX1
        ResultPolyFit=poly_fit(XX1,YY1,8)

        ; Write poynomial to calibration file, with zero y-intercept.
        writeu, calfile, ResultPolyFit
        writeu, calfile, [0.0]
    endfor
    free_lun, calfile
    free_lun, parafile

    ; User reassurance and return error for global amoeba.
    print, optimizationblock.settingsblock.thicknesscu, TotalError
    return,TotalError
end

function calibration
e=0.0D
s=0.0D
Energy = fltarr(300)
SourceSpectrum = fltarr(152,301)
SourceID = " "

finished = userinterface()

; Get settings file
openr, settingsfile, 'settings.txt', /get_lun
settingsblock = create_struct('dummy',0)
settingsblock = create_struct(settingsblock,'extrafiltering', '')
settingsblock = create_struct(settingsblock,'immersionfiltering', '')
for i=0,18 do begin
    temp=''
    readf, settingsfile, temp, format='(a)'
    if i eq 0 then settingsblock = create_struct(settingsblock, 'MaxVoltage', float(temp))
```

```
    if i eq 1 then settingsblock = create_struct(settingsblock, 'CalVoltage', float(temp))
    if i eq 2 then settingsblock = create_struct(settingsblock, 'Angle', fix(temp))
    if i eq 3 then settingsblock = create_struct(settingsblock, 'nts', fix(temp))
    if i eq 4 then settingsblock = create_struct(settingsblock, 'ThicknessAl', float(temp))
    if i eq 5 then settingsblock = create_struct(settingsblock, 'ThicknessCu', float(temp))
    if i eq 6 then settingsblock.extrafiltering = string(temp)
    if i eq 7 then settingsblock.immersionfiltering = string(temp)
    if i eq 8 and settingsblock.extrafiltering eq '1' then settingsblock = create_struct(settingsblock, $
     'ExFilterFile', string(temp))
    if i eq 10  and settingsblock.extrafiltering eq '1' then settingsblock = create_struct(settingsblock, $
     'ThicknessExFilter', float(temp))
    if i eq 11  and settingsblock.extrafiltering eq '1' then settingsblock = create_struct(settingsblock, $
     'DensityExFilter', float(temp))
    if i eq 9 and settingsblock.immersionfiltering eq '1' then settingsblock = create_struct(settingsblock, $
     'ImmersionFile', string(temp))
    if i eq 12  and settingsblock.immersionfiltering eq '1' then settingsblock = create_struct(settingsblock, $
     'DensityImmersion', float(temp))
    if i eq 13  and settingsblock.immersionfiltering eq '1' then settingsblock = create_struct(settingsblock, $
     'DensitySpecimen', float(temp))
    if i eq 14 then settingsblock = create_struct(settingsblock, 'SpecimenFile', string(temp))
    if i eq 15 then settingsblock = create_struct(settingsblock, 'wedgefilename', string(temp))
    if i eq 16 then settingsblock = create_struct(settingsblock, 'calibrationfilename', string(temp))
    if i eq 17 then settingsblock = create_struct(settingsblock, 'parameterfilename', string(temp))
    if i eq 18 then settingsblock = create_struct(settingsblock, 'callines', fix(temp))
endfor
free_lun, settingsfile
if settingsblock.extrafiltering ne '1' then begin
     settingsblock = create_struct(settingsblock, 'ThicknessExFilter', 0.0)
     settingsblock = create_struct(settingsblock, 'DensityExFilter', 0.0)
endif
if settingsblock.immersionfiltering ne '1' then begin
     settingsblock = create_struct(settingsblock, 'DensitySpecimen', 1.0)
endif
reduction = 10 ; Binning of rows for global optimization.

for i = 1,150 do begin
    spectpath = "SourceB_030\" + string(i,format="(i03)") + string(settingsblock.Angle*10,format="(i03)") + ".spc"
    openr, spectfile, spectpath, /get_lun
    readf, spectfile,SourceID ; Remove first line of each spectrum file. Not used again.
    for j = 0,2*i-1 do begin
        readf, spectfile, e, s
        Energy(j) = e
```

```
        SourceSpectrum(i,j) = s
    endfor
    free_lun, spectfile
endfor

spectrumblock = create_struct('Energy',Energy, 'SourceSpectrum', SourceSpectrum, $
     'MaxVoltage', settingsblock.MaxVoltage, 'CalVoltage', settingsblock.CalVoltage)


;f=fltarr(11)
raw = fltarr(600, settingsblock.callines, 9)
openr, wedgefile, settingsblock.wedgefilename, /get_lun
readu, wedgefile, raw
free_lun, wedgefile
rawshrunk = congrid(raw, 600, settingsblock.callines/reduction, 9)


optimizationblock = {settingsblock:settingsblock, spectrumblock:spectrumblock, raw:rawshrunk}

;Reading the Absorption Coefficients from the files
ReadFile,"Al.txt",AbCoeffAl, optimizationblock.spectrumblock
DensityAl=2.698
LinAbCoeffAl = DensityAl*AbCoeffAl
ReadFile,"Cu.txt",AbCoeffCu, optimizationblock.spectrumblock
DensityCu=8.92
LinAbCoeffCu = DensityCu*AbCoeffCu
ReadFile,"W.txt",AbCoeffW, optimizationblock.spectrumblock
DensityW=19.25
LinAbCoeffW = DensityW*AbCoeffW
ReadFile,"CsI.txt",AbCoeffCsI, optimizationblock.spectrumblock
DensityCsI=4.51
LinAbCoeffCsI = DensityCsI*AbCoeffCsI
ReadFile,"Ti.txt",AbCoeffTi, optimizationblock.spectrumblock
DensityTi=4.506
LinAbCoeffTi = DensityTi*AbCoeffTi
ReadFile,"perspex.txt",AbCoeffPerspex, optimizationblock.spectrumblock
DensityPerspex=1.18
LinAbCoeffPerspex = DensityPerspex*AbCoeffPerspex

if fix(optimizationblock.settingsblock.extrafiltering) eq 1 then begin
     ReadFile, optimizationblock.settingsblock.ExFilterFile,AbCoeffExFilter, optimizationblock.spectrumblock
    LinAbCoeffExFilter = optimizationblock.settingsblock.DensityExFilter*AbCoeffExFilter
```

```
endif else begin
     LinAbCoeffExFilter = 0.0
    optimizationblock.settingsblock.ThicknessExFilter = 0.0
endelse

ReadFile, optimizationblock.settingsblock.SpecimenFile, AbCoeffSpecimen, optimizationblock.spectrumblock, MuSpecimen
if fix(optimizationblock.settingsblock.immersionfiltering) ne 1 then optimizationblock.settingsblock.DensitySpecimen=1;
LinAbCoeffSpecimen = optimizationblock.settingsblock.DensitySpecimen*AbCoeffSpecimen
if fix(optimizationblock.settingsblock.immersionfiltering) eq 1 then begin
    ReadFile, optimizationblock.settingsblock.ImmersionFile, AbCoeffImmersion, optimizationblock.spectrumblock
    LinAbCoeffSpecimen = optimizationblock.settingsblock.DensitySpecimen*AbCoeffSpecimen
    LinAbCoeffImmersion = optimizationblock.settingsblock.DensityImmersion*AbCoeffImmersion
    LinAbCoeffSpecimen = LinAbCoeffSpecimen-LinAbCoeffImmersion
    MuIndex=floor(optimizationblock.settingsblock.CalVoltage*2-1+0.01)
    ; (Energy is in half-steps - 0.01 avoids off-by-one errors for anything less than *.995.)
    MuSpecimen = LinAbCoeffSpecimen(MuIndex)
endif

filterblock =     {LinAbCoeffAl:LinAbCoeffAl, LinAbCoeffCu:LinAbCoeffCu, $
                   LinAbCoeffW:LinAbCoeffW, LinAbCoeffCsI:LinAbCoeffCsI, $
                   LinAbCoeffTi:LinAbCoeffTi, LinAbCoeffPerspex:LinAbCoeffPerspex, $
                   LinAbCoeffExFilter:LinAbCoeffExFilter, LinAbCoeffSpecimen:LinAbCoeffSpecimen, $
                   MuSpecimen: MuSpecimen}

; Prepare data blocks for passing to (speedy) global amoeba and (full) local amoeba.
optimizationblock.settingsblock.callines /= reduction
optimizationblock = create_struct(optimizationblock, 'filterblock',filterblock)
optimizationblockfull = {settingsblock:optimizationblock.settingsblock, spectrumblock:optimizationblock.spectrumblock, raw:raw,
filterblock:filterblock}
optimizationblockfull.settingsblock.callines *= reduction
TotalError = 0.0

fulloptimization = amoebafunction(0.00001,Function_Name='optvoltage',Function_Data=optimizationblock, $
     P0=[optimizationblock.settingsblock.thicknesscu],nmax=5000,scale=[optimizationblock.settingsblock.thicknesscu/
10.0],Function_Value=fullerror)
correctedcopper = fulloptimization[0]
; I assert that the minimum is within 1V of the optimized maxvoltage, and that there is an error delta tolerance of 1. The function wi
almost certainly always converge.
localoptimization = amoebafunction(1,Function_Name='optvoltage',Function_Data=optimizationblockfull,
P0=[correctedcopper],nmax=2,scale=0.00001,Function_Value=fullerror)
;;;;;;;;;;;;;;;;;;;;;;;;;;;;;;;;
```

```
endmessage = 'Error = ' + string(fullError) + ' - done with calibration?'
okay = dialog_message(endmessage, /question)
if okay eq 'No' then return, 1 else return, 0
end

;;;;;;;;;; MAIN PROGRAM - allows multiple calibrations
pro carousel
repeating = 1
while repeating eq 1 do begin
    repeating = calibration()
 endwhile
end
```

The script requires the presence of a file names `settings.txt` in the CWD, which contains calibration parameters and documentation. The file is extensible if newer versions of the program require further parameters, by appending the value of the parameter at the end of the section, and the name of the parameter to the end of the file. A sample file is given below.

```
[frame=single]
90
40
22
9
0.120000
0.005000
0
0
D:\Reconstruction\Carousel\water_te.txt
D:\Reconstruction\Carousel\water_te.txt
2.0
1
1
3.156
D:\Reconstruction\Carousel\HAP.TXT
path_to_attenuations_file_CAR.con
calibration_output_file.mcc
parameter_output_file.txt
800
######################### Below are context indicators for the items
above.
Maximum voltage (kV)
Calibration voltage (kV)
Take-off angle (degrees)
Number of thickness steps
```

```
Al filter width (cm)
Cu filter width (cm)
Additional filter (integer - Y/N)*
Liquid immersion (integer - Y/N)**
Additional filter file
Immersion filter file
Additional filter width (cm)
Additional filter density
Immersion liquid density
Specimen density
Specimen absorption coefficient file
Step wedge data file
Calibration output file
Tungsten / CsI parameter output file
Number of lines used for calibration (default: 800)
######################### Empty rows denote empty fields.
If * or ** are 0 then rows may well be empty.
```

Appendix C

Calibration Energy Determination Scripts

The calibration energy determination scripts are written in `Python`. It consists of two parts: the attenuation finder and the LAC/MAC converter.

C.1 Attenuation Finder

The attenuation-producing script is run multiple times in succession in order to optimise the attenuated beam (as detected by the caesium iodide scintillator) to 50% of I_0, thereby finding the half value layer of aluminium for the *MuCAT* 2 system. It contains two procedures, which are called sequentially when the script is run using the command `python attfinder.py beamvoltage filterthickness`.

```
def filterbeam(voltage, filter_thickness):
        """Filters a beam through an aluminium filter.
        Inputs: beam kilovoltage and filter thickness. Output: histogrammed
photon count."""
    from math import exp

    al_density = 2.70 # g cm-3
    al_thicknesses = {'0':0.0, '30':0.1, '40':0.05, '60':0.05, '70':0.05,
'90':0.12, '120':0.0} # cm

    cu_density = 8.94 # g cm-3
    cu_thicknesses = {'0':0.0, '30':0.0, '40':0.0, '60':0.0, '70':0.0, '90':
0.005, '120':0.0411} # cm

    csi_density = 4.51 # g cm-3
    csi_thickness = 0.01419364 # cm

    filter_density = al_density
    filter_thickness = float(filter_thickness)
    filter_name = 'aluminium_50pc_'

    al_thickness = al_thicknesses[voltage]
    cu_thickness = cu_thicknesses[voltage]

    # Prepare X-ray Spectrum
    if voltage == '0':
        printvoltage = '090'
    elif int(voltage) < 100:
        printvoltage = '0'+ voltage
    else:
        printvoltage = voltage
    spectrumfile = open('SourceB_030/' + printvoltage + '220.spc','r')
    spectrumdata = spectrumfile.readlines()
    spectrumfile.close()
    spectrum = [[],[]]
    for i in spectrumdata:
        templine = i.split()
        spectrum[0].append(float(templine[0]))
        spectrum[1].append(float(templine[1]))
    spectrum[0].pop(0) # Remove 0 keV (not in XCOM files)
    spectrum[1].pop(0)

    # Prepare aluminium filter
    aluminiumfile = open('filters/aluminium_sanitized.txt','r')
    aluminiumdata = aluminiumfile.readlines()
    aluminiumfile.close()
    aluminium_filtration = []
    for i in aluminiumdata:
        templine = i.split()
        aluminium_filtration.append(float(templine[1]) * al_density *
al_thickness)

    # Prepare copper filter
    copperfile = open('filters/copper_sanitized.txt','r')
    copperdata = copperfile.readlines()
    copperfile.close()
    copper_filtration = []
    for i in copperdata:
        templine = i.split()
```

```
        copper_filtration.append(float(templine[1]) * cu_density *
cu_thickness)

    # Prepare extra filter
    filterfile = open('filters/didymium_sanitized.txt','r')
    filterdata = filterfile.readlines()
    filterfile.close()
    filter_filtration = []
    for i in filterdata:
        templine = i.split()
        filter_filtration.append(float(templine[1]) * filter_density *
filter_thickness)

    # Prepare CsI 'filter'
    filterfile = open('filters/csi_sanitized.txt','r')
    filterdata = filterfile.readlines()
    filterfile.close()
    csi_filtration = []
    for i in filterdata:
        templine = i.split()
        csi_filtration.append(float(templine[1]) * csi_density *
csi_thickness)
    # Filter and write to file
    outspectrum = []
    if filter_thickness > 0.00000000000001:
        outputname = filter_name + `filter_thickness`
    else:
        outputname = 'nofilter'
    print 'hi'
    outputfile = open(voltage + 'kV_calvoltagefinding/'+ voltage + '_' +
outputname + '.txt','w')
    for i in range(len(spectrum[0])):
        number = spectrum[1][i] * exp(-(filter_filtration[i] +
copper_filtration[i] + aluminium_filtration[i]))
        detected = number * (1 - exp(-csi_filtration[i]))
        output = detected * exp(-filter_filtration[i])
        #if spectrum[1][i] > 0.001:
        #   print `spectrum[0][i]` + '\t' + `output / spectrum[1][i]`
        outputfile.write(`spectrum[0][i]` + '\t' + `output` + '\n')
    outputfile.close()

def attfinder(voltage, thickness):
        """Calculates percentage attenuation."""

    from time import sleep

    #gname = raw_input('Spectrum file: ')
    #fname = raw_input('Attenuated file: ')
    gname = voltage + 'kV_calvoltagefinding/' + voltage + '_nofilter.txt'
    fname = voltage + 'kV_calvoltagefinding/' + voltage + '_aluminium_50pc_' +
thickness + '.txt'

    g = open(gname,'r')
    gdata = g.readlines()
    g.close()

    f = open(fname,'r')
    fdata = f.readlines()
    f.close()
```

```
    gcount = 0.0
    for n in gdata:
        temp = n.split()
        gcount += float(temp[0]) * float(temp[1])

    fcount = 0.0
    for n in fdata:
        temp = n.split()
        fcount += float(temp[0]) * float(temp[1])

    print thickness + 'cm = \t' + `float(thickness)*10000` + ' microns gives '
+ `(1 - fcount/gcount) * 100.0` + ' % attenuation.'

import sys

if __name__ == "__main__":
    if len(sys.argv) == 3:
        filterbeam(sys.argv[1], sys.argv[2])
        attfinder(sys.argv[1], sys.argv[2])
    else:
        print "Incorect syntax. 2 arguments (kilovoltage and thickness) only"
```

C.2 HVL to LAC/MAC Converter

This script prints the linear attenuation coefficient of aluminium (in cm^{-1}) and the mass attenuation coefficient (in $cm^2\ g^{-1}$), and is run using the command `python hvl-lac.py hvl`. It was made separate from the attenuation-finding script in order to maximise portability of code.

```
def getlac(hvl):
        """Calculates LAC and Mass Attenuation Coefficients from Half-Value
Layer for aluminium."""
    from math import log
    aldensity = 2.70 # g cm-3

    lac = -log(0.5)/float(hvl)
    mac = lac / aldensity
    print '\n' + `lac` + ' /cm\n' + `mac` + 'cm2/g\n'

import sys

if __name__ == "__main__":
    if len(sys.argv) == 2:
        getlac(sys.argv[1])
    else:
        print "Incorect syntax. 1 argument (HVL in cm) only"
```

Appendix D

Program Reference

This appendix provides a brief description of the programs and scripts mentioned in the thesis; for a full explanation of their functionality and interrelationships see Chapter 6.

CAROUSEL is the beam hardening calibration program developed in this thesis and described in Section 6.3.3. It can be adapted to optimise different variables.

M2PREPROC applies beam hardening, dark- and light-field corrections to projections.

SHIFTFIX applies horizontal shift and wobble corrections to the projections.

ConeRec reconstructs the projections into a 3D dataset. It may be used to determine the centre of rotation of a specimen in concert with **FBPG**, a graphics-processing unit-enabled reconstruction program, on systems that permit GPU parallelisation.

MTRIM applies cropping and grayscale refinements to allow better visualisation of the reconstruction.

LOAD loads the contents of a `TOM` reconstruction file into IDL for analysis.

AL allows LAC measurements to be averaged over a cylindrical or skewed-cylindrical sample volume, and provides an LAC correction multiplier for aluminium at commonly-used calibration energies. The aluminium correction function has mostly been rendered obsolete.

The programs CAROUSEL, M2PREPROC, SHIFTFIX and ConeRec/FBPG may be combined into a single workflow using the CALRECON Windows batch script.

Appendix E

Abstracts for Conference Presentations and Papers

E.1 List of conference presentations arising from work presented in this thesis

1. Anthony N. Z. Evershed, David Mills, and Graham Davis. Multi-species beam hardening calibration device for x-ray microtomography. In Stuart R Stock, editor, Developments in X-Ray Tomography VIII, volume 8056 of Proc. SPIE, page 85061N, 2012.[1]

   Abstract: Impact-source X-ray microtomography (XMT) is a widely-used benchtop alternative to synchrotron radiation microtomography. Since X-rays from a tube are polychromatic, however, greyscale 'beam hardening' artefacts are produced by the preferential absorption of low-energy photons in the beam path.

   A multi-material 'carousel' test piece was developed to offer a wider range of X-ray attenuations from well-characterised filters than single-material step wedges can produce practically, and optimization software was developed to produce a beam hardening correction by use of the Nelder-Mead optimization method, tuned for specimens composed of other materials (such as hydroxyapatite [HA] or barium for dental applications.) The carousel test piece produced calibration polynomials reliably and with a significantly smaller discrepancy between the calculated and measured attenuations than the calibration step wedge previously in use.

[1] Poster presentation with article in conference proceedings. Poster at E.3 No. 2.

An immersion tank was constructed and used to simplify multi-material samples in order to negate the beam hardening effect of low atomic number materials within the specimen when measuring mineral concentration of higher-Z regions. When scanned in water at an acceleration voltage of 90 kV a Scanco AG hydroxyapatite / poly(methyl methacrylate) calibration phantom closely approximates a single-material system, producing accurate hydroxyapatite concentration measurements. This system can then be corrected for beam hardening for the material of interest.

E.2 List of papers arising from work presented in this thesis

1. Graham R. Davis, Anthony N.Z. Evershed, and David Mills. Quantitative high contrast X-ray microtomography for dental research, Journal of Dentistry (Accepted, e-print pending physical publication.) (2013)
   URL: *http://www.sciencedirect.com/science/article/pii/S0300571213000286*

Abstract:

Objectives X-ray microtomography (XMT or micro-CT) is a miniaturized version of medical CT and has been used extensively for in vitro dental research. The technique allows three-dimensional analyses of both structure and density (or concentration); the latter requiring some a priori knowledge of composition. Commercial XMT systems tend to be optimized for high throughput imaging with less emphasis on accuracy and contrast sensitivity required for mapping mineral concentration in teeth. The aim here is to demonstrate the capabilities of an XMT scanner specifically designed for dental research, especially for studies requiring high contrast resolution or accurate mineral concentration quantification.

Methods The MuCAT scanners use high dynamic range CCD cameras with time-delay integration readout to provide high quality tomographic images, albeit at the cost of long data acquisition times. Accuracy in mineral concentration quantification is achieved using a modelling approach to beam hardening correction, a problem encountered in all XMT systems using conventional X-ray sources.

Results A provisional result shows that the accuracy for quantification of hydroxyapatite concentration of better than 1%.

Conclusion In dentistry, the improved accuracy and contrast sensitivity, together with the non-destructive nature of XMT in general, facilitates studies of de- and re-mineralization and other dynamic processes in teeth. The ability to differentiate subtle differences in mineral concentration allows dead tracts to be traced in three dimensions, linking external pathology in teeth to reactive processes in the pulp. Three examples are presented which

demonstrate the utilization of the MuCAT scanners in current dental research.

Clinical significance The MuCAT X-ray microtomography scanners at Queen Mary, University of London have been optimized for quantification of mineral concentration and are particularly useful for in vitro studies of de- and re-mineralization, excavation and other treatment methodologies as well as gaining further insight into tooth morphology and pathology. Results from such studies will inform development of clinical treatment and management.

E.3 Samples of poster presentations

1. A N Z Evershed, G R Davis, and P Tomlins. Accurate Mineralization Quantification in X-Ray Microtomography. British Society of Oral and Dental Research Meeting (Sheffield, UK, 2011)

EPSRC
Engineering and Physical Sciences Research Council

Institute of Dentistry

Barts and The London School of Medicine and Dentistry

Accurate Mineralization Quantification in X-Ray Microtomography

A. N. Z. Evershed, G. R. Davis, P. Tomlins

Introduction

X-ray microtomography (XMT) is a non-destructive technique for mapping the distribution of X-ray linear attenuation coefficients, which are good proxy measures for mineral concentration, in three dimensions. This has particular relevance to dentistry, as the accurate assessment of dental mineral concentration is crucial to the measurement of effectiveness of remineralization techniques for the treatment of dental caries. The technique is based upon computed tomography (and also known as micro-CT), but with an emphasis on accurate determination of mineral concentration rather than focussing on the structural detail of the sample. A typical XMT system is shown in Figure 1.

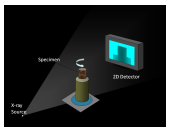

Figure 1. Elements of a cone-beam microtomography system, showing specimen rotation stage. *(Davis, 2011)*

Accuracy in XMT is limited by two main factors arising from the composition of the specimen and the fact that laboratory-based XMT uses a conventional X-ray tube producing a polychromatic beam — a Bremsstrahlung emission spectrum with characteristic peaks depending on the target material used in the X-ray tube. Firstly, materials preferentially absorb low-energy photons as shown in Figure 2, resulting in 'beam hardening' - the X-ray beam becomes more penetrating as it passes through the sample. In specimens with a uniform density (such as the one simulated in Figure 3 and Figure 4) this causes the measured linear attenuation coefficient to dip near the centre of rotation. With more complex samples, streaking and spurious X-ray shadows between denser areas and the centre of rotation can be formed, and the grey level of scanned areas outside the specimen will be artificially raised if the sample has internal voids.

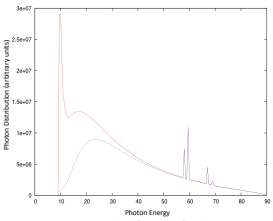

Figure 2. Simulated filtration of 90 kV tungsten emission spectrum by 0.5 mm aluminium, showing before (red solid line) and after (blue dashed line).

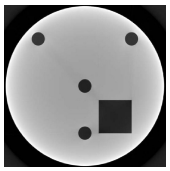

Figure 3. Simulated reconstruction showing beam hardening artefacts in a uniform phantom. Note the faint diagonal streaking between the square cut-out and the top-left round hole. *(Davis and Elliott, 2006)*

Atoms within the sample can also absorb and re-radiate X-ray photons through Compton scattering, leading to increased noise and artefacts from the altered trajectory of the photons. The aim of the project is to quantify and reduce the effect of these errors.

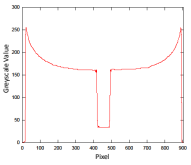

Figure 4. Greyscale line profile taken from the horizontal centre-line of Figure 3, showing cupping artefact and central hole.

Methods

A multi-element 'carousel' (shown in Figure 5) comprising nine well-characterised foils in copper, titanium, aluminium and PMMA, was developed as a test piece in order to generate a wide range of well-defined X-ray attenuations, allowing an eighth-order beam hardening correction polynomial to be generated which is applicable to the major attenuating species in a given specimen (for natural dental specimens, this is generally hydroxyapatite, the major mineral component of teeth).

Figure 5. Beam hardening calibration carousel, showing multi-layer filters.

In some experiments, it is useful to have the specimen immersed during the scanning process, either to reduce the beam-hardening complexity of a multi-species system where one species is water-equivalent, or to allow four-dimensional analysis of a demineralization process. For this, a windowed immersion tank has been constructed (see Figure 6).

Because the tank will be filled with water or an aqueous solution, scatter is a particular concern. It can be quantified by blocking parts of the primary beam using a high atomic number sheet to isolate scatter, and interpolating in the unblocked region by use of Monte Carlo modelling.

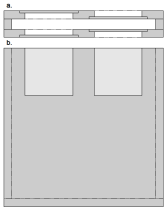

Figure 6. Immersion tank in plan (a) and front elevation (b) views, showing thin viewing windows. A micro-pump is used to circulate fluid in the tank, if needed.

Results and Conclusions

The 'carousel' test piece was brought into service to replace a vertical aluminium step wedge, which provided a smaller range of X-ray attenuations. The summed mean square discrepancy between measured and modelled attenuations was found to be approximately 10 % those typically achieved using the step wedge, and the appearance of beam hardening artefacts was significantly reduced. The immersion tank is currently being characterised before being brought into service. The aim of the project has therefore been partially met, with progress ongoing.

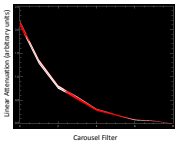

Figure 7. Graph showing eight attenuations of the filter materials at a calibration voltage of 40 kV based on projections taken at 90 kV for the measured (red lines) and modelled (white lines) wedges, showing good agreement.

References and Acknowledgement

(Davis, 2011) G. R. Davis, "Cone-beam tomography," Personal Communication, March 2011.

(Davis and Elliott, 2006) G. R. Davis and J. C. Elliott, "Artefacts in x-ray microtomography of materials," Mater. Sci. Technol., vol. 22, no. 9, pp. 1011–1018, 2006.

We acknowledge the financial support of the Engineering and Physical Science Research Council, under grant EP/G007845/1.

a.n.z.evershed@qmul.ac.uk www.microtomography.com

2. Anthony N Z Evershed, David Mills, and Graham Davis. Multi-species Beam Hardening Calibration Device for X-ray Microtomography. SPIE Optics + Photonics (San Diego, USA, 2012)

EPSRC
Engineering and Physical Sciences Research Council

Barts and The London School of Medicine and Dentistry

Multi-species Beam Hardening Calibration Device for X-ray Microtomography

Anthony N. Z. Evershed, David Mills, Graham Davis

Introduction Impact-source X-ray microtomography, or XMT (as used a modified third-generation geometry with time delay integration at Barts and The London School of Medicine and Dentistry [BLSMD] — see Figure 1), is an inexpensive and readily available alternative to synchrotron radiation microtomography for a wide variety of use cases. It does, however, suffer from a major source of greyscale errors (which measure linear attenuation coefficients [LACs]) as a result of the polychromatic nature of the X-ray beam, known as 'beam hardening'. This poster demonstrates two devices developed to improve the correction of this error source.

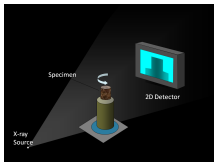

Figure 1. BLSMD's *MuCAT* scanner geometry. The detector is moved past the specimen in synchrony with the CCD clocking rate, in order to eliminate ring artefacts and allow larger projection widths than the detector can itself produce.

Beam Hardening Most materials preferentially absorb low-energy photons by the photoelectric effect, as shown in Figure 2. As polychromatic photons pass through a specimen, the median photon energy is shifted up—the X-rays are 'harder'. This causes LAC under-measurement near the centre of the specimen, producing 'cupping' artefacts in uniform materials, shown in Figure 3.

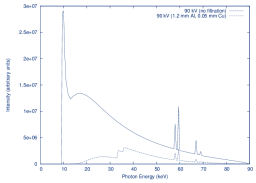

Figure 3a. Filtration of a 90 kVp tungsten X-ray beam through filters used for 90 kVp scanning, showing the up-shift in average photon energy and almost complete attenuation of photons below 20 keV.

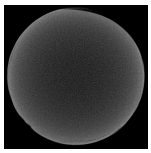

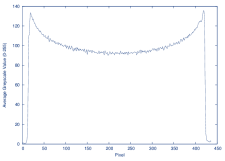

Figures 3b and 3c. Cupping artefact in a macroscopically uniform hydroxyapatite pellet, contrast-enhanced in Figure 3b for clarity and uncorrected for beam hardening. This artefact is similar to the darkening produced by dental caries in dental enamel or dentin, and could generate a false positive. The greyscale profile is the mean of a 20-pixel wide strip surrounding the horizontal centreline of the hydroxyapatite disc.

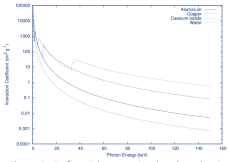

Figure 2. Preferential attenuation by photoelectric absorption of low-energy photons, for commonly-encountered filter and detector materials.

Materials and Methods A multi-species calibration piece comprising nine metal attenuation filters, shown in Figure 4, was used to produce a set of projections measuring attenuation for known thicknesses of metal. The range of metals used (Table 1) allows a much greater spread of attenuations to be produced than from any practical single-species phantom.

Figure 4. 'Carousel' calibration piece, showing filters and frame, including early low-attenuation PMMA filter (since replaced with aluminium.)

These attenuations are used to generate a linearization correction polynomial, initially using an implementation of the Nelder-Mead simplex function to optimise thicknesses of tungsten self-absorption in the X-ray tube target and scintillator thickness, as will as precise accelerating voltage, which are unknown variables in the measurement system. This is then used to simulate the attenuations of a 300-step wedge of the dominant specimen material at the equivalent monochromatic photon energy, to which an eighth-order polynomial is fitted. This polynomial forms the linearization correction.

Projection	Element	Average Thickness (mm)
1	copper	2.093
2	titanium	4.42
3	titanium	2.21
4	titanium	1.105
5	aluminium	3.976
6	aluminium	1.988
7	aluminium	0.994
8	aluminium	0.497
9	aluminium	0.2

Table 1. Material composition of the beam hardening carousel.

In order to generalise the validity of this correction to bimodal specimens with a low-LAC component and a mineralized component, polymethyl methacrylate [PMMA] immersion tanks were constructed with a known thickness (see Figure 5.) This reduces the system to a truncated-LAC mono-modal mineralised specimen with a uniform-thickness water (or water-equivalent) filter. A bimodal (hydroxyapatite/PMMA) commercial calibration phantom produced by Scanco Medical AG was scanned at an accelerating voltage of 90 kV, both in air and immersed in a water-filled tank, and calibrated for hydroxyapatite using the above method.

Results and Discussion The combination of the 'carousel' calibration piece and the linearization correction software produces correction polynomials reliable and significantly more quickly than previous correction methods in use at BLSMD. Initial corrections using the PMMA low-attenuation filter for the ninth projection (as shown in Figure 4), however, had an increased error (typically a total error of 10 rather than 2.) Replacement of this filter by the aluminium foil shown in Table 1 reduced the typical error to 0.05 — a significant reduction.

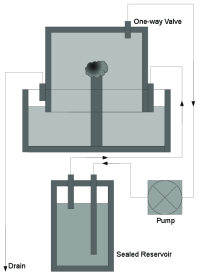

Figure 5. Schematic of the immersion tank system, including multi-species specimen on the mounting post. Clamps not shown for clarity.

The use of an immersion tank successfully reduced the Scanco phantom to a uni-modal system, as shown in Figure 6, with the PMMA region at the centre of the phantom not significantly more attenuating than the water ($\Delta\mu = 0.002 \pm 0.00718$).

Mineral concentration was derived for the four hydroxyapatite rods using the equation below, and found to be consistent with values provided by Scanco Medical AG (see Table 2).

$$C = \frac{\mu_{measured}}{\mu_{specimen} - \mu_{fluid}} \rho_{specimen}$$

Nominal Concentration (g cm^{-3})	Measured LAC (cm^{-1})	Measured Concentration (g cm^{-3})
0.7989	0.74 ± 0.0436	0.82 ± 0.0483
0.3984	0.37 ± 0.0489	0.41 ± 0.0542
0.1990	0.18 ± 0.0464	0.20 ± 0.0524
0.0992	0.08 ± 0.0374	0.09 ± 0.0414

Table 2. Results of immersed scanning of the Scanco Medical calibration phantom. Four rods are shown; the fifth is indistinguishable from the PMMA matrix or the water (as shown in Figure 6.)

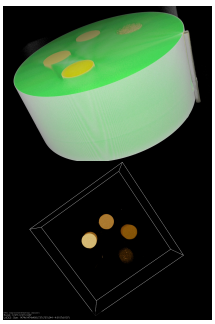

Figure 6. Renderings of the Scanco phantom, in air (top) with manual segmentation, and immersed (bottom) without segmentation, showing reduction to a uni-modal system.

Acknowledgements
The authors wish to thank Mr Steve Figaro of Barts and The London School of Medicine and Dentistry for his advice and technical support in the preparation of this work. Many thanks also to Ajay Limaye of the Australian National University, the writer and maintainer of the *Drishti* volume exploration and presentation tool.

We acknowledge the financial support of the Engineering and Physical Science Research Council, under grant EP/G007845/1.

a.n.z.evershed@qmul.ac.uk www.microtomography.com